Faulting properties and stress field in the northern Alpine foreland: a case study at the Albstadt Shear Zone, Southwest Germany

Zur Erlangung des akademischen Grades einer

Doktorin der Naturwissenschaften (Dr. rer. nat.)

von der KIT-Fakultät für Physik des
Karlsruher Instituts für Technologie (KIT)

genehmigte
Dissertation

von

M.Sc. Mader, Sarah Melanie

Abstract

In the northern Alpine foreland, the region around the town Albstadt on the Swabian Alb is one of the seismically most hazardous areas in Central Europe and characterized by continuous seismic activity. In the last century nine earthquakes with a local magnitude ML ≥ 5.0 occurred. Nevertheless, no surficial expression of the fault is visible.

The earthquakes rupture a N-S or NNE-SSW striking sinistral strike-slip fault zone, located in the upper crust, called the Albstadt Shear Zone (ASZ). The lateral extension and segmentation of the ASZ is under debate. In the area of the ASZ the Hohenzollerngraben (HZG) is the only tectonic feature visible at the surface. The HZG is described as a 2-3 km deep aseismic graben structure with inverted relief. A seismo-tectonic model of Reinecker and Schneider (2002) relates the HZG and other similar graben structures to the north and south with the movement of the ASZ. The ASZ is partially decoupled from the surface resulting in the opening of the step-like arranged graben structures.

The knowledge about the fault characteristics of the ASZ (e.g. extension, segmentation) is limited, as most of the previous studies focused on strong events and their aftershock sequences. Furthermore, the location of the ASZ in the northern Alpine foreland makes it a suitable site to study the stress field and the driving forces of the observed intra-plate seismicity. To analyze the fault characteristics of the ASZ and the related stress field I focus on the continuous seismic activity in the years 2011 to 2020 in the area of the ASZ.

Within the AlpArray seismic project additional seismic stations were installed in the vicinity of the ASZ at the end of 2015. To improve the event locations and the detectability of low-magnitude events I further densified the seismic station network with additional seismic stations in the research area within the StressTransfer seismic network in 2018.

I complemented the earthquake catalog for the years 2011 to 2018 of the state earthquake service of Baden-Württemberg with additional phase arrival times at the AlpArray and StressTransfer seismic stations. With the extended data set I invert for new minimum 1D seismic v_p and v_s velocity models of the upper crust with station delay times. The resulting velocity models ASZmod1 are robust and simple and the seismic velocity increases with depth. The corresponding station delay times can be explained by the lateral depth variation of the crystalline basement.

The relocated continuous seismic activity within 2011 to 2018 aligns north-south slightly east of the 9°E meridian. The main focus of the seismicity is between the towns Albstadt and Tübingen. I observe several subclusters indicating a possible segmentation of the ASZ. The majority of the determined fault plane solutions indicates the already known steeply dipping NNE-SSW striking sinistral strike-slip faulting of the ASZ. Nevertheless, I also observe NNW-SSE striking fault planes and minor components of normal and reverse faulting.

To make use of the densified station network since 2018 I apply a template matching detection routine to search for earthquake sequences within 2018 to 2020. In total, I identified six

earthquake sequences (with more than 10 events), of which the three biggest sequences (more than 100 events) can be separated in one fore- and aftershock sequence and two earthquake swarms (October 2018 and September 2019). This observation is new, as earthquake swarms were so far not observed in the area of the ASZ. By determining relative event locations together with fault plane solutions of the earthquake sequences the active fault planes could be identified. I observe three different fault types: the already known NNE-SSW striking sinistral strike-slip ASZ at depths of 5-10 km. Beneath the HZG in 11-15 km depth I identify a NW-SE striking dextral strike-slip fault zone. Despite of the same orientation as the HZG, the depth difference between the NW-SE striking fault zone and the shallow HZG boundary faults exclude a direct connection. Though the overlapping location may hint at an existing NW-SE striking weakening zone in the upper crust. At the interception of the ASZ and the NW-SE striking fault zone NNW-SSE striking sinistral strike-slip and normal faulting events are observed and indicate a heterogeneous deformation zone with complex faulting.

The determined direction of the maximum horizontal stress of 140-149° is in good agreement with prior studies, indicating that the stress field in the area of the ASZ is mainly generated by the regional plate driving forces and the Alpine topography. I observe a change of the stress field with depth. Down to about 7-8 km depth the maximum horizontal stress is bigger than the vertical stress. Below this depth, the vertical stress is the main stress component.

The newly derived seismo-tectonic model of the seismicity on the Swabian Alb indicates the activation of weakening zones or pre-existing structures favorably aligned in the current tectonic stress field. This is also observed for other areas of intra-plate seismicity.

Contents

List of Figures

List of Tables

1. Introduction

1.1. Research Aims

Seismicity in Germany and the adjacent regions is mainly focused along the Alpine mountain chain, in the northern Alpine foreland and along the Rhine Graben System (Fig. 1.1). In the northern Alpine foreland intra-plate seismicity is observed especially at the Albstadt Shear Zone (ASZ), which is one of the seismically most active regions in Central Europe with nine earthquakes with a local magnitude $ML \geq 5.0$ in the last century and continuous micro-seismic activity (Schwarz et al., 2019; Grünthal and the Global Seismic Hazard Assessment Program (GSHAP) Region 3 Working Group, 1999; Grünthal et al., 2018). Strong earthquakes like the ML 5.7 earthquake in 1978 may cause major damage, with an estimated loss of several 100 million Euro related with damages to buildings only (Tyagunov et al., 2006).

The most dominant driving force behind the seismic activity in Central Europe is the plate collision between the Eurasian, African and the Adriatic plate and its resulting formation of the Alpine orogeny (Müller et al., 1992; Reicherter et al., 2008; Piña-Valdés et al., 2022). As other driving forces far-field tectonic processes are assumed like the mid-Atlantic ridge spreading (Müller et al., 1992; Reicherter et al., 2008; Piña-Valdés et al., 2022). Those processes dominate the tectonic stress field in Central Europe which is characterized by NW-SE horizontal compression and NE-SW extension (Müller et al., 1992; Kastrup et al., 2004; Heidbach et al., 2016). The location of the ASZ in the northern Alpine foreland in combination with its continuous seismic activity and the high seismic hazard and risk makes the ASZ a prominent area to study the driving forces of intra-plate seismicity and the tectonic stresses of the Alpine orogeny transferred into the foreland.

The ASZ is located in the area of the town Albstadt on the Swabian Alb, a low mountain range in Southwestern Germany (Fig. 2.1). At least since the ML 6.1 earthquake in 1911 the region is known for damaging earthquakes and continuous micro-seismic activity (Fig. 2.2, Reicherter et al., 2008; Stange and Brüstle, 2005; Leydecker, 2011; Grünthal et al., 2018). Only two other damaging events are historically described. Those occurred to the north near the town Tübingen in 1655 (Leydecker, 2011). The ASZ is described as N-S or NNE-SSW striking sinistral strike-slip fault based on fault plane solutions and after shock distributions (Fig. 2.2, Haessler et al., 1980; Turnovsky, 1981; Stange and Brüstle, 2005). An expression of the ASZ at the surface is not visible. The only other tectonic feature in the area of the increased seismicity is the NW-SE striking Hohenzollerngraben (HZG, Fig. 2.1, 2.2). The HZG is a 2 - 3 km deep graben structure with inverted relief, which is assumed to be aseismic (Schädel, 1976; Reinecker and Schneider, 2002). As there are several similar graben structures like the HZG to the south and north of the ASZ, Reinecker and Schneider (2002) propose a tectonic model connecting the opening of the graben structures with the movement of the ASZ in the

subsurface. In this tectonic model the ASZ is partially decoupled from the surface and the movement is transferred to step-like graben structures at the surface, like the HZG (Reinecker and Schneider, 2002). This model is supported by the spatial distribution of the seismicity, as the majority of events occur below 2 km depth (Stange and Brüstle, 2005).

As there is no expression of the active fault at the surface one can only study the fault characteristics of the ASZ by its seismicity. For this reason the extension of the ASZ is still under debate. Whereas Reinecker and Schneider (2002) see a extension of the ASZ from the Lake Constance to north of the town of Stuttgart, Stange and Brüstle (2005) doubt this extension due to the focus of the seismic activity on the Swabian Alb (Fig. 2.1). Furthermore, most studies related with the seismicity on the Swabian Alb focused on the strong magnitude events and their aftershocks (e.g. Haessler et al., 1980; Turnovsky, 1981; Stange and Brüstle, 2005). Therefore, the knowledge of the fault characteristics (segmentation, depth extension) of the ASZ is limited. A better knowledge of the fault properties would for example allow to estimate the maximum possible earthquake magnitude (Wells and Coppersmith, 1994). Also the amount of strong seismic events in the last century and the related seismic hazard and risk rises the question what drives the seismic activity on the Swabian Alb.

Within this thesis I want to address the following open questions regarding the ASZ:

- What are the fault characteristics of the ASZ?
    - What are the vertical and horizontal extensions of the ASZ?
    - Is the ASZ one fault or are there several fault zones or a segmentation?
    - If there are several faults, how are they connected?
- Is there a relationship to the graben structure like the HZG?
- How is the local stress field oriented and is there a change in the stress field with depth?
- What mechanisms and related stresses drive the intra-plate seismicity at the ASZ in the northern Alpine foreland?

To analyze the open questions regarding the ASZ I take advantage of the already densified seismic station network in the area due to the AlpArray seismic project from 2016 to 2022 (Hetényi et al., 2018). Additionally, I further densify the seismic station network by installing five seismic stations in the area of the ASZ within the StressTransfer project (2018 - ongoing, Mader and Ritter, 2021). The densified station network allows to analyze the continuous micro-seismic activity of the ASZ, which images the active fault.

I analyze the earthquake catalog of the state earthquake service of Baden-Württemberg (LED) from the year 2011 to 2020. I complement this event catalog with additional phase arrival times at the additional seismic stations (AlpArray since 2016 and StressTransfer since 2018). To improve hypocenter event locations in the area I determine a new minimum 1D seismic velocity model for the area of the ASZ. Fault plane solutions for even small magnitude events allow to analyze the fault characteristics and are further inverted to determine a depth-dependent stress field. Also I implement a template matching event detection routine to search for additional small magnitude events. Finally, I determine relative event locations for the detected
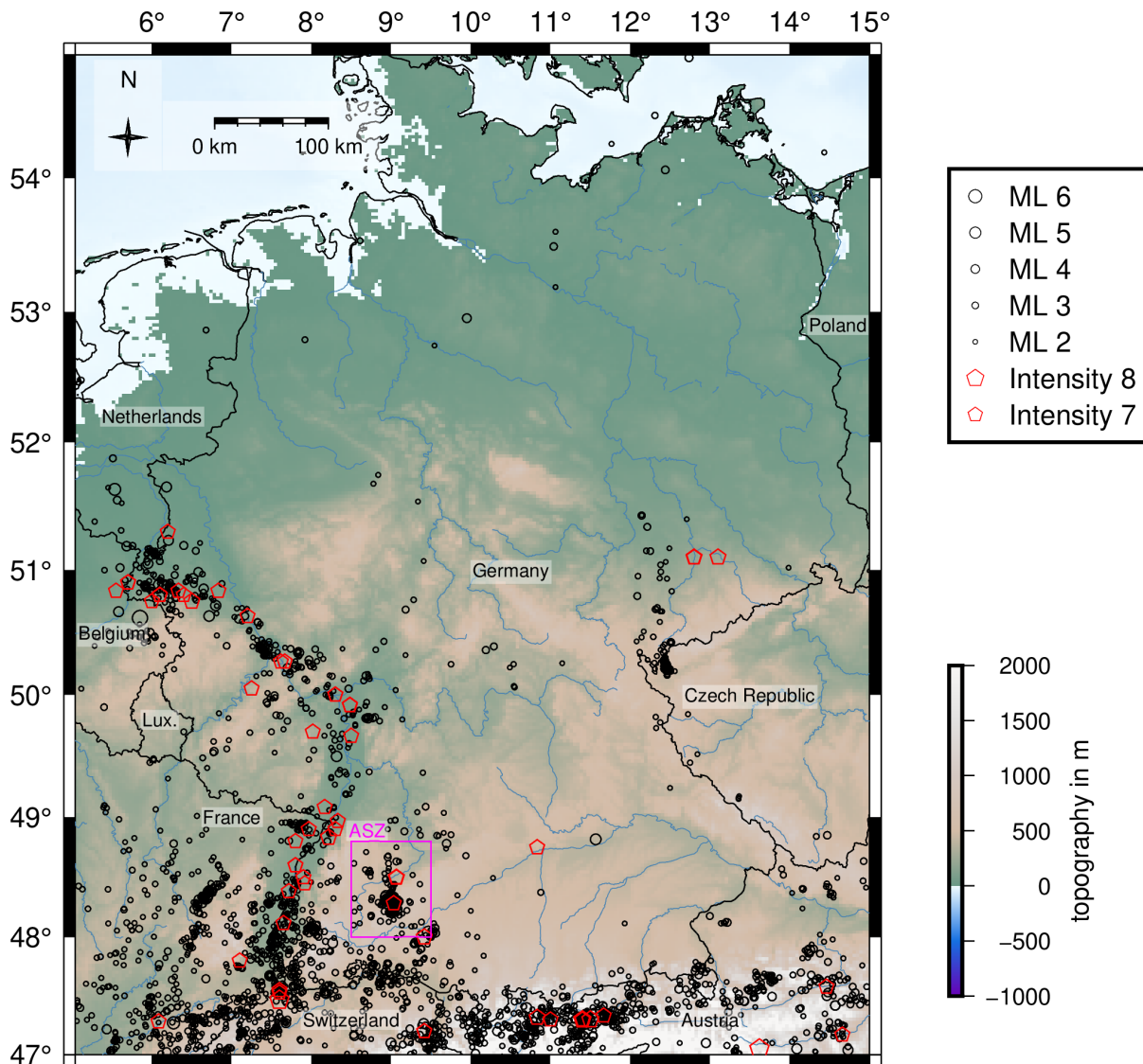
Figure 1.1.: Tectonic event catalog of Bundesanstalt für Geowissenschaften und Rohstoffe (BGR) (2012) from 800 until 27 March 2023 for Germany and adjacent regions. All events with a local magnitude $ML \geq 2$ are displayed as circles and scaled with magnitude. Strong historical events without an estimate of the local magnitude are scaled by their intensity and displayed as pentagons (intensity ≥ 7). Magenta rectangle highlights the area of continuous seismic activity related with the Albstadt Shear Zone (ASZ) (see Fig. 2.2, 6.1b) and 7.2). Topography is based on SRTM15+ (Tozer et al., 2019).

earthquake sequences to get a sharp image of the active fault. All results are combined in a new model describing the rupture processes in the area of the ASZ.

1.2.   Outline of the thesis

In this section the structure of the thesis is outlined. Chapter 2 gives an overview of the geological and seismotectonic setting of Southwestern Germany and the area of the ASZ. Also

the stress field in the research area and the historical and current seismicity of the ASZ is described. Finally, I shortly describe intra-plate seismicity and their related driving forces.

The used data (waveform data of seimic stations and event catalog) are summarized in chapter 3. Furthermore, I describe the self-written picking program for consistent phase arrival time determination at the additional seismic stations. Also a short summary of the used seismological software in relation to this thesis is given. Chapter 4 focuses on the theory behind the used software programs.

To address the research aims, the first step within this thesis was the installation of additional seismic stations in the research area in 2018 to improve the accuracy of event locations and the detection of small magnitude events. The process of site selection, station installation and a quality assessment of the seismic station waveform data can be found in chapter 5. Chapter 5 is already published as Mader and Ritter (2021).

In chapter 6 I analyze the continuous seismic activity from 2011 to 2018. A minimum 1D seismic velocity model with station delay times for the research area is determined, the event catalog is complemented with additional phase arrival times and relocated, fault plane solutions are determined, as well as the stress field. Chapter 6 is published as Mader et al. (2021).

Chapter 7 focuses on the detailed analyses and search for earthquake sequences from 2018 to 2020. I make use of the densified station network and implement a template matching routine to search for small-magnitude events and earthquake sequences. Relative event locations together with fault plane solutions of the identified earthquake sequences allow to identify the faulting mechanism. A new model for the rupture processes is presented. Chapter 7 is submitted to a peer-review journal and currently in review process.

In chapter 8 I summarize all results and answer the research questions. Finally, the thesis is concluded by an outlook on possible future work in the area of the ASZ and the northern Alpine foreland.

2. Geological and seismotectonic overview

2.1. Tectonic and geological setting

In Central Europe the dominating tectonic driving force is the collision of the Eurasian, Adriatic and African tectonic plates and the resulting formation of the Alpine mountain chain (Müller et al., 1992; Reicherter et al., 2008; Piña-Valdés et al., 2022). My area of interest, the ASZ, is located in the northern Alpine foreland on the Swabian Alb, a mountain range in southern Germany (Fig. 2.1).

The South German Block, the Molasse Basin (MB) and the Upper Rhine Graben (URG) are the main tectonic features in southern Germany (Reicherter et al., 2008; Meschede and Warr, 2019; Ring and Bolhar, 2020). The South German Block is a tectonic unit and bounded by
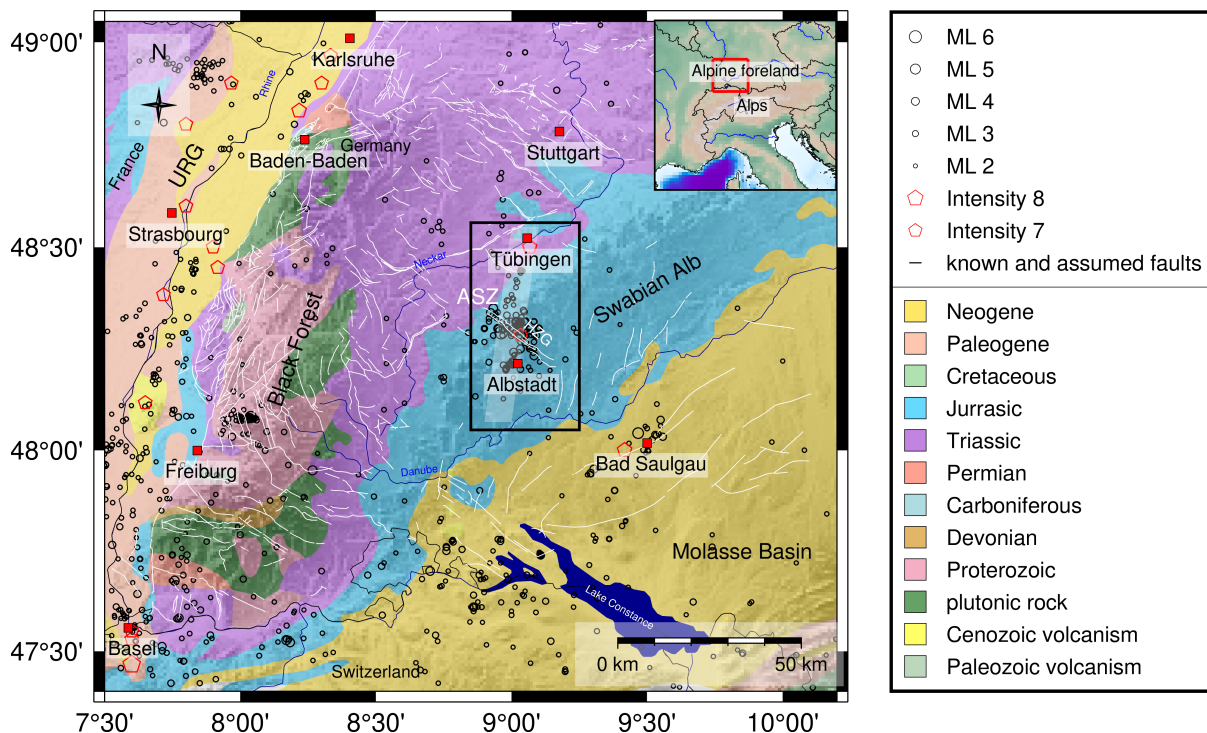
Figure 2.1.: Overview of the geology of Southwestern Germany (geology after Asch, 2005). Tectonic event catalog of Bundesanstalt für Geowissenschaften und Rohstoffe (BGR) (2012) from 800 until 27 March 2023 for Germany and adjacent regions, like in Fig. 1.1. Black frame highlights the area of the Albstadt Shear Zone (ASZ) which is shown as close-up in Fig. 2.2. White lines show known and assumed faults in the area of the state Baden-Württemberg (Regierungspräsidium Freiburg: Landesamt für Geologie, Rohstoffe und Bergbau (Hrsg.), 2019). Topography is based on SRTM15+ (Tozer et al., 2019). HZG = Hohenzollerngraben.
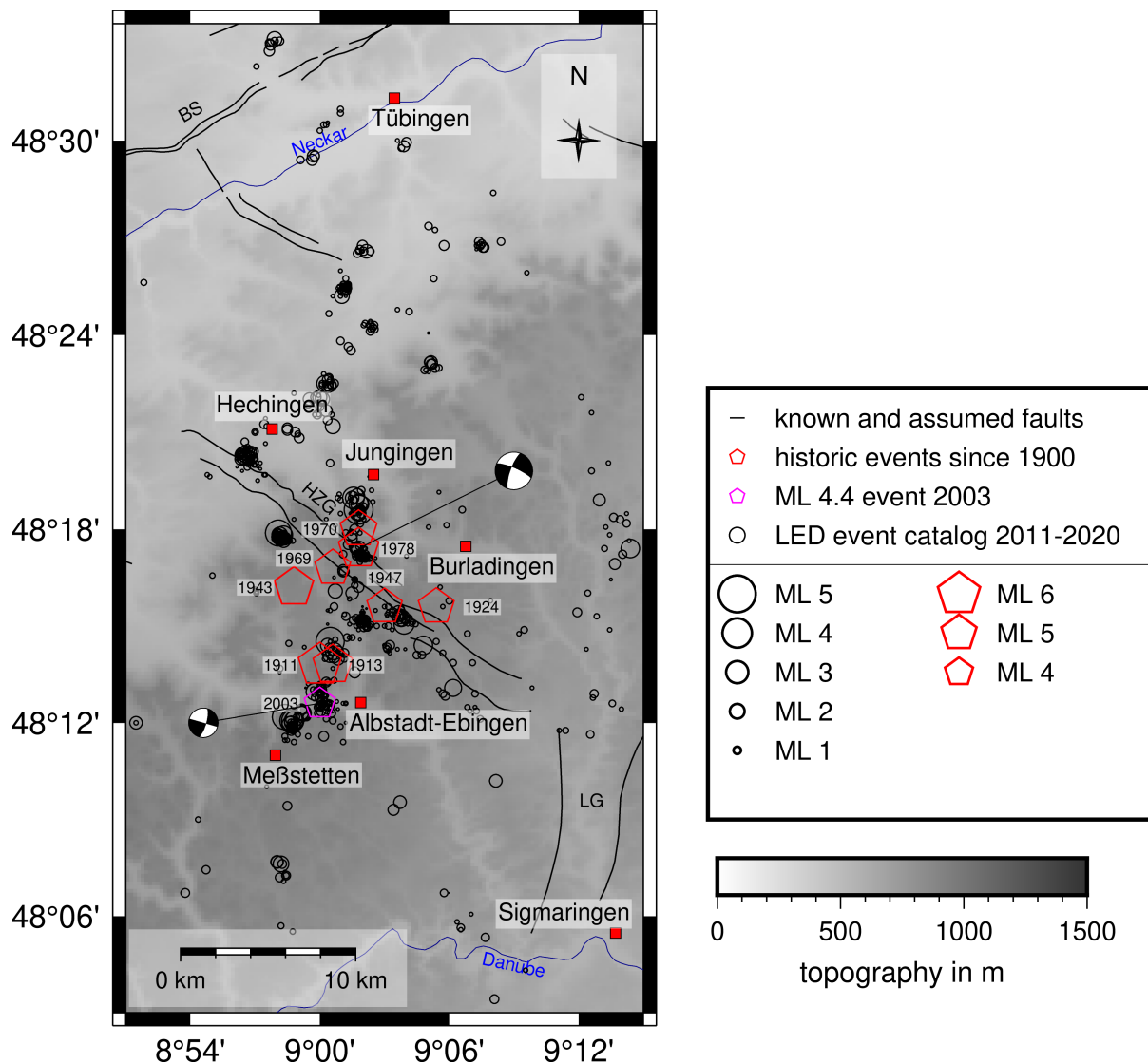
Figure 2.2.: Overview of the area of continuous seismic activity, related with the Albstadt Shear Zone (ASZ). Events within the LED event catalog from 2011 to 2020 are shown as black circles (Bulletin-Files des Landeserd-bebendienstes B-W, 2011-2020), red pentagons are the strongest historic events since 1900 with a local magnitude ML ≥ 5.0 (Schwarz et al., 2019) and the magenta pentagon highlights the ML 4.4 earthquake in 2003, which is one of the best observed events in the area (Stange and Brüstle, 2005). Fault planes solutions of the 1978 earthquake after Turnovsky (1981) and the 2003 earthquake after Stange and Brüstle (2005) are displayed. Black lines show known and assumed faults (Regierungspräsidium Freiburg: Landesamt für Geologie, Rohstoffe und Bergbau (Hrsg.), 2019). Topography is based on SRTM15+ (Tozer et al., 2019). HZG = Hohenzollerngraben, LG = Lauchertgraben, BS = Bebenhausen Fault.

the URG in the west, the MB in the southeast and the crystalline basement of the Bohemian Massif in the northwest in a triangular shape (Meschede and Warr, 2019; Ring and Bolhar, 2020). The URG is part of the European Cenozoic Rift System formed due to the deformation related with the Alpine orogeny (Reicherter et al., 2008; Meschede and Warr, 2019). Due to the extension in the URG, which is partly related with updoming, and the Alpine orogeny the polymetamorphic basement is tilted towards southeast to east (Reicherter et al., 2008;

Meschede and Warr, 2019). Furthermore, the depth of the crystalline basement varies strongly in southern Germany due to the different uplift and erosional states of the tectonostratigraphic units (Rupf and Nitsch, 2008). In the Black Forest mountain range the Paleozoic basement, consisting of metamorphic and magmatic rocks, is exposed, as the area experienced the most uplift during the extension of the URG (Fig. 2.1, Reicherter et al., 2008; Meschede and Warr, 2019). The southern boundary of the South German Block is the MB, the foreland basin of the Alpine mountains. The MB formed due to the subduction of the Eurasian plate under the Adriatic/African plate and the Alpine orogeny (Geyer and Gwinner, 2011; Meschede and Warr, 2019). The MB is filled with Neogene sediments under which the sedimentary layers of the Swabian Alb disappear dipping downwards with 4 - 5° to the southeast due to flexural bending of the lithosphere related with the Alpine mountains (Fig. 2.1, Geyer and Gwinner, 2011; Ibele, 2015; Meschede and Warr, 2019). The sedimentary cover in the area of the Swabian Alb consists of Jurassic limestone, marl, silt and clay (Geyer and Gwinner, 2011; Meschede and Warr, 2019). The resistant carbonates of the Late Jurrasic form an escarpment landscape in the north which is cut by several large fault systems, still detectable in present-day topography (Fig. 2.1, Reicherter et al., 2008). North and northwest of the Swabian Alb the sedimentary cover of the South German Block is made of Triassic rocks (Meschede and Warr, 2019).

In southern Germany one can observe mainly three different types of faults: NNE-SSW to N-S, NW-SE and ENE-WSW oriented fault planes (Reicherter et al., 2008). The first type can be observed at the ASZ, the Lauchertgraben and parallel to the URG (Fig. 2.2). Those fault planes are associated with sinistral strike-slip movement (Reicherter et al., 2008; Geyer and Gwinner, 2011). Dextral strike-slip and/or normal faulting can be observed at the NW-SE striking fault planes, like for example the HZG (Fig. 2.1, Reicherter et al., 2008). Some of the ENE-WSW striking fault planes, like the Bebenhausen Fault, which is a segment of the Swabian Line, are associated with dextral strike-slip or reverse faulting, but are mainly inactive (Fig. 2.2, Reicherter et al., 2008). On most faults only moderate displacements are observed during the last about 5 Myr (Reicherter et al., 2008).

In the current area of continuous seismic activity of the ASZ, only one tectonic feature is visible: the NW-SE striking HZG (Fig. 2.2). The HZG is described as an aseismic graben structure with an inverted relief (Schädel, 1976). Based on the maximum width of 1.5 km and dip angles at the boundary faults of 60 - 70°, the depth range of the HZG is estimated to be 2 - 3 km (Schädel, 1976). Other similar striking graben structures can be observed to the north and south (Filder Graben, Rottenburg Flexure, Achalm half-graben, western Lake Constance faults and Hegau, Reinecker and Schneider, 2002; Geyer and Gwinner, 2011). To relate those graben structures with the movement of the ASZ, Reinecker and Schneider (2002) proposed a neo-tectonic model. Based on the results of Tron and Brun (1991), the movement of the ASZ is partially decoupled from the overlying sedimentary layers. In those sedimentary layers steplike arranged graben structures are opened by the strike-slip movement below (Tron and Brun, 1991; Reinecker and Schneider, 2002). As decoupling horizon Reinecker and Schneider (2002) propose a layer composed of mechanically weak Middle Triassic evaporites. Another possible partially decoupling horizon is the bottom of the sediments, as no earthquake occurs above 2 km depth (Stange and Brüstle, 2005). In the north and northwest of the research area there is the ENE-WSW striking Swabian Line, which extends in the west from the Black Forest along the Swabian Alb escarpment towards east, the segment near Tübingen is called the Bebenhausen Fault (Fig. 2.2, Reicherter et al., 2008; Geyer and Gwinner, 2011). In the east the

N-S striking Lauchert Graben is located, parallel to the ASZ (Fig. 2.2, Geyer and Gwinner, 2011).

2.2. Stress field in the northern Alpine foreland

In the World Stress Map project, stress measurements from different sources are combined. The stress is determined by fault plane solutions, overcoring, borehole breakouts and hydraulic fracturing (Zoback, 1992; Heidbach et al., 2010b, 2016). By analyzing the global data set a relation between the orientation of the maximum horizontal compressional stress S_H and the absolute plate-motion was identified, suggesting the plate boundary forces as major driving forces of the global stress pattern (Zoback, 1992; Heidbach et al., 2010a). Other more regional sources identified are mountain belts and zones of widespread glacial rebound (Müller et al., 1992; Heidbach et al., 2007; Reinecker et al., 2010). The global stress pattern consists of many areas (like eastern US, Canada) where the orientation of S_H is stable over thousands of kilometers (Heidbach et al., 2010a). This trend is not observed for Europe, Alaska and the Aleutians, the Southern Rocky Mountains, Scandinavia, most of Himalaya and Indonesia. In those areas the direction of S_H changes with a shorter wavelength (hundreds of kilometers, Heidbach et al., 2010a). Here either regional or even local stress sources may contribute in the same magnitude like the plate boundary forces, or the plate boundary forces vary over a shorter distance (Heidbach et al., 2010a).

The stress field in Southwestern Germany is characterized by NW-SE horizontal compression and NE-SW extension and developed in the late Miocene (Becker, 1993; Kastrup et al., 2004). The direction of S_H is estimated to be 150° ± 24° for Southwestern Germany and 145° ± 26° for whole Western Europe (Müller et al., 1992; Plenefisch and Bonjer, 1997; Reinecker et al., 2010; Heidbach et al., 2016). As major driving force of the stress field in Western Europe the plate-driving forces are identified. Also there are local variations due to large geological structures like the Alpine mountains. A driving force of the local stress field could be the gravitational potential energy of the Alpine topography, as the stress field orientation in the northern Alpine foreland is always perpendicular to the Alpine front (Reinecker et al., 2010). Kastrup et al. (2004) also observe a variation of the stress field along the Alpine front, but suggests the indentation of the Adriatic Block as driving force.

In the area of the ASZ the direction of S_H is quite constant. Only directly south of the HZG (Albstadt-Truchtelfingen) and within the HZG (Albstadt-Onstmettingen) a rotation of S_H about 20° counterclockwise into the strike of the HZG is observed (130°, Baumann and Becker, 1986), which may be caused by a reduced shear resistance.

2.3. Seismicity of the Albstadt Shear Zone

The ASZ is one of the seismically most active regions in Central Europe with a high probability of damaging earthquake occurrence (Grünthal and the Global Seismic Hazard Assessment Program (GSHAP) Region 3 Working Group, 1999; Grünthal et al., 2018). Before the 19th

century only two earthquakes are documented close to the area of today's continuous seismic activity of the ASZ (Leydecker, 2011; Schwarz et al., 2019). They occurred close to the town Tübingen in the year 1655 and had an intensity of 7 to 7.5 (Fig. 2.1, Leydecker, 2011). Reports of continuous seismic activity in the area close to the towns Albstadt and Hechingen started in the middle of the 19th century (Schneider, 1980; Reinecker and Schneider, 2002; Leydecker, 2011; Schwarz et al., 2019). Since the 20th century the area is also known for damaging earthquakes with local magnitudes ML $\geq$ 5.0 (Fig. 2.2, Leydecker, 2011; Schwarz et al., 2019). The strongest event is the ML 6.1 earthquake on 16th November 1911 (e.g. Schneider, 1979; Stange and Brüstle, 2005; Schwarz et al., 2019). It caused damage to buildings and triggered landslides in the epicentral area and also close to Lake Constance in about 40 - 50 km distance (Sieberg and Lais, 1925; Reicherter et al., 2008). Nevertheless, no surface expression of the fault is visible. Further damaging events with a ML $\geq$ 5.0 occurred in 1913 (ML ~5.6), 1924 (ML ~5.1), 1943 (ML ~5.5 and ML ~5.6), 1947 (ML ~5.0), 1969 (ML ~5.1), 1970 (ML ~5.2) and 1978 (ML ~5.7, Schwarz et al., 2019). The so far best observed event is the 22nd March 2003 ML 4.4 earthquake, which is currently the strongest recorded event in the area of the ASZ since the ML 5.7 event in 1978 (Stange and Brüstle, 2005). Based on the interpretation of the historic seismicity the return period of earthquakes with a magnitude of 5 was estimated to be approximately 1000 years (Schneider, 1980; Reinecker and Schneider, 2002) and the average seismic dislocation rates along the ASZ are about 0.1 mm/a (Schneider, 1993). This determined return period of 1000 years seems to be quite large from the current point of few and needs to be revised with the new earthquake catalogs and for longer time periods.

Fault plane solutions of the stronger events in combination with aftershock distributions or macroseismic analyses identify the ASZ as a N-S or NNE-SSW striking steeply dipping sinistral strike-slip fault (Fig. 2.2, e.g. Schneider, 1979; Haessler et al., 1980; Turnovsky, 1981; Stange and Brüstle, 2005). The N-S trend is also observed in the current continuous seismic activity (Fig. 2.2, Bulletin-Files des Landeserdbebendienstes B-W, 2011-2020). The lateral extension is still under debate, as Schneider (1979, 1980, 1993) or Reinecker and Schneider (2002) discuss an extent of the ASZ based on the seismicity from northern Switzerland close to the Lake Constance up to the North of the town Stuttgart, whereas Stange and Brüstle (2005) question this extension as the focus of the continuous seismic activity is located on the Swabian Alb (Fig. 2.1). The depth range of the seismicity is about 2 - 20 km, which indicates, that the ASZ is located in the crystalline basement of the upper crust (Schneider, 1980; Gajewski and Prodehl, 1985; Aichroth et al., 1992; Stange and Brüstle, 2005).

Currently, an episode of increased seismic activity with several events with a ML $\geq$ 3.0 started in November 2019. In the years 2011 to 2018 the earthquake catalog of the LED reports only three events with ML $\geq$ 3.0 (Bulletin-Files des Landeserdbebendienstes B-W, 2011-2020), whereas since November 2019 until today (2023) already nine earthquakes with a ML $\geq$ 3.0 occurred (Regierungspräsidium Freiburg: Landesamt für Geologie, Rohstoffe und Bergbau, 2023). The determined ML range from 3.0 up to 4.1 (Regierungspräsidium Freiburg: Landesamt für Geologie, Rohstoffe und Bergbau, 2023).

2.4. Intra-plate seismicity

On Earth most seismic activity is observed along the tectonic plate boundaries. Seismic activity not associated with tectonic plate boundaries and mostly located in the upper crust is called intra-plate seismicity (Talwani, 2014). There are several examples for the hazard due to intra-plate seismicity, like the New Madrid Seismic Fault Zone, the Tangshan 1976 earthquake or the Bhuj 2001 earthquake in India (Fig. 2.3, (Liu and Zoback, 1997; Talwani, 2014, 2017)).

As intra-plate seismicity occurs away from tectonic plate boundaries, the question arises what drives the intra-plate seismicity and why does it occur in a particular region. There are different models describing the processes driving intra-plate seismicity. One model describes the occurrence of intra-plate earthquakes in zones of mechanical weaknesses or along pre-existing faults in the crust, which are favorably aligned in the regional stress field (Sykes and Sbar, 1973; Johnston and Kanter, 1990; Talwani, 2017). Other models describe a local concentration of stress, for example in the upper crust due to a weakened lower crust and upper mantle or due to geological structures which act as stress concentrators (Liu and Zoback, 1997; Iio and Kobayashi, 2002; Talwani, 2014, 2017). Geological structures which may act as stress concentrators are for example fault bends, fault intersections, restraining stepovers or buried plutons (Talwani, 1988, 2017). Ancient rift structures are also often related with intra-plate earthquakes (Zoback and Zoback, 1981; Csontos and Van Arsdale, 2008; Talwani, 2014, 2017). In the following I describe some examples of intra-plate seismicity in different geological settings and if known the related driving mechanisms.

Areas where intra-plate seismicity is related with a rift structure are for example the Kachchh rift basin in Western India, where the 2001 M 7.7 Bhuj earthquake and the M 7.8 Kutch earthquake occurred (Fig. 2.3, Johnston and Kanter, 1990; Talwani, 2014). In this area a thinned lithosphere is observed, furthermore, a high-density mafic body may have acted as stress concentrator (Talwani, 2014). The St. Lawrence Rift System and the Lower Rhine Embayment are other examples for rift related intra-plate seismicity (Fig. 2.3, Talwani, 2014).

The seismicity of the New Madrid seismic fault zone, occurs along several faults, some related with the ancient Reelfoot rift, which are favorably aligned in the regional stress field, leading to NE-SW dextral strike-slip faulting with a reverse-slip component, reverse faulting on N-S striking fault planes and WNW-ESE striking sinistral strike-slip faulting also with a reverse-slip component (Fig. 2.3, Zoback and Zoback, 1981; Csontos and Van Arsdale, 2008; Talwani, 2017). Furthermore, an elevated heat flow in the lower crust and upper mantle in the area, weakening the lithosphere, may also facilitate the origin of the seismicity in this area (Liu and Zoback, 1997).

An example for intra-plate earthquakes within the Proterozoic shield of Australia are the Tennet Creek sequence (Fig. 2.3). Within a 12 hour period on the 22nd January 1988 three earthquakes of M_S 6.3-6.7 occurred (Bowman et al., 1990). Interestingly, the area was not known for seismic activity until 1987 (Bowman et al., 1990). The aftershock distribution imaged a complicated fault structure of three differently inclined faults (Bachmann et al., 1987).

In the foreland of the Himalaya intra-plate seismicity is observed at the Kopili fault in India, which is known for damaging earthquakes (Fig. 2.3, (Dey et al., 2022)). The Kopili fault, together with other faults in the Indian plate (e.g. Tista fault, Patna fault) are pre-existing fracture zones, subdividing the Indian plate in several sub-blocks (Diehl et al., 2017; Dey et al.,
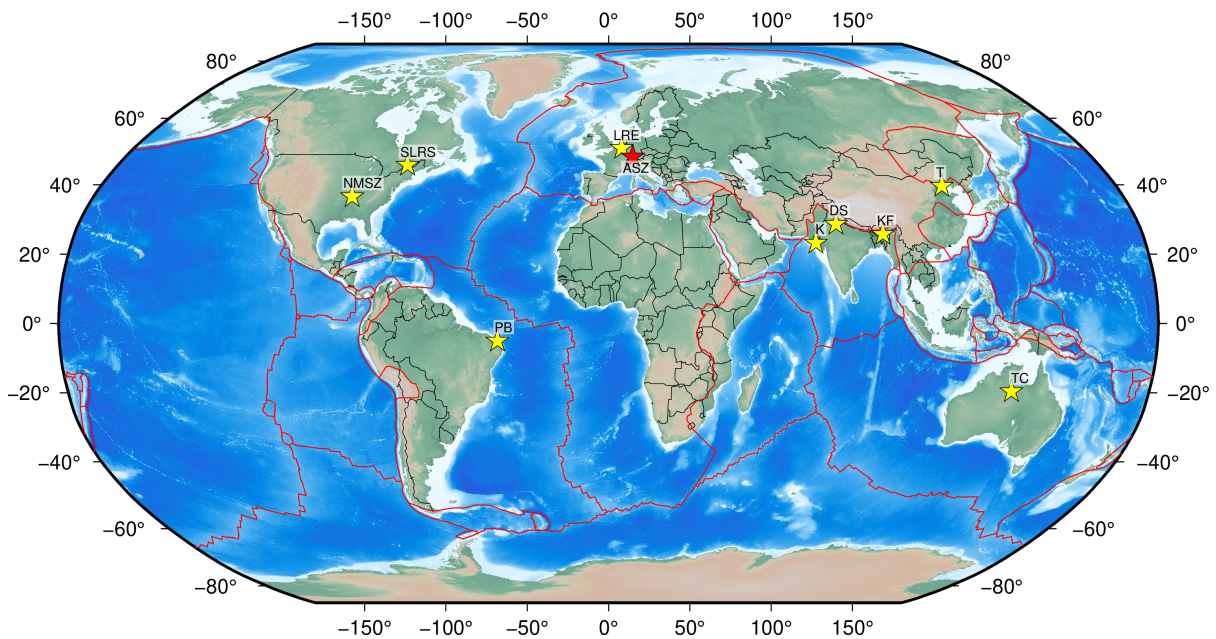
Figure 2.3.: Exemplary sites of intra-plate seismicity (yellow stars). Location of the ASZ indicated by red star. Plate tectonic boundaries are displayed in red after Bird (2003). Topography is based on SRTM15+ (Tozer et al., 2019). NMSZ = New Madrid Seismic Zone, SLRS = St. Lawrence Rift System, PB = Potiguar Basin, LRE = Lower Rhine Embayment, K = Kachchh rift basin, DS = Delhi Seismic Zone, KF = Kopili Fault, T = Tangshan 1976 earthquake, TC = Tennet Creek 1988 earthquake sequence.

2022). Dey et al. (2022) suggest a reactivation of those pre-existing fault zones as they are favorably aligned to rupture in the current stress field, which is dominated by the collision and subduction tectonics in the area (Dey et al., 2022). Another example in the Himalayan foreland is the Delhi seismic zone (Fig. 2.3). Along the Delhi seismic zone in the Himalayan foreland also existing fault zones are activated within the current stress field dominated by the plate boundary forces and the ongoing plate collision and related orogeny (Manglik et al., 2023). A critical factor for the occurrence of earthquakes in this area seems to be intra-plate stresses due to the flexure of the Indian plate (Manglik et al., 2023).

In Brazil intra-plate seismicity locations show a trend towards thinned lithosphere and the craton edges (Talwani, 2014). The continental shelf seems to be seismically more active than the continental center (Talwani, 2014). The Potiguar Basin is located at the craton edge (Fig. 2.3). The analysis of NW-SE and NE-SW trending clusters of intra-plate seismicity identified the superposition of the local and regional stress field as driving forces (Fonsêca et al., 2021). Furthermore, Fonsêca et al. (2021) observed an intersection of two faults at one location, suggesting the fault intersection as additional stress concentrator facilitating the moderate size earthquakes observed.

3.   Data and Methods

The aim of this work is to better understand the seismicity and its origin on the western Swabian Alb near Albstadt. Therefore, precise earthquake hypocenter locations, a good local seismic velocity model and well determined fault plane solutions are necessary. Furthermore, additional faulting properties of micro-earthquakes could help to image the active fault planes. To accomplish this aim an earthquake catalog with precise phase arrival times and phase polarities is necessary as well as a dense seismic station network to locate even small magnitude events (ML < 0.5).

3.1.   Data

Here, I use the earthquake catalog of the LED (Bulletin-Files des Landeserdbebendienstes B-W, 2011-2020) as starting point. The LED catalog consists of events from 2011 to 2020 within Baden-Württemberg and some in adjacent regions, with corresponding event origin time, hypocenter location, P and S phase arrival times, P polarities and local magnitude ML. The LED determines the phase arrival times at their own permanent seismic recording stations, their own strong motion seismic stations and permanent seismic recording stations of other agencies (Fig. 3.1, e.g. Swiss Seismological Service (SED) at Eidgenössische Technische Hochschule (ETH) Zurich, 1983; Federal Institute for Geosciences and Natural Resources (BGR), 1976; GEOFON Data Centre, 1993).
The network of permanent seismic stations was densified from 2015 to 2022 during the AlpArray project (Hetényi et al., 2018), which aims to study the Alpine orogeny. Close to the area of the ASZ four additional AlpArray stations were installed (Fig. 3.1). Additionally, in 2018 further seismic recording stations were installed within the StressTransfer project (Mader and Ritter, 2021) to improve the monitoring and analysis of the seismic activity in the area of the ASZ, the Molasse Basin around Bad Saulgau and the Upper Rhine Graben (see section 5). Five seismic stations were installed strategically in each area of interest. I conducted most of the related site selection, installation and service of the StressTransfer seismic stations (Fig. 3.2, Mader and Ritter, 2021). The five stations in the area of the ASZ are still recording, whereas the stations in the Molasse Basin and the Upper Rhine Graben were deinstalled at the end of 2021. The combined seismic station network of the permanent recording stations and the nine temporary stations gives the unique opportunity to study the seismicity related with the ASZ in great detail and to search for and locate low-magnitude events.
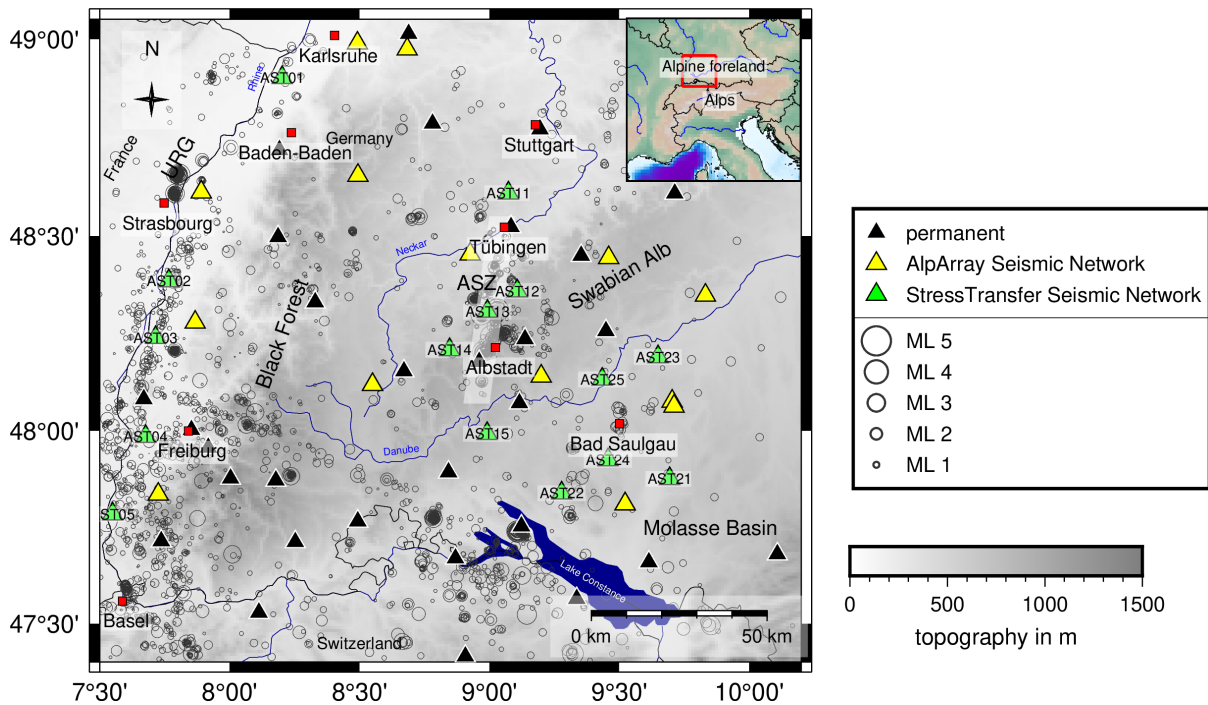
Figure 3.1.: Seismic broadband station distribution in the research area. Permanent seismic broadband stations are from the Seismological Service Baden-Württemberg, network LE (Erdbebendienst Südwest Baden-Württemberg and Rheinland-Pfalz, 2009; Bulletin-Files des Landeserdbebendienstes B-W, 2011-2020), the Switzerland Seismological Network CH (Swiss Seismological Service (SED) at Eidgenössische Technische Hochschule (ETH) Zurich, 1983), the German Regional Seismic Network GR (Federal Institute for Geosciences and Natural Resources (BGR), 1976) and the GEOFON seismic network GE (GEOFON Data Centre, 1993). Additional seismic stations due to the AlpArray (yellow, network Z3 AlpArray Seismic Network (AASN), 2015; Hetényi et al., 2018) and StressTransfer seismic network (green, network 5N Mader and Ritter, 2018, 2021) densify the permanent seismic station network. Gray circles display the events within the earthquake catalog of the LED from 2011-2020 (Bulletin-Files des Landeserdbebendienstes B-W, 2011-2020). Topography is based on SRTM15+ (Tozer et al., 2019). ASZ = Albstadt Shear Zone, URG = Upper Rhine Graben.

3.2. Methods

3.2.1. Determination of additional seismic phase arrival times

To make use of the additional nine seismic stations I determine direct P and S phases and their corresponding polarity. The program used for determining phase arrival times at AlpArray (Hetényi et al., 2018) and StressTransfer (Mader and Ritter, 2021) seismic stations to complement the LED event catalog is coded in Python using the Obspy package (Beyreuther et al., 2010b). The processing steps of the routine are based on the recommendations of Diehl et al. (2012) for consistent phase arrival time determination of local earthquakes. The routine (semi)automatically calculates error boundaries of the approximate phase arrival time. Afterwards, the phase arrival time and its corresponding polarity is chosen manually between the error boundaries (Fig. 3.3). Finally, a quality value is given to the phase arrival time based on its error boundaries. Before determination of the phase arrival time and polarity the raw data are inspected to exclude a FIR filter effect, if the station is equipped with an EarthData PR6-24
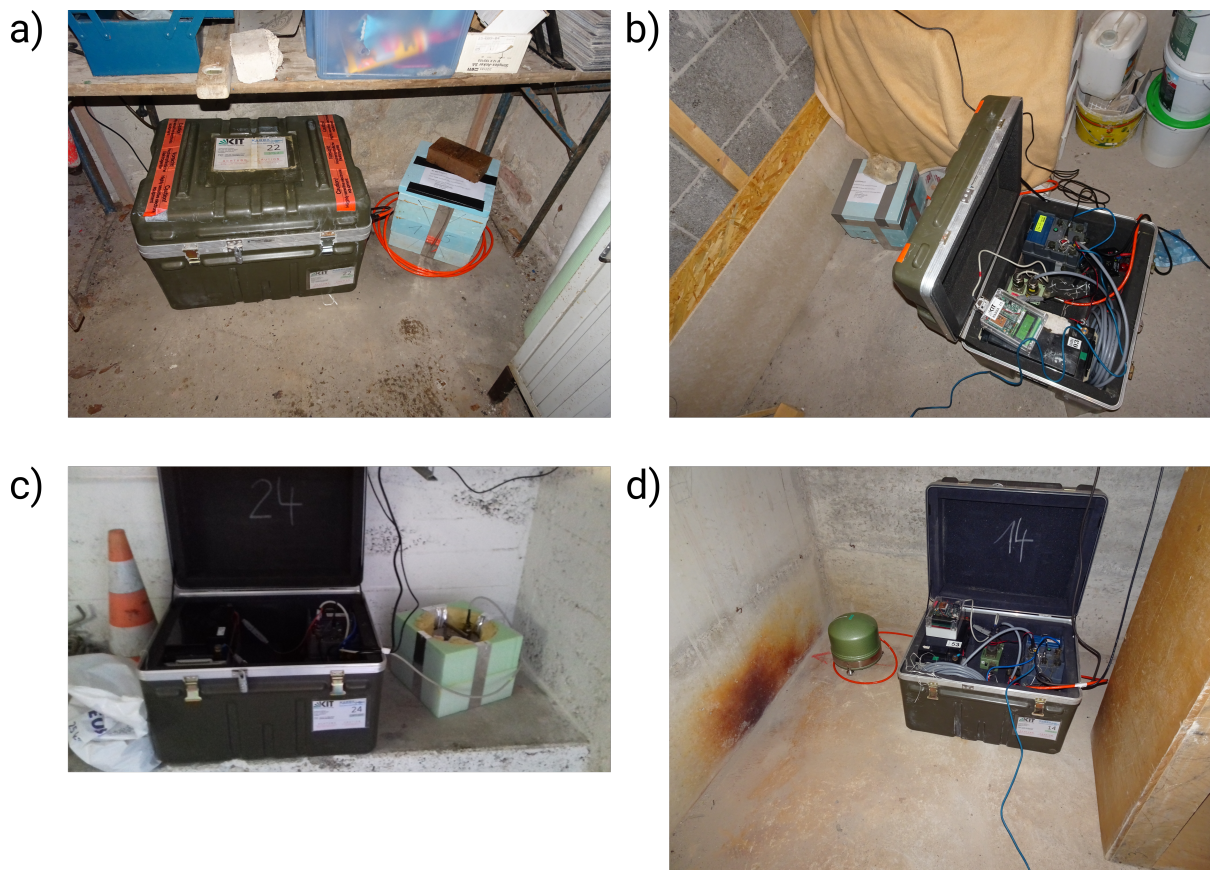
Figure 3.2.: Examplary pictures of four StressTransfer seismic stations (a) AST11, b) AST12, c) AST13, d) AST02 Mader and Ritter, 2021). All 15 StressTransfer seismic stations are equipped with instrumentation of the KArlsruhe BroadBand Array (KABBA). The electronic equipment is placed within the green box (data logger, battery, cables and if necessary the breakout-box of the seismometer). The data logger equipment is an EarthData PR6-24 at all sites. The seismometers are placed separately next to the box, isolated with a styropor encasing (a,b) or are buried. The majority is equipped with Streckeisen STS-2 broadband seismometers (d), other seismometers deployed are two Güralp CMG-40T (c), one Steckeisen STS-2.5, and one Geotech KS-2000.

data logger. If a FIR filter effect is visible, it is removed before the conversion of the amplitude from digital counts to ground velocity (see paragraph FIR filter effect). All analyzed seismic stations are three component (Z, N, E) broadband stations and the analysis is done using all three components.

P phase onset   The phase arrival time determination program is meant to apply already known information of the event and determine additional phase arrival times and polarities. As I want to add phase arrival times to the LED catalog from the additional seismic stations in the area of the ASZ, I use the events already within the catalog of the LED (Bulletin-Files des Landeserdbebendienstes B-W, 2011-2020). For the event (for which an additional phase arrival time shall be determined) an approximate onset time (AP) for the direct P and S phase is calculated using the TauP toolbox of ObsPy (Beyreuther et al., 2010a; Crotwell et al., 1999) and the standard Earth velocity model ak135 (Fig. 3.4, Kennett et al., 1995). Other velocity models could be used, nevertheless only a first guess of the arrival time is needed, so the ak135 model
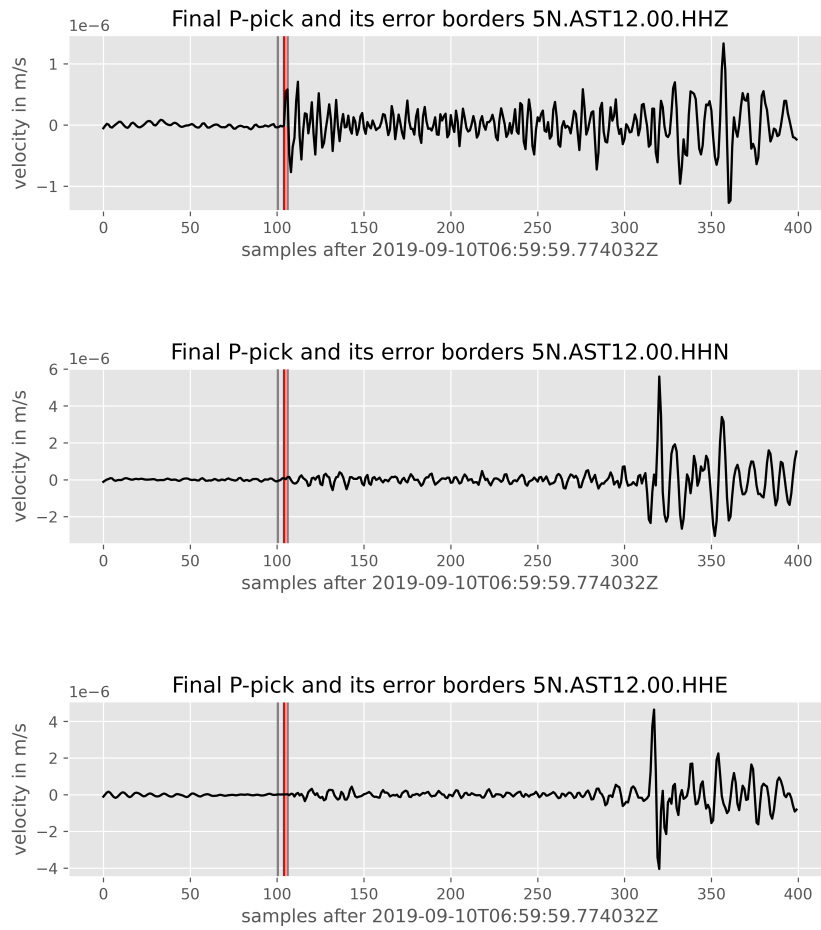
Figure 3.3.: Example of a P phase arrival at station AST12 of the StressTransfer network on all three components (Z, N, E). The gray lines represent the automatically determined earliest (ep) and latest possible (lp) pick and the red line is the manually determined phase arrival time.

Table 3.1.: Weighting factor w1 for calculation of ws (formula 3.1) depending on the ASNR. Time tlen defines the time before the AP for which ws is calculated.

	ASNR ≥ 5	5 > ASNR ≥ 3	ASNR < 3
weight w1	1	0.5	0.1
time tlen in s	3	1	0.5

satisfies this criteria. Around the AP the amplitude signal to noise ratio (ASNR) is determined. Thereby the window of the noise ends 0.5 s before the AP and is 3 s long. The window for the signal and noise amplitude is located 0.1 s after the AP and is 0.5 s long (Fig. 3.4). Using the data amplitude in the time windows the root mean square (rms) is calculated and finally the signal and noise window rms is divided by the noise window rms to get the ASNR. The earthquake hypocenters considered are mostly located near the used station, so that motion of the P phase is not only visible on the vertical component Z but also on the horizontal components (E, N). Therefore, not only the Z-component is used but also the horizontal components.

 The program first calculates the second error boundary or the latest possible pick (lp). As for
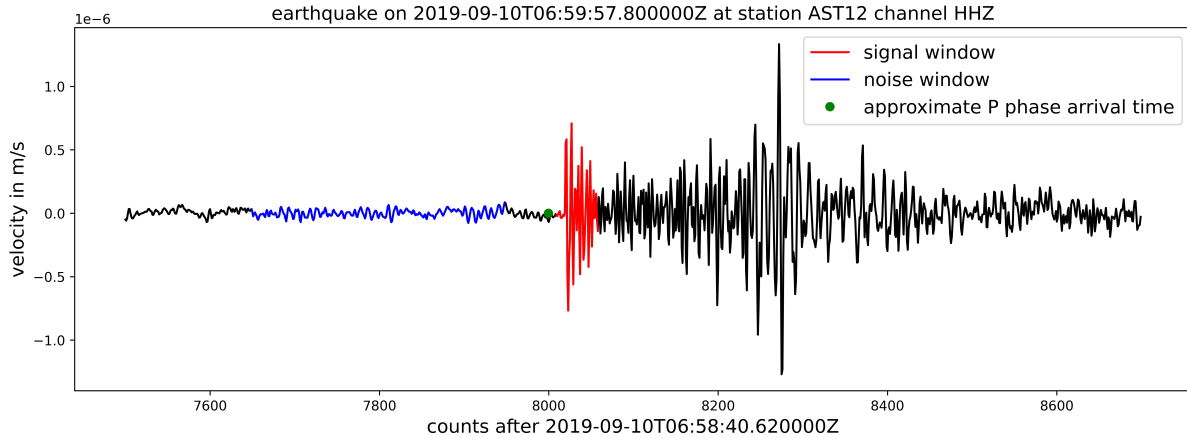
Figure 3.4.: Exemplary waveform of the vertical component Z at station AST12 of the StressTransfer network. The approximate onset time (AP) is marked by a green point. The windows in which the noise and signal amplitude are determined for the amplitude signal to noise ratio (ASNR) are highlighted in blue and red, respectively.

the first error boundary determination or earliest possible pick (ep), the lp needs to be known. To find the lp I use an weighted sum of the squared velocity amplitude of the data of all three components (*ws*) to increase the visibility of amplitude changes.

$$ws = \sum_{i=1}^{3} w1(i) \cdot x_i(t)^2 \qquad (3.1)$$

With $x_i(t)$ the signal amplitude of the component i at time t. The weighting factor w1 is defined to account for earthquakes with a steeper incidence angle at the station, so mainly signal on the vertical component, or noise overlaying in the data. It is defined based on the ASNR of each component (Table 3.1). Furthermore, the time window, in which the *ws* is calculated, varies with the ASNR. The time before the AP is defined as tlen, depending on the ASNR (Table 3.1). tlen is determined for all three components independently and the mean of tlen of all three components is used to trim the data before the AP. The length of the time window after the AP is defined as 0.9 times the theoretical phase arrival time. The variation of tlen with the ASNR is applied to get a better automatic detection of the true P phase arrival. If the ASNR is low a shorter time window before the AP improves the correct identification. The calculated *ws* is smoothed by a lowpass filter. If the smoothed ws rises above a defined threshold value the lp is found. The threshold is calculated as following:

$$threshold = mean(ws) + w2 \cdot \sigma_{ws} \qquad (3.2)$$

w2 is the second weight which depends on the mean of weight w1 (Table 3.2) and σ_{ws} is the standard deviation of ws. If the selected lp is not reasonable based on visual inspection, one may manually overwrite lp. After lp is determined the first error boundary or ep can be determined. To find ep one goes backward in time from lp until the derivative gets zero (Diehl et al., 2012). From this point we step backward in time again by the period T of the dominating noise (Diehl et al., 2012) multiplied with the weighting factor w3. The frequency f_{dom} of the dominating noise is calculated in the noise window, defined before, using a weighted

Table 3.2.: The weighting factor w2 depends on the mean of the weighting factor w1 of all three components.

	mean(w) ≥ 1	1 > mean(w) ≥ 0.5	mean(w) < 0.5
weight w2	0.3	1	1.5

Table 3.3.: The weighting factor w3 is used to find ep. It depends on the ASNR and the lower corner frequency f1 of the filter applied to the data.

	ASNR ≥ 5	5 > ASNR ≥ 3	ASNR < 3
f1 ≤ 5 Hz	0.4	0.8	1.6
5 Hz < f1 ≤ 10 Hz	1.4	1.8	2.6

arithmetic mean of all three components ($f_{dom} = \frac{\sum f\widetilde{X}}{\sum \widetilde{X}}$, with $\widetilde{X}$ the amplitude spectra of the data signal in the noise window). As f_{dom} depends on the filter frequencies, the weighting factor w3 depends not only on the ASNR but also on the minimum corner frequency f1 of the filter (Table 3.3). The additional step back is done to account for noise overlaying the phase onset. ep is searched for every component separately. To determine a common final ep the median of all three components is taken. Again, if ep is unreasonably early or late one may overwrite ep manually. As both error boundaries are now determined one picks manually the phase onset between the error boundaries and identifies its polarity. Finally, a quality value is given to the pick depending on the error boundaries time difference lp-ep. This is done to get a consistent quality value for the whole data set, independent of the person determining the phase arrival time (Table 3.4). The quality assignment is done with similar uncertainties like the quality assignment of the picks of the LED, also for consistency. The weighting factors of the program are selected based on test runs resulting in reasonable error boundaries for different events (impulsive or emergent onsets, noisy data). The program is applied for determining direct P and S phase arrival times and polarities of earthquakes within the LED event catalog at additional AlpArray and StressTransfer seismic stations.

S phase onset   The S phase is picked in the same way as the P phase except that it is only picked on the transverse component, which is obtained through rotation of the ZNE-components system to the ZRT-system (vertical, radial, transverse) using the backazimuth of the earthquake to the station. This means everything described above for the P phase is done in the same way for the transverse component for the S phase arrival time, which means we determine the horizontal direct S phase SH. Another difference is that tlen is not used to trim the data to the AP but a fixed time window is applied with 0.5 times the theoretical phase arrival time (in seconds after the origin time) before the AP and one time the theoretical phase arrival time after the AP. The S phase is more difficult to identify in comparison with the P phase

Table 3.4.: Phase arrival quality depending on the time difference between lp and ep.

error boundaries in s	lp-ep ≤ 0.05	0.05 < lp-ep ≤ 0.1	0.1 < lp-ep ≤ 0.2	0.2 < lp-ep ≤ 0.4	lp-ep > 0.4
quality	0	1	2	3	4

as the P wave coda may obscure the S phase onset. In case the S phase is difficult to identify, one may consider component products and particle motion. The component product of the R and Z component hints to a vertically polarized S phase (SV) if negative, a P phase if positive, and a SH phase if zero (Plešinger et al., 1986). In the particle motion plots we expect a higher amplitude on the transverse component relative to the radial component. For the SH phase also a quality similar to P and a polarity is assigned, with the polarity up meaning a ground movement to the right and the polarity down corresponding to a ground movement to the left.

Linear phase FIR filter effect correction after Scherbaum (1996)   Modern seismic recording systems use digital anti-aliasing filters with very steeply flanked transition bands. Those filters are needed to obtain the best resolution for the frequency band of interest and also should not cause amplitude or phase distortion.
The seismometer measures the discrete time signal $x(i)$ (i = sample of signal). This signal is recorded with a high sampling rate to allow the best resolution for each selected frequency band. To receive the sampling rate of interest the signal $x(i)$ is downsampled several times. Before decimation, a linear phase FIR filter with the filter transfer function $F(z)$ (z = a continuous complex variable) is used to inhibit aliasing. Mathematically, to filter the signal $x(i)$ means that the spectrum of the signal $X(z)$ is multiplied with the filter transfer function $F(z)$ in the Z- or frequency-domain. In the time-domain this is equivalent with directly calculating the convolution sum of the signal $x(i)$ and the filter impulse response $f(i)$.

$$Y(z) = X(z) \cdot F(z) \tag{3.3}$$

$$y(i) = x(i) * f(i) = \sum_{k=-\infty}^{\infty} x(k) \cdot f(i-k) \tag{3.4}$$

To relate the input signal $x(i)$ with the output $y(i)$ one can use the properties of the inverse Z-Transform. After partial fraction expansion, for a rational function z, one can describe the inverse Z-Transform by linear difference equations with constant filter coefficients a_k and b_l:

$$\sum_{k=0}^{N} a_k \cdot y(i-k) = \sum_{l=0}^{M} b_l \cdot x(i-l) \tag{3.5}$$

M and N represent the maximum number of filter coefficients a_k and b_l. Considering those linear difference equations 3.5 one can recognize that there are two types of filters: recursive and non-recursive ones. For recursive filters the output $y(i)$ depends on the input $x(i)$ and the output $y(i)$ of samples before i. The output $y(i)$ of non-recursive filters, in contrast, only depends on the input $x(i)$ at sample i and earlier samples. Here the filter coefficient a_k equals one for the first sample and zero for the index k larger than zero. Those non-recursive filters are called Finite Impulse Response (FIR) filters. Such a filter can completely be described by its roots of the filter transfer function $F(z)$. Those roots can be separated in poles, the roots of the denominator, and zeros, the roots of the numerator. The special feature about a FIR filter transfer function $F(z)$ is that it only consists of zeros. FIR filters are often used in
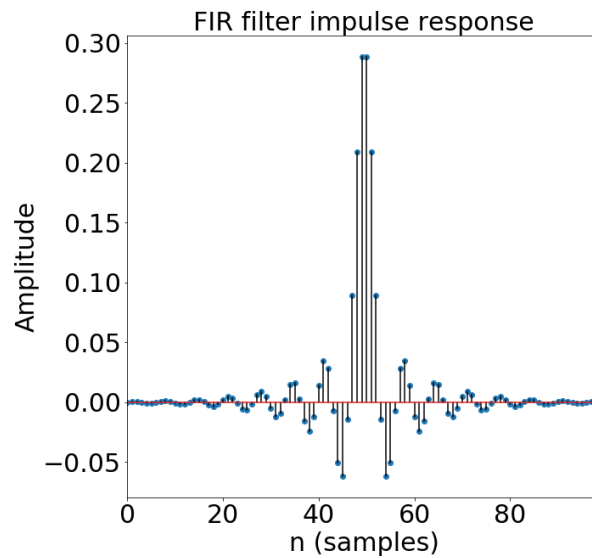
Figure 3.5.: Impulse response of the 4th stage FIR filter of the Earth Data PR6-24 data logger, which was used as data logger of the StressTransfer seismic stations (Mader and Ritter, 2021) and some of the AlpArray stations (Hetényi et al., 2018; Schlömer et al., 2022).
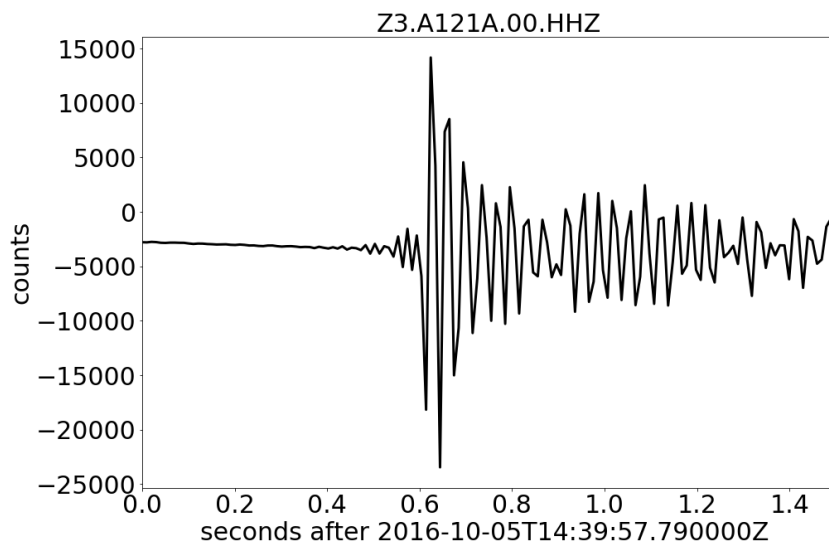
Figure 3.6.: Precursory signal before the impulsive P-phase onset on the Z-component of the seismic station A121A of the AlpArray seismic network, which uses the Earth Data PR6-24 datalogger.

seismic recording systems as they are easier to implement for a given design like for example steep and linear phase filters. As the implemented FIR filters are linear phase filters, they produce no phase distortion but a constant time shift, which can be corrected for. They have a symmetrical impulse response (Fig. 3.5) and hence are acausal. This means that the FIR filter implemented as digital anti-aliasing filter before decimation produces unwanted precursory signals especially for impulsive signals (Fig. 3.6).

To remove the unwanted effect of the FIR filter one needs to consider that those filters are implemented before decimation of the oversampled data to suppress aliasing. Mostly there are

distribution of roots of FIR filter
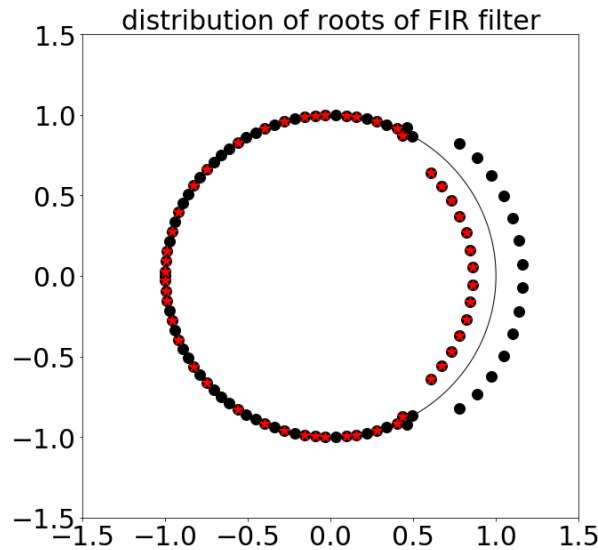
Figure 3.7.: Roots of the 4th stage FIR filter of the Earth Data PR6-24 datalogger in the Z-plane. The black dots represent the zeros related to the minimum phase, the black dots with the red stars show the zeros of the maximum phase. The black line represents the unit circle.

several stages of filtering and decimation before the sampling rate of interest is obtained. Here I only remove the FIR filter effect of the last stage because this works well enough. As the data are decimated after filtering, one needs to recover the sampling rate before the decimation process to remove the FIR filter effect.

The digital seismogram $\widetilde{Y}(z)$ before decimation is described as

$$\widetilde{Y}(z) = F(z)z^{lp}\widetilde{X}(z) \tag{3.6}$$

The FIR filter is described by its transfer function $F(z)$ and a time shift z^{lp} for lp samples, as the filter is a linear phase filter.

After Scherbaum (1996) I first consider only the effect of the transfer function $F(z)$ of the filter effect on the data in equation 3.6. The FIR filter is composed of a minimum and a maximum phase component. The right-sided or causal part is the minimum phase and the left-sided or acausal part is the maximum phase. The filter is defined as the product of both phases. To reduce the FIR filter effect one needs to change the maximum phase of the FIR filter into its minimum phase equivalent. To distinguish the two phases one can use the characteristics of the Z-transform. As stated before the FIR filter transfer function $F(z)$ can be completely described by its zeros c. The zeros c_{max} inside the unit circle in the Z-plane represent the maximum phase component (important, it depends on the definition of the Z-transform) and the zeros c_{min} outside the unit circle the minimum phase component (Fig. 3.7). So it is possible to separate the transfer function $F(z)$ into it's minimum and maximum phase components.

To determine the minimum phase equivalent of the maximum phase, the fact is used, that replacing a singularity by its complex conjugate reciprocal does not change the amplitude part of the transfer function $F(z)$ except for a constant scaling factor. If all zeros c_{max} of the

maximum phase component move outside the unit circle, $F(z)$ becomes minimum phase. This is done by replacing $F_{max}(z)$ by $F_{max}(\frac{1}{z})$:

$$MinPhase[F_{max}(z)] = F_{max}(\frac{1}{z}) \tag{3.7}$$

Due to the properties of the Z-transform this corresponds to inverting $F_{max}(z)$ in time. This means, that one deconvolves the maximum phase component and then convolves the remaining sequence with the time-inverted maximum phase component. To avoid a stability problem all signals in equation 3.6 are inverted in time before filtering. The corrected seismogram $Y(z)$ can be expressed as:

$$Y(\frac{1}{z}) = \frac{1}{F_{max}(\frac{1}{z})} \cdot F_{max}(z) \cdot \widetilde{Y}(\frac{1}{z}) \tag{3.8}$$

Practically, Scherbaum (1996) writes equation 3.8 as follows:

$$F_{max}(\frac{1}{z}) \cdot Y(\frac{1}{z}) = F_{max}(z) \cdot \widetilde{Y}(\frac{1}{z}) \tag{3.9}$$

I use the minimum phase equivalent of the maximum phase component $F_{max}(\frac{1}{z})$ times my aim, the corrected seismogram $Y(\frac{1}{z})$, which is the same as the maximum phase component $F_{max}(z)$ times the filtered seismogram $\widetilde{Y}(\frac{1}{z})$ with the unwanted effect. This can be written, for easier reading as:

$$A(z) \cdot Y(z) = B(z) \cdot X(z) \tag{3.10}$$

Written as convolution sum this means with mx as the number of zeros of the maximum phase component:

$$\sum_{k=0}^{mx} a(k)y(i-k) = \sum_{l=0}^{mx} b(l)x(i-l) \tag{3.11}$$

Equation 3.11 can be converted to:

$$y(i) = \sum_{k=1}^{mx} \frac{-a(k)}{a(0)}y(i-k) + \sum_{l=0}^{mx} \frac{b(l)}{a(0)}x(i-l) \tag{3.12}$$

which is formally identical to the definition of the implementation of the filter process (Equation 3.5).

$$\frac{-a(k)}{a(0)} = \frac{-f_{max}(mx-k)}{f_{max}(mx)} \quad \text{with k = 1,..., mx} \tag{3.13}$$

$$\frac{b(l)}{a(0)} = \frac{f_{max}(l)}{f_{max}(mx)} \quad \text{with l = 0,...,mx} \tag{3.14}$$

$a(0)$ equals $f_{max}(mx)$ due to the reason that $a(k)$ is inverted in time.

If $f_{max}(x)$ is known, the seismogram can be corrected for the FIR filter effect. But how can $f_{max}(x)$ practically be calculated?

As one can identify the maximum phase part through the zeros c_{max} of the filter transfer function, Scherbaum (1996) uses this to define the maximum phase part by its zeros c_{max}. First of all, I determine all zeros c of the filter transfer function $F(z)$ (the zeros of the impulse

response $f(i)$ of the FIR filter are also the zeros of its Z-Transform). Then one can determine all mx zeros c_{max} inside the unit circle, as they represent the maximum phase part in the Z-domain (Fig. 3.7).

For the transfer function $F(z)$ in the Z-domain applies:

$$F(z) = \sum_{l=0}^{M} b_l z^l = b_0 \sum_{l=1}^{M} b_l z_l = b_l \prod_{l=1}^{M} (z - c_l) \quad \text{M = max. number of zeros} \tag{3.15}$$

For the maximum phase component $F_{max}(z)$ follows:

$$F_{max}(z) = b_0 \prod_{l=1}^{mx} (z - c_{l_{max}}) = b_0 \sum_{l=1}^{mx} b_{l_{max}} z^l = b_0 \sum_{l=1}^{mx} f_{max}(l) z^l \quad \text{mx = max. number of zeros } c_{max} \tag{3.16}$$

To substitute z in equation 3.16 with $e^{i\omega T}$ ($\omega = 2\pi f$, with frequency $f = 0...$sampling rate, $T = 1/$sampling rate) is equivalent to calculating the inverse discrete Fourier-Transform (DFT) for $F_{max}(e^{i\omega T})$, which means getting the spectral values of the DFT of $f_{max}(x)$.

$$F_{max}(z) = F_{max}(\omega) = b_0 \sum_{l=1}^{mx} f_{max}(l) e^{i\omega T l} \tag{3.17}$$

Now Scherbaum (1996) uses the definition of the Fourier-Transform to calculate f_{max}

$$f_{max}(l) = \frac{1}{b_0 N} \sum_{\omega=0}^{N} F_{max}(\omega) e^{-i\omega T l} \tag{3.18}$$

Inserting the definition of F_{max} by its zeros (equation 3.16) into equation 3.18 results in a representation of $f_{max}(l)$ by the zeros c_{max} of the maximum phase part:

$$f_{max}(l) = \frac{1}{b_0 N} \sum_{\omega=0}^{N} (b_0 \prod_{l=1}^{mx} (e^{i\omega T} - c_{l_{max}})) e^{-i\omega T l} = \frac{1}{N} \sum_{\omega=0}^{N} (\prod_{l=1}^{mx} (e^{i\omega T} - c_{l_{max}})) e^{-i\omega T l} \tag{3.19}$$

Now inserting equation 3.19 into the convolution sum (equation 3.12), one can calculate the corrected seismogram $y(i)$. Finally, one only needs to account for the constant time shift of lp samples of the corrected seismogram (equation 3.6). To determine lp I use a simple crosscorrelation between $\widetilde{Y}(z)$ and $Y(z)$. After the decimation back to the sampling rate of interest the corrected seismogram is determined (Fig. 3.8). Whether a correction for the FIR filter effect is necessary, depends on the onset of the phase. The more impulsive the onset of the phase the more necessary is the correction for the FIR filter effect. If a phase arrival time shall be determined at a seismic station equipped with an Earth Data PR6-24 data logger, the data is inspected before processing for the effect of the linear phase FIR filter. If the effect is visible, the above correction is applied after Scherbaum (1996).

3.2.2. Used seismological software

For the further analysis of the complemented event catalog I use well-tested programs. In the following the application of each program in the context of this thesis is given and in section
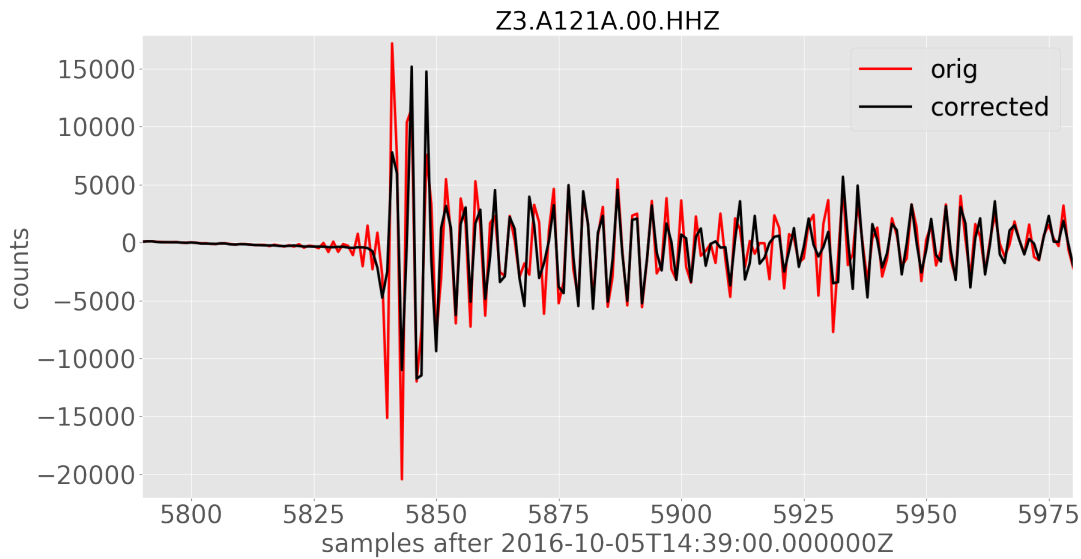
Figure 3.8.: Result of the FIR filter effect correction. In red the original trace of Fig. 3.6. In black the corrected trace without the precursory signals before the P-phase onset.

4 I describe the basic theory behind the programs.

First to get a good seismic velocity estimate of my research area I invert for a minimum 1-D seismic v_p and v_s velocity model with station delay times using VELEST (Kissling et al., 1994). This seismic velocity model is used as basis for all further processing. The local velocity model is used to relocate the complemented event catalog with the software NonLinLoc (Lomax et al., 2000) to get improved event locations due to the new local velocity model and the additional phase arrival times. The NonLinLoc output includes not only event locations, but also error estimates for the event locations and the angles describing the ray properties of the seismic wave relative to each station (takeoff angle, backazimuth). Those angles together with the polarity of the P and SH phases, as well as SH/P amplitude ratios are used to determine fault plane solutions with FOCMEC (Snoke, 2003), which describe the source mechanism. Fault plane solutions describe the source mechanism, but one always has two ambivalent solutions. One is the active fault plane, whereas the other is the auxiliary fault plane. To distinguish between those two additional information is necessary, like aftershock distributions. Therefore, a template matching detection routine based on the Python package EQcorrscan (Chamberlain et al., 2018) is implemented to search for earthquake sequences. The identified event sequences, which show similar waveforms and similar event location, hence a common fault plane, are located using the double-difference earthquake location algorithm HypoDD (Waldhauser and Ellsworth, 2000). The relative event locations image the active fault plane and in combination with the fault plane solutions the source mechanism of the event is described. Finally, the fault plane solutions are inverted for the stress field, needed to activate the faults in the area of the ASZ, using the program StressInverse (Vavryčuk, 2014, 2020).

4. Theoretical background

4.1. Determination of hypocenter locations

An earthquake can be described by the hypocenter location, origin time, magnitude, and faulting mechanism. To determine the hypocenter location and origin time the arrival times of seismic phases at seismic recording stations are used. The arrival time $T_{station}$ depends on the origin time t_0 of the event, as well as on the travel time t of the seismic wave from the event location $(x_{event}, y_{event}, z_{event})$ to the station $(x_{station}, y_{station}, z_{station})$ through the medium with velocity $v(x, y, z)$.

$$T_{station} = t_0 + t(x_{event}, y_{event}, z_{event}, x_{station}, y_{station}, z_{station}, v(x, y, z)) \qquad (4.1)$$

The travel time t is a non-linear function depending on the hypocenter, the station location and the velocity v along the ray path s from hypocenter to the station (Thurber, 1981):

$$t = \int_{event}^{station} \frac{1}{v(x, y, z)} ds \qquad (4.2)$$

As in most cases hypocenter, origin time and velocity are unknown and we only know the arrival time and the corresponding station location. Using a first guess of the hypocenter, origin time and velocity structure one can calculate theoretical arrival times $T_{station_{calc}}$ and compare them to the observed ones by calculating the residuals r:

$$r = T_{station} - T_{station_{calc}} \qquad (4.3)$$

If only earthquake location is wanted, then the Earth's velocity structure is assumed to be known and the problem is reduced to the unknowns of hypocenter and origin time. The optimum solution can be found via a grid-search approach or inversion. In the following section three different approaches are described to determine hypocenter parameters. The first approach determines simultaneously the velocity structure of the Earth in the study area, which is mostly unknown, and the hypocenter parameters. The improved knowledge of the velocity structure improves the absolute event locations. The second approach is the probabilistic earthquake location, which provides not only hypocenter locations, but also uncertainty estimates based on the probabilistic density function (pdf). The third section describes the determination of precise relative event locations. With this approach one can overcome location uncertainties due to a heterogeneous 3D velocity structure for closely located events, which can help to sharpen the image of the active fault plane outlined by the hypocenter locations.

4.1.1. Simultaneous inversion for velocity structure and hypocenter parameters

The aim of the simultaneous inversion is to determine the Earth's velocity structure in combination with the hypocenter parameters. Varying the hypocenter, origin time as well as the unknown velocity structure to minimize the residuals one gets:

$$T_{station} - (T_{station_{calc}} + \Delta T_{clac}) = 0 (+error) \tag{4.4}$$

ΔT_{calc} represents the change of calculated arrival time due to the parameter variation. Combining equation 4.3 and 4.4 it follows:

$$r = \Delta T_{calc} (+error) \tag{4.5}$$

As we know from equation 4.1 the change of ΔT_{calc} depends on the variation of the origin time Δt_0 and the travel time Δt from an event to the recording station:

$$\Delta T_{calc} = \Delta t_0 + \Delta t \tag{4.6}$$

By linearizing the non-linear problem using first order Taylor expansions (for all parameters) one can describe the residual by the changes in velocity and hypocentral parameters (Thurber, 1981):

$$r = \Delta t_0 + \frac{\delta t}{\delta x_{event}} \Delta x_{event} + \frac{\delta t}{\delta y_{event}} \Delta y_{event} + \frac{\delta t}{\delta z_{event}} \Delta z_{event} + \sum_{j=1}^{N} \frac{\delta t}{\delta v_j} \Delta v_j \tag{4.7}$$

If we consider a set of equations for several seismic events, equation 4.7 can also be written as:

$$\vec{r} = \underline{A}\vec{m} \tag{4.8}$$

were $\vec{r}$ represents the vector of the residuals, $\underline{A}$ the matrix with the partial derivatives and $\vec{m}$ the searched for adjustments of the parameters. Regarding several events one achieves an overdetermined system of linearized equations which can be solved by inverse theory:

$$\vec{m} = (\underline{A}^T \underline{A})^{-1} \underline{A}^T \vec{r} \tag{4.9}$$

The solution of equation 4.9 may become instable due to spatially unevenly distributed input data, non-uniqueness of the model parameters or inter-dependence between model parameters. By applying a regularisation via the Marquardt-Levenberg approach one can damp the solution, to avoid large changes of the parameters due to close to zero singular values (Thurber, 1981):

$$\vec{m} = (\underline{A}^T \underline{A} + \lambda^2 \underline{1})^{-1} \underline{A}^T \vec{r} \tag{4.10}$$

Here λ^2 represents the damping and $\underline{1}$ is the unit matrix. As the problem is non-linear the solution is searched for iteratively and λ^2 functions as a damping of the model parameter adjustments per each iteration step.

The simultaneous inversion for both velocity model and hypocenter parameters described above is implemented in the program VELEST (Kissling et al., 1994) for a 1D velocity structure. The program VELEST is applied in section 6 to phase arrival times from the earthquake catalog of the LED, which is complemented with additional phase arrival times at the AlpArray (Hetényi et al., 2018) and StressTransfer seismic stations (Mader and Ritter, 2021), to determine a minimum 1D seismic P-wave and S-wave velocity model for the region of the ASZ.

4.1.2. Probabilistic earthquake localization

To calculate the hypocenter and origin time from the arrival times of seismic phases at seismic stations typically an iterative location method is used by linearizing the inversion problem or by solving the problem using direct grid-search methods. The aim is to minimize the residuals between calculated and observed arrival times (equation 4.3). Another possibility is to formulate the inversion problem using probability density functions (pdf, Tarantola and Valette, 1982). The observed data $\vec{d}$ (in our case the observed arrival times) are located in the data space D and the pdf p($\vec{d}$) describes the uncertainty within the data space D for $\vec{d}$ (Tarantola and Valette, 1982; Lomax et al., 2000). One searches for the event location parameters $\vec{m}$ (hypocenter location (x_{event}, y_{event}, z_{event} and origin time t_0) within the parameter space M, leading to the prior pdf p($\vec{m}$) describing the knowledge before localization (e.g. restricted area for event localization, Tarantola and Valette, 1982; Lomax et al., 2000). To relate the observed data $\vec{d}$ with the event location parameters $\vec{m}$ one needs to solve the forward problem by determining the theoretical arrival times $\vec{d_{calc}}$. The pdf F($\vec{d}$,$\vec{m}$) describes the fit between observed and calculated arrival times achieved by the forward modelling (Tarantola and Valette, 1982; Lomax et al., 2000). The combination of the information included in the three pdf functions (p($\vec{d}$), p($\vec{m}$), F($\vec{d}$,$\vec{m}$)) constructs within the probabilistic framework the pdf Q($\vec{d}$,$\vec{m}$) (Tarantola and Valette, 1982; Lomax et al., 2000). To achieve a pdf function Q($\vec{m}$), only dependent on the searched for earthquake location parameter $\vec{m}$, one needs to integrate over $\vec{d}$ (Tarantola and Valette, 1982; Lomax et al., 2000):

$$Q(\vec{m}) = \kappa p(\vec{m}) \int_D \frac{p(\vec{d}) F(\vec{d}, \vec{m})}{\mu(\vec{d}, \vec{m})} \, dd \tag{4.11}$$

Here, the pdf Q($\vec{m}$) is normalized to get the unit integral. For this the constant κ normalizes Q($\vec{m}$) to unit integral over the data space D and parameter space M. $\mu(\vec{d}, \vec{m})$ is the homogeneous distribution over $\vec{d}$ and $\vec{m}$. Equation 4.11 is the solution to the inversion problem via probabilistic analysis, describing the uncertainties of event location parameter $\vec{m}$ with respect to a priori information and uncertainties (Tarantola and Valette, 1982; Lomax et al., 2000). The integral over data $\vec{d}$ in equation 4.11, describing the fit of observed data by the model, is called the likelihood function L($\vec{m}$) (Lomax et al., 2000). By assuming that the uncertainties are Gaussian distributed, $\vec{d}$ and $\vec{m}$, are independent and a priori information of the origin time t_0 is uniform, one can determine the non-normalized L2 likelihood function:

$$L(\vec{m}) = e^{-\frac{1}{2}(\vec{d_0} - f(\vec{m}))^T \underline{C_d}^{-1} (\vec{d_0} - f(\vec{m}))} \tag{4.12}$$

With $\vec{d_0}$ the mean of the observed data and $\underline{C_d}$ the covariance matrix (Lomax et al., 2000). Furthermore, if above assumptions are valid, one can determine the maximum likelihood origin time t_0 by:

$$t_0(\vec{x}) = \frac{\sum_i \sum_j w_{ij} (T_i - T_{i_{calc}}(\vec{x}))}{\sum_i \sum_j w_{ij}} \tag{4.13}$$

The weights w_{ij} are defined by the covariance matrix and $\vec{x}$ are the hypocenter parameters (x_{event}, y_{event}, z_{event}, Tarantola and Valette, 1982; Lomax et al., 2000). The non-normalized likelihood function only depending on $\vec{x}$ is then given by:

$$L(\vec{x}) = e^{-\frac{1}{2}\sum_i \frac{(t_i - t_{i_{calc}}(\vec{x}))^2}{\sigma_i^2}} \tag{4.14}$$

With t representing the travel times (observed and calculated) and σ_i the uncertainties of those (Tarantola and Valette, 1982; Lomax et al., 2000). $L(\vec{x})$ defines the relative probability for any point $\vec{x}$ being the best estimate of the hypocenter (Tarantola and Valette, 1982; Lomax et al., 2000). Via a grid-search or importance sampling (e.g. Oct-Tree or Metropolis-Gibbs sampling) one can determine the (unnormalized) location pdf $Q(\vec{x})$ only depending on the spatial event location parameter $\vec{x}$:

$$Q(\vec{x}) = p(\vec{x})L(\vec{x}) \tag{4.15}$$

From the gridded location pdf one can determine the covariance matrix, which can be used as uncertainty estimate of the event location (Tarantola and Valette, 1982; Lomax et al., 2000). The program NonLinLoc (Lomax et al., 2000) applies the probabilistic earthquake location theory after Tarantola and Valette (1982) described above. The program allows to not only determine the maximum likelihood function using the L2 norm, but also using the equal differential time formulation (Lomax et al., 2000). Furthermore, one can select between grid-search, Metropolis-Gibbs sampling and Oct-Tree sampling for determination of the location pdf from which the maximum likelihood hypocenter is determined. The output contains also the covariance matrix, as well as the 68% confidence ellipsoid obtained from the covariance matrix (Lomax et al., 2000). I applied the program NonLinLoc to locate the events in the area of the ASZ (see section 6 and 7). Therefore, I always used the calculation of the location pdf based on the L2 likelihood function and the determination via the Oct-Tree sampling.

4.1.3. Relative event locations

In the previous paragraphs I already describe methods to determine hypocenter and origin time of an event. An incorrect seismic velocity model may introduce a bias in the hypocenter parameters, as well as in the phase arrival time accuracy or the distribution of stations relative to the event. Equation 4.1 highlights this dependency of the event parameters. By using only a minimum 1D seismic velocity model of the subsurface one may introduce uncertainty in the hypocenter parameters due to 3D variations of the seismic velocity structure. To improve the hypocenter parameters one can determine relative event locations (Waldhauser and Ellsworth, 2000). If two earthquakes i and j are sufficiently closely located to each other, the ray path to a station k can be assumed to be identical. The difference between the travel times of both events can then be related to the location difference of their hypocenters (Waldhauser and Ellsworth, 2000). Like before one can use a first guess to calculate the travel times from event to station and compare them with the observed ones (equation 4.3), but now the time difference of the travel times between the events i and j is used to calculate the double-difference travel time residuals (Waldhauser and Ellsworth, 2000):

$$dr_{k_{ij}} = (t_{k_i} - t_{k_j})_{obs} - (t_{k_i} - t_{k_j})_{cal} \tag{4.16}$$

Here one can either use the observed time differences in the event catalog, or one determines highly precise time differences from waveform cross-correlation (Waldhauser and Ellsworth, 2000). If one assumes the seismic velocity to be constant between the two events, which should be true for close events, one can determine the change in hypocenter difference between two events i and j by applying the difference of equation 4.7 (but for a fixed seismic velocity structure, Waldhauser and Ellsworth, 2000).

$$dr_{k_{ij}} = \frac{\delta t_{k_i}}{\delta \vec{m}} \Delta \vec{m}_i - \frac{\delta t_{k_j}}{\delta \vec{m}} \Delta \vec{m}_j = (\frac{\delta t_{k_i}}{\delta x} \Delta \vec{x}_i + \frac{\delta t_{k_i}}{\delta y} \Delta \vec{y}_i + \frac{\delta t_{k_i}}{\delta z} \Delta \vec{z}_i + \Delta t_{0_i}) - (\frac{\delta t_{k_j}}{\delta x} \Delta \vec{x}_j + \frac{\delta t_{k_j}}{\delta y} \Delta \vec{y}_j + \frac{\delta t_{k_j}}{\delta z} \Delta \vec{z}_j + \Delta t_{0_j})$$
(4.17)

One, therefore, needs to assume a reasonable velocity and origin time for both events. By combining equation 4.17 for several events and all stations, one gets a set of linear equations:

$$\underline{W} \, \underline{A} \vec{m} = \underline{W} \vec{d}$$
(4.18)

Here $\underline{W}$ is a diagonal matrix to weight each equation, $\underline{A}$ contains the partial derivatives, $\vec{m}$ the changes in hypocentral parameters and $\vec{d}$ the double-differences after equation 4.16 (Waldhauser and Ellsworth, 2000). This equation can be solved via inversion. As the aim of the relative event locations is not a change in absolute event location of the linked events, one can add as further constraint, that the mean shift during inversion for all events may be zero (Waldhauser and Ellsworth, 2000):

$$\sum_{i=1}^{N} \Delta \vec{m}_i = 0$$
(4.19)

The input data may still contain uncertainties in absolute event locations, so one may have to weight down equation 4.19 during the inversion to allow variations of the absolute event locations (Waldhauser and Ellsworth, 2000).

I apply the program HypoDD (Waldhauser and Ellsworth, 2000) which solves the double-difference problem (equation 4.18) either via singular value decomposition (SVD) or by using the conjugate gradient algorithm LSQR (Paige and Saunders, 1982; Waldhauser and Ellsworth, 2000). The SVD allows to determine appropriate uncertainties, but for large data sets the SVD is computationally inefficient. I applied the double-difference event location algorithm HypoDD to earthquake sequences on the Swabian Alb which exhibit highly similar waveforms to image the active fault plane (see section 7).

4.2. Template matching event detection

Earthquakes occurring on the same fault in close vicinity to each other show highly similar waveforms due to the common source process. This property of the recorded waveforms can be used to search for additional low magnitude earthquakes, which can later help to image the active fault. Via cross-correlation of the waveform data of known events (the template or master event waveform) with the continuous waveform data one can identify similar events

(detection or slave event). The normalized cross correlation coefficient cc (4.20) can be used as a measure of waveform similarity:

$$cc(y) = \frac{\sum_{x=0}^{n}(t(x) - \bar{t})(d(x + y) - \bar{d}(y))}{\sqrt{\sum_{x=0}^{n}(t(x) - \bar{t})^2 \sum_{x=0}^{n}(d(x + y) - \bar{d}(y))^2}} \qquad (4.20)$$

Here cc is the normalized cross correlation coefficient for the sample y, t represents the template waveform, n is the length of the template itself, d is the continuous waveform data and $\bar{d}(y)$ is the local mean of the continuous waveform data from sample y to sample y+n, $\bar{t}$ represents the mean of the template waveform (Chamberlain et al., 2018). If the cc exceeds a threshold value a detection is found.

Template matching event detection can be applied for single station or channel or multi-station and/or multi-channel data. The advantage of the latter two is the inclusion of additional information helping to reduce the detection of noise. In case of multi-channel and multi-station data a delay-and-stack method for the cc can be applied (Chamberlain et al., 2018). The delay depends on the shift within the template waveforms.

The template matching event detection is applied to events of the ASZ in section 7 using the Python package EQcorrscan (Chamberlain et al., 2018). I implemented a multi-station and multi-channel approach detecting the P-wave on the vertical and the S-wave on both horizontal components. By separating both wave types an automatic phase arrival time determination is possible between template and detection (Shelly and Hardebeck, 2010; Chamberlain et al., 2018).

4.3. Fault plane solutions

Earthquakes develop from rupture processes occurring in the Earth due to stresses. If the stress exceeds the failure point of the rock or a preexisting fault a slip occurs along the fault. The movement of the fault can be described by the two unit vectors $\vec{a}$ and $\vec{n}$, with $\vec{a}$ oriented in the direction of the slip along the fault and $\vec{n}$ orthogonal to the fault plane (Fig. 4.1, Snoke, 1989). A fault plane or focal plane solution describes this rupture process, based on the observation of the seismic wave field at seismic recording stations.

The nth component of the ground displacement u of a point source at location $\vec{x}$ at time t can be described by:

$$u(\vec{x}, t) = M_{pq} * G_{np,q} \qquad (4.21)$$

Where G represents the Green's function, which contains the information of the propagation effects from event to seismic station and M is the moment tensor, representing the source properties (Aki and Richards, 2002; Snoke, 1989). The moment tensor M_{pq} represents the force couple which is oriented in direction p and separated in direction q. Most earthquake source processes can be sufficiently described by a point source with the acting forces oriented in a quadrupole pattern, namely the double couple source model. The corresponding point source moment tensor can be described as:

$$M(t)_{jk} = M_0(t)(n_j a_k + n_k a_j) \qquad (4.22)$$
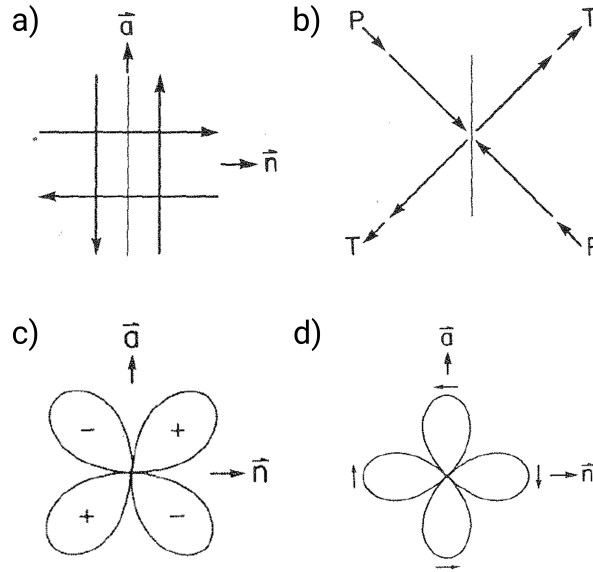
Figure 4.1.: Different representations of the forces of the double-couple moment tensor in equation 4.22. a) Result if coordinate system is oriented with x direction along $\vec{a}$, y direction along $\vec{n}$ and z direction into the plane. b) Result if coordinate system is rotated 45° clockwise around z direction relative to the coordinate system in a). P represents the pressure axis and T the tension axis. c) Radiation pattern of the P-wave. d) Radiation pattern of the SH-wave. (Figure taken from Snoke, 1989)

with a_k, a_j, n_k and n_j being the kth and jth component of $\vec{a}$ and $\vec{n}$ and $M_0(t)$ the total seismic moment (Snoke, 1989). Depending on the coordinate system in which one analyzes equation 4.22, one gets a different representation of the acting forces (Fig. 4.1). The representation of the double-couple in Fig. 4.1b) displays the direction of the pressure (P) and tension (T) axes. The axis orthogonal to the P and T axes is the B axis. It is also orthogonal to $\vec{a}$ and $\vec{n}$ (Snoke, 1989). With $\vec{a}$ and $\vec{n}$ or the P and T axes one can describe the fault mechanism on the focal sphere (sphere with unit radius and the point source in the center, Snoke, 1989). Another possibility is to describe the fault process by the strike Φ_s, rake λ and dip δ angle of the fault plane (Fig. 4.2, Aki and Richards, 2002; Snoke, 1989). Based on the symmetry of equation 4.22 a direct differentiation of the active fault plane ($\vec{a}$) and the auxiliary fault plane ($\vec{n}$) is not possible (Snoke, 1989). The differentiation can only be made with additional data, like for example the aftershock distribution.

By analyzing the far-field displacement $\vec{u}$ in an Earth-based coordinate system (spherical coordinates $\vec{r}$, Φ, Θ) on the focal sphere one can determine the displacement for P, SH and SV waves:

$$\vec{u}_P = (\frac{v_s}{v_p})^3 F R_P = (\frac{v_s}{v_p})^3 F r_j M_{jk} r_k = (\frac{v_s}{v_p})^3 F(2(\vec{a} \cdot \vec{r})(\vec{n} \cdot \vec{r})) \tag{4.23}$$

$$\vec{u}_{SV} = F R_{SV} = F r_j M_{jk} \Theta_k = F((\vec{a} \cdot \vec{\Theta})(\vec{n} \cdot \vec{r}) + (\vec{n} \cdot \vec{\Theta})(\vec{a} \cdot \vec{r})) \tag{4.24}$$

$$\vec{u}_{SH} = F R_{SH} = F r_j M_{jk} \Phi_k = F((\vec{a} \cdot \vec{\Phi})(\vec{n} \cdot \vec{r}) + (\vec{n} \cdot \vec{\Phi})(\vec{a} \cdot \vec{r})) \tag{4.25}$$

F is a common factor and R is the normalized radiation factor for each wave type, v_p and v_s represent the seismic P- and S-wave velocity (Aki and Richards, 2002; Snoke, 1989). With equations 4.23-4.25 we can determine the radiation pattern for each wave type (Fig. 4.1). In case of the direct P wave onset we observe the radiation pattern as up or downward movement
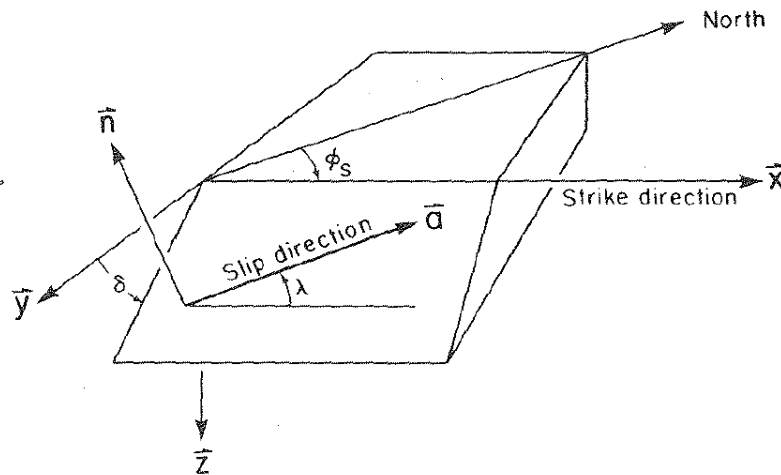
Figure 4.2.: Definition of the fault parameters: strike Φ_s, rake λ, dip δ, slip direction $\vec{a}$ and normal to the fault $\vec{n}$. (Figure taken from Snoke, 1989 after Aki and Richards, 2002)

on the vertical component of seismic recordings, for SH waves we observe a movement either to the left or right on the transversal component (Fig. 4.1). The movement of the recordings is called the phase polarity. The areas where the radiation pattern is zero are called nodal surface. For the P waves those areas correspond to the fault and auxiliary fault plane and they are always planes (Snoke, 1989). For SH waves we do not observe planes, but the nodal surfaces contain the B, P and T axes (Snoke, 1989).

To determine a fault plane solution of an event one uses the phase polarity and determines for each station-phase combination the azimuth of the event to the station and the take-off angle. With those two angles one can map the polarities on a planar projection of the focal sphere (equal-area Lambert-Schmidt projection) imaging the radiation pattern (Snoke, 1989, 2003). Via a grid search one can determine the fault and auxiliary fault plane (Snoke, 1989, 2003). To display the fault plane solution graphically the beach ball representation is typically used, with areas of compression colored in black and areas of dilation colored in white.

I apply the program FOCMEC (Snoke, 2003) to the events of the ASZ (see section 6 and 7). To determine the fault plane solution a grid search over the trend and plunge of the B axis and the angle that $\vec{n}$ makes with the plane defined by the vertical and the trend of the B axis is conducted (Snoke, 2003). The output consists of strike Φ_s, rake λ, dip δ, as well as the trend and plunge of $\vec{a}$, $\vec{n}$, P, T and B axes, thus a representation of the fault plane solution by all possible quantities is determined. One can input P, SH and SV polarities. Furthermore, there is the possibility to also input the SH/P, SV/P and SV/SH amplitude ratios (see section 6). To use those amplitude ratios one has to correct for attenuation effects and phase conversion effects at the free surfaces (Snoke, 2003). I determine fault plane solutions by using P and SH polarities as well as SH/P amplitude ratios (see section 6 and 7).

4.4. Stress inversion

Like stated above earthquakes develop from rupture processes in the Earth due to stresses. Stresses are defined as forces per unit area. If we consider a Cartesian coordinate system, the stress tensor $\underline{\sigma}$ describes the traction force $\vec{F}(\vec{n})$ acting on an infinitesimal plane with a normal vector $\vec{n}$ (Plenefisch, 1996; Shearer, 2009):

$$\underline{\sigma} = \begin{pmatrix} \sigma_{11} & \sigma_{12} & \sigma_{13} \\ \sigma_{21} & \sigma_{22} & \sigma_{23} \\ \sigma_{31} & \sigma_{32} & \sigma_{33} \end{pmatrix} \tag{4.26}$$

$$\vec{F}(\vec{n}) = \underline{\sigma}\vec{n} \tag{4.27}$$

The forces acting orthogonal to the plane are called normal stresses, the forces parallel to the plane are shear stresses. The stress tensor $\underline{\sigma}$ is symmetric, as a body in static equilibrium is observed, which reduces the independent components to six. By rotating the coordinate system one can find one system in which the shear stresses are zero, leaving only the normal stresses σ_1, σ_2, σ_3, also called principal stresses ($\sigma_1 > \sigma_2 > \sigma_3$, Plenefisch, 1996; Shearer, 2009). I am interested in those principal stresses, as these describe the current state of stress.

$$\underline{\sigma}^R = \begin{pmatrix} \sigma_1 & 0 & 0 \\ 0 & \sigma_2 & 0 \\ 0 & 0 & \sigma_3 \end{pmatrix} \tag{4.28}$$

The mean normal stress σ_m is invariant to any coordinate transformation and represents the isotropic part of the stress tensor. By subtracting the mean normal stress from the normal stresses one gets the deviatoric part of the stress tensor $\underline{\delta\sigma}$ (equation 4.30).

$$\sigma_m = \frac{\sigma_1 + \sigma_2 + \sigma_3}{3} = \frac{\sigma_{11} + \sigma_{22} + \sigma_{33}}{3} \tag{4.29}$$

$$\underline{\sigma} = \underline{\delta\sigma} + \sigma_m\underline{I} = \begin{pmatrix} \sigma_{11} - \sigma_m & \sigma_{12} & \sigma_{13} \\ \sigma_{21} & \sigma_{22} - \sigma_m & \sigma_{23} \\ \sigma_{31} & \sigma_{32} & \sigma_{33} - \sigma_m \end{pmatrix} + \begin{pmatrix} \sigma_m & 0 & 0 \\ 0 & \sigma_m & 0 \\ 0 & 0 & \sigma_m \end{pmatrix} \tag{4.30}$$

To determine the state of stress in a region via inversion from fault plane solutions, there are several approaches (Gephart and Forsyth, 1984; Michael, 1984; Angelier, 1979; Rivera and Cisternas, 1990; Vavryčuk, 2014). In case of a homogeneous medium the P, T, and B axes of the fault plane solutions would represent the direction of the principle stresses. However, this is normally not the case for earthquakes, which can occur along zones of weakness in the rock, e.g. preexisting fault zones. To determine the stress tensor from fault plane solutions the assumption that the maximum shear traction/stress $\vec{\tau}(\vec{n}, \sigma)$ is oriented in the same direction as the slip direction $\vec{a}$ on the fault is applied (Fig. 4.2, Wallace, 1951; Bott, 1959; Michael, 1984).

$$\frac{\vec{\tau}(\vec{n}, \sigma)}{|\vec{\tau}(\vec{n}, \sigma)|} = \frac{\vec{a}}{|\vec{a}|} \tag{4.31}$$

$\vec{\tau}$ represents the unit vector of the maximum shear stress. From here on σ is always only the deviatoric part of the stress tensor, as the full stress tensor as well as the magnitude of the

stresses can not be resolved from fault plane solutions only. By applying the assumption of Wallace (1951) and Bott (1959) and assuming a stress tensor and the orientation of the fault plane, one can determine the slip direction $\vec{a}$ (Gephart and Forsyth, 1984; Plenefisch, 1996). The stresses acting on the fault plane due to the assumed stress tensor can be determined by a tensor transformation to the coordinate system of the fault plane (Plenefisch, 1996):

$$\sigma_{ij}^R = \sigma_{km}^{R_{fps}} \beta_{ik} \beta_{jm} \quad \text{for } i, j, k, m = 1, \ldots, 3 \tag{4.32}$$

Here $\underline{\sigma}^R$ is the stress tensor in the coordinate system of the principal stresses and $\underline{\sigma}^{R_{fps}}$ represents the stress tensor in the coordinate system of the fault plane. The matrix $\underline{\beta}$ contains the directional cosines mapping from the fault plane (first index) to the coordinate system of the principal stresses (second index, Plenefisch, 1996). With equation 4.32 we can now determine the stress components on the fault plane, so also the tangential shear stress. Together with the assumption that the maximum shear stress $\vec{\tau}(\vec{n}, \sigma)$ is oriented in the same direction as the slip vector $\vec{a}$ one can determine via inversion the shape ratio R which describes the relative stress magnitude and the angles of the direction of the principal stresses (Plenefisch, 1996).

$$R = \frac{\sigma_2 - \sigma_1}{\sigma_3 - \sigma_1} = -\frac{\beta_{13}\beta_{23}}{\beta_{12}\beta_{22}} \tag{4.33}$$

I apply the program StressInverse (Vavryčuk, 2014) to determine the direction of the principal stresses and their relative magnitude from the fault plane solutions (see section 6). The program determines R and the direction of σ_1, σ_2, σ_3 using the stress inversion after Michael (1984). Additionally to the assumption after Bott (1959), Michael (1984) assumes that the size of the maximum shear stress $|\vec{\tau}(\vec{n}, \sigma)|$ is similar on all faults in the region and as the inversion only resolves relative magnitudes of the stress tensor, $|\vec{\tau}(\vec{n}, \sigma)|$ is set to be one. This results in a linear relationship between the stress tensor and the maximum shear stress. Furthermore, the isotropic part of the stress tensor is assumed to be zero, also due to the fact that one cannot determine absolute stress magnitudes. This results in a set of linear equations, which can be solved by direct inversion, which makes it a computationally fast approach (Michael, 1984; Vavryčuk, 2014).

$$\underline{A}^i \vec{\Sigma} = \vec{a}^i \tag{4.34}$$

$\underline{A}$ can be determined from the fault normal vector $\vec{n}$, i stands for the ith fault analyzed and $\vec{\Sigma}$ contains the stress components, which are assumed to be the same for all faults. A problem of the stress inversion after Michael (1984) is that one has to know the active fault plane as the inversion was first defined for slip data (Michael, 1984; Vavryčuk, 2014). For this reason Vavryčuk (2014) adds the fault instability criteria to the stress inversion. The Mohr-Coulomb failure criterion describes the critical shear traction τ_c which needs to be exceeded on the fault plane to rupture:

$$\tau_c = C + \mu(\sigma_n - p) \tag{4.35}$$

Here C is the cohesion, μ the fault friction, p the pore pressure and σ_n the compressive normal traction (Vavryčuk, 2014). Based on the Mohr-Coulomb failure criterion Vavryčuk et al. (2013) defines the fault instability criterion I. A fault which is most stable in the stress field is defined with the maximum compression σ_1 in direction of the fault normal $\vec{n}$ and the fault instability

I is zero. Whereas a fault, which is optimally oriented in the stress field and most likely to failure, achieves a fault instability I of one (Vavryčuk et al., 2013).

$$I = \frac{\tau - \mu(\sigma - \sigma_1)}{\tau_c - \mu(\sigma_c - \sigma_1)} \tag{4.36}$$

Here τ_c and σ_c represent the shear stress and normal stress of the fault most likely to failure in the stress field and τ and σ are the shear and normal stresses of the fault plane analyzed. The fault instability can be determined directly from the output of the stress inversion after Michael (1984), by assuming a realistic fault friction μ. By evaluating I for all fault plane solutions used as input in the stress inversion, the nodal plane with the higher fault instability can be identified and used for the next stress inversion as input (Vavryčuk, 2014). The joint iterative inversion of the stress field and the fault orientation stops if some optimal value is reached (Vavryčuk, 2014). As output one not only gets the relative stress magnitudes and the direction of the principal stresses, but also the nodal plane, which is most likely the one which ruptured during the earthquake.

5. The StressTransfer Seismic Network - An Experiment to Monitor Seismically Active Fault Zones in the Northern Alpine Foreland of Southwestern Germany

The following section describes the StressTransfer Seismic Network. It consists of 15 seismic broadband stations located in research areas with striking seismic activity in the Alpine foreland region. One of those regions is the Swabian Alb around the town Albstadt which is analyzed in this thesis. The station locations are chosen to complement and densify the existing seismic broadband station network in the selected areas. As part of the thesis the seismic station locations were selected, seismic stations were installed and maintained. A quality control for all stations is performed in the following section. The following section is completely published as Mader and Ritter (2021).

5.1. Abstract

In the northern Alpine foreland of southwest Germany, continuous microseismic activity is observed, with the potential for strong earthquakes up to magnitude 5 or even 6+. The StressTransfer network is designed to complement the existing seismic networks in three defined areas: the southern Upper Rhine graben, the Albstadt shear zone, and the central Molasse basin around the town of Bad Saulgau. The network monitors mainly the microseismic activity, and will allow us to study the related faults and the stress field. The network consists of 15 seismic broadband stations, five for each region that complement permanent and other temporary recording stations. The data-quality analysis proves an overall good recording quality, despite the problems due to the densely populated area. Recording stations located inside the Upper Rhine graben are characterized by a relatively high-noise level due to freeways and railways located nearby as well as sites on thick, partly unconsolidated fluvial sediments. The comparison of the I95 noise amplitude level at our recording stations with the double P-wave onset amplitude of an exemplary ML 1.0 earthquake in 12 km distance reveals the ability to detect even lower magnitude events at most of the StressTransfer seismic stations. For six stations, it is difficult during daytime; at four stations, we are probably not able to detect comparable small events. From March to May 2020, we observe a reduction of the daily noise amplitude of 20% - 30%, due to the severe restrictions related to the severe acute respiratory syndrome coronavirus 2 (SARS-CoV-2) pandemic, giving us the chance to search

for really low-magnitude events. Our study demonstrates that a careful selection of recording sites allows to monitor faulting processes even in highly populated regions with unfavorable subsurface conditions. In addition, we record teleseismic waveforms at the new locations, to improve the resolution of deeper structures.

5.2. Introduction

The northern Alpine foreland is characterized by distinct seismic activity that causes damage and even fatalities (Leydecker, 2011). In southwestern Germany, the majority of these events is restricted to defined areas: the southern Upper Rhine graben (URG), the Swabian Alb around the Albstadt shear zone (ASZ), and the Bad Saulgau focal zone in the central Molasse basin (MB, Fig. 5.1). These areas are not only characterized by continuous microseismic activity but also have the hazardous potential of earthquakes with local magnitude greater than 5 (Grünthal and the Global Seismic Hazard Assessment Program (GSHAP) Region 3 Working Group, 1999), sometimes reaching even more than 6 (Fäh et al., 2009; Shipton et al., 2017). Here, we introduce our seismic network StressTransfer (Mader and Ritter, 2018) and its performance so far, which focuses on the seismicity in the areas of the URG, the ASZ, and the MB to monitor the continuous seismic activity at selected active fault zones in the northern Alpine foreland. A main issue is the noise characterization, because seismic background noise limits the capability to observe seismic signals. The StressTransfer seismic network is part of the StressTransfer project, which started in 2018 and focused on the seismicity in the northern Alpine foreland of southwest Germany and the related stress field. The project is part of the Priority Program Mountain Building Processes in Four Dimensions and is also a piggyback experiment related to the AlpArray Seismic Network (AASN; Hetényi et al., 2018).

5.3. Tectonic Setting and Damaging Earthquakes

Our three research areas are located in the northern Alpine foreland (Meschede and Warr, 2019) and are influenced by the ongoing Alpine mountain building processes, rift-related tectonics in the URG (Reicherter et al., 2008), and the related tectonic stress field (Kastrup et al., 2004; Reinecker et al., 2010, Fig. 5.1).

5.3.1. URG

The URG is a part of the European Cenozoic rift system, and it has a length of about 300 km and a width of 30–50 km. The graben formation started about 47 Ma ago, due to a changing stress field (Grimmer et al., 2017) most probably related to the Alpine collision. The displacements along the eastern and western main boundary faults happened asymmetrically, with more subsidence in the east (3–5 km). The graben is filled with Cenozoic sediments, reaching a
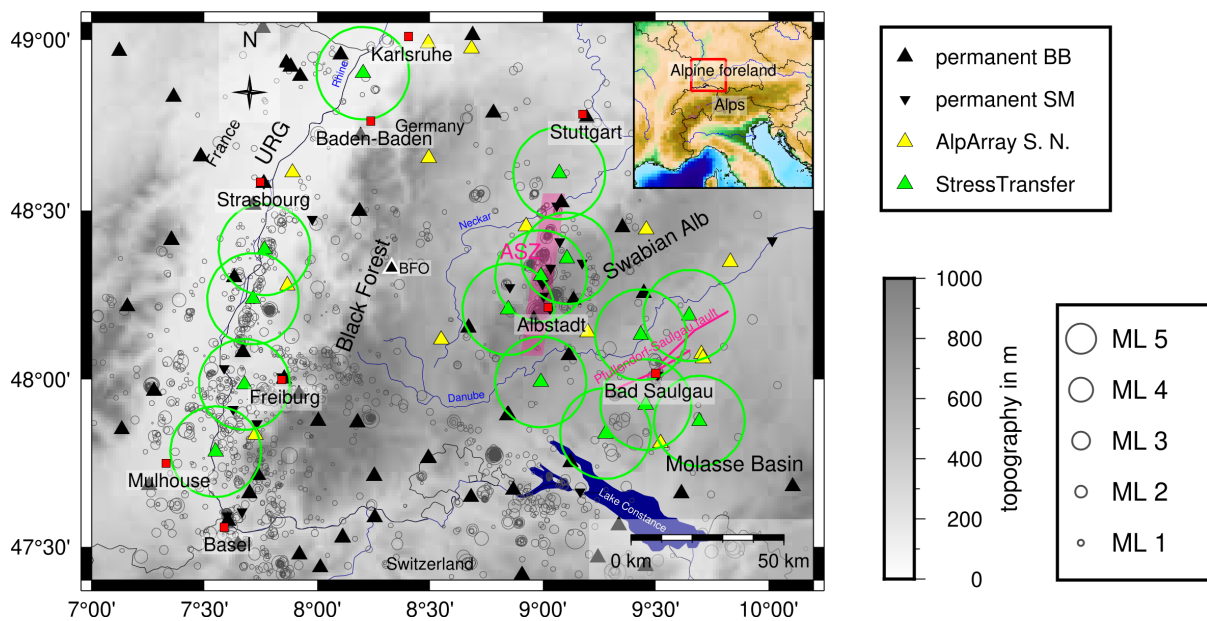
Figure 5.1.: Overview of the research area, together with all available seismic recording stations (see section Data and Resources Mader and Ritter, 2021). Black triangles indicate permanent broadband seismic stations (BB), and inverted black triangles indicate strong-motion seismic stations (SM). Yellow triangles indicate the stations of the AlpArray Seismic Network (AASN). Green triangles are StressTransfer stations surrounded by a 15 km radius circle, illustrating the closure of observational gaps in our three selected research areas. The white-framed triangle marks the location of the station at the Black Forest Observatory (BFO). Gray circles indicate seismic events from the bulletin of the State Seismological Service of Baden-Württemberg (LED) from 2011 to 2018 (Bulletin-Files des Landeserdbebendienstes B-W, 2011-2020). Red frame in the inset shows the location of our research area in the northern Alpine foreland. ASZ, Albstadt shear zone; URG, Upper Rhine graben.

maximum thickness of 3.5 km (Grimmer et al., 2017). In the southern URG, the depth of the crust–mantle boundary (Moho) is still under discussion. In some models, the Moho seems to be warped upward and shallow (about 24 km) (Edel et al., 1975; Zucca, 1984), whereas another interpretation prefers a nearly flat Moho at about 27 km depth (Mayer et al., 1997).

During the period A.D. 800 - 2008, six damaging earthquakes with intensities of 7 — 8 or higher occurred in the URG (Leydecker, 2011). The 1356 Basel earthquake with Mw between 6.7 and 7.1 was the strongest felt event. Paleoseismic studies indicate that similarly strong earthquakes occurred along the URG (Shipton et al., 2017; Reicherter et al., 2020) during the Quaternary. Nowadays, there is frequent weak and occasional moderate seismicity (Bonjer et al., 1984; Barth et al., 2015). The b-value varies: in the south, close to the Basel region, the b-value is 0.83; it increases to 1.42 around Freiburg and Mulhouse, and then it decreases again to about 0.93 toward north (Barth et al., 2015). A possible explanation for the high b-value is an increased segmentation of the faults in the area around Freiburg and Mulhouse with distributed seismicity. Despite the continuous microseismic activity, it is difficult to correlate the seismically active faults with known or suspected geologically identified faults, because location uncertainties of more than 2 km result in a scattered seismicity pattern (Lutz, 2015). Analyses of the stress field from focal mechanisms hint to different stress-field regimes in the upper and lower crust. Plenefisch and Bonjer (1997) suggest a compressional stress regime in the upper crust due to the Alpine mountain building as well as ridge push from the

Mid-Atlantic Ridge and a dilatational stress regime in the lower crust due to the subduction pull of the Eurasian plate.

5.3.2. ASZ

The ASZ is a north–south-striking sinistral strike-slip fault zone, with no expression on the surface and located on the Swabian Alb - a mountain range in southwestern Germany (Fig. 5.1; e.g., Schneider, 1971; Reinecker and Schneider, 2002). The only morphologically visible tectonic feature is the smallscale Hohenzollern graben (HZG) - a northwest-southeast striking, 25 km long graben structure, and an estimated depth extension of 2 - 3 km (Schädel, 1976). The ASZ is associated with continuous seismic activity and reoccurring damaging earthquakes around the town of Albstadt (Leydecker, 2011). In the past century, damaging earthquakes with Mw 5.7 (1911), 5.0 (1913), 4.9 and 5.3 (1943), and 5.1 (1978) occurred, making the ASZ to one of the seismically most active regions in central Europe (Grünthal and the Global Seismic Hazard Assessment Program (GSHAP) Region 3 Working Group, 1999; Stange and Brüstle, 2005). Because no surface expressions of the fault are visible, the geometry, extension, possible segmentation, and faulting pattern of the ASZ only can be studied by its seismicity. Reinecker and Schneider (2002) propose a neotectonic model that relates the tectonic graben structures at the surface with the ASZ in the subsurface. They suggest that the small grabens like the HZG are en-echelon structures as a result of the movement of the ASZ, partly decoupled from the upper layers. The northern and southern terminations of the ASZ are still unclear; some authors propose an extension from Switzerland to the north of Stuttgart (Reinecker and Schneider, 2002), whereas others expect a shorter extension focused on the Swabian Alb around Albstadt (Stange and Brüstle, 2005).

5.3.3. MB

The MB is the northern Alpine foreland basin reaching from northern Switzerland in the west to eastern Bavaria in the east. The central part is located south of the Swabian Alb and is filled up to 4 km with Cenozoic sediments (Meschede and Warr, 2019). The major tectonic features are west-southwest - east-northeast to west-northwest - east-southeast-striking normal faults, like the Pfullendorf-Saulgau fault (Fig. 5.1, Stange and Brüstle, 2003; Geyer and Gwinner, 2011). The hazardous potential of the MB is reflected by the 27 June 1935 Mw 5.6 earthquake, which happened close to the town of Bad Saulgau with an intensity of 7 - 8 (Leydecker, 2011) causing building collapses. Stange and Brüstle (2003) describe the seismicity around Bad Saulgau as episodic and swarm like. Most of the events exhibit a northeast-striking sinistral strike-slip character, with some indications for normal faulting in the lower crust. The determined b-value is 0.4, which is not explained yet (Stange and Brüstle, 2003). The stress field inside the MB is always perpendicular to the Alpine front, hinting to gravitational potential energy as driving force (Reinecker et al., 2010).

5.4. Network Description

Our StressTransfer network has the International Federation of Digital Seismograph Networks (FDSN) network code 5N (Mader and Ritter, 2018) and is composed of three subnetworks, each consisting of five seismic broadband stations focusing on the URG, the ASZ, and the MB. Installation started on 5 July 2018 in the URG area and was finished on 9 January 2019 on the Swabian Alb. The installation time span took half a year, because it was difficult to find appropriate installation sites due to the partly dense population, disturbing traffic routes or permission issues. Recording is scheduled until the end of 2021.

5.4.1. Instrumentation

All instruments used are part of the KArlsruhe BroadBand Array (KABBA). The majority is equipped with Streckeisen STS-2 broadband seismometers (12); in addition, two Güralp CMG-40T, one Steckeisen STS-2.5, and one Geotech KS-2000 are deployed. Data logger equipment is an EarthData PR6-24 at all sites. To ensure security and power supply, most of the recording stations are located inside buildings; we also deployed two buried stations close to a building. During installation, we could only apply a classical magnetic compass to adjust the seismometers to the north direction. Later, we redetermined a high-quality north direction with a gyrocompass (iXBlue Quadrans), to fix a possible deviation of the seismometer orientation from the true north direction (Table 5.1). This readjustment resulted in a maximum heading of 20° to north for station AST02 (Table 5.1). The well-adjusted horizontal components can be used for wave-polarization analyses, event location, and teleseismic receiver functions or SKS splitting studies. For a high-quality time signal, we use Global Positioning System synchronization. The station codes are named AST for AlpArray StressTransfer project (Fig. 5.2), with numbers 01 - 05 for stations in the URG, numbers 11 - 15 for stations around the ASZ, and numbers 21 - 25 for stations in the MB.

5.4.2. Location selection

The station locations were selected to best fill observational gaps in each research area (Fig. 5.1). As starting point, we took the combined network of all permanent broadband stations (Seismological Service Baden-Württemberg, network LE (Landesamt für Geologie, Rohstoffe und Bergbau, 2009; Bulletin-Files des Landeserdbebendienstes B-W, 2011-2020), Switzerland Seismological Network CH (Swiss Seismological Service (SED) at Eidgenössische Technische Hochschule (ETH) Zurich, 1983), Réseau Sismologique et géodésique Français (RESIF) - Réseau Large-Bande Permanent French broadband network FR (RESIF, 1995), German Regional Seismic Network GR (Federal Institute for Geosciences and Natural Resources (BGR), 1976), GEOFON seismic network GE (GEOFON Data Centre, 1993, see section Data and Resources Mader and Ritter, 2021), and the temporary AASN Z3 (AlpArray Seismic Network (AASN), 2015; Hetényi et al., 2018), as displayed in Figure 5.1. The goal was to reduce the maximum distance between

Table 5.1.: Station Information Including Installation Date, Seismometer Type, Heading to North Direction and In-Situ Rock at Station Location (see section Data and Resources Mader and Ritter, 2021)

Station	Installation Date (yyyy/mm/dd)	Seismometer	Heading Relative to North	In-Situ Rock Type
AST01	2018/7/25	KS-2000	14.1°	Fluvial sediments
AST02	2018/7/5	STS-2	19°	Glacial deposits
AST03	2018/7/10	STS-2	−9°	Loess on glacial deposits
AST04	2018/7/5	STS-2	4°	Jurassic clayey limestone
AST05	2018/8/24	STS-2	−7.7°	Fluvial sediments
AST11	2019/1/8	STS-2	−1°	Sandstone
AST12	2018/8/20	STS-2	5.3°	Jurassic limestone
AST13	2018/10/30	CMG-40T	6°	Jurassic limestone
AST14	2018/9/19	STS-2	1.98°	Jurassic clayey limestone
AST15	2019/1/9	STS-2.5	6.7°	Jurassic limestone
AST21	2018/7/17	STS-2	-	Glacial deposits
AST22	2018/7/18	STS-2	−4°	Molasse limestone and glacial deposits
AST23	2018/9/20 - 2019/10/2	STS-2	-	Molasse limestone
	2019/10/2	CMG-40T		
AST24	2019/1/8	STS-2	3.7°	Molasse limestone
AST25	2018/7/17	STS-2	11°	Fluvial sediments and glacial deposits
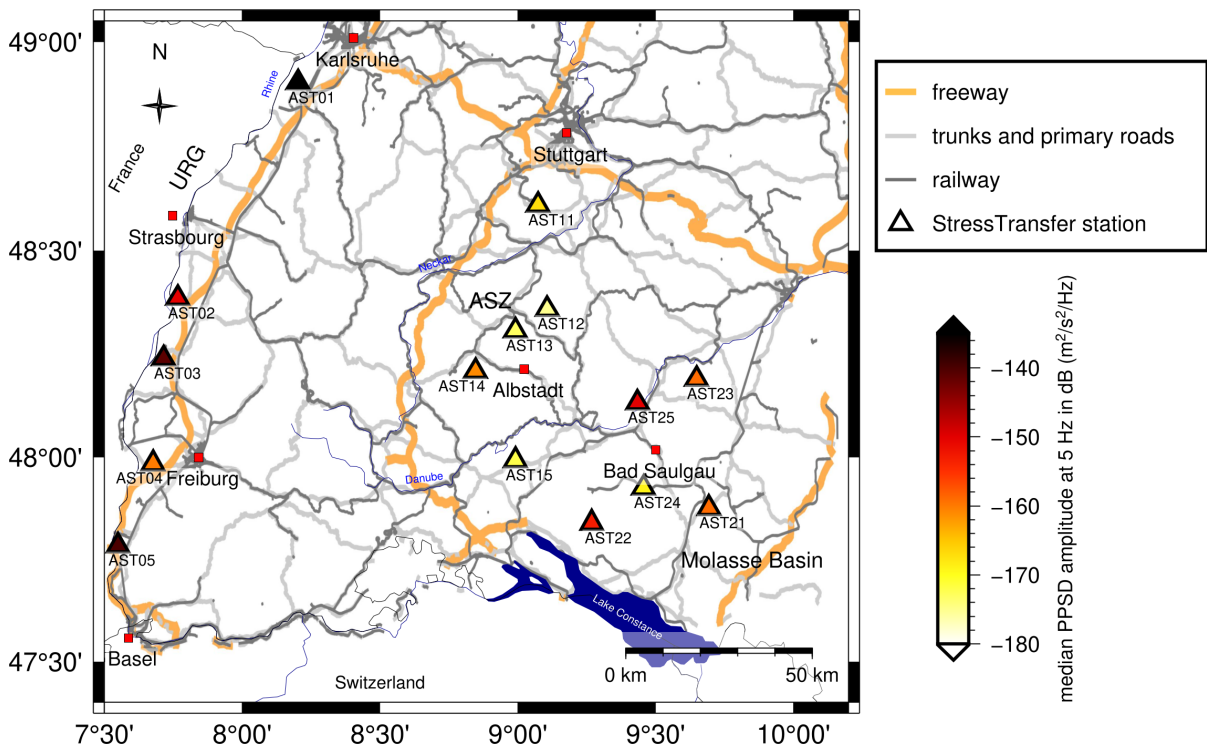
Figure 5.2.: Area of the state of Baden-Württemberg with the main freeways (Autobahn), railways, and major roads (see section Data and Resources Mader and Ritter, 2021). StressTransfer stations are colored with the median probabilistic power spectral density (PPSD) amplitude at 5 Hz. Clearly visible is the difference in seismic noise amplitude between the stations in the URG (AST01 - 05) and the ASZ (AST11 - 15). For the area of the surrounding states of Bavaria, Austria, Switzerland and France, no information is plotted.

broadband stations to less than 15 - 30 km. Furthermore, we also selected recording sites based on the requirements of our research topics:

1. In the URG region, permanent recording stations (networks CH, FR, GE, GR, and LE, see section Data and Resources Mader and Ritter, 2021) are mainly placed outside the graben on the rift shoulders at hard-rock sites, to avoid the noisy unconsolidated rift sediments. Yet, we installed the StressTransfer stations along the strike of the URG to receive recordings inside the graben itself, to improve the earthquake locations in depth and horizontally. An improved correlation of the hypocenters with the known geological fault zones should help analyze the origin of the variations of b-values in more detail (Barth et al., 2015). Furthermore, the combined networks (StressTransfer, AASN, and permanent networks [CH, FR, GE, GR, and LE], see section Data and Resources Mader and Ritter, 2021) should allow us an investigation of the uncertain Moho depth underneath the URG (Edel et al., 1975; Zucca, 1984; Mayer et al., 1997), for example, by determination of teleseismic receiver functions inside the graben. Because teleseismic processing is done below about 0.1 - 0.2 Hz to avoid oceanic microseisms, the mostly highfrequency cultural noise is less disturbing.

2. The StressTransfer recording stations around the ASZ are installed along strike and oblique to the ASZ, crossing the HZG. The StressTransfer stations to the north and south
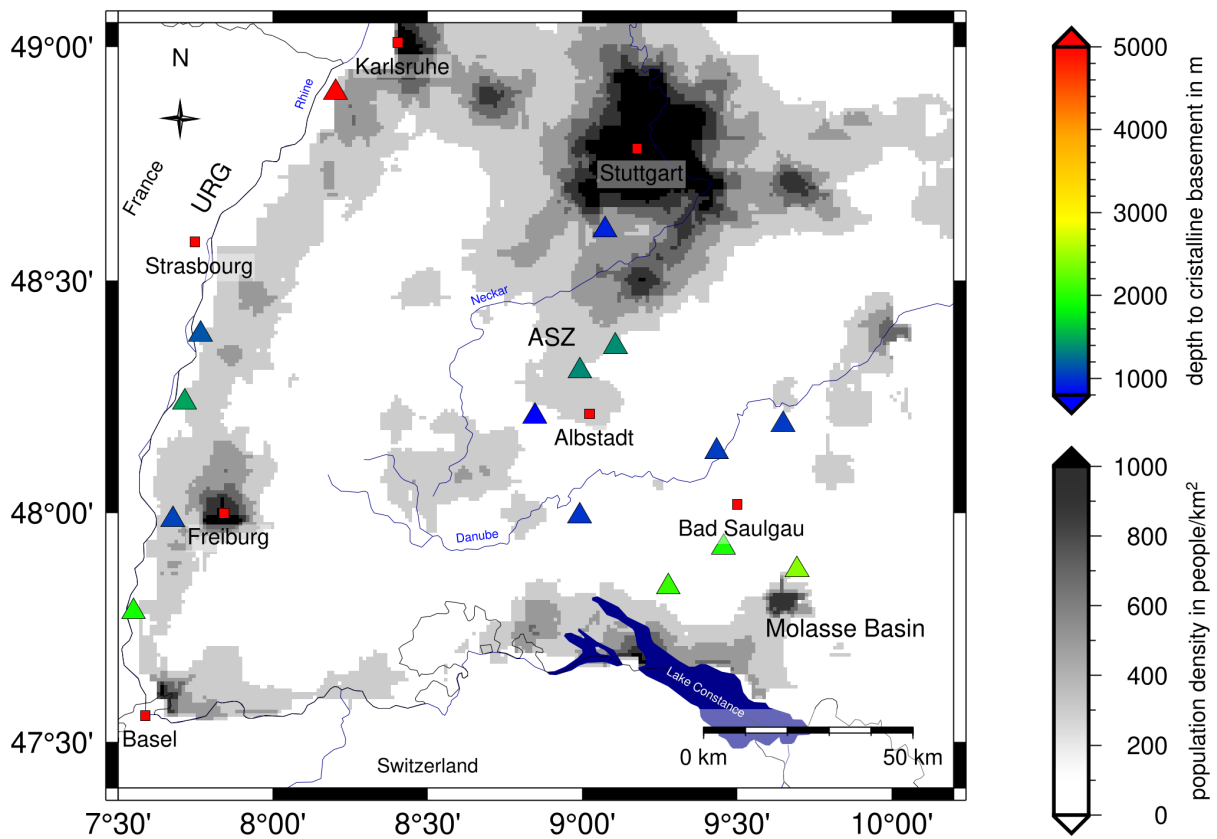
Figure 5.3.: Area of the state of Baden-Württemberg with the interpolated population density (see section Data and Resources Mader and Ritter, 2021, people per km^2) and the StressTransfer stations colored with depth to the crystalline basement in meters (see section Data and Resources Mader and Ritter, 2021) for correlation with seismic noise properties (Figs. 5.2 and 5.4). Clearly visible are the densely populated areas in and around the major cities such as Stuttgart, Karlsruhe, and Freiburg. For the area of the surrounding states of Bavaria, Austria, Switzerland, and France, no information is plotted.

will help better identify the northern and southern terminations of the ASZ that are still under debate (Reinecker and Schneider, 2002; Stange and Brüstle, 2005). Improved detections and locations of the continuous seismic activity should help image the corresponding fault structure, especially, the geometry, depth extension, and segmentation of the ASZ, including possible seismic activity related to the HZG.

3. In the central MB, the StressTransfer recording stations are distributed around the town Bad Saulgau. This configuration is selected due to the epicenter distribution of the 1935 earthquake and the majority of the swarm-like events occurring in the close vicinity (Stange and Brüstle, 2003; Leydecker, 2011). The microseismic activity may reveal the nature of the fault zone and its geometry, as well as give new insights into the low b-value of the area (Stange and Brüstle, 2003). From time to time, lower-crustal seismicity (>20 km depth) is observed in the MB. We hope to better understand the still unclear mechanisms of this unusual seismicity with our recordings.

The selection of the actual recording sites was a stepwise procedure. After the identification of the observational gaps, we used Google Maps to identify possible sites within the closer

area of the preselected positions. This was, particularly, difficult in the URG due to the Rhine River, the railways, and freeways on both sides of the Rhine River, settlements, and industry facilities within the graben (Fig. 5.2). The increased population density in the URG is visible in Figure 5.3 as northeast-southwest-trending corridor. Therefore, our installation sites had to be shifted, because no adequate quiet recording site could be found (e.g., AST11, Figs. 5.2 and 5.3). AST11 should monitor the northern extension of the ASZ, just south of Stuttgart, where it would have been located in an area with a high population density (Fig. 5.3, more than 600 people per km^2). Here, we shifted the location about 10 km to the southeast, to get into a less-populated area. A shift of the recording location to the southwest was also difficult, as the freeway A81 is passing by from Stuttgart toward the southwest. In the end, most of the stations are installed in areas with a population density of less than 200 - 400 people per km^2 (Fig. 5.3). The preferred sites (including low noise, power supply, and security) were six club houses from gun and sport clubs (mostly remote sites with few activity), as well as three cemeteries. The other station locations are sites of different use, like a water container, a water-pumping house, a broadcast station, and secluded agriculture and forestry houses with few activities.

5.4.3. Network operation and data handling

The StressTransfer network is operated offline, and real-time acquisition is not possible due to financial limitations. The data are recorded on hard disks and collected during two service tours per year. This time interval is also necessary to minimize instrument failures or accidental power failures. The data are archived at our institute at Karlsruhe Institute of Technology, according to the European Integrated Data Archive concept in a standardized data system. Data analysis is done after merging all available recordings (from about 5–6 different networks) in a consistent way, to improve routinely determined hypocenters and add fault-plane solutions as well as seismotectonic interpretations. Teleseismic analysis will follow at a later stage. Public opening of the archive is planned for April 2022 (see section Data and Resources Mader and Ritter, 2021).

5.5. Data Quality

To check the noise conditions at our StressTransfer seismic stations, we calculated probabilistic power spectral densities (PPSDs; Fig. 5.4 and Figs. A.1 and A.2 in the supplemental material available to this article) with ObsPy (e.g., Beyreuther et al., 2010a). As reference, we take the new high-noise model (NHNM, Peterson, 1993), although, it is more adapted to permanent recording stations, which are selected more carefully concerning noise conditions. Such a selection was often not possible in our case due to the project goals (see previously). However, all StressTransfer stations have an average noise level below the NHNM, for frequencies higher than 1 Hz (Figs. 5.4 and 5.5), except of stations AST01 and AST05. During less than 5% of the 1 hr duration time windows, there is an increased noise level at stations AST03, AST04, AST11, and AST21 over the whole frequency range. These disturbances may be due to station
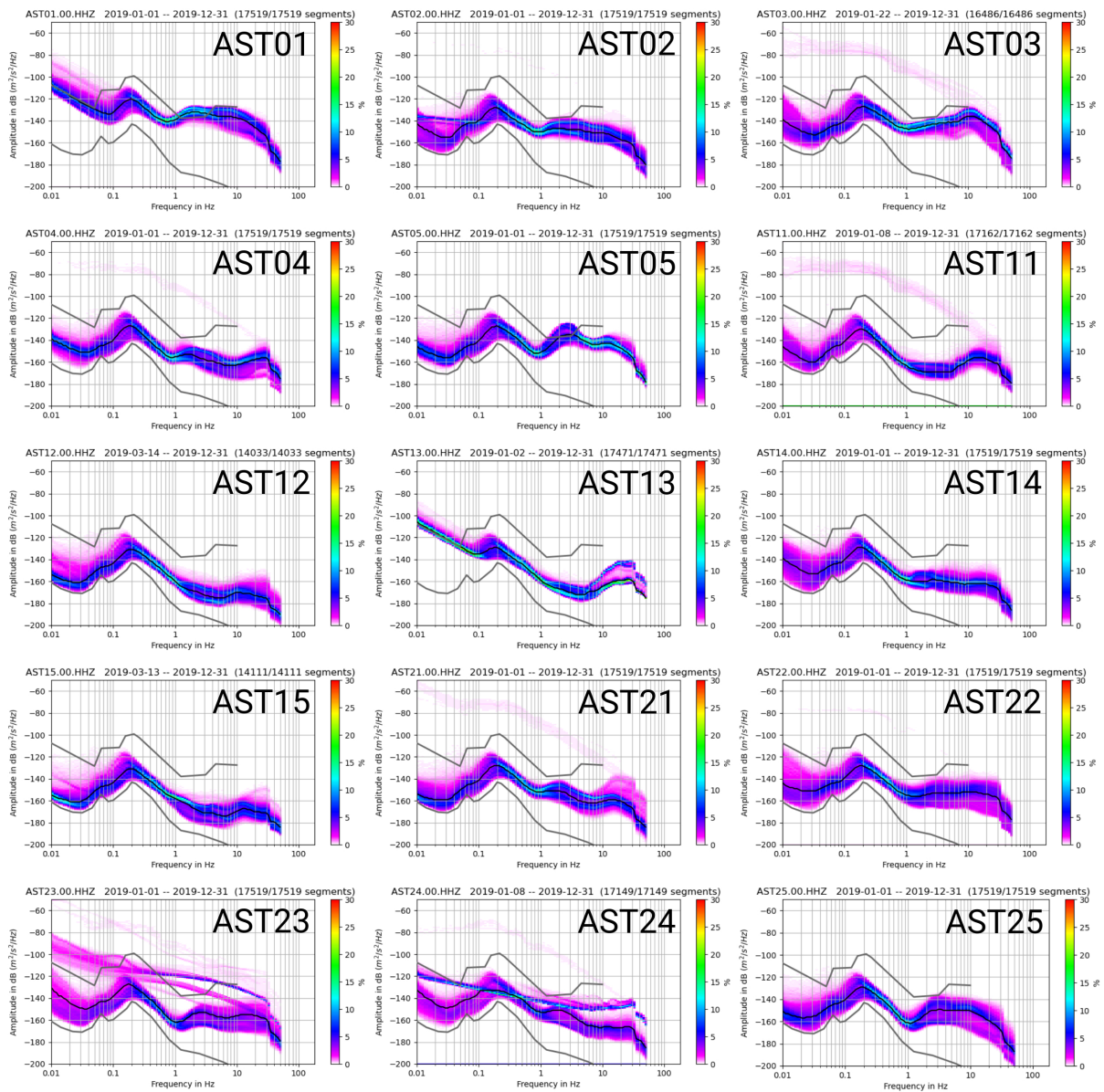
Figure 5.4.: PPSDs for the year 2019 for each StressTransfer station vertical component (for horizontal components, see Figs. A.1 and A.2). The Power spectral densities (PSDs) are calculated for 1 hr segments and overlap by 50%. The color coding represents the probabilistic occurrence of an amplitude at a certain frequency. The black line shows the median of all PSDs. Gray lines mark the new low-noise model (NLNM) and the new high-noise model (NHNM) after Peterson (1993).

service activities or people coming unusually close to the sensor as well as construction or agricultural work close-by or shooting exercises in gun clubs, which last typically for only a few hours per week (Fig. 5.4). Because StressTransfer is closely related to the AASN, the AASN technical recommendations (Brisbourne et al., 2013) were taken into account: stations on hard rock or rural sites should have a noise level 20 dB below the NHNM. This is fulfilled at the stations around the ASZ (Fig. 5.5b). Station noise in basins or at soft soil sites (URG and MB in our case) should not exceed the NHNM (Brisbourne et al., 2013). This is well achieved
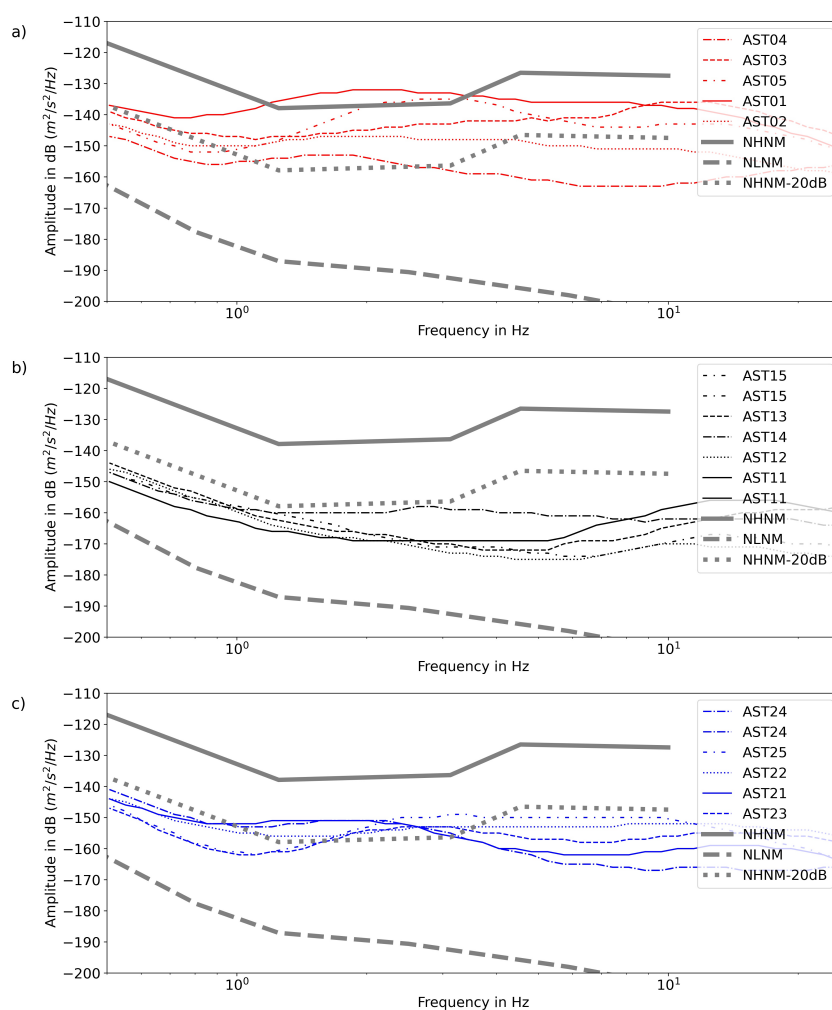
Figure 5.5.: Comparison of medians of PPSD for 2019 for each StressTransfer station (black line in Fig. 5.4). Stations in the (a) URG have a clearly higher noise level (mean amplitude at 5 Hz: $-145.4dB$) than stations close to the (b) ASZ (mean amplitude at 5 Hz: $-156.6dB$), and in (c) the Molasse basin (MB; mean amplitude at 5 Hz: $-169.8dB$). Gray lines illustrate the NLNM and the NHNM after Peterson (1993). The NHNM minus 20 dB is the maximum recommended noise level for hard rock and rural sites of the AASN after Brisbourne et al. (2013).

in the MB (Fig. 5.5c) and mostly in the URG (Fig. 5.5a).

  For the majority of the StressTransfer stations, we observe a clear day and night change of the noise level above 1 Hz as separated bands in Figure 4, due to human-induced noise during daytime (see also Fig. 5.6). Exceptions are the stations AST05, AST11, AST14, AST22, and AST25. Here we observe no clear splitting into two similar probable band-like amplitude peaks, but more a smearing (AST22 and AST25) or a splitting in the spectra (Fig. 5.4) for few frequencies (AST05, AST11, and AST14). Stations AST23 and AST24 had temporary instrumentation problems, which are visible in the PPSDs as linear lines of noise along the whole frequency range. The frequency range below 1 Hz contains the typical oceanic microseism peaks, and all stations equipped with an STS-2 or STS-2.5 seismometers record a low–median noise level. Recording stations AST11, AST12, AST15, AST21, and AST25 do even reach close to the new low-noise model (Peterson, 1993) for some time spans (Fig. 5.4). For the

year 2019, the medians of the PPSDs of all recording stations indicate that sites located in the URG (AST01 - AST05) suffer from the highest seismic noise level in our main frequency range of interest for microseismic observation (higher than 1 Hz, Fig. 5.5). The comparison with the seismic stations on the Swabian Alb (AST11 - AST15) shows an average decrease by 24 dB (relative $1 m^2/(s^2 Hz)$), relative to the URG. The seismic stations in the MB (AST21 - AST25) have a slightly smaller average decrease of 11 dB at a frequency of 5 Hz, relative to the URG. These differences originate mainly from the different immission of human-generated seismic noise at a recording station as well as the geological underground conditions (Table 5.1). The later are partly unconsolidated sediments in the URG, compared to hard Jurassic limestone close to the ASZ. Especially, sites close to freeways and railways suffer from higher PPSD noise amplitudes (Fig. 5.2, stations AST01–AST05, AST21, and AST25). At station AST22, we also observe higher noise, although, its location is the furthermost distant to major roads and railways. Here, we clearly record a local site effect due to nearby agriculture and forestry. The polarity and individual instrument response were checked for correctness, by comparing the first-motion onsets of three teleseismic earthquakes at all StressTransfer stations (Fig. 5.7 and Figs. A.3 and A.4). We assume that the waveforms should be very coherent at the different sites, due to the long epicentral distances. This comparison of waveforms results in a good agreement for all StressTransfer stations, indicating a proper instrumental operating mode. Only the recordings from station AST01 have systematically higher amplitude relative to the other stations. The most possible explanation is amplitude amplification due to a much thicker sedimentary cover on top of the crystalline basement (see section Data and Resources Mader and Ritter, 2021) below station AST01 relative to the other stations (Fig. 5.3). An additional effect may be instrument related, because station AST01 is the only station equipped with a KS-2000 seismometer (Table 5.1), which had an about 10% increased amplitude during a previous comparison of the KABBA instruments. The waveform examples for the horizontal components in Figures A.3 and A.4 do show the same amplification effects for AST01.

To further analyze the noise conditions, we use the statistical time-series scheme from Groos and Ritter (2009) to classify the measured noise at our recording stations. Thereby, we determine the I95 noise curve for all our recording stations (Fig. 5.6), which represents 95% of the observed noise amplitudes. For comparison, we also plot the I95 curve of the station BFO (Black Forest Observatory (BFO), 1971), which is supposed to be one of the quietest places worldwide (Fig. 5.1). There is a clear day and night trend for almost all sites that reflects the influence of the human-induced seismic noise at our stations, which is also visible in the PPSDs (Fig. 5.4). The sites in the URG are characterized with a much higher noise level, in comparison with the ASZ and MB stations. This difference is about a factor of 10 for I95. The I95 noise level at station BFO is, as expected, the lowest one with another factor of about 10 less than at the sites of the ASZ and MB stations. To check the capability to detect microearthquakes, we picked the double amplitude of the direct P wave of a representative 28 January 2020 ML 1.0 earthquake at 07:42 UTC near Albstadt (see Data and Resources) at station AST12, which is in 12 km distance to the epicenter (pink line in Fig. 5.6). The comparison of the P-wave amplitude with the I95 noise curves demonstrates that we should be able to observe such an earthquake at 6 of our stations (AST04, AST11, AST12, AST15, AST23, and AST24), and that the detection of events with even a lower magnitude should be possible, even on daytime. Nevertheless, one station (AST02) has a higher-noise level during daytime, and the three remaining stations (AST01, AST03, and AST05 - all in the URG) are, probably, too noisy to detect comparable
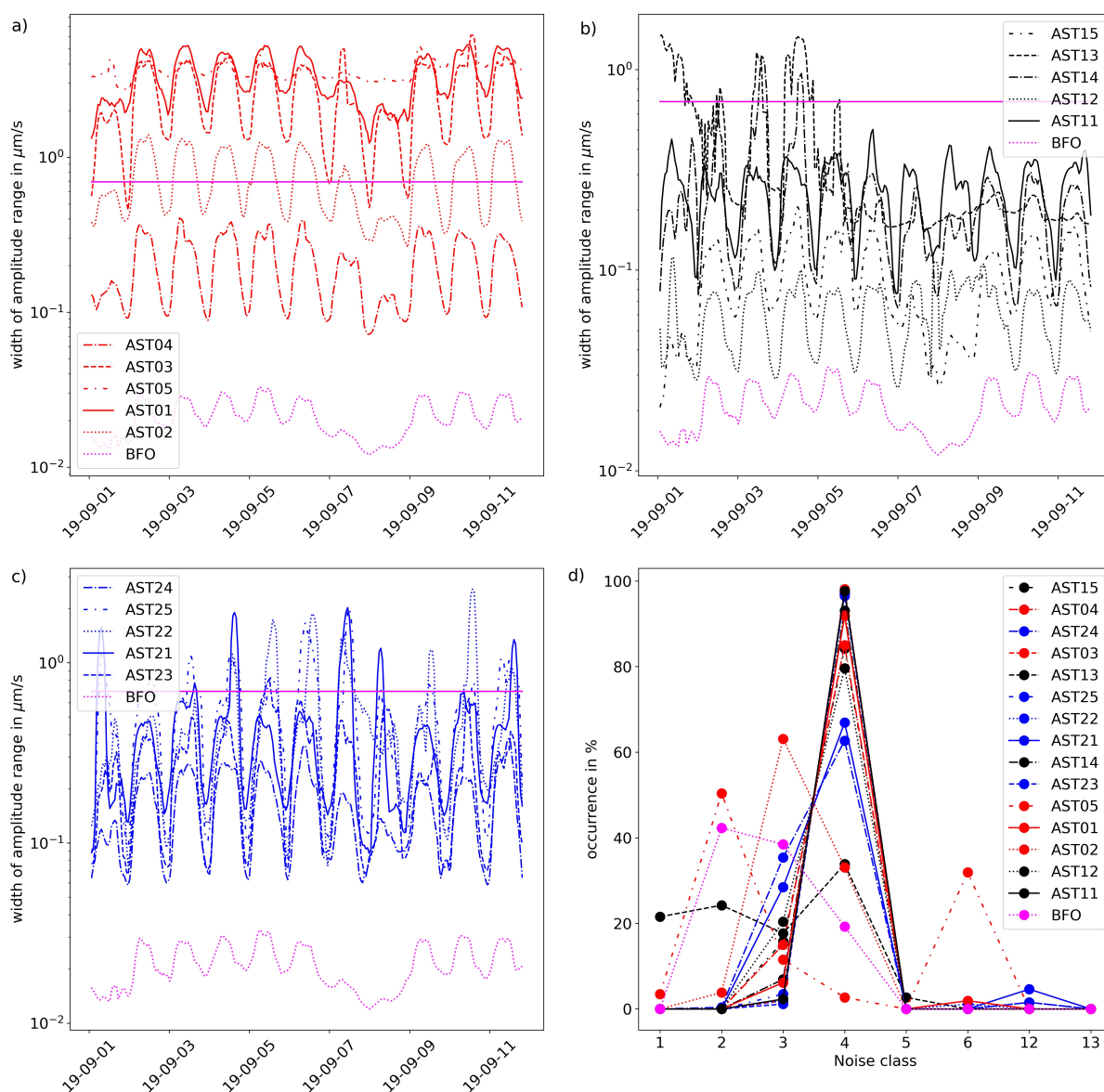
Figure 5.6.: I95 noise curves and noise classes after Groos and Ritter (2009) for all StressTransfer stations during 1 - 11 September 2019. The vertical-component recordings were band-pass filtered at 1 - 25 Hz. A clear day and night cycle is visible due to human activities. Stations in the (a) URG have a higher noise level than stations in (b) the ASZ, or (c) the MB. I95-noise curves from BFO are given for comparison. The pink solid line indicates the double amplitude of the direct P wave of a representative 28 January 2020 ML 1.0 earthquake in 12 km distance at 07:42 UTC near Albstadt. (d) Noise classes 1 - 5 indicate Gaussian distributed noise. Other noise classes hint to unusual noise (6, 12, and 13), but occur less frequently.

events. At five stations (AST13, AST14, AST21, AST22, and AST25), the I95 curve is above the double amplitude of the direct P wave (ML 1.0) at some days during daytime, but detection and phase picking of comparable and smaller events should be possible for most of the time (see example in the following). We also calculated the corresponding noise classes (Fig. 5.6d) to identify if there is non-Gaussian noise, which may result from specific noise sources or may be due to corrupt time series (Groos and Ritter, 2009). Noise classes 1 - 5 correspond to noncorrupt
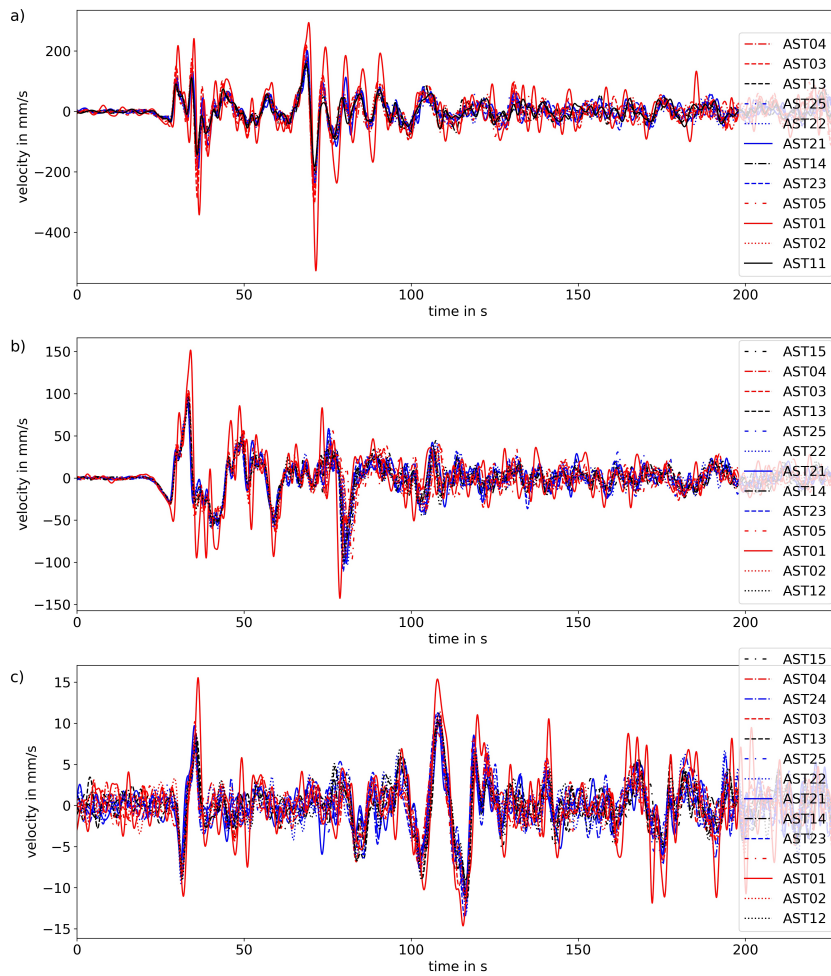
Figure 5.7.: Teleseismic waveform recordings at the StressTransfer stations for channel HHZ (vertical component) to check amplitude and polarity properties. The seismograms are shifted relative to the expected compressional wave arrival time of each event: (a) P phase of a 22 February 2019 Mw 7.5 earthquake below the Peru-Ecuador border region in 46 km depth, (b) PKP phase of a 15 June 2019 Mw 7.3 earthquake below the Kermadec Islands in 212 km depth, and (c) Pdiff and pPdiff phases of a 24 June 2019 Mw 7.3 earthquake below the Banda Sea in 132 km depth. For the horizontal components, see Figures A.3 and A.4.

symmetric time series with noise class 1 meaning Gaussian-distributed noise, noise class 2 exhibits small deviations from the normal distribution, noise class 3 has a slightly peaked histogram, data characterized as noise class 4 shows a stronger peaked histogram, and data in noise class 5 have a flattened histogram in comparison to the normal distribution. Noise class 6 represents time series with an asymmetric histogram. Data time series with noise classes 12 and 13 represent typically corrupt data (Groos and Ritter, 2009). The dominating noise classes are 3 and 4 for the StressTransfer sites (Fig. 5.6d), indicating a typical background noise distribution close to a Gaussian distribution (Groos and Ritter, 2010). Data at station AST05 have also time windows with noise class 6 (Fig. 5.6d), which is hardly observed at the other stations. This observation is likely a site effect, because AST05 is situated in a building for seasonal agricultural water pumping. The pumping process and related water flow may excite non-Gaussian-distributed noise. However, such disturbances have to be tolerated, because
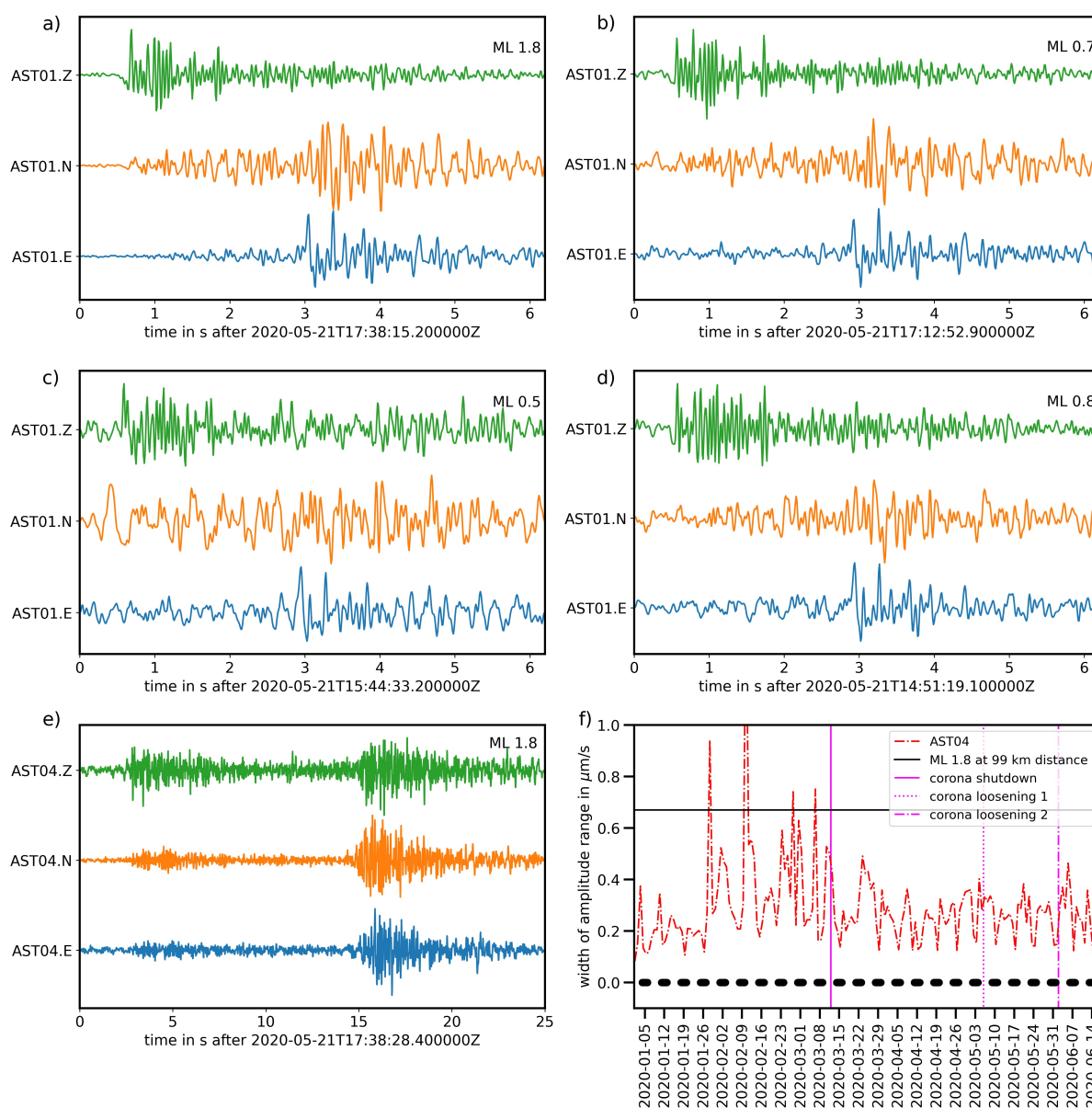
Figure 5.8.: (a - d) Waveform examples at noisy conditions for a small-magnitude earthquake series. Station AST01 is at 10 km distance and clearly records the events down to ML 0.5. Note the similarity especially on the east–west component. (e) The seismic phases in 99 km distance at station AST04 are only visible due to the noise reduction related to the (f) SARS-CoV-2 shutdown. The black line in panel (f) is the direct P-wave double amplitude of the ML 1.8 event. All waveforms are trace normalized and band-pass filtered from 1 to 25 Hz.

other suitable sites could not be found in this densely populated and highly cultivated region (Figs. 5.2 and 5.3).

To demonstrate the benefit of the densified station network, we show an example from a 21 May 2020 small, low-magnitude earthquake series (Fig. 5.8). The Seismological Service reported on four events with ML 0.5 - 1.8 east of Baden-Baden in the URG (Fig. 5.1). The epicenters could be well located (±0.3 to ±1.1 km for latitude and longitude, see section Data and Resources Mader and Ritter, 2021), but the depth h could be determined for only one

event (ML 0.5 with h = 5.0 ± 2.0 km), whereas, for the other events, only a fixed depth of 5 km is provided. We looked at this event series, which happened at a distance of about 10 km from StressTransfer station AST01 and 99 km from AST04. The P-wave amplitude is above the increased URG noise level, and onset times could be picked for P and S waves (Fig. 5.8). The observation at station AST04 is enabled due to the reduced noise during the severe acute respiratory syndrome coronavirus 2 (SARS-CoV-2) pandemic (Fig. 5.8e,f). Further analysis with refined velocity models and relative locations is under way, and we expect improved locations.

5.6. SARS-CoV-2-Related Noise Reduction

Even on a worldwide scale, seismic noise is affected by the SARS-CoV-2 crisis (Lecocq et al., 2020). In spring 2020, the strict shutdown and even the less-strict policies afterward lead to a reduction of human-induced ground motions, due to generally reduced activities. Such an effect is also visible at several StressTransfer stations. In Fig. 5.9, there is the variation of the daily mean background noise (from 05:00 to 20:00 local time) as I95 value in the frequency range 1 - 25 Hz for the first half in the year 2020. Following the holiday season (including the first week in January), the noise slowly increases, especially, in February, when the first agricultural field operations started during relatively mild weather in the end of winter (the second warmest winter ever in Germany, see section Data and Resources Mader and Ritter, 2021). In Germany, the first official warnings concerning SARS-CoV-2 were released on 12 March, and people started to reduce travel and began to work from home. Cross-border traffic was restricted from 18 and 22 March; the federal government announced a strict shutdown. These policies are reflected in Fig. 5.9, at the StressTransfer stations AST04, AST11, AST14, and AST21. Our first estimations, also from looking at other seismic stations, find that the effect of the SARS-CoV-2 shutdown has the same effect on seismic noise as the season holidays from end of December to beginning of January. More quantitatively, about 20% - 30% reduction in noise amplitude can be achieved. AST12 is not much affected, because it is more remote from traffic lines (Fig. 5.2). After stepwise loosening the SARS-CoV-2-related restrictions at the beginning of May and June, the noise level slowly returned to a typical near-average level. The time window of March - May 2020, with the reduced noise, will be a special time period to search for low-magnitude events. The example in Fig. 5.8e,f illustrates the relation between the noise level on the vertical component in the southern URG and the measured P-wave amplitude from an event at station AST04 in 99 km distance.

5.7. Conclusion

The StressTransfer network is designed to complement the existing permanent broadband stations (networks CH, FR, GE, GR, and LE, see section Data and Resources Mader and Ritter, 2021) and the AASN (Hetényi et al., 2018), to monitor the continuous mainly microseismic
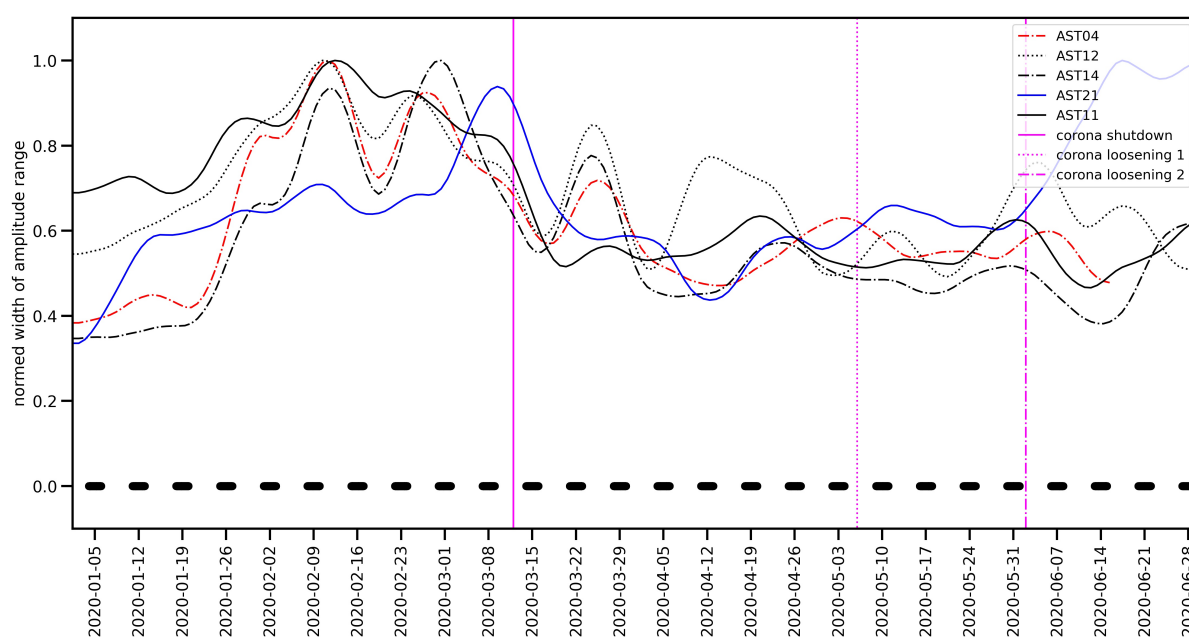
Figure 5.9.: I95 daytime noise level from 1 January until 30 June 2020, including the shutdown related to the SARS-CoV-2 crisis. Smoothed mean values from 05:00 to 20:00 local time are shown in the frequency range 1 - 25 Hz, and the dashed line at the bottom indicates weekly time durations.

activity in the northern Alpine foreland and to allow us the analysis of the related faulting processes and the local stress field. Although, it was important to find low-noise installation sites to enable the recording of the microseismic activity, the actual conditions forced us to find suitable compromises. Most of the StressTransfer stations are now installed at places with rare activity, like gun clubs and cemeteries. Nevertheless, in some areas, we had to accept a less quiet installation site with site-specific noise due to dense population, disturbing traffic routes, or permitting issues, like in case of station AST05. The quality control of the recording data hints to a good data quality at almost all stations, allowing us to further investigate our research aims. As expected from the distribution of traffic lines and the thick sediment cover, the StressTransfer stations in the URG suffer from a higher noise level than the StressTransfer stations around the ASZ or in the MB. A comparison of the I95 noise amplitude with the doubled P-wave onset amplitude of an exemplary ML 1.0 earthquake in 12 km distance is used to check whether our stations are capable to detect such an event. At four stations, it will become difficult to identify earthquakes with ML smaller than 1 at 12 km distance, and at six stations there is a higher noise at some days during daytime. Overall, near-by events with ML 1.0 should mostly be observed and together with the permanent networks (CH, FR, GE, GR, and LE, see section Data and Resources Mader and Ritter, 2021) and the AASN (Hetényi et al., 2018); this will lead to an improved hypocenter location. An example with events lower than ML 1.0 (Fig. 5.8) demonstrates the resolution properties inside the noisy URG. Because of the SARS-CoV-2 crisis-related shutdown in March 2020, we observe a decreased noise level at some of our stations during March–May 2020 by about 20% - 30%. This specific incident may give us the opportunity to detect low-magnitude earthquakes or other events that were not observable before. First results of our StressTransfer research at the ASZ using a part of the StressTransfer network can be found in Mader et al. (2021). Here, we demonstrate that

additional recordings, together with improved seismic velocity models, increase the resolution for outlining active faults. At the moment, the data of the StressTransfer network are restricted. We will make the data publicly available via our own FDSN webservice, on 1 April 2022 (see section Data and Resources Mader and Ritter, 2021).

6.   Seismicity and seismotectonics of the Albstadt Shear Zone in the northern Alpine foreland

The following section analyses the continuous micro-seismic seismicity on the Swabian Alb in the area of the Albstadt Shear Zone (ASZ) from 2011-2018. A new minimum 1-D seismic velocity model with corresponding station delay times is presented and the distribution of the relocated seismicity is discussed. Fault plane solutions are presented and are inverted for the stress field. The section is published as Mader et al. (2021).

6.1.   Abstract

The region around the town Albstadt, SW Germany, was struck by four damaging earthquakes with magnitudes greater than 5 during the last century. These earthquakes occurred along the Albstadt Shear Zone (ASZ), which is characterized by more or less continuous microseismicity. As there are no visible surface ruptures that may be connected to the fault zone, we study its characteristics by its seismicity distribution and faulting pattern. We use the earthquake data of the state earthquake service of Baden-Württemberg from 2011 to 2018 and complement it with additional phase picks beginning in 2016 at the AlpArray and StressTransfer seismic networks in the vicinity of the ASZ. This extended data set is used to determine new minimum 1-D seismic v_p and v_s velocity models and corresponding station delay times for earthquake relocation. Fault plane solutions are determined for selected events, and the principal stress directions are derived. The minimum 1-D seismic velocity models have a simple and stable layering with increasing velocity with depth in the upper crust. The corresponding station delay times can be explained well by the lateral depth variation of the crystalline basement. The relocated events align about north– south with most of the seismic activity between the towns of Tübingen and Albstadt, east of the 9 °E meridian. The events can be separated into several subclusters that indicate a segmentation of the ASZ. The majority of the 25 determined fault plane solutions feature an NNE-SSW strike but NNW-SSE-striking fault planes are also observed. The main fault plane associated with the ASZ dips steeply, and the rake indicates mainly sinistral strike-slip, but we also find minor components of normal and reverse faulting. The determined direction of the maximum horizontal stress of 140-149° is in good agreement with prior studies. Down to ca. 7-8 km depth $S_{H_{max}}$ is bigger than S_V; below this depth, S_V is the main stress component. The direction of $S_{H_{max}}$ indicates that the stress field in the area of the ASZ is mainly generated by the regional plate driving forces and the Alpine topography.
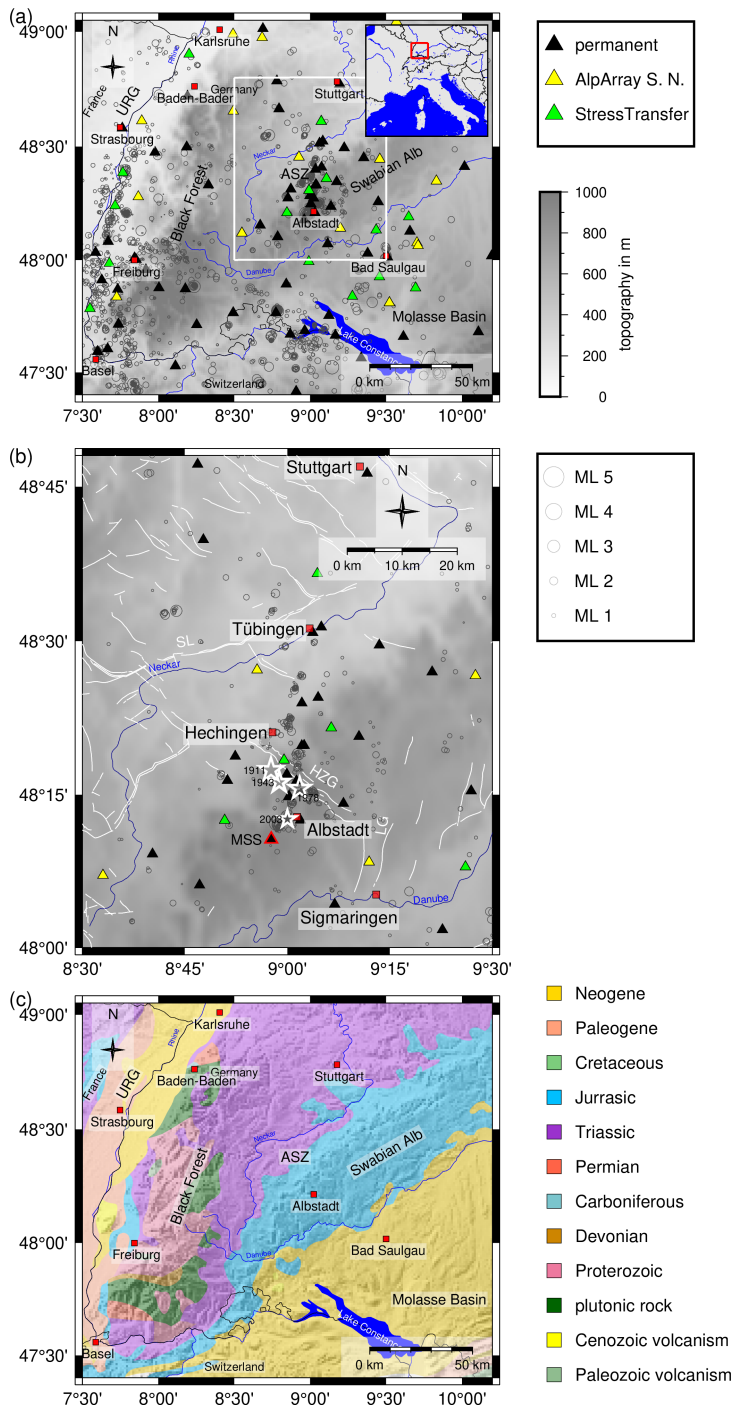
Figure 6.1.: (a) Overview over our research area located in southwestern Germany in the northern Alpine foreland. The ASZ is our research target (framed area). Black triangles represent permanent seismic stations of the LED and other agencies. Yellow triangles represent temporary AlpArray seismic stations. Green triangles display the 15 temporary seismic stations of the StressTransfer network. The gray circles display the seismicity scaled by magnitude from 2011 to 2018. URG stands for Upper Rhine Graben.

(b) Close-up of the area of the ASZ (framed area in (a)). Symbols are the same as in (a). The red-framed triangle highlights the central station Meßstetten (MSS) of the minimum 1-D seismic velocity model. White stars mark epicenters of the four strongest events, which had a magnitude greater than 5 in 1911, 2 in 1943 (same epicenter) and 1978, as well as the earthquake on 22 March 2003 with a local magnitude of 4.4 (Leydecker, 2011) these events are not included in the earthquake catalog from 2011 to 2018 (gray circles scaled with magnitude like in Fig. 6.1a). White lines indicate known and assumed faults (Regierungspräsidium Freiburg: Landesamt für Geologie, Rohstoffe und Bergbau (Hrsg.), 2019). The Hohenzollern Graben (HZG) is the only clear morphological feature in the close vicinity of the ASZ. Other large tectonic features are the Lauchert Graben (LG) and the Swabian Line (SL). Topography is based on the ETOPO1 Global Relief Model (Amante and Eakins, 2009; NOAA National Geophysical Data Center, 2009).

(c) Overview on the geology of the research area region; geology data are taken from Asch (2005). Topography is based on SRTM15+ (Tozer et al., 2019).

6.2. Introduction

The Swabian Alb near the town of Albstadt (Fig. 6.1) is one of the most seismically active regions in Central Europe (Grünthal and the Global Seismic Hazard Assessment Program (GSHAP) Region 3 Working Group, 1999). In the last century, four earthquakes with magnitudes greater

than 5 occurred in the region of the Albstadt Shear Zone (ASZ, Fig. 6.1, e.g., Stange and Brüstle, 2005; Leydecker, 2011). Today, such events could cause major damage, with economic costs amounting to several hundred million Euros (Tyagunov et al., 2006). Although the earthquakes caused major damage to buildings, such as fractures in walls and damaged roofs or chimneys, no surface ruptures have been found or described (e.g., Schneider, 1971). For this reason, the ASZ can only be analyzed by its seismicity to derive the geometry, possible segmentation and faulting pattern. One of the best observed earthquakes happened on 22 March 2003, and it was described as a sinistral strike-slip fault with a strike of 16° from north (Stange and Brüstle, 2005). This faulting mechanism is similar to the models of former major events (e.g., Schneider, 1973; Turnovsky, 1981; Kunze, 1982). In 2005, the seismic station network of the state earthquake service of Baden-Württemberg (LED) was changed and extended (Stange, 2018), and in summer 2015 the installation of the temporary Alp Array Seismic Network (AASN) started (Hetényi et al., 2018). In 2018 we started our project StressTransfer, in which we investigate areas of distinct seismicity in the northern Alpine foreland of southwestern Germany and the related stress field (Mader and Ritter, 2021). The StressTransfer network consists of 15 seismic stations, equipped with instruments of the KArlsruhe BroadBand Array (KABBA), in our research area (Fig. 6.1a).

Here we present a compilation of different data sets to refine hypocentral parameters of the ASZ. For this we analyze the earthquake catalog of the LED from 2011 to 2018 (Bulletin-Files des Landeserdbebendienstes B-W, 2011-2020) and complement it with additional phase picks from recordings of AASN (AlpArray Seismic Network (AASN), 2015) and our own StressTransfer seismic stations. We calculate a new 1-D seismic velocity model and relocate the events. For several relocated events we calculate fault plane solutions. This procedure gives us a new view of the geometry of the fault pattern at depth in the ASZ based on its microseismic activity. Furthermore, we use the fault plane solutions to derive the orientation of the main stress components in the area of the ASZ and discuss these with known results.

6.3.   Geological and tectonic setting

Southwestern Germany is an area of low to moderate seismicity. The most active fault zones are the Upper Rhine Graben (URG) and the area of the ASZ and the Hohenzollern Graben system (HZG, Fig. 6.1b). In the region of the URG, the seismicity is distributed over a large area. In comparison, in our research area the seismicity clusters in the close area around the ASZ and the HZG.

The ASZ is named after the town of Albstadt, situated on the Swabian Alb, a mountain range in southern Germany (Fig. 6.1a). Southern Germany consists of several tectonostratigraphic units, a polymetamorphic basement with a Mesozoic cover tilted towards southeast to east due to extension in the URG (Fig. 6.1c), associated with updoming (Reicherter et al., 2008; Meschede and Warr, 2019). The URG forms the western tectonic boundary, whereas the eastern boundary comprises the crystalline basement of the Bohemian Massif. To the south, the foreland basin of the Alps (Molasse Basin, Fig. 6.1c) frames the area in a triangular shape. The Molasse Basin covers the whole area south of the Swabian Alb up to the Alpine mountain chain. It is filled with Neogene terrestrial, freshwater and shallow marine sediments (Fig. 6.1c,

Meschede and Warr, 2019). The Swabian Alb is bounded by the rivers Neckar in the north and Danube in the south (Fig. 6.1a). The sedimentary layers of the Swabian Alb, which consist of Jurassic limestone, marl, silt and clay, dip downwards by 4° to the southeast and disappear below the Molasse Basin (Fig. 6.1c) and the Alpine mountain chain (Meschede and Warr, 2019). The sedimentary cover of the Swabian Alb forms a typical cuesta landscape with major escarpments built up by resistant carbonates of the Late Jurassic that is cut by several large fault systems, which are detectable in the present-day topography (Reicherter et al., 2008). The Black Forest to the west of the Swabian Alb experienced the most extensive uplift due to the extension of the URG. Here, even metamorphic and magmatic rocks of the Paleozoic basement are exposed. To the north and northwest of the Swabian Alb, Triassic rocks crop out (Meschede and Warr, 2019). Due to the different uplift and erosional states of southern Germany, the depth of the crystalline basement varies strongly between -5.4 and 1.2 km a.s.l. (Rupf and Nitsch, 2008).

The current regional stress field of southwestern Germany is dominated by an average horizontal stress orientation of 150° (e.g., Müller et al., 1992; Plenefisch and Bonjer, 1997; Reinecker et al., 2010; Heidbach et al., 2016) and was determined from focal mechanism solutions, overcoring, borehole breakouts and hydraulic fracturing (e.g., Bonjer, 1997; Plenefisch and Bonjer, 1997; Kastrup et al., 2004; Reiter et al., 2016; Heidbach et al., 2016). It is characterized by NW-SE horizontal compression and NE-SW extension (e.g., Kastrup et al., 2004) and developed during late Miocene (Becker, 1993). Analysis of several kinematic indicators hint that fault planes were already activated repeatedly during the Cenozoic (Reicherter et al., 2008). Three main groups of fault planes can be observed. First, mainly sinistral NNE-SSW-to-N-S-striking fault planes, which are similar to the ASZ or the Lauchert Graben (Fig. 6.1b) and parallel the URG. Second, NW-SE-striking normal and/or dextral strike-slip fault planes, which correspond to the HZG in our area. Older kinematic indicators, like fiber tension gashes and stylolites, hint at a sinistral initiation of those NW-SE striking fault planes during the Late Cretaceous–Paleogene with a maximum horizontal compression in the NE-SW direction (Reicherter et al., 2008). Third, ENE-WSW-oriented fault planes, which are mainly inactive but with some exhibiting dextral strike-slip or reverse movement, for example, the Swabian Line (Schwäbisches Lineament, Fig. 6.1b). The direction of $S_{H_{max}}$ in our research area is quite constant, except of an area directly south of the HZG (Albstadt-Truchtelfingen) and within the HZG (Albstadt-Onstmettingen). There the $S_{H_{max}}$ direction rotates about 20° counterclockwise into the strike of the HZG (130°, Baumann and Becker, 1986), which may be caused by a reduced marginal shear resistance.

The only morphologically visible tectonic feature close to Albstadt is the HZG (Fig. 6.1b), a small graben with an inversion of relief and a NW-SE strike (Schädel, 1976; Reinecker and Schneider, 2002). The 25 km long HZG has dip angles between 60-70° at the main faults and a maximum graben width of 1.5 km, which leads to a convergence depth of the main faults in 2-3 km depth (Schädel, 1976). Thus, the HZG is interpreted as a rather shallow tectonic feature. To the north and south of Albstadt there are further similar graben structures like the HZG, namely the Filder Graben, Rottenburg Flexure, western Lake Constance faults and Hegau, which are also about parallel to the main horizontal stress field (Reinecker et al., 2010) like the HZG. Reinecker and Schneider (2002) propose a tectonic model to relate the graben structures with the ASZ below. They apply the result of Tron and Brun (1991), who showed that the movement of a partly decoupled strike-slip fault in the subsurface can generate graben structures at the surface in a steplike arrangement. In the regional tectonic model, the graben

structures are the HZG, the Rottenburg Flexure, western Lake Constance faults and the Filder Graben (Reinecker and Schneider, 2002). The ASZ itself is the strike-slip fault, partly decoupled from the surface by a layer of Middle Triassic evaporites in the overlying sedimentary layers (Reinecker and Schneider, 2002). Stange and Brüstle (2005) consider the bottom of the Mesozoic sediments a mechanical decoupling horizon as no earthquakes occur above 2 km depth.

Another tectonic feature in our research area is the ENE-WSW-striking Swabian Line north of the river Neckar (Fig. 6.1b). It extends from the Black Forest area partly parallel along the cuesta of the Swabian Alb to the east (Reicherter et al., 2008). The sense of movement along the Swabian Line is dextral. To the east of the ASZ near Sigmaringen, the Lauchert Graben strikes N-S, about parallel to the ASZ with a sinistral sense of displacement (Geyer and Gwinner, 2011, Fig. 6.1b).

The faults in southwestern Germany exhibit mainly moderate displacements during the last ca. 5 Myr (Reicherter et al., 2008). At the HZG, for example, the maximum vertical offset is of the order of 100-150 m. The horizontal offset is considerably lower and more difficult to determine (Reicherter et al., 2008).

Along the 9°E meridian Wetzel and Franzke (2003) identified a 5-10 km broad zone of lineations pursuable from Stuttgart to Lake Constance (Fig. 6.1a). Those lineations strike predominantly N-S, NW-SW and ENE-WSW. The N-S and ENE-WSW-striking faults limited the NW-SE-striking graben structures like the HZG (Reicherter et al., 2008). The NW-SE-striking faults are expected to be possibly active at intersections with N-S-striking faults due to a reduction in shear resistance accompanied by aseismic creep (Schneider, 1979, 1993; Wetzel and Franzke, 2003).

The first documented earthquakes in the area of the ASZ occurred in 1655 near Tübingen and had an intensity of 7 to 7.5 (Leydecker, 2011). A similarly strong earthquake with a local magnitude of 6.1 occurred in 1911 near Albstadt-Ebingen (Fig. 6.1b, Leydecker, 2011), causing damage to buildings (Reicherter et al., 2008). The seismic shock triggered landslides with surface scarps in both the superficial Quaternary deposits and the Tertiary Molasse sediments (Sieberg and Lais, 1925) in the epicentral area and close to Lake Constance, demonstrating the potential of hazardous secondary earthquake effects (Reicherter et al., 2008). Since the 1911 earthquake, the Swabian Alb has been one of the most seismically active regions in the northern Alpine foreland, with a further three earthquakes with a local magnitude greater than 5 (Fig. 6.1b, 2 events in 1943, 1978, e.g., Reinecker and Schneider, 2002; Stange and Brüstle, 2005). The latest strong events occurred on 4 November 2019 (ML 3.8), 27 January 2020 (ML 3.5) and 1 December 2020 (ML 4.4, Regierungspräsidium Freiburg: Landesamt für Geologie, Rohstoffe und Bergbau, 2023). The average seismic dislocation rates along the ASZ are on the order of 0.1 mm/a, respectively (Schneider, 1993). The return period of earthquakes along the ASZ with a magnitude of 5 is approximately 1000 years (Schneider, 1980; Reinecker and Schneider, 2002). Both estimates are based on historic earthquake records. From aftershock analyses and focal mechanism calculations we know that the ASZ is a steep NNE-SSW oriented sinistral strike-slip fault (e.g., Haessler et al., 1980; Turnovsky, 1981; Stange and Brüstle, 2005) in the crystalline basement, as all earthquakes occur at a depth greater than 2 km (Stange and Brüstle, 2005). The lateral extent of the fault zone in an N-S direction is still under debate: Reinecker and Schneider (2002) propose an extension from northern Switzerland towards the north of Stuttgart, whereas Stange and Brüstle (2005) do not find this large extension as most of the seismicity happens on the Swabian Alb.

6.4.   Earthquake data and station network

As a basis for our study, we use the earthquake catalog of the LED from 2011 to 2018 for earthquakes within the area close to the ASZ (8.5–9.5°E, 48–48.8°N, Fig. 6.1b). For these 575 earthquakes we received the bulletin files of the LED (Bulletin-Files des Landeserdbebendienstes B-W, 2011-2020), consisting of hypocenter location, origin time, local magnitude ML, and all phase travel time picks with corresponding quality and P-phase polarity. The LED picks from 2011 to 2018 are from 51 LED seismic stations and 14 seismic stations run by other agencies like the state earthquake service of Switzerland (Fig. 6.1a). Locations are determined with HYPOPLUS, a Hypoinverse variant modified following Oncescu et al. (1996), which allows the usage of a 1.5-D seismic velocity model approach (Stange and Brüstle, 2005). Most hypocenter depths are well determined, but around 9.7% of the depth values are manually fixed. The median uncertainties for longitude, latitude and depth within the catalog are 0.5, 0.6 and 2.0 km, respectively. The magnitude ML ranges from 0.0 to 3.4, with average uncertainties of about ±0.2, and the magnitude of completeness is around ML 0.6 (see Fig. B.1 in the Supplement). The catalog used only contains natural events, as quarry blasts are sorted out and induced events do not occur in the study region.

Additionally, within the AlpArray Project (Hetényi et al., 2018), nine seismic stations were installed starting in summer 2015 within 80 km distance to the ASZ, four of them directly around the ASZ (AlpArray Seismic Network (AASN), 2015, Fig. 6.1b). To get an even denser network and to detect microseismicity we started to install another 15 seismic broadband stations from the KABBA beginning in July 2018 in areas with striking seismicity in the northern Alpine foreland within our project StressTransfer (Fig. 6.1a, Mader and Ritter, 2021). Five of those stations are located in the vicinity of the ASZ (Fig. 6.1b), and three of them were already running at the end of 2018.

We complemented the LED catalog with additional seismic P- and S-phase picks from the four AASN stations located around the ASZ from 2016 to 2018 and our StressTransfer stations recording in 2018. In total, our combined data set consists of 575 earthquakes (Fig. 6.1b) with 4521 direct P-phase and 4567 direct S-phase travel time picks from 69 seismic stations.

6.5.   Data processing

6.5.1.   Phase picking

To complement the LED catalog, we use a self-written code in ObsPy (e.g., Beyreuther et al., 2010a) for semi-automatic manual picking of the direct P and S phases. The raw waveform recordings are bandpass-filtered with a zero-phase four corners Butterworth filter from 3 to 15 Hz. Using the hypocenter coordinates of the LED we calculate an approximate arrival time at a seismic station. Around this arrival time, we define a noise and a signal time window following Diehl et al. (2012) so that we can calculate the signal to noise ratio (SNR) of our phase onsets. Our code automatically calculates the earliest possible pick (ep) and the latest possible pick (lp) (see Diehl et al., 2012) to get consistent error boundaries for each pick. Finally,
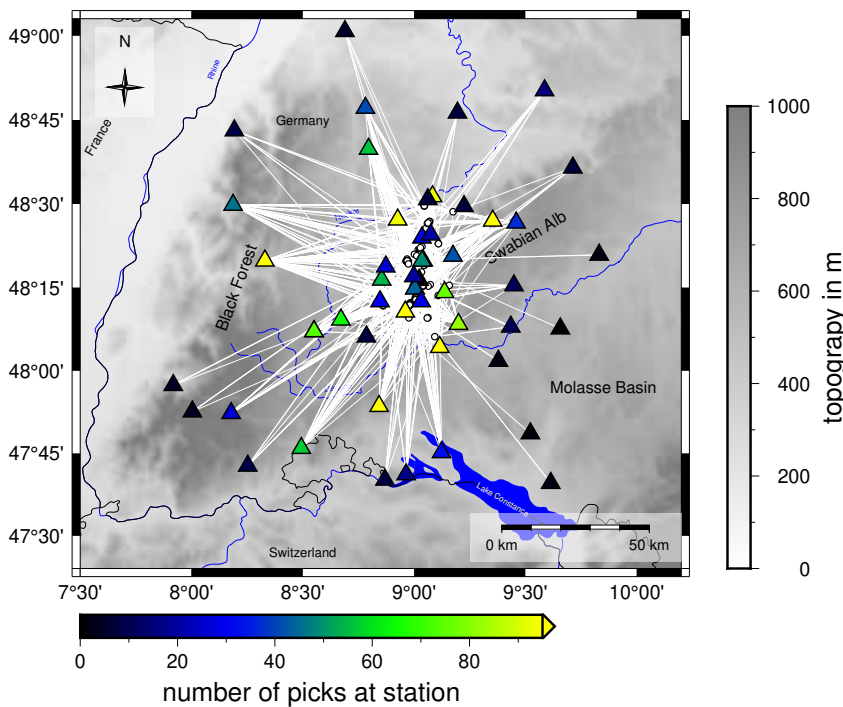
Figure 6.2.: Ray coverage and input data set for the inversion with VELEST. White circles represent the 99 selected events that are used for v_p and v_s inversion. Seismic stations are indicated as triangles and color-coded with the number of high-quality picks at a station used for the v_p and v_s inversion. Topography is based on the ETOPO1 Global Relief Model (Amante and Eakins, 2009; NOAA National Geophysical Data Center, 2009).

the error boundaries are checked by eye, and the phase pick is done manually between the two error boundaries. The qualities of 0 up to 4 of the picked arrival time are set depending on the time difference between ep and lp (Table B.1 in the Appendix). For consistency, a similar relationship is used between picking quality and uncertainty as defined by the LED (Bulletin-Files des Landeserdbebendienstes B-W, 2011-2020).

6.5.2. Inversion for minimum 1-D seismic velocity models with VELEST

The LED uses the program HYPOPLUS (Oncescu et al., 1996) for routine location, with which one can apply a 1.5-D approach by using several 1-D seismic velocity models for selected regions (Stange and Brüstle, 2005; Bulletin-Files des Landeserdbebendienstes B-W, 2011-2020). They use two P-wave velocity (v_p) models, a Swabian Jura model and a model for the state of Baden-Württemberg, and they define the S-wave velocity (v_s) model using a constant $\frac{v_p}{v_s}$-ratio (Stange and Brüstle, 2005; Bulletin-Files des Landeserdbebendienstes B-W, 2011-2020, Fig. 6.4a, b). Furthermore, no station delay times are used (Bulletin-Files des Landeserdbebendienstes B-W, 2011-2020).

To determine a complemented catalog, we invert for new minimum 1-D seismic v_p and v_s models in the region of the ASZ with station delay times, using the program VELEST (Kissling et al., 1994, 1995, VELEST Version 4.5). As central recording station we chose the station Meßstetten (MSS, Fig. 6.1b), as this station was running during our complete observational

period and it is the oldest seismic recording site on the Swabian Alb, having been recording since 2 June 1933 (Hiller, 1933). To get the best subset of our catalog for the inversion, we select only events with at least eight P-arrival times for the inversion for v_p and either eight P-arrival or eight S-arrival times for the simultaneous inversion for v_p and v_s. The P-pick times exhibit a quality of 1 or better, and the S-picks need a quality of 2 or better (Table B.1). Events outside of the region of interest, 48.17-48.50° N and 8.75- 9.15° E, with an azimuthal GAP greater than 150° and an epicentral distance of more than 80 km are rejected. This selection leads to a high-quality subset of 68 events with 789 P-phase picks for v_p and 99 events with 945 P-picks and 1019 S-phase picks for the v_p and v_s inversion (Fig. 6.2).

To probe our seismic velocity model space, inversions with 84 different starting models are calculated with four differently layered models from seismic refraction profile interpretations (Gajewski and Prodehl, 1985; Gajewski et al., 1987; Aichroth et al., 1992), the LED Swabian Jura model (Stange and Brüstle, 2005) and realistic random v_p variations (Fig. 6.3). We apply a staggered inversion scheme following Kissling et al. (1995) and Gräber (1993), first inverting for v_p and then for v_p and v_s together while damping the v_p model. The inversion for v_p was done with the 84 different starting models described previously, always using the resulting velocity model of the prior inversion as input for the next inversion with VELEST. After three to four inversion runs, the velocity models converged, and the results did not change (Fig. 6.3). Following this, the inversion for station delay times was done. The minimum 1-D v_p model with the smallest rms and the simplest layering was selected as the final v_p model for the simultaneous v_p and v_s inversion. Together with a $\frac{v_p}{v_s}$-ratio of 1.69 (Stange and Brüstle, 2005), it was also used to calculate the v_s starting model, which was randomly changed to get a total of 21 v_s starting models (Fig. 6.3). The inversion was done like the staggered inversion for v_p. The resulting minimum 1-D v_p and v_s models (ASZmod1, Fig. 6.4) were selected due to their small rms.

To test the stability of ASZmod1, we randomly shifted all 99 events in space by maximum 0.1° horizontally and 5 km with depth (Kissling et al., 1995). The result of this shift test demonstrates that we can determine stable hypocenters, with an average deviation of less than 0.005° horizontally and of less than 2 km in depth for more than 90% of the events in the catalog (Fig. B.2). The seismic velocities are stable, except for the first and second layer (Fig. B.3 a, b). The first layer was unstable already during the inversion process (Fig. 6.3); therefore, we damped its layer velocities and set them to realistic v_p and v_s values based on the seismic v_p of the refraction profile interpretations (Gajewski et al., 1987). The instability in both upper layers may be caused by few refracting rays and thus small horizontal ray lengths through the layers. Furthermore, there are only a few earthquakes located within these layers (Fig. B.3 c). In total, the stability test (Figs. B.2 and B.3) indicates that the model represents the data and region very well and that the determined hypocenter locations are stable. We calculated an error estimate based on the variation of the 21 output v_p and v_s models with our chosen layer model of Gajewski et al. (1987) for ASZmod1 (Table 6.1). For a precise estimation we determined 2 times the standard deviation (2σ) of the velocity models for each layer. For the uppermost layer we could not estimate any error, as the first layer was manually set and strongly damped during the inversion process. The 2σ range is small for the third and fourth layers. This was expected as most of the events are located within those layers and as all other models (which also have different layering) converge to similar velocities in those layers
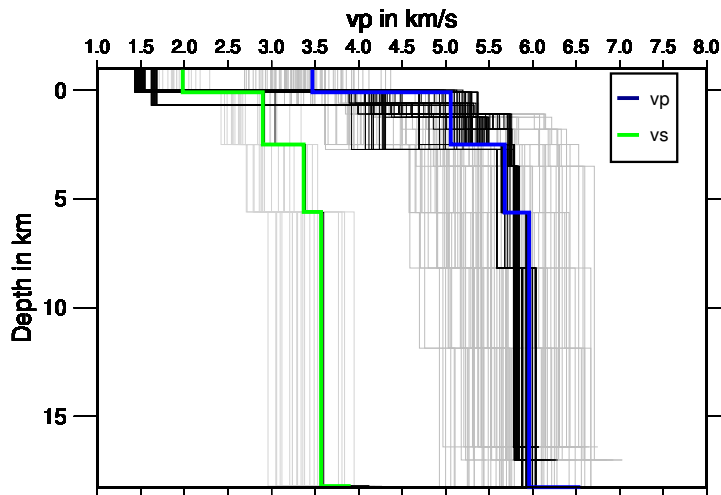
Figure 6.3.: VELEST input models for v_p (84) and v_s (21) (gray) and output v_p (84) and v_s (21) after inversion (black) together with the chosen model ASZmod1 (colored). A good convergence of the models can be observed, especially for v_s. The second layer converges worst. An instability of the first layer with a tendency to unrealistic low seismic velocities can be seen. For this reason, the velocity of ASZmod1 was fixed in the first layer.

Table 6.1.: ASZmod1 with corresponding error estimates based on 2σ.

	Layer top in km	v_p in km/s	$2\sigma v_p$ in km/s	v_s in km/s	$2\sigma v_s$ in km/s
Layer 1	-2	3.47	–	1.98	–
Layer 2	0.1	5.06	0.30	2.90	0.06
Layer 3	2.5	5.68	0.03	3.37	0.01
Layer 4	5.63	5.95	0.02	3.57	0.01
Layer 5	18.25	6.55	0.31	3.91	0.32

(Fig. 6.3). The error estimate for the second layer has to be considered carefully as this layer revealed strong instabilities during the stability test (Fig. B.3). The fifth layer also has larger 2σ uncertainties relative to layers three and four, which is caused by less ray coverage and there being no events located below 18.25 km depth.

6.5.3. Relocation, station corrections and error estimation with NonLinLoc

To relocalize the complete earthquake catalog we use the program NonLinLoc (NLL, Lomax et al., 2000), a nonlinear oct-tree search algorithm. NLL calculates travel time tables following the eikonal finite-difference scheme of Podvin and Lecomte (1991) on a predefined grid, here using 1 km grid spacing. With the implemented oct-tree search algorithm, (density) plots of the probability density function (PDF) of each event are determined following the inversion approach of Tarantola and Valette (1982) with either the L2-rms likelihood function (L2) or the equal differential time likelihood function (EDT). The determined PDF contains location uncertainties due to phase arrival time errors, theoretical travel time estimation errors and the geometry of the network (Husen et al., 2003). Based on the PDFs an error ellipsoid (68% confidence) is determined, which we use to calculate latitude, longitude and depth error esti-
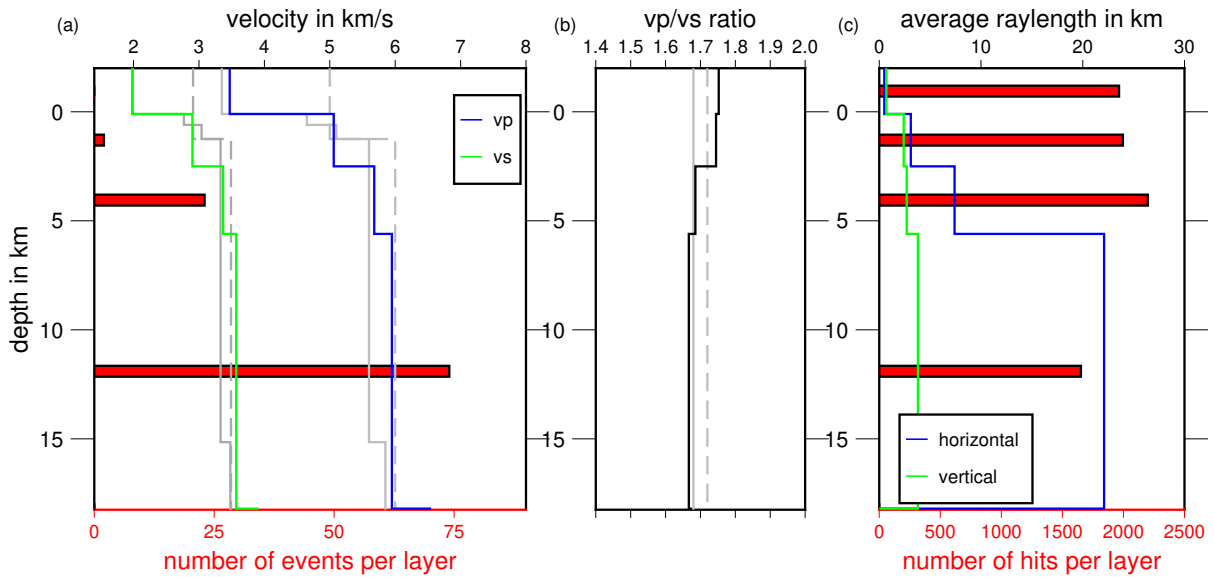
Figure 6.4.: (a) Final minimum 1-D seismic velocity models (ASZmod1): v_s is in green, and v_p is in blue. Gray lines represent velocity models of the LED (Bulletin-Files des Landeserdbebendienstes B-W, 2011-2020): solid lines show Swabian Jura models, and dashed lines show Baden-Württemberg models. Red bars are scaled with the number of events in each layer of the velocity model.
(b) $\frac{v_p}{v_s}$-ratio of ASZmod1 and the LED models.
(c) Ray statistics of used ray paths. Red bars display number of hits per layer. Blue and green lines give the average horizontal and vertical ray length.

mates for each earthquake (Fig. 6.5). The estimated errors of our events (especially the depth error estimate) have been getting smaller since 2016. This reduction correlates well with the increased number of picks per event and thus with the increased number of seismic stations around the ASZ due to the modification of the LED network and the installation of the AASN and the StressTransfer stations from 2018 (Hetényi et al., 2018; Stange, 2018, Fig. 6.5). As a final hypocenter solution the maximum likelihood hypocenter is selected, which corresponds to the minimum of the PDF.

We compared the resulting hypocenters and error estimates using the L2 or the EDT likelihood function. The comparison mainly indicates similar earthquake locations, but we find EDT errors (Fig. B.4) for many events that are too large and that are unrealistic (some greater than 50 km, leading to hypocenter shifts across the whole region). For this reason, we decided to use L2 for relocating our combined catalog. In NLL one can examine station delay times calculated from the station residuals. The station delay times are defined as the time correction subtracted from the observed P- and S-wave arrival times. This implies that negative station delay times exhibit faster velocities relative to ASZmod1 and positive station delay times exhibit slower velocities relative to ASZmod1. We used ASZmod1 and the corresponding VELEST station delay times, as well as our high-quality subset of 99 earthquakes, as input for NLL. After four iterative runs of NLL, always using the output station delay times as new input station delay times, the determined station delay times become stable. As we want to relocate the whole catalog with NLL, we use the NLL updated VELEST station delay times for consistency. Since ASZmod1 is a 1-D seismic velocity model below the reference station MSS, we expect the
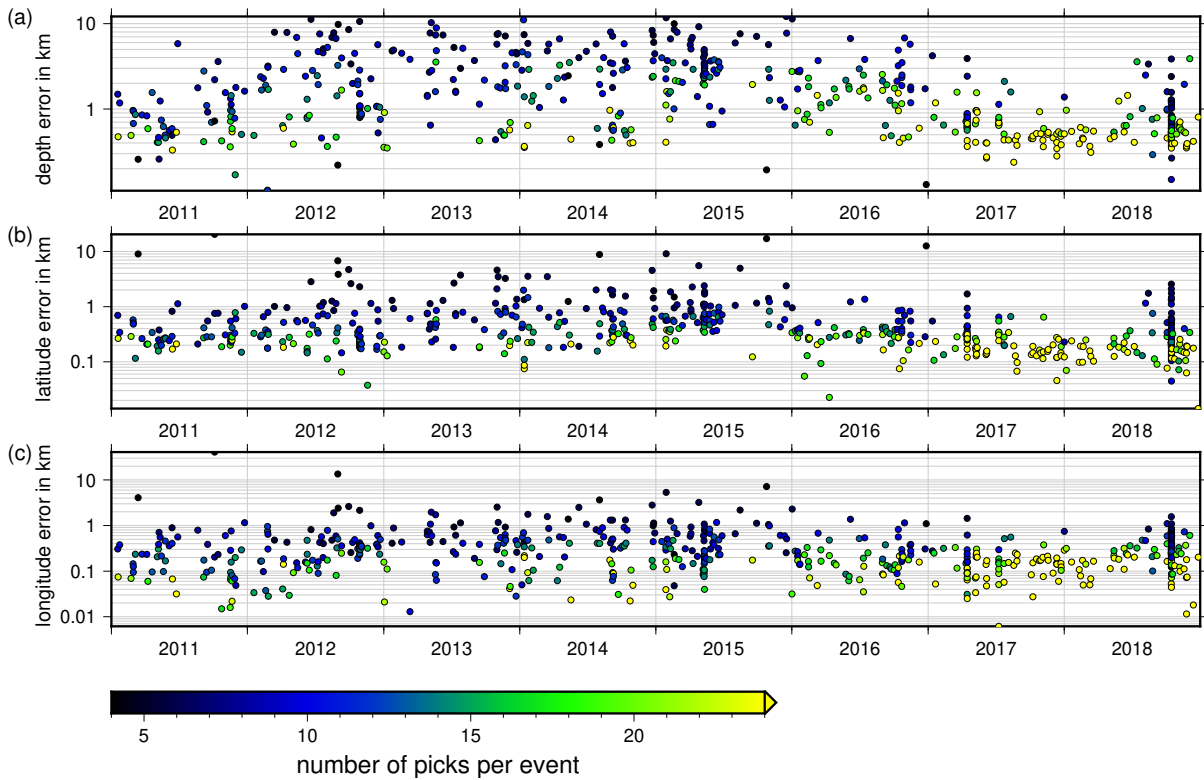
Figure 6.5.: Errors calculated from the 68 % confidence ellipsoid from NLL with L2 (L2-rms likelihood function) for each event in the combined catalog for (a) depth, (b) latitude and (c) longitude. The errors are color-coded depending on the number of picks, with dark colors indicating fewer picks and bright colors indicating many picks. Hypocenters with many observations are determined with smaller errors in depth and lateral position.

station delay times to become zero for MSS. After four iterative runs the actually determined station delay times of MSS are 0.014 s with σ of 0.083 s for v_p and -0.027 s with σ of 0.064 s for v_s. As σ is bigger than the actual station delay time and the station delay time of MSS is smaller than the maximum error range of 0.05 s of our best determined picks (Quality 0, Table B.1), we consider the station delay times of MSS to be practically zero. To account for similar small station delay times and σ, we state that all station delay times in the range of -0.05 to 0.05 s are practically zero station delay times if σ is greater than the actual station delay time (Fig. 6.6). The fact that the NLL station delay times of MSS and surrounding stations are close to zero indicates that even though they use a different (and nonlinear) relocation algorithm for delay time estimation than VELEST, our determined minimum 1-D seismic velocity model ASZmod1 represents the seismic velocity structure below MSS and its surroundings very well. We compared the relocated catalog with the original LED locations. Some events have large differences in hypocenter coordinates ($>0.1°$ in latitude or longitude), which we identified as events with only a few arrival time picks (fewer than nine picks), a large azimuthal GAP (GAP$>180°$) or wrong phase picks. Furthermore, a large deviation of expectation and maximum likelihood hypocenters indicates an ill-conditioned inverse problem with a probable non-Gaussian distribution of the PDF (Lomax et al., 2000), which was the case for some events with only a few picked arrival times. Similar problems were also identified by Husen et al.

(2003), who compared NLL locations with the routine locations of the state earthquake service of Switzerland. They also found that a good depth estimate with NLL depends on the station's distance from the earthquake. Especially for events with many observations, the depth estimate was worse if the closest station was further away than the focal depth of the event (Husen et al., 2003).

Our well-located earthquakes are selected by the following criteria: more than eight travel time picks, a GAP less than 180°, a horizontal error estimate of less than 1 km and a depth error estimate of less than 2 km (Fig. 6.7). Some of our well-located events have quite different depth estimates compared to the LED solution (Fig. B.5). Thus, we checked the station distribution for those events as proposed by Husen et al. (2003) and looked for incorrect phase picks. Nevertheless, all of these events have good phase picks, a small depth error estimate, evenly distributed stations and small deviations of expectation and maximum likelihood hypocenter coordinates. For this reason, we consider our new depth locations well determined and reliable. In comparison with the LED catalog, the majority of our relocated earthquakes are characterized by a small eastward shift and a stronger clustering, especially in depth (Fig. B.5). The latter may result from the hand-set depth location for some events of the LED.

6.5.4. Focal mechanism models with FOCMEC

We determine fault plane solutions for 25 selected events with the program FOCMEC (Snoke, 2003), which conducts a grid search over the complete focal sphere and outputs all possible fault plane solutions. For this we used the P-polarity picks of the LED (Bulletin-Files des Landeserdbebendienstes B-W, 2011-2020), and for events since 2016 we added P and SH polarities, as well as SH/P amplitude ratios, at the four AASN and three StressTransfer seismic stations. The local magnitude ML of those 25 events is in the range 0.6 to 3.4 (Table 6.2, Fig. 6.7, Bulletin-Files des Landeserdbebendienstes B-W, 2011-2020).

To determine the SH/P amplitude ratios we only used SH- or P-picks with a quality of 2 or better and the SNR of the picked phase needed to be greater than 5. Furthermore, we compared the frequency content of the P and SH phase to assure that the waves have the same damping properties, and the the source process was simple (Snoke, 2003). If the determined frequency of P and SH phases differed by more than 5 Hz the SH/P amplitude ratio was omitted. All waveforms are instrument-corrected and bandpassfiltered between 1 and 25 Hz. As FOCMEC uses the ratio on the focal sphere we need to correct our amplitudes for attenuation effects and phase conversion effects at the free surface (Snoke, 2003). To correct for attenuation effects we use Q_P and Q_S values determined by Akinci et al. (2004) for southern Germany. The measured phase amplitude A depends on Q, the frequency of the phase f, the travel time t and the amplitude A_0 at the source (e.g., Aki and Richards, 2002):

$$A = A_0 e^{-\pi \frac{ft}{Q}}. \tag{6.1}$$

The correction factor for the free surface effect of SH waves is always 2 and independent of the incidence angle of the seismic wave. For the P wave the free surface correction strongly depends on the incidence angle and the $\frac{v_p}{v_s}$-ratio (e.g., Aki and Richards, 2002). We calculated the incidence angle for our P phases of interest with the TAUP package of ObsPy (e.g., Beyreuther

Table 6.2.: Parameters of the FOCMEC solutions. Values with (aux) refer to the assumed auxiliary plane.

| ID	Time	ML	° N	° E	Depth in km	P	SH	SHP	Strike in °	Dip in °	Rake in °	δ strike in °	δ dip in °	δ rake in °	Strike(aux) in °	Dip (aux) in °	Rake (aux) in °	Quality
ev335	2016-04-10T15:08	1.1	48.44	9.05	9.44	8	3	0	353	43	-5	7.6	9.7	14.5	87	87	-133	1
ev353	2016-09-02T07:58	2.2	48.20	9.00	5.09	14	3	0	12	81	65	0.0	0.0	0.0	263	26	159	0
ev364	2016-10-13T01:54	1.0	48.34	8.96	11.45	9	2	1	338	35	-43	46.1	50.0	57.8	105	67	-117	4
ev378	2016-12-07T20:55	1.4	48.61	8.87	15.46	8	2	2	181	82	-5	14.2	18.8	68.2	272	85	-172	4
ev402	2017-04-15T17:16	2.1	48.33	8.96	11.15	17	4	1	162	35	-81	0.0	0.0	0.0	331	55	-96	0
ev405	2017-05-07T15:19	0.6	48.30	9.10	10.65	10	3	1	42	49	-41	56.8	35.4	41.8	162	60	-131	4
ev423	2017-07-09T11:52	0.8	48.33	8.96	11.36	8	4	0	158	37	-75	22.0	11.4	29.6	319	54	-101	2
ev426	2017-07-23T13:48	1.4	48.44	9.04	10.03	14	3	0	1	87	-10	0.0	0.0	0.0	92	80	-177	0
ev432	2017-08-27T06:00	1.7	48.20	8.87	12.18	29	4	0	37	78	12	3.1	17.3	7.6	304	78	168	1
ev457	2018-02-10T12:44	2.3	48.33	8.95	12.41	27	3	2	197	70	-9	2.0	6.9	19.0	290	82	-160	1
ev463	2018-03-13T05:14	1.0	48.20	8.99	3.30	11	3	1	15	79	-9	26.9	31.9	63.3	107	81	-169	4
ev514	2018-10-15T18:46	0.8	48.25	9.04	10.35	8	4	1	289	61	-65	23.3	15.5	31.6	65	38	-127	3
ev522	2018-10-15T19:37	1.3	48.25	9.04	10.00	17	4	3	341	76	-1	2.8	6.8	10.2	71	89	-166	1
ev525	2018-10-15T19:41	1.6	48.25	9.04	10.08	27	4	4	341	75	-4	3.8	8.0	12.0	72	86	-165	1
ev552	2018-10-17T03:02	1.0	48.25	9.04	10.38	14	4	2	338	57	-7	9.3	32.0	11.4	72	84	-147	3
ev554	2018-10-24T07:12	1.7	48.27	9.03	5.22	23	4	2	185	50	-17	5.2	14.8	0.6	286	77	-139	1
ev561	2018-11-18T16:23	1.6	48.60	8.65	14.44	10	3	0	336	45	-78	22.0	25.4	32.4	139	46	-102	3
ev564	2018-11-25T02:22	1.4	48.25	9.04	10.20	25	3	2	344	53	-65	0.0	0.0	0.0	126	44	-119	0
ev565	2018-11-25T07:36	0.9	48.25	9.04	10.24	21	2	0	190	35	-84	32.3	40.1	12.2	3	55	-94	4
ev566	2018-11-25T10:25	0.9	48.25	9.04	10.22	13	5	1	323	50	-45	35.3	15.6	14.5	86	57	-130	3
ev171	2013-12-04T19:42	2.9	48.31	9.04	5.76	13	0	0	188	63	-39	11.4	41.3	44.7	298	56	-147	4
ev183	2014-01-12T23:45	1.3	48.04	8.63	16.29	12	0	0	187	64	-57	42.7	34.9	37.2	311	41	-138	4
ev221	2014-09-09T00:46	2.3	48.21	9.12	9.31	14	0	0	179	29	-67	47.3	59.2	44.8	333	64	-102	4
ev232	2014-10-24T02:09	2.0	48.35	9.02	9.11	11	0	0	300	51	-76	53.8	39.9	38.5	98	41	-107	4
ev245	2015-01-28T00:05	3.4	48.20	8.99	4.99	19	0	0	19	77	24	5.3	18.5	61.3	283	67	166	4
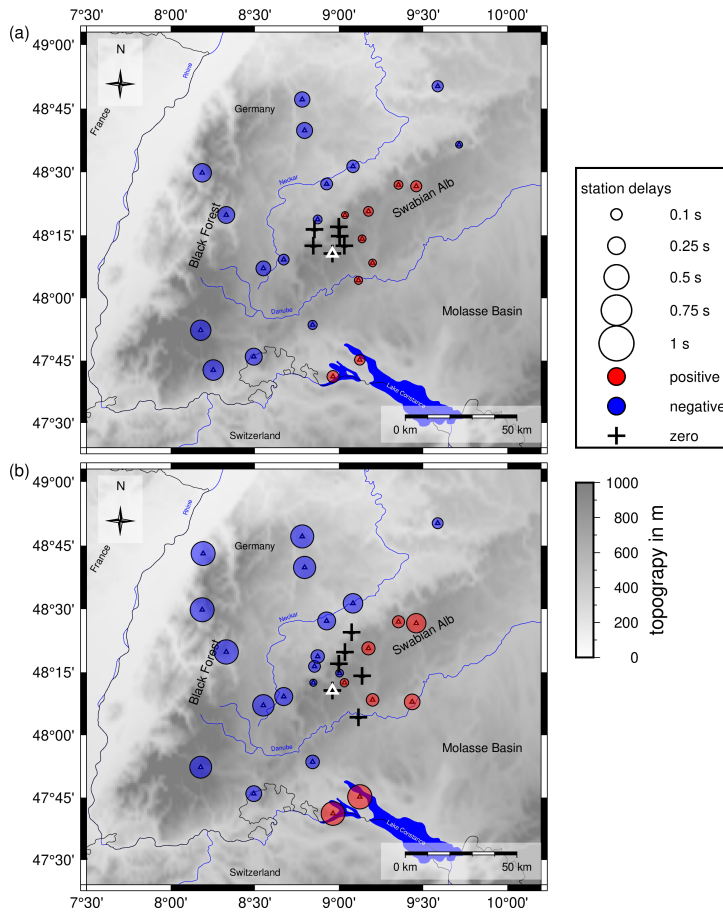
Figure 6.6.: (a) Station delay times for the v_p velocity model ASZmod1. (b) Station delay times for the v_s velocity model ASZmod1. Blue circles represent negative station delay times, indicating areas with faster velocities than ASZmod1. Red circles illustrate positive station delay times, indicating slower velocities than ASZmod1. Crosses are stations with zero station delays. Only stations with more than five travel time picks are included. The small white triangle highlights reference station MSS. Topography is based on the ETOPO1 Global Relief Model (Amante and Eakins, 2009; NOAA National Geophysical Data Center, 2009).

et al., 2010a) using the AK135 model (Kennett et al., 1995) and find incidence angles in a range between 22.9 and 23.2°. As the variation between the incidence angles for the different station event combinations is very small, we use for all events the median incidence angle of 23.05°. To calculate the $\frac{v_p}{v_s}$-ratio, we use v_p and v_s of the second layer of our model ASZmod1 (Table 6.1) because in the first layer the velocities are considered to be unstable. After this correction the logarithm of the SH/P amplitude ratio is used as input in FOCMEC together with the P- and SH-polarities.

To find the appropriate solution one can allow different types of errors in FOCMEC. We compare the relative weighting mode and the unity weighting mode of the FOCMEC inversion for all events. This is done to explore if the results differ significantly, which could mean that they are questionable (Snoke, 2003). In the unity weighting mode each wrong polarity in the FOCMEC solution counts as an error of 1. In the relative weighting mode, polarity errors near a nodal plane count less than polarity errors in the middle of a quadrant. Thus, the polarity errors are weighted with respect to their distance to the nodal planes. This means an incorrect

polarity is weighted by the calculated absolute value of the radiation factor (ranging between 0 and 1). For both weighting modes we searched for a solution. This is done by varying and systematically increasing the different possible errors. Those errors are uncertainties in the P- and SH-polarities and the total error of wrong SH/P amplitude ratios, as well as the error range in which they are expected to be correct. For example, we might consider the unity weighting mode and an event with P- and SH-polarities. First, we check if we achieve a solution with zero errors for both. If no solution is found, we increase the allowed errors for the SH-polarities to 1, as the SH-polarities are more insecure than the P-polarities. If still no solution is found, we check for a wrong P-polarity and without wrong SH-polarity. This procedure is done for unity weighting and relative weighting, and it is stopped if a solution is found. To check for a dependency of the result on a single polarity, the next inversion runs for more errors are also determined.

The output of FOCMEC results in a set of possible strike, dip, and rake combinations for each event. The fault plane solution closest to the medians of strike, dip and rake was chosen as the preferred solution (Table 6.2, Fig. B.6). We use the other possible solutions to determine uncertainties for our preferred fault plane solution. For this we recalculate all strikes into a range between 90 and 270° to exclude large differences in strike by the transition from 360° back to 0° and by the 180° ambiguity of the strike. We determine the 5% and 95% percentiles of strike, dip and rake and calculate the width of the 5% to 95% percentile range (δ strike, δ dip, δ rake, Table 6.2). These widths are taken as uncertainty ranges to account for a non-uniform solution distribution and to assign a quality factor to the determined fault plane solutions (Tables B.2, 2). To get rid of non-unique or problematic cases the following restrictions are used: the median of the strike and dip of the unity and relative weighting modes has to be within a range of 15°, the median of the rake must be within ±20°, and the total allowed number of solutions is limited to 500. Furthermore, if the solutions yield a quality of 4 with δ strike, δ dip or δ rake greater than 75°, the fault plane solutions is omitted. Finally, all remaining fault plane solutions are inspected manually.

We observe a low quality (3 and 4), especially for low-magnitude events (ML<1.4) and events without SH-polarities and SH/P ratios (Table 6.2). In Fig. 6.7 the fault plane solutions are displayed scaled with magnitude and their individual event ID.

6.5.5. Stress inversion

Our focal mechanisms are used to derive the directions of the principal stress axes σ_1, σ_2, σ_3 with the python code StressInverse (Vavryčuk, 2014). The algorithm runs a stress inversion following Michael (1984) and modified to jointly invert for the fault orientations. To find the fault plane orientation, Vavryčuk (2014) includes the fault instability I, which can be evaluated from the friction on the fault plane, the shape ratio R and the inclination of the fault planes relative to the principal stress axes. The input into StressInverse is the strike, dip and rake of our 25 fault plane solutions (Table 6.2). To achieve an accuracy estimate we allow 100 runs with random noise and define the mean deviation of our fault planes of 30°, which is reasonable considering a maximum δ rake of 68.2° (Table 6.2). The friction is allowed to vary between 0.4 and 1, and R varies between 0 and 1. The stress inversion is calculated for three different input data sets: all 25 fault planes (Fig. 6.8a), only focal mechanisms with a depth
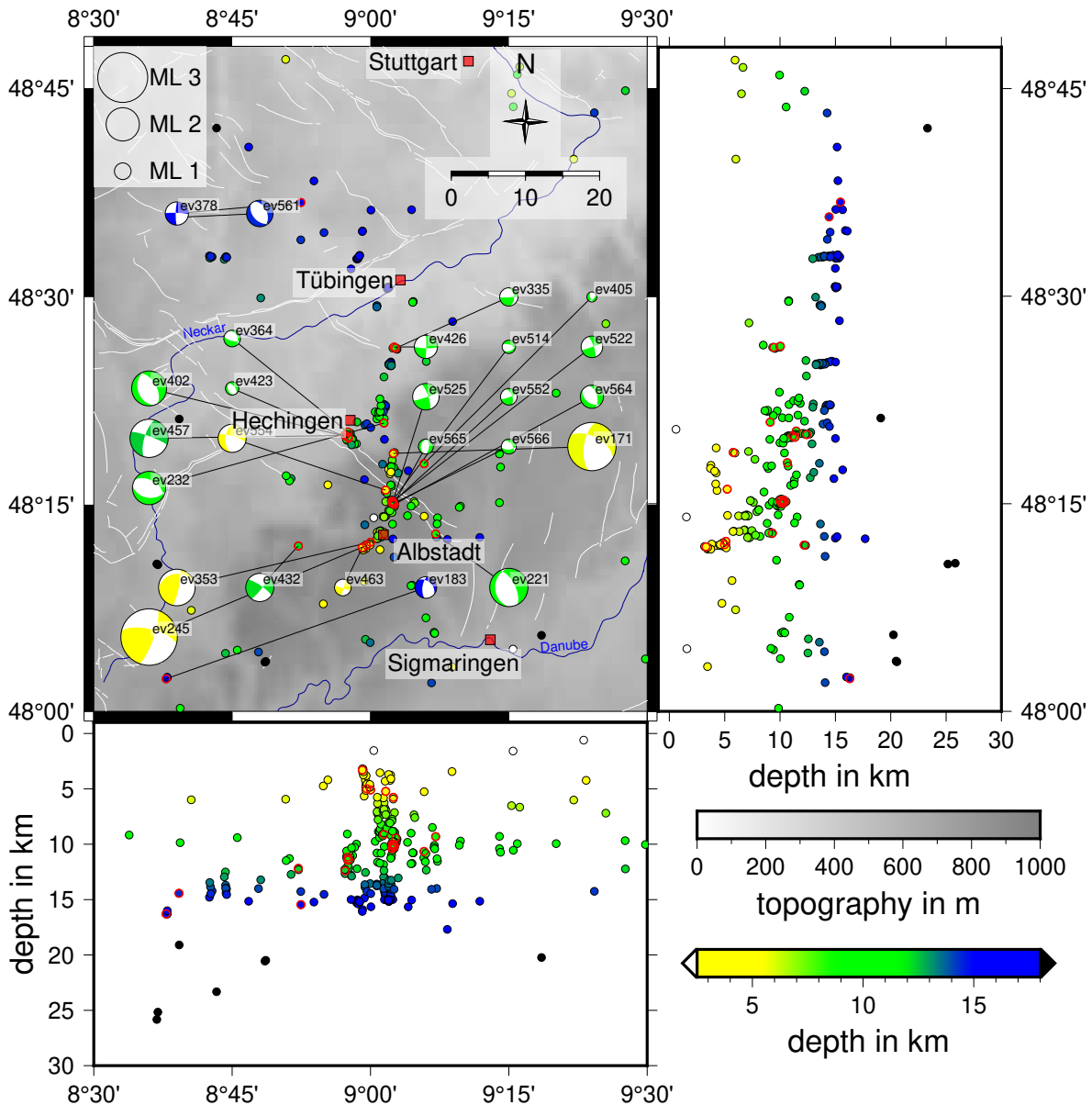
Figure 6.7.: Hypocenters of the 337 best-located events with a horizontal error of less than 1 km and a depth error of less than 2 km. Only events with a GAP smaller than 180° and more than eight travel time picks are included. Hypocenters are plotted as circles that are color-coded by depth. All 25 focal mechanisms are displayed also color-coded by depth; red circles indicate the corresponding event hypocenter. The size of the focal mechanisms is scaled depending on ML of the event. Cluster codes are placed next to the fault plane solutions. White lines indicate known and assumed faults (Regierungspräsidium Freiburg: Landesamt für Geologie, Rohstoffe und Bergbau (Hrsg.), 2019). Topography is based on the ETOPO1 Global Relief Model (Amante and Eakins, 2009; NOAA National Geophysical Data Center, 2009).

Table 6.3.: ASZmod1 with corresponding error estimates based on 2σ.

Input	All fault planes		Depth >= 7.5 km		Depth < 7.5 km	
	azimuth	plunge	azimuth	plunge	azimuth	plunge
σ_1	360	81	332	67	149	47
σ_2	140	7	140	22	343	42
σ_3	231	6	231	4	246	7
R	0.2		0.4		0.6	
Friction	0.5		0.6		0.4	

greater than 7.5 km (20 fault planes, Fig. 6.8b) and focal mechanisms with a depth shallower than 7.5 km (5 fault planes, Fig. 6.8c). The selected azimuth and plunge of σ_1, σ_2 and σ_3 are given in Table 6.3. The separation into two data sets was necessary due to a wide variation of the confidence levels of σ_1 and σ_2 along the NW-SE direction (Fig. 6.8a). With a separation into shallow and deep events, this variation is reduced, indicating a depth dependency of the stress field (Fig. 6.8b). Nevertheless, due to the small amount of fault plane solutions in the depth range of 0.0-7.5 km, we find higher scatter of the confidence of the three principal stress axes (Fig. 6.8c). The measured and predicted fault planes from the stress inversion are shown in Fig. 6.8d). The predicted fault planes do not change for the different inversion runs.

6.6. Results and discussion

6.6.1. Velocity model and station delay times

The finally selected minimum 1-D seismic velocity model ASZmod1 consists of 5 layers (Fig. 6.4a and b). The layer boundaries are based on the seismic refraction interpretation of Gajewski et al. (1987). Layers with very similar seismic velocities were combined during the inversion process to keep the model as simple as possible (Occam's principle). The determined seismic velocities increase with depth and they are well constrained between 2.50 and 18.25 km depth (Table 6.1). The layers between -2.00 to 2.50 km depth are not very stable due to the non-uniform distribution of rays and sources. Below 18.25 km depth we also have low resolution, as all events used for inversion occur above this point. The comparison with the LED models gives a good agreement with both the Swabian Jura and the Baden-Württemberg models (Fig. 6.4a). Our layer between 2.50 and 5.60 km depth is in good agreement with the Swabian Jura model, whereas the deeper layer has a higher agreement with the Baden-Württemberg model (Fig. 6.4a). The Swabian Jura model has a finer layering for the uppermost 2 km. We also used the Swabian Jura model as the input model for inversion, but due to the short horizontal ray length in comparison with the vertical ray length and the lack of events in the uppermost layers, the random seismic velocity starting models did not converge in the uppermost layers (Fig. 6.3); therefore, we chose the very simple layering.

The $\frac{v_p}{v_s}$-ratio is between 1.67 and 1.75 for all layers and it decreases with depth. In comparison, the LED uses a constant $\frac{v_p}{v_s}$-ratio of 1.72 for Baden-Württemberg and 1.68 for the Swabian
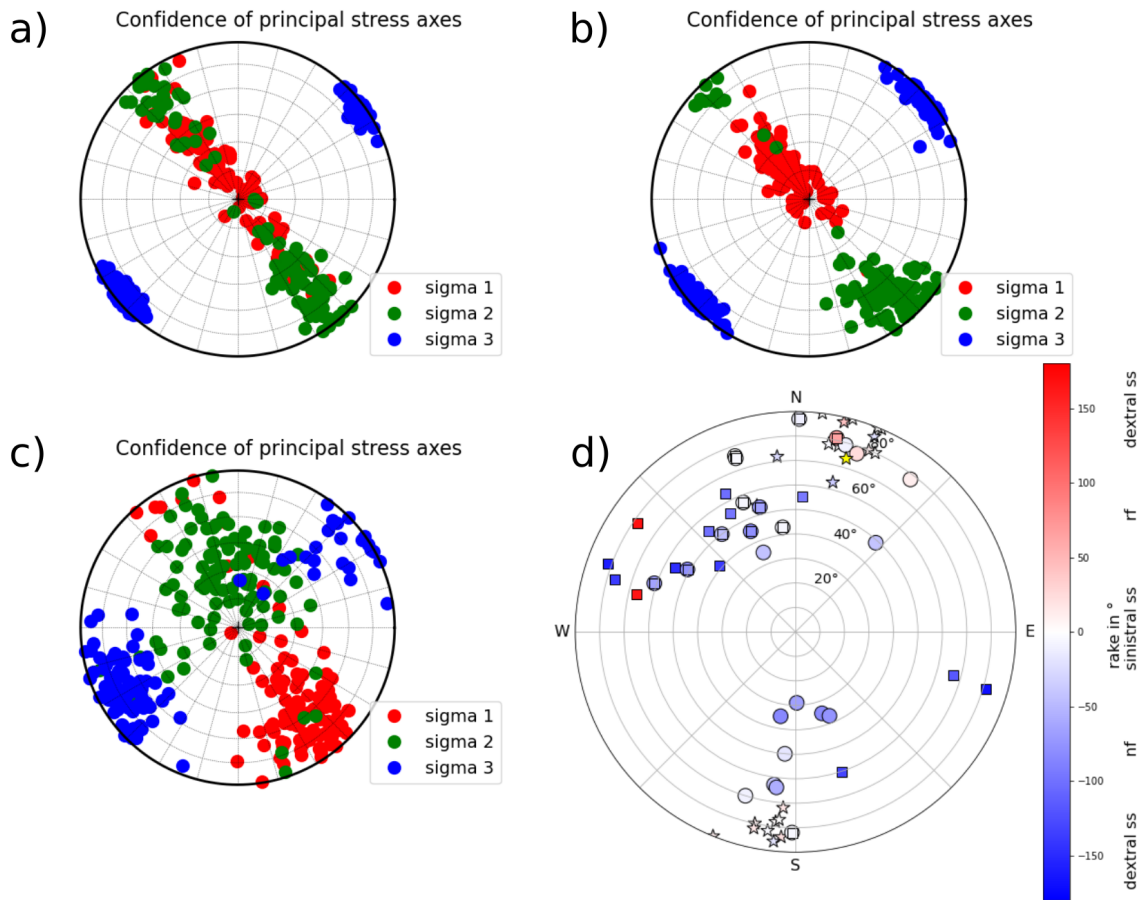
Figure 6.8.: (a) Confidence plot of the principal stress axes σ_1, σ_2 and σ_3 after the stress inversion of all fault plane solutions (Table 2) for the 100 different noise realizations.
(b) The same as Fig. 6.8a but only for fault plane solutions with a depth greater than 7.5 km.
(c) The same as Fig. 6.8a but only for fault plane solutions with a depth less than 7.5 km.
(d) Strike, dip and rake of all measured fault plane solutions (circles). The yellow star represents strike and dip of the 22 March 2003 earthquake (Stange and Brüstle, 2005). Other stars represent fault plane solutions calculated by Turnovsky (1981) for the earthquake series in 1978. Fault planes of StressInverse (Vavryčuk, 2014) are displayed by squares. Negative rake angles hint at normal faulting (nf) components, and positive angles hint at reverse faulting (rf) components. Events with a rake close to zero exhibit sinistral strike-slip (sinistral ss) components; events with rake angles close to -180 or 180° hint to dextral strike-slip (dextral ss).

Alb, which agrees with our overall observed $\frac{v_p}{v_s}$-ratio (Fig. 6.4b, Bulletin-Files des Landeserd-bebendienstes B-W, 2011-2020). The higher $\frac{v_p}{v_s}$-ratio of 1.75 in the first layer is a result of the manually fixed seismic velocities during the inversion process. In the second layer the $\frac{v_p}{v_s}$-ratio is also 1.75, which may be caused by the numerical instability during the inversion of this layer and should be interpreted with care. In our best determined layers (layer 3 and 4) our model has similar $\frac{v_p}{v_s}$-ratios to the Swabian Jura model of the LED (Fig. 6.4b, Bulletin-Files des Landeserdbebendienstes B-W, 2011-2020).
The station delay times of the P and S waves have a simple pattern of increasing delay times

with distance to reference station MSS (Fig. 6.6). Their very low values in the area of the ASZ demonstrate that the v_p and v_s distributions of ASZmod1 represent the true seismic velocities in this area very well. Around the ASZ, the central Swabian Alb and the Molasse Basin are characterized by positive station delay times and thus slower seismic velocities along the propagation paths relative to ASZmod1. Other areas like the Black Forest exhibit negative delay times and thus faster seismic velocities than ASZmod1.

The lateral seismic velocity contrasts of the different nearsurface layers of Baden-Württemberg are small in comparison to our station delay times. For this reason, we compare our station delay times with the lateral depth variations of the crystalline basement to find a possible relationship. The basement depth is described by the 3-D geological model of the Geological Survey of Baden-Württemberg (Rupf and Nitsch, 2008). Based on this model we estimate the vertical travel time at all our recording stations that have more than 5 of either P- or S-phase travel time picks using the seismic velocities of the first layer in ASZmod1 from the basement top to each recording station. For these values, we calculated the travel time differences of all stations relative to station MSS and compared the results (Fig. 6.9) with our real station delay times (Fig. 6.6). As result we find that the calculated travel time differences due to basement depth variations correlate to more than 85% with our station delay times. Hence, basement depth variations are the main reason for the observed station delay times in our study region. The remaining 15% of the station delay time terms may be explained by non-vertical ray path effects and lateral variations in seismic velocity due to different near-surface rock types. Furthermore, other lateral heterogeneities like dipping or wave-guiding layers may influence the station delay times as well.

6.6.2. Seismicity and fault plane solutions of the ASZ

The seismicity of the ASZ (Fig. 6.7) aligns almost N-S. Our relocated earthquakes occur in a depth range of 1 to 18 km. If we follow the seismicity distribution from south to north, the minimum hypocenter depth increases from around 3 to 5-14 km. Earthquakes below 18 km depth are rare at the ASZ. The top of the lower crust is at about 18-20 km depth (Gajewski and Prodehl, 1985; Aichroth et al., 1992); therefore, seismicity is concentrated in the upper crust. The hypocenters can be separated into several fault segments. This segmentation gets more obvious if we analyze E-W and N-S slices (Figs. 6.10, 6.11). To the north of the river Neckar (48.5-48.7° N), mainly deep (around 15 km depth) earthquakes occur, which can be separated into two clusters, one at 8.75° E ($C6_1$) and one at 8.95° E ($C6_2$, Fig. 6.10). Between the river Neckar and the town of Hechingen (48.3-48.5° N) we observe seismicity in the depth range of 5-15 km. There are three separate clusters, one west of 9° E, directly south of Hechingen (C4), and two clusters east of 9° E (C5 and C3). Near the town of Albstadt (48.2-48.3° N) the seismicity occurs across the whole seismically active depth range (1.5-18 km). Most of the seismicity happens between 9 and 9.1° E (C2, C3). At 2 to 8 km depth we find a small seismicity cluster southwest of Albstadt (8.9-9.0° E, C1). This cluster can be traced southward to 48.2° N (48.1-48.2° N, C1).

Most of the fault plane solutions are characterized by the typical NNE-SSW strike of the ASZ, but we also observe some events with NNW-SSE strike (Figs. 6.7, 6.8d, Table 6.2). Most of the events with a strike of NNE-SSW are characterized by steep fault planes (dip angle greater
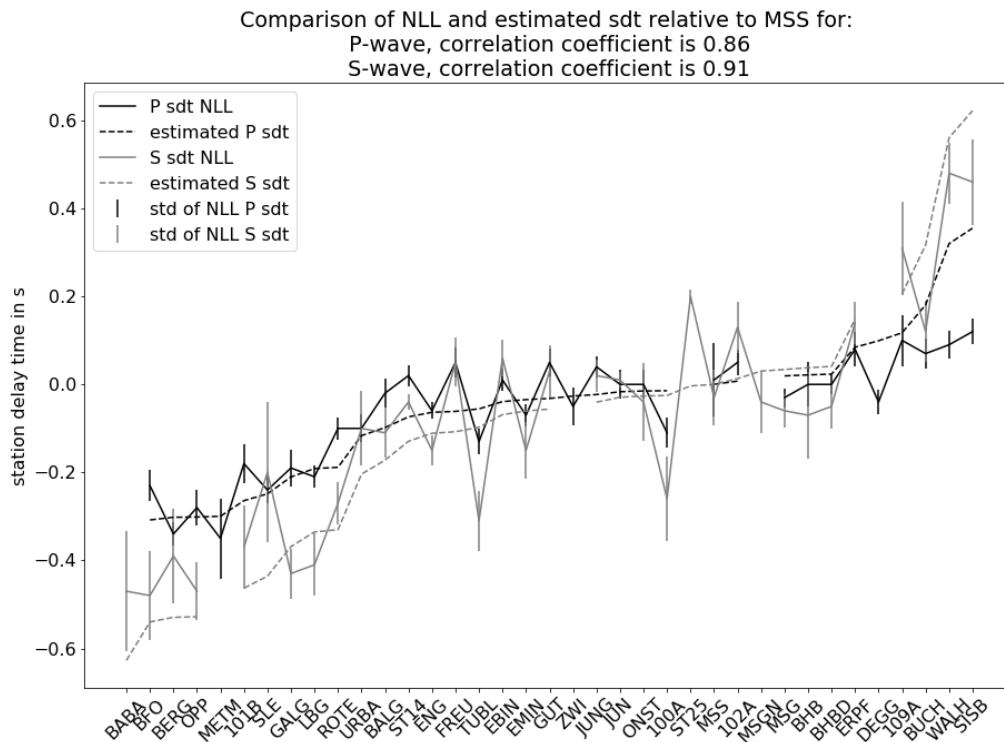
Figure 6.9.: Comparison of NLL station delay times (sdt) and estimated station delay times due to depth variations of the crystalline basement: P waves (black) and S waves (gray). Stations along the x axis are sorted from shallow to deep crystalline basement model depth.

60°) and rake angles around 0°, hinting at sinistral strike-slip. This is the typical or main faulting mechanism of the ASZ (Fig. 6.8d, Turnovsky, 1981; Stange and Brüstle, 2005). We also observe one event with an NNE-SSW strike, a clear reverse faulting component and a steep fault plane of 86° (Fig. 6.8d). The other events with an NNE-SSW strike and the events with an NNW-SSE strike have lower dip angles (smaller 60°) and mainly negative rake angles, hinting at normal faulting (Fig. 6.8d). The here-observed faulting behaviors can all be explained by a compressional stress regime with an average horizontal stress orientation of around 150° (Müller et al., 1992; Reinecker et al., 2010; Heidbach et al., 2016) acting on either the NNE-SSW- or NNW-SSE-oriented fault planes. The stress inversion following that of Vavryčuk (2014) also inverts for the probable rupturing fault plane in the current stress field (Fig. 6.8d). By comparing strike, dip and rake of the fault planes of the events in Table 6.2 with the probable fault plane of StressInverse, we observe that the NNW-SSE-oriented fault planes - typical for the ASZ - changed to their auxiliary fault planes, i.e., dextral strike-slip with a strike of WNW-ESE (Fig. 6.8d). As the aftershock distribution of the stronger events is NNE-SSW (e.g., Stange and Brüstle, 2005), as are our relocated events in Fig. 6.7, of course a sinistral fault plane with NNE-SSW strike is the preferred one. As explanation for this discrepancy we suggest that the ASZ is an inherited weak structure that needs much less stress for failure than the more probable WNW-ESE-oriented fault planes predicted by StressInverse. Ring and Bolhar (2020) find that the ASZ coincides with the NNE-SSW-oriented boundary fault between the
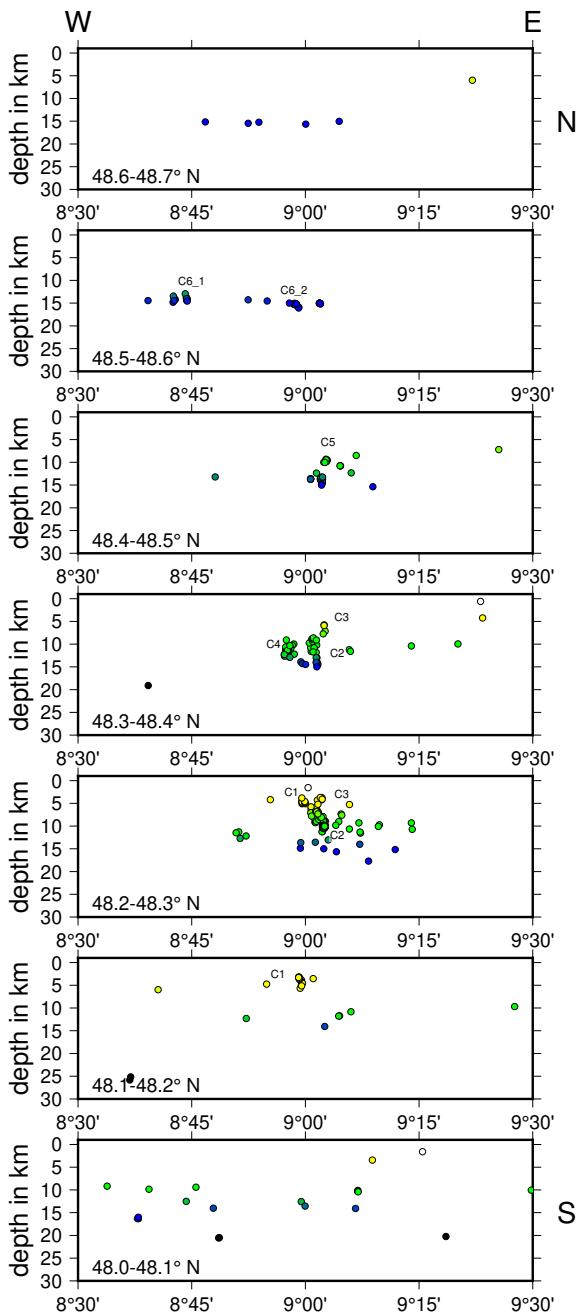
Figure 6.10.: Seismicity distribution of the ASZ from north (top) to south (bottom). Circles indicate hypocenters in the corresponding slice, color-coded by depth (as in Fig. 6.7); cluster codes are given for orientation.

Triassic-Jurassic Spaichingen high and the Mid-Swabian basin, also hinting at a preexisting structure. The earthquake cluster C4 south of Hechingen (Figs. 6.10, 6.11) consists of events with normal faulting components (ev402, ev423, ev364) and the strike-slip event ev457 (Fig. 6.7). This cluster aligns along the boundary faults of the HZG and the events strike almost parallel to the HZG (Figs. 6.7, 6.8d). Other earthquakes close to the HZG boundary fault also strike almost parallel to the HZG (e.g., ev552, ev566, ev564). The depth extension of the HZG is not well known but is estimated from its extensional width and the dip angles of the main
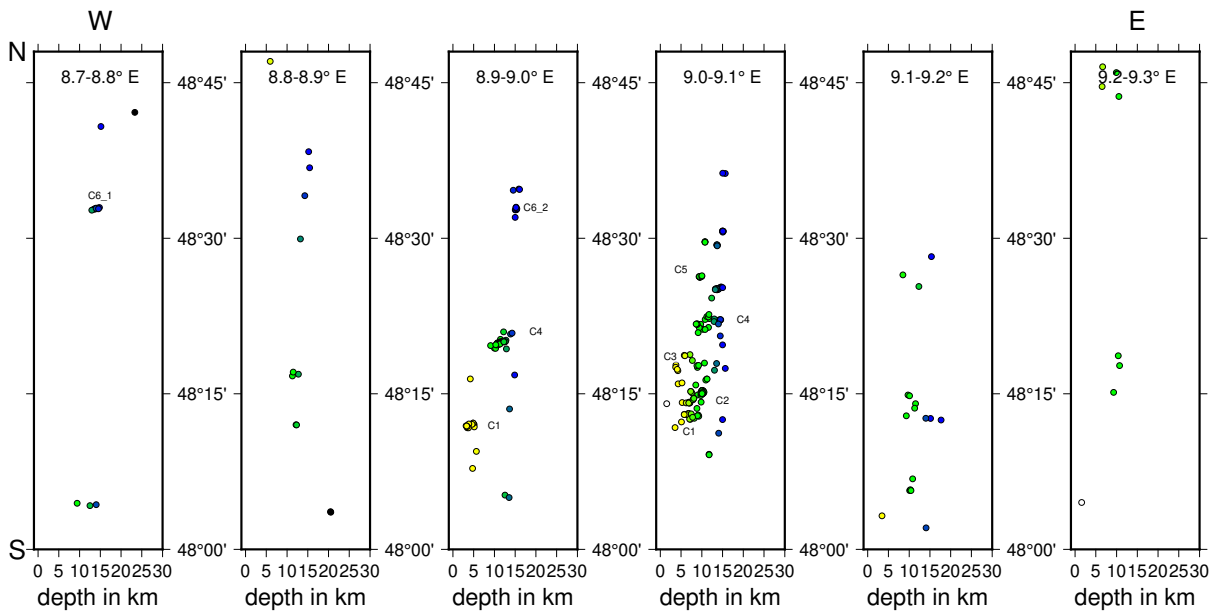
Figure 6.11.: Seismicity distribution of the ASZ from west (left) to east (right). Circles indicate hypocenters in the corresponding slice, colorcoded by depth (as in Fig. 6.7); cluster codes are given for orientation.

boundary faults at the surface. Based on these parameters, the boundary faults are thought to converge in about 2-3 km depth (Schädel, 1976). The faulting pattern of events close to HZG may indicate that the HZG boundary faults reach to greater depth, as already suggested by Schädel (1976) or Illies (1982). This may also imply that ev457 is a dextral strike-slip event, as is suggested by the result of the stress inversion. Relative event locations may help to identify the active fault planes in more detail using more data in future work.

6.6.3. Stress field around the ASZ

We inverted our fault plane solutions for the direction of the principal stress axes σ_1, σ_2, σ_3 (Table 6.3). As for a combined run, the differentiation between σ_1 and σ_2 is difficult (Fig. 6.8a); we also inverted a split data set separated by the depth of 7.5 km (Fig. 6.8b, c). For depths shallower than 7.5 km, we observe the horizontal maximum stress $S_{H_{max}}$ with an azimuth of 149° to be greater than the vertical stress S_V (Table 6.3). For a depth range greater than 7.5 km, we observe $S_V > S_{H_{max}}$. The depth dependence of the relative stress magnitudes is also known from other sites in the region. In the deep boreholes in Soultz (central Upper Rhine Graben), $S_V > S_{H_{max}}$ is found in the upper ca. 2.5 km. Below this, $S_{H_{max}} > S_V$ is valid to at least 5 km depth (Valley and Evans, 2007). Here $S_{H_{max}}$ has a direction of 169° E ± 14°. In the southern Upper Rhine Graben, Plenefisch and Bonjer (1997) determined $S_{H_{max}} > S_V$ in the upper crust to 15 km depth, whereas $S_V > S_{H_{max}}$ was determined in the lower crust (>15 km depth) from fault plane solutions. Our results indicate a shallower level (∼7 km) for the change of the maximum stress components, which may be due to a change in the rock rheology and needs to be studied with more data. Our direction of $S_{H_{max}}$ is 140–149°. The orientation of $S_{H_{max}}$ for southwestern Germany is estimated to be around 150° with a σ of 24° (Reinecker

et al., 2010) and for all of western Europe it is 145° with a σ of 26° (Müller et al., 1992), which are both in agreement with our local $S_{H_{max}}$ orientation. Houlié et al. (2018) also observes a similar stress field in eastern Switzerland, southeast of our research area. Reinecker et al. (2010) suggest the gravitational potential energy of the Alpine topography as the main source of the local stress field because the stress field orientation in the northern Alpine foreland is always perpendicular to the Alpine front. Kastrup et al. (2004) also observe a change of stress field orientation with the Alpine front for the northern Alpine foreland in Switzerland. They explain the change of the orientation of the minimum horizontal stress Sh parallel to the Alpine front with a perturbation of the regional European stress field due to the indentation of the Adriatic Block. Müller et al. (1992) identify the plate-driving forces as sources of the maximum compression in the NW to NNW direction for all of western Europe, which are only perturbated by large geological structures like the Alps. As our study area is quite small, we cannot observe major lateral stress variations; however, the good coincidence with the regional stress field (Müller et al., 1992; Reinecker et al., 2010) is a strong indication that the driving tectonic forces of the seismicity of the ASZ are the regional plate-driving forces combined with the Alpine topography. Small-scale stress perturbations and variations of faulting mechanisms (Figs. 6.7 and 6.8) may be due to local heterogeneities of crustal material causing variations in rigidity or preexisting structures. These factors may also play a role in the segmentation of the ASZ, which will be analyzed in more details in the next few years.

6.7.   Conclusion and outlook

We used our newly complemented seismicity catalog to invert for a robust new minimum 1-D seismic velocity model with station delay times for the ASZ region. These station delay times can be explained by the depth variation of the crystalline basement in the upper crust of Baden-Württemberg (Fig. 6.9). The relocated seismicity of the years 2011 to 2018 pictures the ASZ as a complex fault structure, with its current main active focus between the cities Albstadt and Tübingen on the Swabian Alb. The hypocenter error estimates clearly become smaller for events after 2016 due to the densified seismic station network of the LED and the complementing AASN stations. Thus, we expect another improvement and an increase in detectable events from 2019 onwards due to our additionally installed StressTransfer stations (Fig. 6.1). Future work will take advantage of the densified seismic station network and focus on small-magnitude event detection based on template matching in the area of the ASZ.
Most of the seismicity takes place in a N-S-oriented band east of 9° E (Fig. 6.7). A spatial clustering of events is found, which may indicate separate fault planes. If such a separation can be verified in the future, this segmentation would limit the maximum size of earthquake rupture planes and its related hazard potential (Grünthal and the Global Seismic Hazard Assessment Program (GSHAP) Region 3 Working Group, 1999). Nevertheless, we find the shallow cluster C1 slightly separated to the west from the other events, as well as the deeper cluster C4 near Hechingen. Furthermore, we observe clear normal faulting events, which were so far not observed for the ASZ. A relation of the clusters C4 with a continuation of the HZG into the crystalline basement is possible and needs further observational constraints to better describe the seismic potential of the HZG. Ongoing work will determine relative locations for

all events from 2016 and following years to obtain an even sharper image of the fault planes of the ASZ. We will also continue complementing our catalog with new earthquakes and fault plane solutions after 2018.

The estimated $S_{H_{max}}$ has a NNW-SSW trend. This is in good agreement with other studies (Müller et al., 1992; Kastrup et al., 2004; Reinecker et al., 2010; Houlié et al., 2018). As plausible driving forces of our local stress field, we identify the regional plate driving forces and the Alpine topography (Müller et al., 1992; Kastrup et al., 2004; Reinecker et al., 2010). In the upper part of the crust $S_{H_{max}}$ exceeds S_V (Fig. 6.8). Below about 7-8 km depth S_V seems to be the dominating stress component. Within the StressTransfer project, similar investigations are planned for the URG to the west and the Molasse Basin southeast of the ASZ to get a better understanding of the stress field in the northern Alpine foreland of southwestern Germany.

7. Fault imaging using earthquake sequences: A new model for rupture processes at the Albstadt Shear Zone, Southwest Germany

In the following section a new model for the rupture processes in the area of the ASZ is presented. A template matching event detection algorithm is applied to search for earthquake sequences (fore- and aftershocks or earthquake swarms) during 2018 - 2020 in the area of the ASZ. The active faults are imaged by determining fault plane solutions and relative event locations for the identified earthquake sequences. This section is submitted to the Journal of Seismology and currently under review.

7.1. Abstract

In Germany, the highest seismic hazard is located at the Albstadt Shear Zone (ASZ) on the western Swabian Alb, a low mountain range in southwest Germany. There occurs continuous micro-seismic activity with the potential for damaging earthquakes (nine events with ML ≥ 5 in the last century). Within the AlpArray and StressTransfer projects nine temporary seismic stations have been installed in the region of the ASZ to densify the permanent seismic monitoring. In October 2018 and September 2019, the state seismological survey (LED) detected two low-magnitude earthquake sequences with hundreds of events in the area. The temporarily densified local network allows us to systematically analyze these sequences and to search for other sequences by applying a template matching routine on data from 2018 to 2020. In total, six earthquake sequences could be identified with at least 10 events. The three biggest sequences (> 100 events) consist of one fore- and aftershock sequence and two earthquake swarms, so far not observed around the ASZ. Precise relative event locations and the determination of fault plane solutions allow us to propose a seismotectonic model based on the three imaged fault types: The well-known NNE-SSW striking sinistral strike-slip ASZ at depths of 5-10 km, a NW-SE striking dextral strike-slip fault zone at depths of 11-15 km beneath the Hohenzollerngraben, a shallow aseismic NW-SE striking graben structure, and at the intersection of the ASZ and the NW-SE striking fault zone, complex faulting in form of NNW-SSE striking sinistral strike-slip and normal faulting.
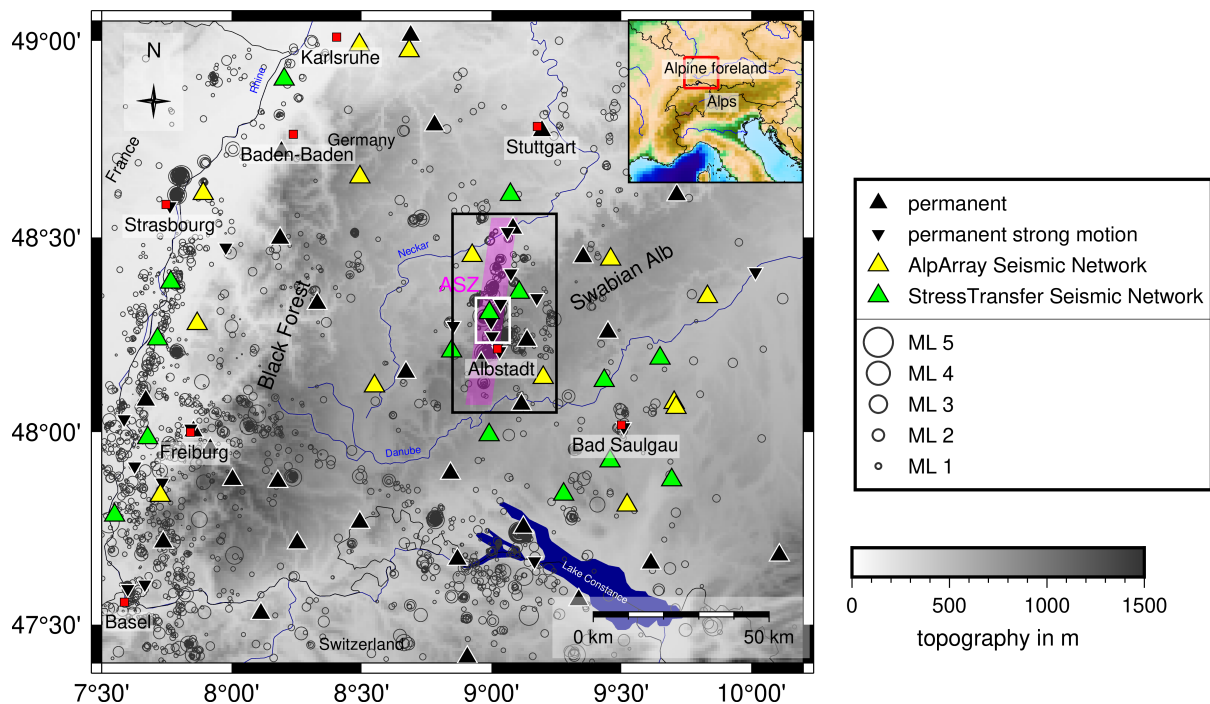
Figure 7.1.: Overview of the research area with seismic station distribution (triangles) during the studied time period and the epicenters of the LED event catalog from 2011 to 2020 (gray circles, Bulletin-Files des Landeserd-bebendienstes B-W, 2011-2020). The black frame surrounds the research area with the Albstadt Shear Zone (ASZ, white shaded area). The white frame borders the close-up area of Fig. 7.6. Topography is based on SRTM15+ (Tozer et al., 2019). The inset gives the position within Central Europe.

7.2. Introduction

In Central Europe intra-plate seismicity is driven by low deformation rates due to far-field tectonic processes (Müller et al., 1992; Piña-Valdés et al., 2022). This tectonic stress regime is especially related to the Alpine orogeny as well as to the Adriatic indenter and cause seismic activity preferably on faults which are oriented favourably in the stress field (Reicherter et al., 2008; Röckel et al., 2022). The reoccurrence times of strong, damaging earthquakes are in general up to several hundreds or even thousands of years (Hürtgen et al., 2020). Therefore, the study of regions with high microseismic activity is necessary to better understand the mechanisms and stresses related to intra-plate seismicity in the northern Alpine foreland. The Albstadt Shear Zone (ASZ) in SW Germany is a suitable site (Fig. 7.1), because of frequent micro-seismicity and, since the last century, mid-size magnitude earthquakes about every 20-30 years. Those earthquakes causing major damage are a major hazard and risk studies estimate losses of several 100 million EURO just related to residential buildings (Tyagunov et al., 2006). Such risks are quite reasonable if one recalls that the November 1911 Albstadt earthquake was felt about 400 km towards north in Germany and well into France, Switzerland, Austria and northern Italy (Sieberg and Lais, 1925).

The ASZ is located on the Swabian Alb, a plateau-like mountain range composed of Jurassic limestone (Fig. 7.1). Continuous microseismic activity is documented since the 16th century with two major earthquakes near Tübingen in 1655 with intensities of EMS-98 VI or VII
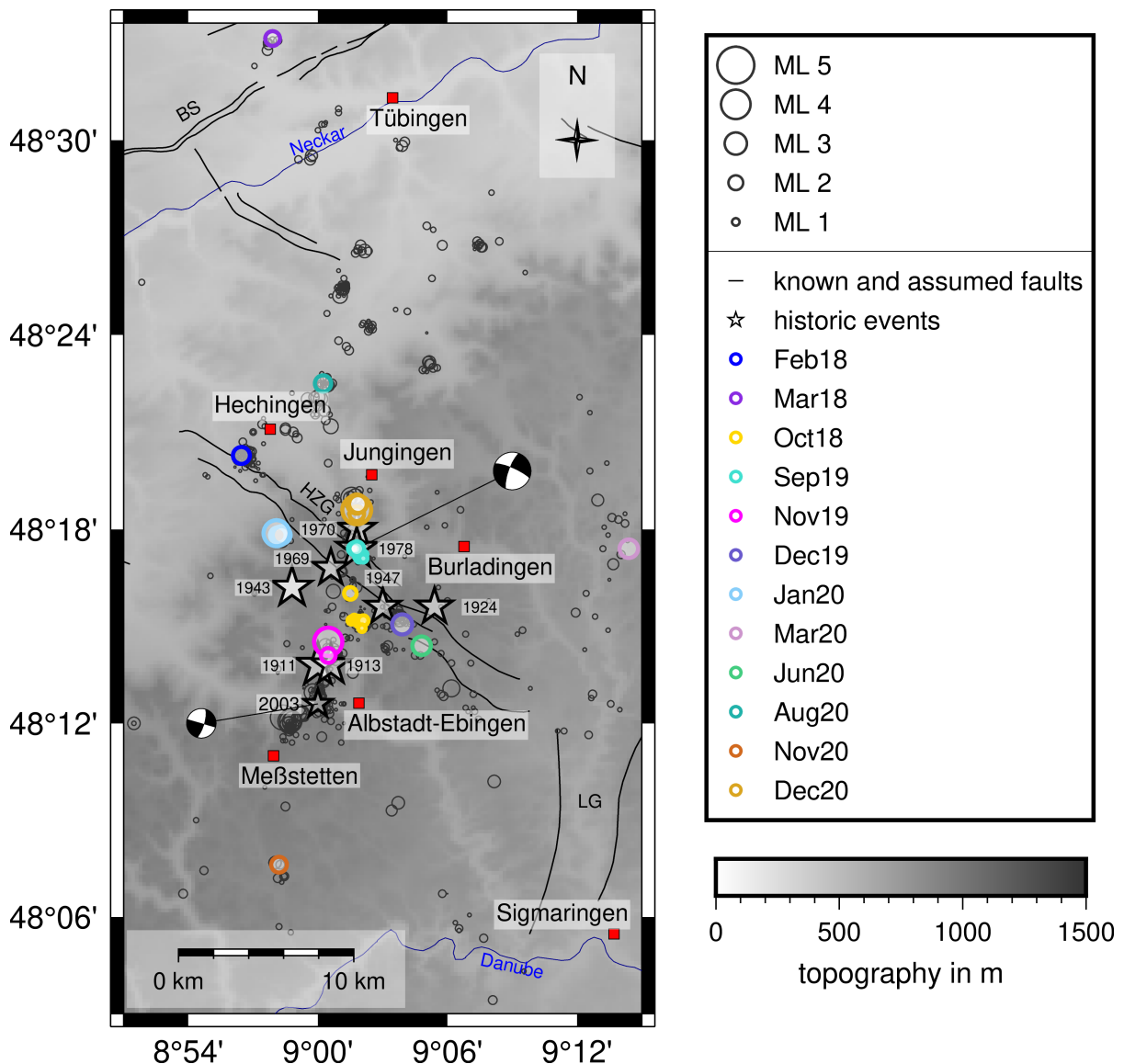
Figure 7.2.: Research area on the Swabian Alb. Gray circles are earthquake epicenters between 2011 and 2020 (LED event catalog, Bulletin-Files des Landeserdbebendienstes B-W, 2011-2020). Stars represent important historic earthquakes with ML greater than 5 and the ML 4.4 earthquake in 2003 (Schwarz et al., 2019; Stange and Brüstle, 2005). Fault planes solutions of the 1978 earthquake after Turnovsky (1981) and the 2003 earthquake after Stange and Brüstle (2005). Colored circles indicate epicenters of earthquakes used for the template matching event detection. Black lines indicate faults in the area (BS = Bebenhausen Fault, HZG = Hohenzollerngraben, LG = Lauchertgraben, Regierungspräsidium Freiburg: Landesamt für Geologie, Rohstoffe und Bergbau (Hrsg.), 2019). Topography is based on SRTM15+ (Tozer et al., 2019).

(Bulletin-Files des Landeserdbebendienstes B-W, 2011-2020). Especially since the occurrence of a local magnitude (ML) 6.1 earthquake in 1911, several strong earthquakes with ML ≥ 5 shook the region causing major damage in 1913 (ML ~5.6), 1924 (ML ~5.1), 1943 (ML ~5.5 and ML ~5.6), 1947 (ML ~5.0), 1969 (ML ~5.1), 1970 (ML ~5.2) and 1978 (ML ~5.7, Schwarz et al., 2019). Nevertheless, no morphological expression of the ASZ is visible at the Earth's surface. Seismotectonic analyses of the earthquakes revealed a NNE-SSW striking fault zone in the

upper crust (Fig. 7.2, Reinecker and Schneider, 2002; Stange and Brüstle, 2005; Mader et al., 2021), but the NS extension of the ASZ is still debated (e.g. Haessler et al., 1980; Reinecker and Schneider, 2002; Stange and Brüstle, 2005). The largest proposed extension of more than 120 km reaches from the Lake Constance to the north of the town of Stuttgart (Fig. 7.1, Reinecker and Schneider, 2002). Stange and Brüstle (2005) and Mader et al. (2021) question this extension due to the limited focus of the seismically active area on the Swabian Alb (Fig. 7.1). Mader et al. (2021) suggest an extension of about 40 km between the towns Tübingen to the north and Meßstetten to the south, which is well outlined by the current seismic activity (Fig. 7.2). Fault plane solutions of the ML 5.7 earthquake in 1978 and the ML 4.4 earthquake in 2003, as well as recent events indicate a dominant sinistral strike-slip faulting regime in a stress field with a maximum horizontal stress direction in $140° - 149°$ (Fig. 7.2, e.g., Haessler et al., 1980; Turnovsky, 1981; Reiter et al., 2016; Stange and Brüstle, 2005; Mader et al., 2021).

At the surface the only visible tectonic structure is the Hohenzollerngraben (HZG), an about 25 km long NW-SE striking graben structure with an inverted relief (Fig. 7.2, Schädel, 1976). Its depth range of about 2 - 3 km is based on the opening width of 1.5 km and the dip angles at the graben boundary faults of around $60°$ (Schädel, 1976). A potential depth continuation of the graben boundary faults into the crystalline basement is unclear and still under discussion (Illies, 1982; Reinecker and Schneider, 2002). As there are several graben structures like the HZG to the north and south (e. g. Fildergraben, Rottenburg Flexure, western Lake Constance faults and Hegau, Reinecker and Schneider, 2002), Reinecker and Schneider (2002) propose a tectonic model for the ASZ, with a decoupling horizon between the crystalline basement and the sedimentary cover. As a result, the movement of the ASZ in the crystalline basement is transferred as en-echelon graben structures to the surface, due to the partly decoupled horizon in between.

In October 2018 the state seismological service of Baden-Württemberg (LED) detected an earthquake sequence with more than 200 events in the area of the ASZ. In September 2019 another sequence with at least 800 earthquakes was identified by the LED. Such large earthquake sequences were so far not recorded in the region. Due to the large amount of very low magnitude earthquakes (ML < 0.5), a location of the majority of the detected events was not possible with the permanent seismic network (Bulletin-Files des Landeserdbebendienstes B-W, 2011-2020).

The densification by the temporary seismic stations of the AlpArray (2016 - 2022, Hetényi et al., 2018) and the StressTransfer seismological experiments (since September 2018, Mader and Ritter, 2021) in the area offer a unique opportunity to systematically analyze these two earthquake sequences and the local microseismic activity to image active fault structures (Fig. 7.1, Erdbebendienst Südwest Baden-Württemberg and Rheinland-Pfalz, 2009; Swiss Seismological Service (SED) at Eidgenössische Technische Hochschule (ETH) Zurich, 1983; Federal Institute for Geosciences and Natural Resources (BGR), 1976; GEOFON Data Centre, 1993). In the following, we use a multi-station template matching detection routine with an automatic phase picking routine to detect and locate additional earthquakes. In this way we can analyze small magnitude events, which are so far not included in the event catalog of the LED. We study the two time windows with known unusual seismic activity (October - November 2018 and September 2019) and all time windows around events with a ML ≥ 2 of a month duration in the years 2018 to 2020 to search for other possible earthquake sequences and aftershocks.

With the detected earthquake sequences, we image the active fault planes by relative event locations and identify the source mechanisms using fault plane solutions.

7.3.   Data

We use the waveform data of all available permanent seismic stations in up to about 100 km distance to the ASZ (Fig. 7.1). Permanent recordings are provided by the LED (Erdbebendienst Südwest Baden-Württemberg and Rheinland-Pfalz, 2009), the Swiss Earthquake Service (SED, Swiss Seismological Service (SED) at Eidgenössische Technische Hochschule (ETH) Zurich, 1983), German Regional Seismic Network (GRSN, Federal Institute for Geosciences and Natural Resources (BGR), 1976) and GEOFON seismic network (GEOFON Data Centre, 1993). This network of about 30 permanent seismic stations was densified by up to 10 seismic stations in the vicinity of the ASZ (Fig. 7.1). The temporary seismic stations are part of the AlpArray Seismic Network (2015 - 2022, Hetényi et al., 2018) and the StressTransfer Seismic Network (September 2018 - 2030, Mader and Ritter, 2021).
Furthermore, the LED provided its event catalog (Bulletin-Files des Landeserdbebendienstes B-W, 2011-2020), including origin time, hypocenter coordinates (Fig. 7.1), local magnitude ML, P as well as S phase arrival times and P phase polarities. Based on this event catalog master events are defined for the template matching event detection. The LED magnitudes are used for the relative magnitude estimation and the P phase polarities for the calculation of fault plane solutions.

7.4.   Methods

To gain a better understanding of the active faults in the area of the Swabian Alb we apply a template matching detection routine with an automatic phase arrival time determination routine to find hitherto unknown events. For the newly detected events we determine the source parameters and calculate a relative magnitude to complement the LED event catalog. Finally, we calculate relative event locations for the larger event sequences to image the seismically active fault planes.
We use the LED earthquake catalog as starting point of our processing (Fig. 7.3, step 1). We add direct P and S phase arrival times from the AlpArray and StressTransfer stations to the LED earthquake catalog to take advantage of the densified station network (Fig. 7.3, step 2). In a next step, we select the events, which are used as waveform templates for the event detection process, from the complemented LED event catalog (Fig. 7.3, step 3). Waveform templates from 17 events with ML > 1.0 are selected for the known earthquake sequences in October - November 2018 and September 2019. Additionally, we choose 16 event template waveforms for events with ML ≥ 2.0 during the years 2018 to 2020 to search for new sequences. As we are interested in fore- and aftershock sequences as well as swarm-like sequences we run

the detector for about a month duration around the event time of the templates. Templates of events with similar event time and event location are combined to one time series. This approach leads to 12 time series for event detection (Table 7.1). For each time series we run a multi-station template matching detector and automatically determine P and S phase arrival times using the Python package EQcorrscan (Chamberlain et al., 2018, Fig. 7.3, step 4). The output is reduced to event detections with at least four reliable phase arrival times based on a cross-correlation coefficient (ccc) ≥ 0.5 (Fig. 7.3, step 5). To verify the correctness of the automatically determined phase arrival times we visually inspect all phase arrival times and delete or repick false arrival times (Fig. 7.3, step 6). Finally, we complement the detection catalog of each time series with the source parameters by locating the events with NonLinLoc (Lomax et al., 2000), using the minimum 1-D seismic velocity model ASZmod1 (Mader et al., 2021, Fig. 7.3, step 7), and the calculation of a relative event magnitude after Schaff and Richards (2014) (Fig. 7.3, step 8). Our processing steps lead to 12 detection catalogs from each analyzed time series (Fig. 7.3, step 9, Table 7.1).

To identify the fault mechanism we determine fault plane solutions of the event templates using FOCMEC (Snoke, 2003, Fig. 7.3, step 10). Furthermore, we determine relative event locations with HypoDD (Waldhauser and Ellsworth, 2000) for the six detection catalogs which feature at least ten events to image the seismically active fault plane (Fig. 7.3, step 11, Table 7.1).

7.4.1. Preprocessing

We preprocess all waveform data in the exactly same way to achieve a consistent dataset. The preprocessing is done for all processing steps which use the waveform data (Fig. 7.3, event detection, visual inspection of the automatic phase arrival times, relative magnitude estimation and input creation of the HypoDD cross-correlation time data set). We start with daylong time windows plus 30 s of continuous waveform data. The daylong time window is chosen because the event detection routine is run day-wise. The additional 30 s are necessary to create an overlap to the next day due to the multi-station approach of the event detection to avoid missing events around midnight, as the waveform templates of all seismic stations are shifted in time relative to each other depending on the phase arrival times at each station. The waveform data are resampled to 50 Hz to reduce the overall data size, detrended and filtered with a fourth-order Butterworth bandpass filter between 1 - 20 Hz. The waveform of an event or phase is extracted from the preprocessed waveform.

7.4.2. Additional phase arrival times

At first we determine the direct P and S phase onset times in the recordings of the six StressTransfer and four AlpArray seismic stations within our target region (Fig. 7.1) by applying the semi-automatic picking routine described in Mader et al. (2021) (Fig. 7.3, step 2). The uncertainty of an identified phase arrival time is based on an automatically determined earliest and latest possible phase arrival time around the approximate phase onset time after Diehl et al. (2012). This results in 508 additional phase arrival times to the LED event
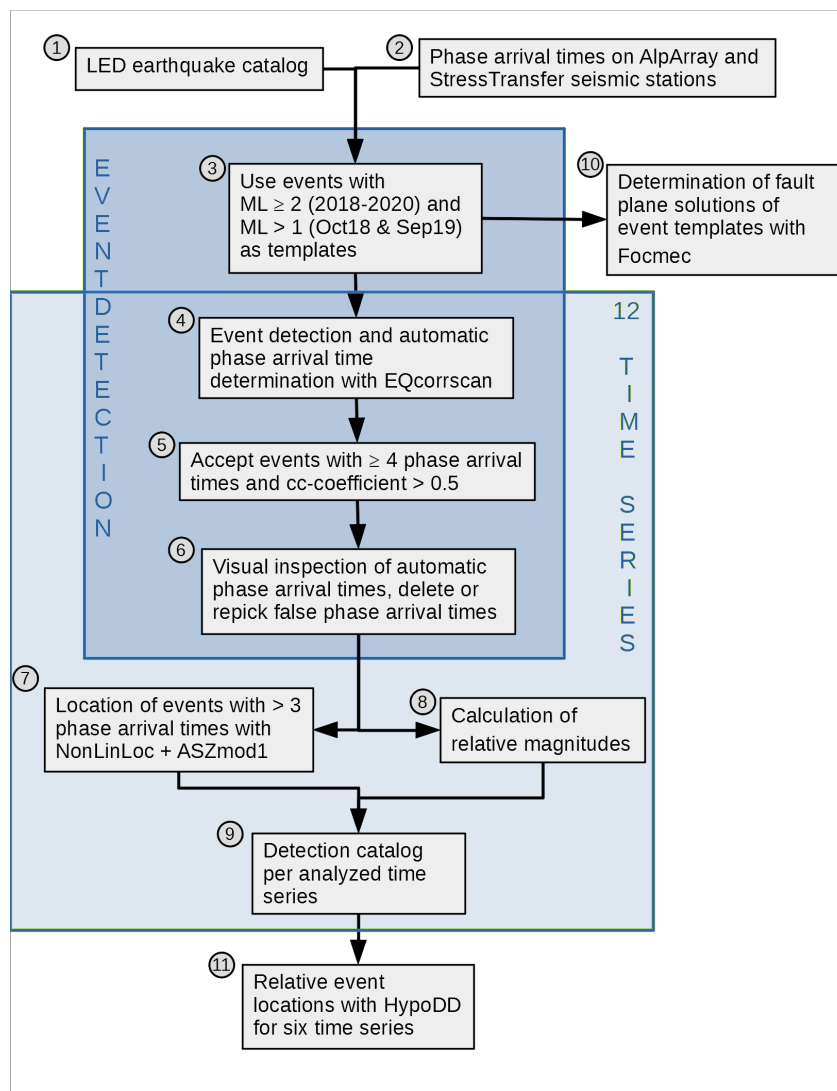
Figure 7.3.: Workflow for this work from 1: *LED event catalog* to 11: *relative event locations*. The 12 times series are listed in Table 7.1.

catalog in the years 2019 and 2020. For the year 2018, phase arrival times at the AlpArray and StressTransfer seismic stations are taken from Mader et al. (2021), where the dataset was already processed in the same way.

7.4.3. Event detection

To identify additional small magnitude earthquakes we use the routines of the Python toolbox EQcorrscan (Chamberlain et al., 2018) for our multi-station template matching detection routine. We define as master events all events with ML ≥ 1.0 for the two time periods with known earthquake sequences (October to November 2018 and September 2019) as well as all events with ML ≥ 2.0 of the remaining time period (2018-2020). Waveform templates are generated of each event that satisfies our selection criteria (see below, Table 7.1, Fig. 7.2, 7.3,

Table 7.1.: Time overview, event templates and results for event detection for the 12 different time series. The resulting number of detected events with more than three phase arrival times have a ccc exceeding 0.5. The number of well-located events corresponds to events located with NonLinLoc (Lomax et al., 2000) with a horizontal and vertical location uncertainty of ≤ 2 km and at least 6 phase arrival times. The number of similar events in the LED catalog is based on the event sequence location and event time. All of those events within the LED catalog were detected with our approach.

ID	time-span	templates time	magnitude ML	coordinates °N	coordinates °E	depth in km	number of detections	number of well located events	similar events in LED catalog	number of relative magnitudes
Feb18	2018-01-31 - 2018-03-02	2018-02-10T12:44:38	2.3	48.33	8.95	13	23	17	4	15
Mar18	2018-02-28 - 2018-03-30	2018-03-10T21:16:33	2.0	48.55	8.98	15	1	1	1	1
Oct18	2018-10-01 - 2018-12-31	2018-10-15T10:14:42	1.1	48.25	9.04	10	220	150	71	154
		2018-10-15T15:01:43	1.2	48.25	9.05	9				
		2018-10-15T18:04:37	1.0	48.25	9.04	10				
		2018-10-15T19:37:35	1.3	48.25	9.04	10				
		2018-10-15T19:41:47	1.6	48.25	9.04	10				
		2018-10-17T03:02:32	1.0	48.25	9.04	10				
		2018-10-24T07:12:07	1.7	48.27	9.02	5				
		2018-11-25T02:22:18	1.4	48.25	9.06	13				
		2018-11-26T18:47:43	1.0	48.25	9.04	10				
Sep19	2019-09-01 - 2019-09-30	2019-09-08T16:12:48	1.1	48.27	9.06	11	590	319	59	280
		2019-09-08T16:22:44	1.7	48.29	9.04	12				
		2019-09-08T17:45:52	1.1	48.27	9.05	12				
		2019-09-09T01:49:08	1.5	48.28	9.05	12				
		2019-09-10T06:59:58	1.1	48.28	9.04	13				
		2019-09-10T07:00:31	1.1	48.29	9.04	13				
		2019-09-11T19:00:10	1.6	48.28	9.04	12				
		2019-09-19T03:19:20	2.0	48.28	9.05	12				
Nov19	2019-10-25 - 2019-11-24	2019-11-04T00:59:47	3.8	48.24	9.01	5	4	4	4	4
		2019-11-06T10:08:51	2.0	48.23	9.01	5				
Dec19	2019-11-25 - 2019-12-25	2019-12-05T10:14:17	2.7	48.25	9.07	5	3	3	1	3
Jan20	2020-01-17 - 2020-02-16	2020-01-27T03:48:22	2.1	48.29	8.98	11	411	297	108	251
		2020-01-27T22:05:25	2.4	48.29	8.98	11				
		2020-01-27T22:05:41	3.5	48.29	8.98	11				
Mar20	2020-02-25 - 2020-03-26	2020-03-06T19:10:41	2.5	48.29	9.24	7	3	2	1	3
Jun20	2020-06-08 - 2020-07-08	2020-06-18T22:41:12	2.5	48.23	9.09	7	2	2	1	2
Aug20	2020-08-02 - 2020-09-01	2020-08-12T18:42:19	2.2	48.37	9.01	10	4	3	1	4
Nov20	2020-11-07 - 2020-12-07	2020-11-17T07:20:23	2.1	48.12	8.98	6	17	13	8	12
Dec20	2020-11-20 - 2020-12-31	2020-11-30T23:25:46	3.9	48.31	9.04	8	74	63	23	42
		2020-12-01T01:59:13	2.0	48.31	9.04	8				
		2020-12-09T04:55:13	2.6	48.31	9.04	8				
		2020-12-25T15:10:33	2.4	48.31	9.04	8				

step 3). As we are interested in earthquake sequences the event detection is executed around the origin time of the event template. Similar origin time and location of event templates lead to a combination into one time series. This leads to 12 separate time series. The event detection process is run independently for each time series and only the corresponding master event templates are used (Table 7.1).

As templates we use the waveforms of direct P and S phases. P phases are detected on the vertical component Z and S phases on both horizontal components, N and E. The waveform of a phase arrival time contributing to a template needs a minimum signal-to-noise ratio (SNR) of 7.5 and is cut 0.15 s before the actual phase arrival time and has a length of 1.3 s. Final input templates are accepted only for earthquakes with at least three P phase waveforms on the vertical component and three S phase waveforms on the horizontal components satisfying the SNR criteria (Fig. C.1).

For the template matching event detection we apply the EQcorrscan function *match_filter* (Chamberlain et al., 2018, Fig. 7.3, step 4). The continuous waveform data are prechecked for data gaps and corresponding days are skipped, if more than a third of the recording time is missing. The function *match_filter* determines a shifted stacked cross-correlation function (ccsum) for all waveforms. We use as detection threshold the Median Absolute Deviation ($MAD = threshold \cdot median(abs(cccsum))$) with a threshold value of 9, which is selected after some exemplary test runs to achieve a good ratio of real detections (seismic events) to wrong detections (noise). As we search with several master events with similar waveforms we reject double detections within a second from different master events and keep the detection with the highest ccsum value, after the detection process is completed for each 24 h plus 30 s time window. The detection process results in event catalogs per each analyzed day. Those event catalogs are combined to one detection catalog for each of the 12 time series after double detections due to the 30 s time overlap are rejected.

We use the EQcorrscan function *lag_calc* to determine automatic relative phase arrival times (Fig. 7.3, step 4). P phase arrival times are determined on the Z-component and S phase arrival times on the horizontal components after Shelly and Hardebeck (2010) (Fig. C.2). Only correlations between detection and template waveform with a ccc greater than 0.5 are accepted (Fig. 7.3, step 5). As our waveform templates begin 0.15 s before the actual phase arrival time, we correct the automatic relative phase arrivals for this time shift. Furthermore, we combine double S phase arrival times to one S phase arrival time, if they are found for the same station on both horizontal components. For this we use the horizontal component with the higher ccc, if the determined arrival time differs for the N and E component. To assess an uncertainty to each phase arrival time we convert the ccc to a time uncertainty following Table 7.2.

The following analysis is done for detected events with at least four automatic phase arrival times as we want to locate the events at a later stage (Fig. 7.3, step 5). To ensure the reliability of the automatic phase arrival times we manually recheck all phase arrival times and sort out wrong ones, which corresponds to about 20% (Fig. 7.3, step 6). If there are problems like cycle shifts, we redetermine the phases by hand, what happened for less than 1% (Fig. 7.3). For repicking we again use the semi-automatic picking routine of Mader et al. (2021). After the visual inspection, events with three or less phase arrival times are kept in the detection catalog as counted events, which cannot be localized (228 events).

The event detection results in 12 detection catalogs, one for each analyzed time series (Fig. 7.3,

Table 7.2.: Cross-correlation coefficient (ccc) and corresponding time uncertainty of the detected phase arrival times.

cross-correlation coefficient	time uncertainty in s
$ccc >= 0.8$	0.01
$0.6 <= ccc < 0.8$	0.05
$0.5 <= ccc < 0.6$	0.1

step 3 - 6, Table 7.1). The earthquakes used as templates are also included in those detection catalogs.

7.4.4. Event location

To complement the 12 detection catalogs with origin time and hypocenter coordinates we relocate all events with at least 4 phase arrival times with the non-linear location algorithm NonLinLoc (Lomax et al., 2000) following Mader et al. (2021) (Fig. 7.3, step 7, Fig. 7.4). As velocity model we use the local minimum 1-D seismic velocity model ASZ-mod1 and its corresponding station corrections which was determined for the ASZ by Mader et al. (2021). In the same way we relocate the LED event catalog of the years 2019 and 2020 supplemented with the phase arrival times from the AlpArray and StressTransfer seismic stations (Fig. 7.4). The relocated LED event catalog of the years 2011 to 2018 is taken from Mader et al. (2021).

7.4.5. Relative Magnitude Estimation

We use the method of Schaff and Richards (2014) to determine a relative magnitude for each event based on the comparison of the seismic phase amplitudes of template and detection waveforms (Fig. 7.3, step 8). Schaff and Richards (2014) introduce two possible ways to calculate relative magnitudes: one with correction terms for ccc and SNR (after formula 10, Schaff and Richards, 2014) and another one without correction terms and only the application of the ratio of the L2 norm of the amplitude of the observed slave and master waveforms (formula 11, Schaff and Richards, 2014). The master waveform corresponds to the waveform of the detection template and the slave waveform to the correspondingly detected waveform. Schaff and Richards (2014) suggest the first one to be a good choice for highly similar waveforms even with high noise conditions. Nevertheless, for low ccc like 0.5, a bias is introduced to the actual magnitude of up to 0.3 (Schaff and Richards, 2014). This bias originates from dissimilar waveforms and noise on the master waveform. For this case they introduce the calculation of relative magnitudes based on the ratio of the L2 norm. This calculation is insensitive on bias due to the ccc but sensitive for high noise conditions. We decide to calculate our relative magnitudes based on the ratio of the L2 norm, because we kept phase arrival times with ccc values > 0.5 in our event catalog and we also searched for aftershock events which may have different source time functions or focal mechanisms. To account for the high sensitivity on noise during the relative magnitude calculation, we include only phase arrivals with a SNR > 3. As we have both, P and S phase arrival times, we modified the method of Schaff and
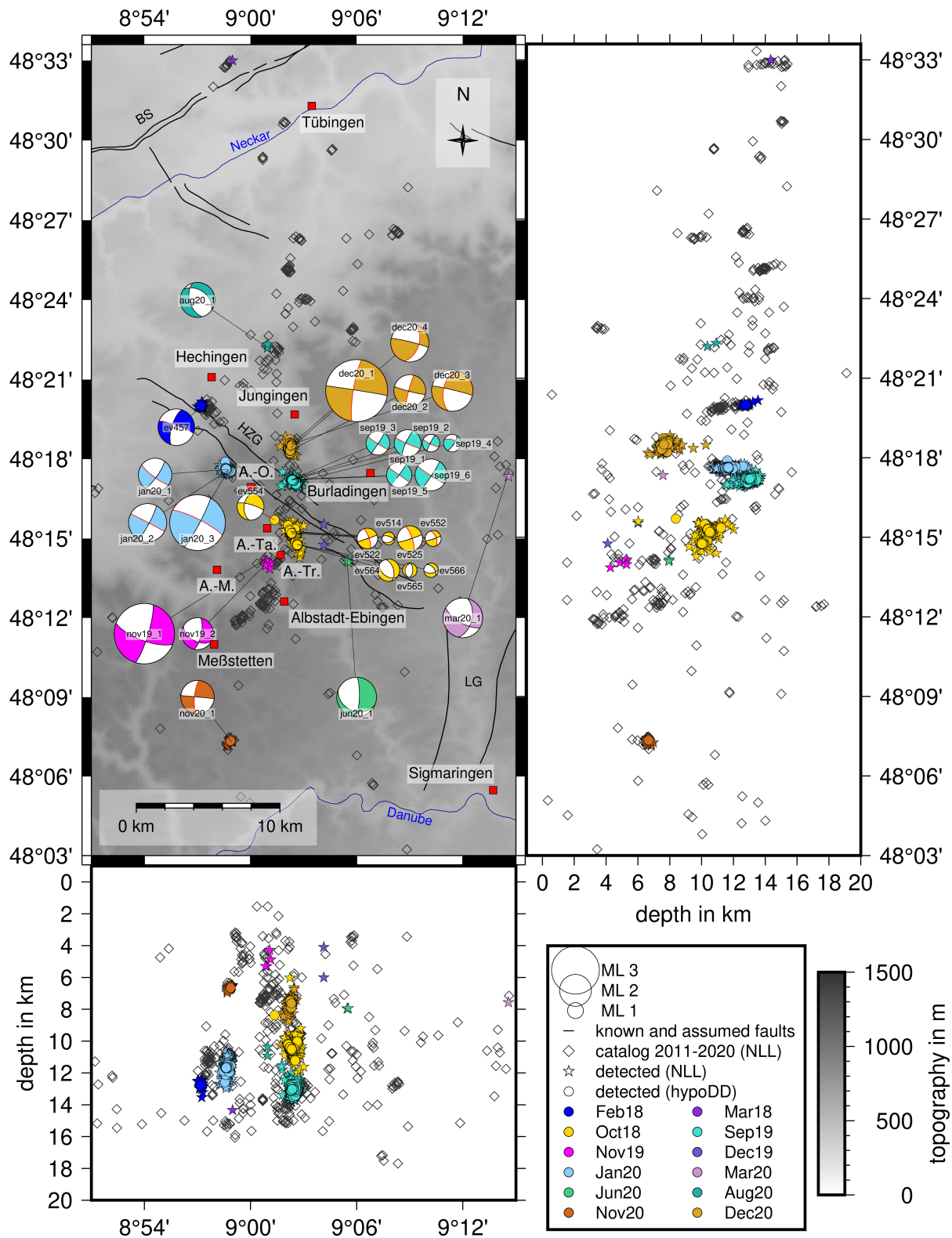
Figure 7.4.: HypoDD (circles) and NonLinLoc (stars, uncertainty < 2 km and at least 6 phase picks) hypocenter locations of detected events, templates are included. Best located events (squares) from 2011 to 2018 of Mader et al. (2021) complemented with newly located events in 2019 to 2020 using ASZmod1 and station corrections in NonLinLoc (Mader et al., 2021). Topography is based on SRTM15+ (Tozer et al., 2019). (A.-O.: Albstadt-Onstmettingen, A.-Ta.: Albstadt-Tailfingen, A.-Tr.: Albstadt-Truchtelfingen, A.-M.: Albstadt-Margrethausen)

Richards (2014) to determine a relative magnitude for both, P and S phases separately, using the waveform of the corresponding recording channel (Z for P and E or N for S). This leads to a single relative magnitude for each phase and station combination for each event. The median of all single magnitude estimates per event is calculated to determine the overall relative magnitude of each event.

To analyze the stability of the relative event magnitude calculation and estimate its uncertainty range we analyze the difference of the median magnitude minus the single magnitudes. We determine the mean, median and the standard deviation of the difference between median and single magnitudes for different subsets. In these subsets we vary the allowed minimum magnitude (0.1, 0.3, 0.5, 0.7, 1 or 1.5) and the allowed number of single magnitudes (at least 3, 5 or 10) used for the median magnitude calculation. For all subsets we observe a similar mean and median of zero and a standard deviation σ of 0.1 magnitude units (Fig. C.3). This result demonstrates that the method is very stable for all our magnitude determinations and that it is independent of the number of used single magnitudes. Therefore, we determine also relative magnitudes based on only one single magnitude. We find 2σ to be a reasonable uncertainty estimate for our relative magnitudes as around 95% of our determinations lie within this range. To compare our relative magnitudes with the LED ML we determined the difference between both (Fig. C.4). To interpret this difference we have to consider all uncertainties of the magnitude values. The LED ML have a similar uncertainty range as our magnitudes of ±0.2 (Bulletin-Files des Landeserdbebendienstes B-W, 2011-2020). If we consider the uncertainty propagation, we can expect a maximum difference between both magnitudes of ±0.6 within the measurement accuracy. We observe a good agreement with the LED magnitudes as most of the calculated differences are within ±0.6 magnitude values (Fig. C.4). Only the Oct18 sequence contains a few events with differences greater than -0.6. For those events we control again the phase arrival times and waveforms, but we could not find an explanation for the bigger differences visible in Fig. C.4b.

In total we determine for 771 events a relative magnitude (Table 7.1). We are not able to determine a relative magnitude for all events due to our SNR criterion which is used to account for the noise sensitivity of the method.

7.4.6. Fault plane solutions

The source mechanisms of our master events are calculated with FOCMEC (Snoke, 2003) as described in Mader et al. (2021) based on P and SH polarities, as well as SH/P amplitude ratios (Table 7.3, Fig. 7.3, step 10, Fig. 7.4, Fig. 7.6 and Fig. C.5). The focal mechanisms of the 2018 time series are taken from Mader et al. (2021). We use the same quality assignment as in Mader et al. (2021) based on the width of the 5% to 95% percentile ranges of strike, dip and rake (δ strike, δ dip, δ rake, Table 7.3) for comparability purposes (see Mader et al., 2021, Table A2). In total we determined 19 fault plane solutions (Table 7.3).

Table 7.3.: Input data to FOCMEC and parameters of the resulting solutions. Values with (aux) refer to the assumed auxiliary fault plane. δ strike, δ dip and δ rake are the width of the 5% to 95% percentile range of strike, dip and rake and represent the uncertainty of the determined fault plane solution.

ID	time	ML	°N	°E	depth in km	P	SH	SH/P	strike in °	dip in °	rake in °	δ strike in °	δ dip in °	δ rake in °	strike (aux) in °	dip (aux) in °	rake (aux) in °	quality
sep19_1	2019-09-08T16:23	1.7	48.29	9.04	11.99	25	8	2	114	86	169	13.1	23.7	28	205	79	4	2
sep19_2	2019-09-08T17:46	1.1	48.27	9.05	12.10	16	8	0	116	80	174	21.0	18.0	69.0	207	84	10	4
sep19_3	2019-09-09T01:49	1.5	48.28	9.05	12.37	25	9	3	123	86	-177	4.2	5.1	33.4	33	87	-4	2
sep19_4	2019-09-10T07:00	1.1	48.28	9.04	12.96	12	5	1	291	59	160	14.3	27.1	25.1	32	73	33	2
sep19_5	2019-09-11T19:00	1.6	48.28	9.04	12.44	29	8	2	305	90	-180	4.5	4.5	0.4	35	90	0	0
sep19_6	2019-09-19T03:20	2.0	48.28	9.05	12.29	32	9	4	123	86	-176	5.0	10.1	22.0	33	86	-4	2
nov19_1	2019-11-04T01:00	3.8	48.24	9.01	4.82	35	6	1	17	80	-19	5.2	11.5	20.0	110	71	-169	2
nov19_2	2019-11-06T10:09	2.0	48.23	9.01	4.83	28	3	1	12	71	-42	8.1	16.1	38.1	118	51	-155	3
jan20_1	2020-01-27T03:48	2.1	48.29	8.98	11.40	26	4	1	127	79	-169	0.0	0.0	0.0	35	79	-11	0
jan20_2	2020-01-27T22:05	2.4	48.29	8.98	11.18	28	4	2	298	89	173	7.1	15.5	24.3	28	83	1	2
jan20_3	2020-01-27T22:05	3.5	48.29	8.98	10.89	32	5	0	297	80	174	6.9	17.4	18.1	28	84	10	1
mar20_1	2020-03-06T19:10	2.5	48.29	9.24	7.37	34	5	1	13	52	-27	1.6	7.0	7.2	120	69	-139	0
jun20_1	2020-06-18T22:41	2.5	48.23	9.09	7.40	30	4	0	2	79	-62	0.3	3.5	5.0	112	30	-158	0
aug20_1	2020-08-12T18:42	2.2	48.37	9.01	10.04	33	5	1	164	53	-65	0.0	0.0	0.0	306	44	-119	0
nov20_1	2020-11-17T07:20	2.1	48.12	8.98	6.40	27	7	2	186	76	0	3.6	16.1	45.9	96	90	166	3
dec20_1	2020-11-30T23:26	3.9	48.31	9.04	7.65	37	5	1	189	81	-1	0.5	5.7	8.4	279	89	-171	0
dec20_2	2020-12-01T01:59	2.0	48.31	9.04	8.04	26	2	1	195	85	4	5.6	16.8	37.3	105	86	175	3
dec20_3	2020-12-09T04:55	2.6	48.31	9.04	7.80	31	4	1	191	55	-4	2.3	18.2	9.6	283	87	-145	1
dec20_4	2020-12-25T15:10	2.4	48.31	9.04	7.63	31	2	1	18	50	6	7.5	24.9	17	284	85	140	2
Mader et al. (2021)																		
ev457	2018-02-10T12:44	2.3	48.33	8.95	12.41	27	3	2	290	82	-160	2.0	6.9	19.0	197	70	-9	1
ev514	2018-10-15T18:46	0.8	48.25	9.04	10.35	8	4	1	289	61	-65	23.3	15.5	31.6	65	38	-127	3
ev522	2018-10-15T19:37	1.3	48.25	9.04	10.00	17	4	3	341	76	-1	2.8	6.8	10.2	71	89	-166	1
ev525	2018-10-15T19:41	1.6	48.25	9.04	10.08	27	4	4	341	75	-4	3.8	8.0	12.0	72	86	-165	1
ev552	2018-10-17T03:02	1.0	48.25	9.04	10.38	14	4	2	338	57	-7	9.3	32.0	11.4	72	84	-147	3
ev554	2018-10-24T07:12	1.7	48.27	9.03	5.22	23	4	2	185	50	-17	5.2	14.8	0.6	286	77	-139	1
ev564	2018-11-25T02:22	1.4	48.25	9.04	10.20	25	3	2	344	53	-65	0.0	0.0	0.0	126	44	-119	0
ev565	2018-11-25T07:36	0.9	48.25	9.04	10.24	21	2	0	190	35	-84	32.3	40.1	12.2	3	55	-94	4
ev566	2018-11-25T10:25	0.9	48.25	9.04	10.22	13	5	1	323	50	-45	35.3	15.6	14.5	86	57	-130	3

7.4.7. Relative event location

Highly similar waveforms of the detected earthquakes within a time series indicate a possible common or similar fault plane and close-by hypocenter locations. To study this relationship, we use the double-difference earthquake location algorithm HypoDD (Waldhauser and Ellsworth, 2000, Fig. 7.3, step 11, Fig. 7.4). In this way we determine relative event locations for each of the 12 detected sequences with more than 10 events (six earthquake sequences, Table 7.1). We use both the relative phase times of the detection catalog (ct) and the relative phase times calculated with cross-correlation (cct) as combined input data set for HypoDD. For the ct we convert our uncertainty times into the weighting schema described in Table 7.4. Then we use the HypoDD code ph2dt to create the ct input file. The maximum hypocentral separation between two earthquakes was set to 10 km to ensure that all events within the catalog may be linked and all phase arrival times are accepted, independent of their pick weight. To become a neighboring event only event pairs with at least eight links are accepted and a maximum of 50 links per event pair are allowed to keep the double-difference problem in a solvable size for our computational power.

To create the cct input we determine a list of all possible event pairs. If the distance between an event pair is larger than 5 km we reject the event pair. The neighboring events are checked for similar phase arrival times per station. The cct is determined, if the median amplitude-squared coherence of the signal is greater than 0.5 in the frequency range between 1 - 20 Hz. P phases are correlated on the Z-component and S phases are compared on horizontal components (N, E). If the cct of the S phase on the two horizontal components is identical, the maximum of the estimated median amplitude-squared coherence is used. Otherwise, the mean of the cct and the mean of the median amplitude-squared coherence of the two components are saved. The median amplitude-squared coherence is used as a cct quality (Waldhauser and Ellsworth, 2000).

To check if the result depends on the different input data types (P or S, ct or cct), we calculate the relative event locations for different subsets, see Fig. 7.5, here exemplary the Sep19 sequence is displayed, for other sequences see Fig. C.6-C.10. We consider our solution as stable, if all subsets show similar hypocenter distibutions within around hundred meters. We always apply the conjugate gradient method (LSQR) to solve the double difference equations. To get an estimate of the relative uncertainty, we run the singular value decomposition (SVD) on the combined P and S phase ct and P and S phase cct input data sets if possible. For larger data sets (event sequences Sep19 and Jan20) we run the SVD on a smaller subset, due to our maximum computing power. The maximum relative location uncertainty estimate is 113 m horizontally and 242 m vertically (Table 7.5).
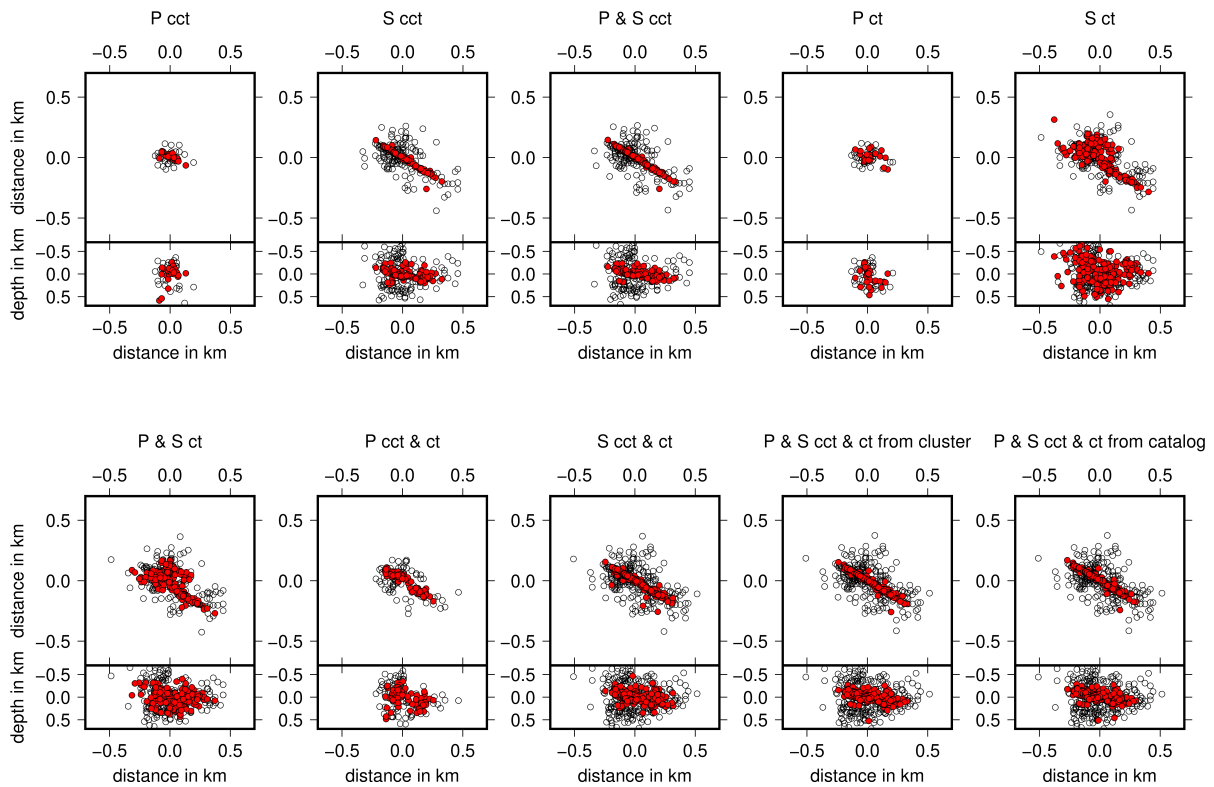
Figure 7.5.: Comparison of HypoDD performance with different data sets of the Sep19 earthquake sequence. Gray circles represent NLLoc hypocenter locations. Red filled circles show the result of HypoDD relative event locations. Titles represent the data set used (ct=catalog times, cct=cross-correlation times, from cluster or catalog represents the inversion starting point)). Hypocenter locations are always displayed in map view and corresponding West-East depth slice below.

Table 7.4.: Uncertainty of the catalog phase arrival times and corresponding weighting value for HypoDD ct input.

Uncertainty time range in s	weighting value
$uncertainty <= 0.025$	1
$0.025 < uncertainty <= 0.05$	0.5
$0.05 < uncertainty <= 0.1$	0.2
$0.1 < uncertainty <= 0.2$	0.1
$0.2 < uncertainty$	0

7.5. Results

7.5.1. Detection catalog

We analyzed 12 time series from 2018 to 2020 with striking seismic activity in the area of the ASZ using a template matching detection routine (Table 7.1). Six event catalogs of these time series are characterized by single main-shocks with only a few aftershocks (less than ten events, Table 7.1). The remaining six time series contain the already known earthquake

Table 7.5.: Uncertainty estimates of relative event locations in x (ex), y (ey) and z (ez) direction based on HypoDD SVD run.

ID	median ex in m	median ey in m	median ez in m	maximum ex in m	maximum ey in m	maximum ez in m
Feb18	13	9	39	51	30	84
Oct18	8	27	58	41	59	115
Sep19	7	23	47	29	26	60
Jan20	6	23	60	35	34	242
Nov20	6	6	17	17	11	33
Dec20	9	21	52	94	113	209

sequences from October to November 2018 and September 2019, as well as further earthquake sequences in February 2018 and in January, November, and December 2020 (Table 7.1). For all detected events we determined, if possible, hypocenter locations using NonLinLoc (Lomax et al., 2000) and a relative magnitude after Schaff and Richards (2014). By applying this procedure we have identified 1070 additional earthquakes to the LED event catalog. We were able to locate 840 earthquakes, from which 592 were classified as well located with a maximum location uncertainty of less than 2 km and at least six phase arrival times. In this way we added more than twice the number of well located events to the used LED event catalog for the analyzed time windows by applying the multi-station template matching detection approach in combination with the densified station network (Table 7.1, Fig. 7.3). Furthermore, we determined relative magnitudes ranging from -0.6 up to 1.2 for 489 earthquakes of the newly detected events (Table 7.1). With the newly detected events we complement the used LED event catalog for our 12 time series especially for earthquakes of small magnitude. The minimum magnitude ML in the used LED event catalog 2011 to 2020 is 0.0 (Bulletin-Files des Landeserdbebendienstes B-W, 2011-2020). Those numbers indicate that our strategy is successful and that it is possible to add well-located low-magnitude events to the LED event catalog using additional temporary recording stations and refined detection methods.

7.5.2. Fault characterisation

To analyze the active faults in detail we calculated 19 focal mechanisms using FOCMEC (Snoke, 2003) for the master events of the time series in 2019 and 2020 (Fig. 7.4). For the 2018 time series in February 2018 and October 2018, Mader et al. (2021) already determined nine focal mechanisms of the strongest events. To image the active fault plane we calculated relative event locations with HypoDD (Waldhauser and Ellsworth, 2000) for each time series with at least 10 earthquakes (Fig. 7.4, 7.5, 7.6). The main source mechanism of our events is strike-slip faulting and only a minor number of events show oblique or normal faulting (Fig. 7.4, Table 7.3).

7.5.2.1. NNE-SSW striking fault planes

We observe two event sequences in November and December 2020 (Nov20 and Dec20), which relative event locations are located at 5 - 10 km depths and indicate a nearly NNE-SSW striking, steep dipping fault plane (Fig. 7.6, 7.4, C.9, C.10). Together with the corresponding fault plane solutions we identify as source mechanism a sinistral strike-slip motion (Fig. 7.6, 7.4). The Dec20 sequence is located between the towns Albstadt-Onstmettingen and Jungingen, just north of the HZG in an area of continuous seismic activity. The Nov20 sequence is located about 6 km south of the town Meßstetten, about 20 km south of the HZG, in an area of reduced seismic activity (Fig. 7.4).

7.5.2.2. NW-SE striking fault planes

The relative event locations of earthquake sequences in February 2018, September 2019 and January 2020 (Feb18, Sep19, Jan20) outline steeply dipping NW-SE oriented fault planes which are nearly parallel to the strike of the HZG (Fig. 7.6). This is in good agreement with the dextral fault plane of the strike-slip focal mechanisms. The depth range of the three earthquake sequences is 11 - 15 km. The Feb18 and Sep19 sequences are located below the northern HZG boundary fault, with the Feb18 sequence close to the Hohenzollern Castle and the Sep19 sequence between the towns Albstadt-Onstmettingen and Hausen i. K.. The Jan20 sequence is located just south of the southern HZG boundary fault, NW of Albstadt-Onstmettingen.

7.5.2.3. NNW-SSE striking fault planes

During the event series from October to November 2018 we observe two separate earthquake sequences south of the HZG just east of Albstadt-Tailfingen and Albstadt-Truchtelfingen (Fig. 7.6, 7.7). The first earthquake sequence started on 15 October 2018 until end of October 2018 (Oct18-1, Fig. 7.8). The second, a smaller sub-sequence happened at the end of November 2018 (Oct18-2, Fig. 7.8). We first interpreted those two sequences as one sequence due to the temporal and spacial closeness. The analysis of all events with a similarity matrix highlights a slight difference between the events in October 2018 (Oct18-1) and November 2018 (Oct18-2) (Fig. C.11). This observation is also supported by fault plane solutions determined by Mader et al. (2021) changing from dominantly strike-slip in October 2018 to normal faulting in November 2018 (Fig. 7.6). Also, relative event locations indicate a clear NNW-SSE oriented fault plane for the Oct18-1 earthquake sequence, which corresponds to the sinistral stike-slip nodal plane of the focal mechanisms (Fig. 7.6). The relative event locations of Oct18-2 are located about 1 km to the south of Oct18-1 (Fig. 7.6, 7.7). The depth range of the two sequences is 9 - 12 km (Fig. 7.6).
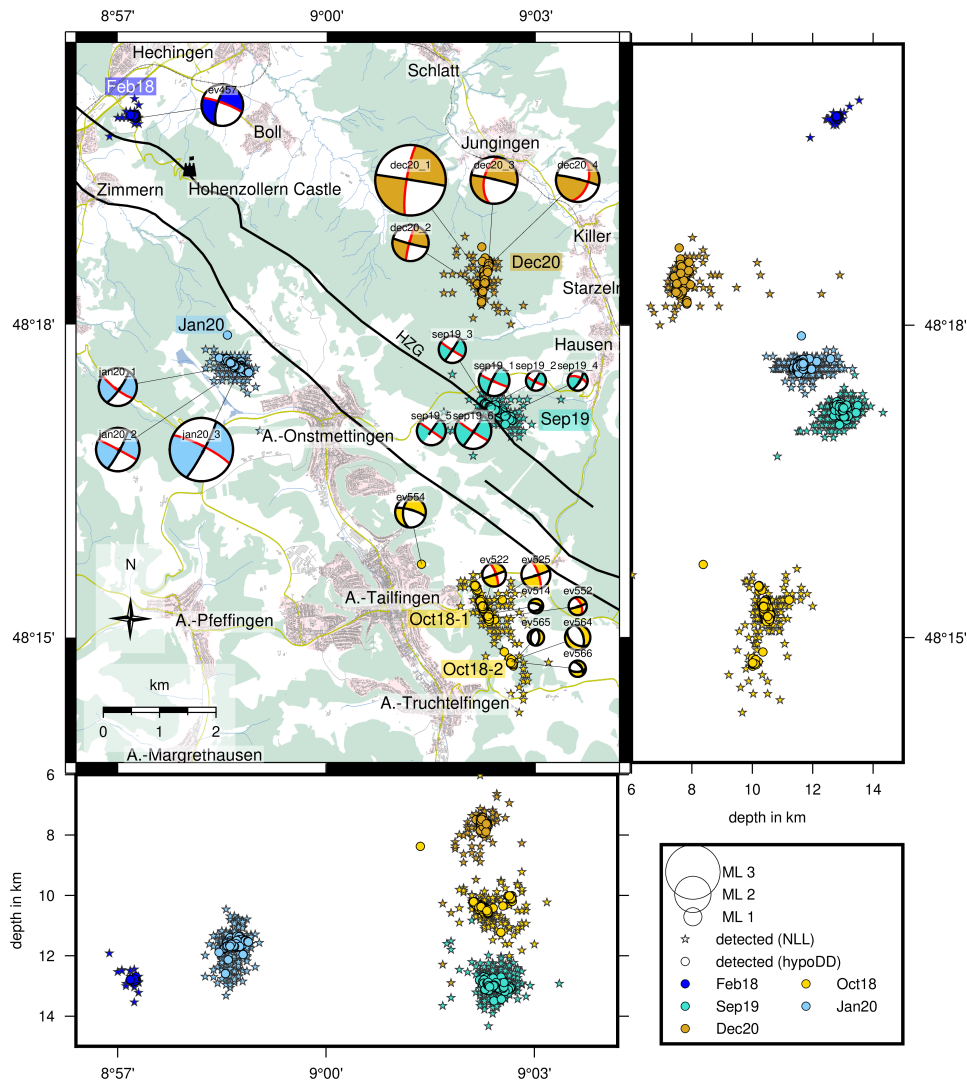
Figure 7.6.: HypoDD (circles) and NonLinLoc (stars, uncertainty < 2 km and at least 6 phase picks) hypocenter locations of the earthquake sequences Feb18, Oct18, Sep19, Jan20, and Dec20 and corresponding fault plane solutions (Feb18 and Oct18 fault plane solutions after Mader et al. (2021)). If known, the active fault plane is colored in red. Black lines indicate boundary faults of the Hohenzollerngraben (HZG, Regierungspräsidium Freiburg: Landesamt für Geologie, Rohstoffe und Bergbau (Hrsg.), 2019). Background map created with OpenStreetMap Data (2022, downloaded via geofabrik.de).

7.6. Discussion

7.6.1. Characterization of earthquake sequences

Earthquake sequences on the Swabian Alb are mostly related to fore- and aftershock sequences, whereas the observation of earthquake swarms was so far not described (e.g. Haessler et al., 1980; Turnovsky, 1981; Stange and Brüstle, 2005; Mader et al., 2021). To investigate, if our earthquake sequences with the most events (Oct18, Sep19, Jan20) are swarm-like or fore- and aftershock sequences we estimated the b-value of the magnitude-frequency distributions,
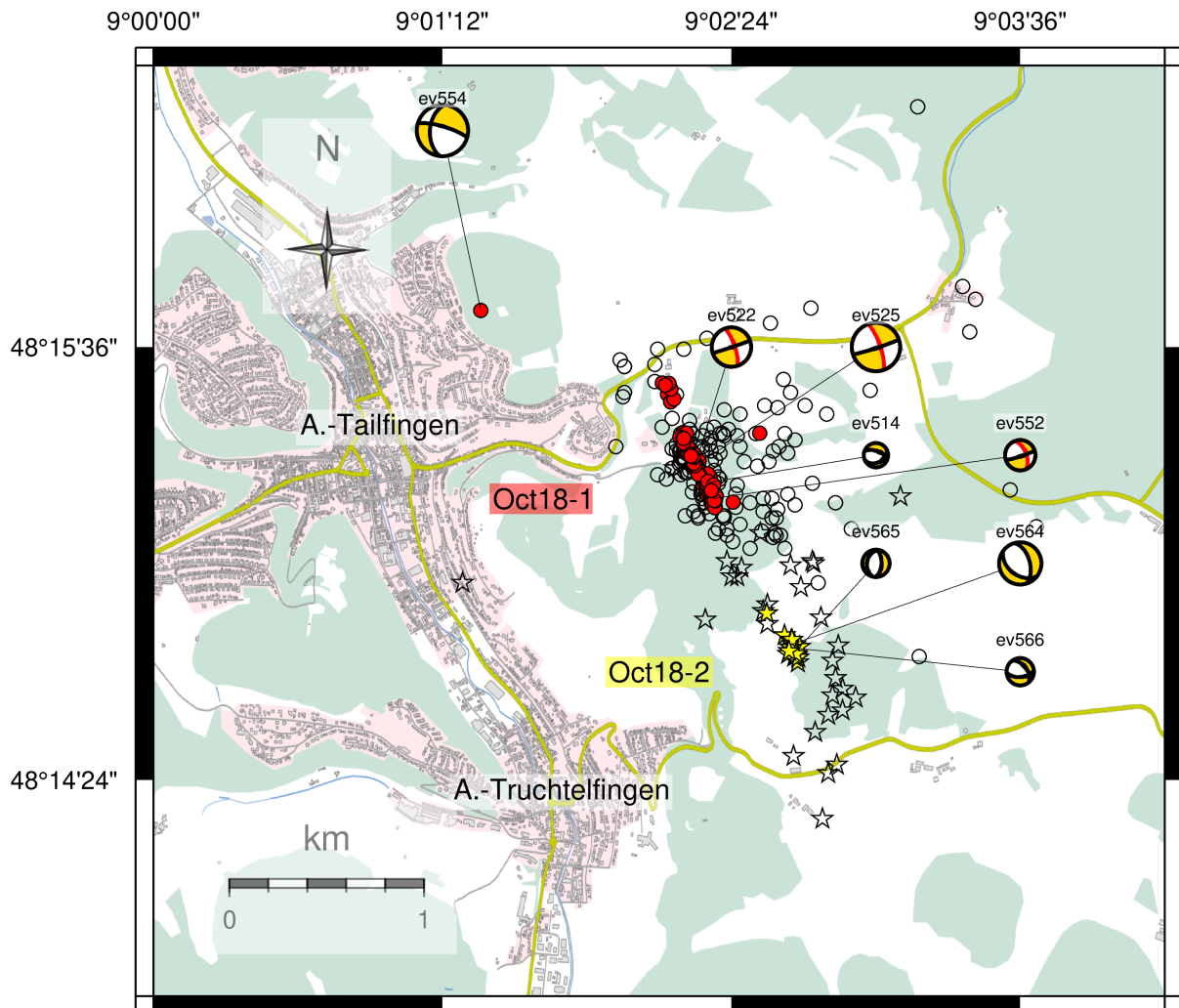
Figure 7.7.: The Oct18 earthquake sequence color-coded by time. Red filled circles (HypoDD hypocenter locations) and black circles (NLL hypocenter locations) represent earthquakes from October 2018 and yellow filled stars (HypoDD) and black stars (NLL) show events during November 2018. The color-coding by month highlights the temporal and spatial separation of the Oct18 sequence in two separate sequences: Oct18-1, Oct18-2.

considered the temporal evolution of the sequences and the magnitude distribution within the sequences (Fig. 7.8). The b-values of these three sequences are all close to 1, which is the typical b-value observed in tectonic regions (Fig. 7.8, Mogi, 1962; Frohlich and Davis, 1993). After Mogi (1963) we consider a sequence as earthquake swarm, if we observe a more gradual increase and decrease of event occurrences with time without a clear main shock. The main activity of the Jan20 sequence is focused during two days and the strongest event has a magnitude ML of 3.5, which is more than one magnitude stronger than the second strongest event with ML 2.4 of the sequence (Fig. 7.8e), f)). For this reason we identify the ML 3.5 earthquake as main shock of the Jan20 earthquake sequence and classify this sequence as a fore- and aftershock sequence with 287 foreshocks and 61 aftershocks.

The strongest event during the main activity of the Oct18-1 earthquake sequence is the magnitude 1.7 earthquake on the 15th October 2018 (Fig. 7.8a), b)). The magnitude difference
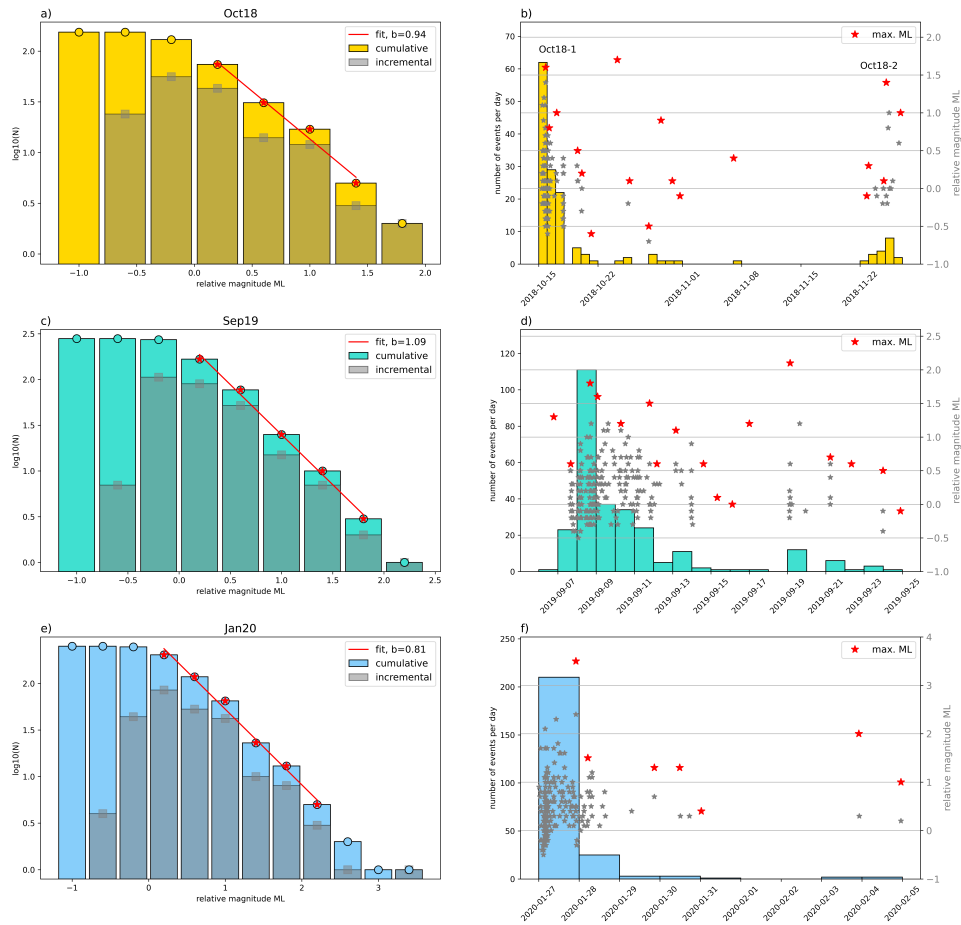
Figure 7.8.: Magnitude-frequency distributions (a,c,e) and temporal distributions of the events (b,d,f) of largest earthquake sequences (Oct18, Sep19, Jan20). Red lines give the b-value fit (a,c,e).

to other events is only 0.1 magnitude units, which is within the uncertainty range of ±0.2 of the magnitude estimation, so a clear main shock cannot be identified. The temporal distribution of the Oct18-1 sequence exhibits similarity to a fore- and aftershock sequence. Nevertheless, we classify the Oct18-1 sequence as a swarm-like activity due to the lack of a clearly identifiable main shock (Fig. 7.8a), b), Mogi, 1963).

We clearly observe a gradual increase and decrease of event occurrences with time during the Sep19 earthquake sequence, which is typical for an earthquake swarm (Fig. 7.8d), Mogi, 1963). The strongest events of the Sep19 sequence have magnitudes of 2.1, 1.8 and 1.6. As we do not observe a magnitude difference bigger than 0.3 between the strongest events and we observe no typical fore- and aftershock sequence distribution, a main shock is difficult to be defined. For this reason we consider the Sep19 earthquake sequence to be an earthquake swarm.

7.6.2. Fault characterisation

The analysis of the six earthquake sequences with more than 10 events (Feb18, Oct18, Sep19, Jan20, Nov20, Dec20) allows us to identify and image three different types of faults which were seismically active on the Swabian Alb during 2018 to 2020 (Fig. 7.4, 7.6, 7.9).

7.6.2.1. NNE-SSW striking fault planes

The first fault type observed by the Nov20 and Dec20 sequence is NNE-SSW striking sinistral strike-slip in a depth range of 5 - 10 km (Fig. 7.4). This fault mechanism is part of the ASZ (e.g. Haessler et al., 1980; Turnovsky, 1981; Stange and Brüstle, 2005). The Dec20 sequence is located between Jungingen and the northern graben boundary of the HZG in the area of continuous seismic activity (Fig. 7.4 and 7.6). The Nov20 sequence resolves the NNE-SSW striking active fault plane south of Meßstetten about 20 km south of the HZG in an area of reduced seismic activity (Fig. 7.4). This observation suggests an extension of the seismically active area of the ASZ further to the south as proposed by Mader et al. (2021). The reduced seismicity in the area south of Meßstetten may result from either an aseismic creeping component or a seismic gap caused by a locked fault plane, which was partially activated during the Nov20 sequence. The here observed fault planes related with the ASZ cover a depth extension of maximum 10 km. Due to previous studies we know that the seismicity related with the ASZ is located even deeper in the upper crust (about 1 - 18 km depth, Mader et al., 2021). The limited depth range of the here observed NNE-SSW sinistral strik-slip faults may be related with the short observation times of the two sequences from 2018 to 2020.

7.6.2.2. NW-SE striking fault planes

Second, we clearly observe dextral strike-slip faulting with a NW-SE strike, almost parallel to the HZG close to its near-surface boundary faults (Fig. 7.6, Feb18, Sep19, Jan20). This type of faulting was so far not directly observed in the area of the town Albstadt. Nevertheless, the stress inversion by Mader et al. (2021) already suggested the NW-SE striking fault plane of the event ev457 (Feb18 sequence, Fig. 7.6) as the most probable active fault plane to rupture in the current stress regime. However, due to the NS alignment of the seismicity in the area so far always the about NNE-SSW striking fault plane was expected to be the active one. The active faults of the Feb18, Sep19 and Jan20 earthquake sequences are located about parallel and close to the HZG boundary faults. We observe at least two very steep faults (~ 84° dip) outlined by the sequences, one close to the southern boundary fault and one along the northern boundary fault of the HZG. All three sequences are located at depths of 11 - 15 km, which is significantly below the estimated depth extension of 2 - 3 km of the boundary faults of the HZG (Schädel, 1976; Illies, 1982). A continuation of the HZG to greater depth is debated but not proven yet (Schädel, 1976; Illies, 1982). We suggest that our identified faults are not directly connected to the HZG. Instead, we propose an inherited zone of weakness in the area below the HZG which may facilitate the origin of the observed earthquakes. Thus, the earthquake sequences Feb18, Sep19, and Jan20 may be due to a activation of pre-existing faults in the upper crust

induced by the present stress field. This rupture mechanism is supported by the results of Mader et al. (2021) and Röckel et al. (2022) who suggest that fault planes with NW-SE strike are favorably aligned for rupture in the NNW-SSE directed maximum horizontal stress.

7.6.2.3. NNW-SSE striking fault plane

The Oct18-1 earthquake sequence is located in the area of major seismic activity of the ASZ near the town Albstadt and close to the southern graben boundary fault of the HZG (Fig. 7.6). The sinistral strike-slip fault plane strikes NNW-SSE and is therefore rotated westwards ($\sim 50°$) relative to the typical NNE-SSW fault orientation of the ASZ (Fig. 7.9, e.g. Haessler et al., 1980; Turnovsky, 1981; Stange and Brüstle, 2005) and it is also rotated eastwards ($\sim 40°$) relative to our newly observed NW-SE striking fault planes. The Oct18-2 sequence is offset from the Oct18-1 by about 1 km to the southeast and the fault plane solution points to a normal faulting mechanism, clearly different from the known strike-slip mechanisms of the ASZ (e.g. Haessler et al., 1980; Turnovsky, 1981; Stange and Brüstle, 2005). Both sequences, Oct18-1 and Oct18-2, are located in a depth range of 9 - 12 km, which places them above the 11 - 15 km deep NW-SE striking fault planes about parallel to the HZG and below the NNE-SSW striking fault plane of the ASZ observed here. The different rupture mechanism, including a normal faulting component, of the Oct18-1 and Oct18-2 sequences may be interpreted as a regionally confined stress accommodation between the displacement of the NNE-SSW striking ASZ and the deeper NW-SE oriented inherited zone of weakness.

7.6.3. Seismically active faults in the area of the ASZ

The analysis of the earthquake sequences in the years 2018 to 2020 reveals a complex faulting structure below the Swabian Alb close to the town Albstadt (Fig. 7.9). Reinecker and Schneider (2002) describe in their tectonic model the connection of the HZG and the ASZ. In this model the HZG is an en-echelon graben structure, which is a result of the partially decoupled, sinistral strike-slip movement of the ASZ. Seismic activity indicates that the ASZ is limited to the upper crust at about 1 - 18 km depth (Reinecker and Schneider, 2002; Mader et al., 2021). We here suggest an addition to the tectonic model of Reinecker and Schneider (2002) in the form of an about NW-SE striking dextral strike-slip fault system below the HZG in about 11 - 15 km depth, also located in the upper crust (Gajewski and Prodehl, 1985; Aichroth et al., 1992). A straight connection between the HZG and the NW-SE striking faults cannot be resolved because of the differences in depth between the observed seismically active faults and the depth projection of the boundary faults of the HZG (Schädel, 1976). At the intersection of the NNE-SSW striking ASZ and the NW-SE striking fault system, we suggest a heterogeneous deformation zone, which was active during the Oct-1 and Oct-2 earthquake sequences. In this way faults, which are not preferentially aligned in the stress field, may be activated in this deformation zone. Due to the limited study period of three years, further analysis is necessary to better verify or modify our proposed faulting model around the town Albstadt and the HZG. Such an improved model of the faulting styles and the possible maximum extensions of the
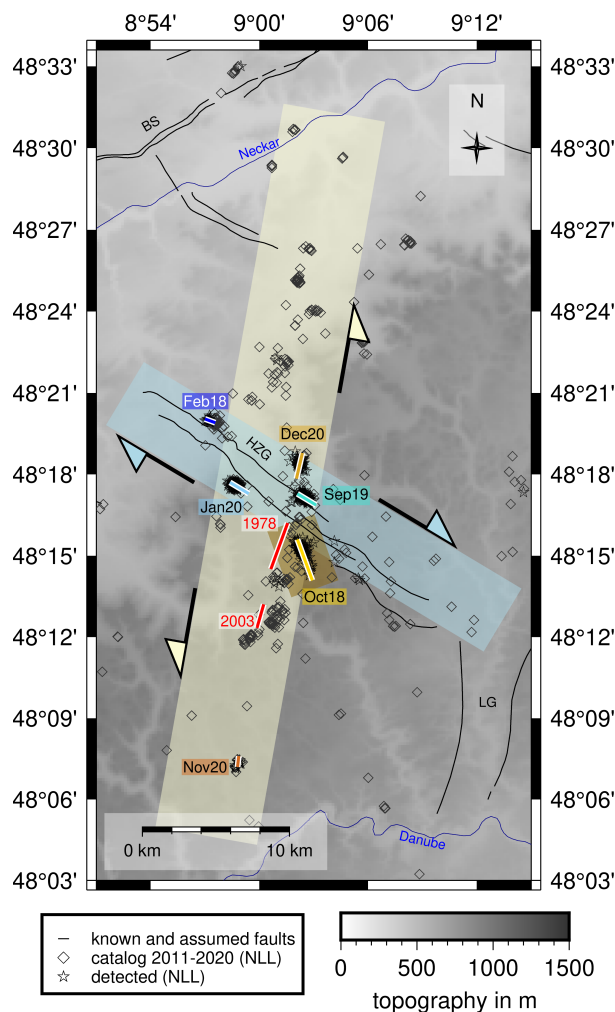
Figure 7.9.: New tectonic model of the Swabian Alb around Albstadt. Colored lines indicate active faults of earthquake sequences. Length is based on HypoDD hypocenter distribution. Red lines show rupture planes of the 1978 and 2003 earthquakes (after Stange and Brüstle, 2005). Blue (NW-SE dextral strike-slip) and yellow (ASZ) shaded areas represent the two active fault zones on the Swabian Alb. Arrows indicated the movement of the strike slip faults. NonLinLoc (stars, uncertainty < 2 km and at least 6 phase picks) hypocenter locations of detected events. Best located events (squares) from 2011 to 2018 of Mader et al. (2021) complemented with new located events in 2019 to 2020 using ASZmod1 and station corrections in NonLinLoc (Mader et al., 2021). Topography is based on SRTM15+ (Tozer et al., 2019).

involved faulting segments could also help to better determine the seismic hazard potential and prepare for future ground shaking.

7.7. Conclusion

We analyze 12 time series with earthquakes in the area of the Swabian Alb using a multi-station template matching approach. This allows us to complement the official LED catalog with 1070 additional earthquakes, 592 of which are well located. Furthermore, we determine a relative

event magnitude for 489 earthquakes, with the smallest event magnitude being -0.6. The observed earthquake sequences can be separated into fore- and aftershock sequences as well as earthquake swarms. The latter type was so far not observed on the Swabian Alb. Relative event locations and fault plane solutions of the six major earthquake sequences allow us to image three different seismically active fault sets below the Swabian Alb near Albstadt. This complex fault structure consists not only of the typically known NNE-SSW striking sinistral ASZ, but also NW-SE striking dextral fault planes parallel to the HZG and NNW-SSE striking sinistral fault planes with a normal faulting component. As a result, we introduce an addition to the tectonic model of Reinecker and Schneider (2002) by an 11 - 15 km deep NW-SE striking dextral fault zone below the HZG. This fault zone may be placed in the crystalline basement which acts as a zone of mechanical weakness and is driven by the tectonic stress field (of the Alpine orogeny). At the intersection of the newly identified NW-SE striking fault zone and the ASZ very complex faulting is observed. Furthermore, the depth of the NW-SE striking fault planes may be restricted to a certain depth range, which should be analyzed in future work, as we only investigated a three years time span. A straight connection of the HZG to the NW-SE striking dextral fault planes is unlikely as their depth ranges do not overlap. However, NW-SE zones of weakness in the upper crust may assist the development of the NW-SE oriented shallow grabens in the region (Reinecker and Schneider, 2002).

8. Summary

In this thesis I analyze the seismic activity of the ASZ to get a better understanding of the faulting properties and the related stress field. First, I installed additional seismic stations to densify the seismic network in the research area (see chapter 5). The additional seismic stations help to address the research aims by improving the accuracy of the event locations and the detection of small magnitude events (Mader and Ritter, 2021; Mader et al., 2021). Second, I analyze the continuous micro-seismic activity of the ASZ from 2011 - 2018 to get a better idea of the fault structure and faulting processes, as well as the related stress field (see chapter 6, Mader et al., 2021). Finally, I focus on earthquake sequences in 2018 to 2020 to find and image the active fault planes in the area of the ASZ (see chapter 7). In the following I shortly summarize the main results of this thesis, answer the research questions and give an outlook to further studies.

I densified the seismic station network in the area of the ASZ with five additional seismic recording stations within the StressTransfer seismic project (Mader and Ritter, 2021). The five site locations were selected in order to address the research aims. Three seismic stations are located in the area of continuous seismic activity crossing the HZG and oblique to the ASZ. The remaining two are located along strike of the ASZ to the north and south to help identify the termination of the ASZ, which is still under debate (Reinecker and Schneider, 2002; Stange and Brüstle, 2005). The quality control of the seismic station recordings in the area of the ASZ indicates that a good data quality is achieved, allowing to address the research aims. Due to the SARS-CoV-2 crisis the detection of low-magnitude events may be enhanced as I observe a reduction of noise at the StressTransfer seismic stations of about 20% - 30%. The StressTransfer seismic stations are still recording, allowing to continue the study of the currently increased seismic activity of the ASZ since 2019. I refer to a currently increased seismic activity since 2019 as the LED reported nine earthquakes with a ML $\geq$ 3.0 in 2019 to 2023, whereas in the LED event catalog from 2011 to 2018 only three events are listed with a ML $\geq$ 3.0 (Bulletin-Files des Landeserdbebendienstes B-W, 2011-2020; Regierungspräsidium Freiburg: Landesamt für Geologie, Rohstoffe und Bergbau, 2023).

At the additional seismic stations of the densified seismic station network due to the AlpArray (Hetényi et al., 2018) and the StressTransfer seismic projects (Mader and Ritter, 2021), I determine the direct P and SH phase arrival times and polarities for the events in the LED event catalog from 2016 to 2018 in the area of the ASZ. The observation at the additional seismic stations not only increases the number of the observations but also reduces the azimuthal GAP for the events. By inverting a high quality subset of the complemented LED event catalog from 2011 to 2018 I determine the robust and simple minimum 1D seismic v_p and v_s velocity model ASZmod1 with station delay times. The station delay times reflect the lateral depth variation of the crystalline basement in the upper crust of Baden-Württemberg (Rupf

and Nitsch, 2008). I relocated the complemented LED event catalog from 2011 to 2018 with ASZmod1. The uncertainty estimate of the event location decreases from 2016 on, due to the increased number of phase arrival time observations per event and seismic stations.

The densified seismic station network enhanced the ability to locate and detect small magnitude events. With an automatic multi-station template matching detection routine I detected 1070 additional events for 12 analyzed time series from 2018 to 2020, so far not listed in the LED event catalog. 592 of those events were well located, with location uncertainties ≤ 2 km and at least six phase arrival times. If possible a relative event magnitude was determined, with the smallest magnitude being -0.6. During six time series I identified earthquake sequences with up to 590 events within a month duration. The earthquake sequences could be classified as either fore- and aftershock sequence or earthquake swarm, the latter so far not observed in the area of the ASZ. In the following I come back to the questions raised in chapter 1.

What are the fault characteristics of the ASZ?:

- **What are the vertical and horizontal extensions of the ASZ?**
  The relocated continuous seismicity outlines a N-S oriented fault zone at around 9°E and the main focus is between the towns Albstadt and Tübingen on the Swabian Alb. The analysis of the earthquake sequence Nov20 suggests a continuation of the ASZ at least about 10 km to the south of Albstadt, as the relative event locations in combination with the fault plane solutions identify NNE-SSW striking sinistral strike-slip faulting, which is the typical faulting mechanism of the ASZ. Nevertheless, this is an area with sparse seismic activity. A continuation further to the north and south could not be verified, as only few and also scattered seismicity is observed. The depth range of the ASZ is between 1 - 18 km ± 2 km, focused on the upper crust.

- **Is the ASZ one fault or are there several fault zones or a segmentation? If there are several faults, how are they connected?**
  The imaged fault structure of the ASZ is complex and spatial clustering of the events may hint at separate fault planes. Examples for separate clusters are the shallow cluster C1 close to Albstadt and the deeper cluster C4 close to Hechingen (Fig. 6.7, 6.10, 6.11). Both are located to the west relative to the mainly N-S oriented seismicity.
  The majority of the fault plane solutions are strike-slip faulting mechanisms, hinting with the N-S aligned seismicity at sinistral strike-slip faulting (Fig. 6.7). This observation is confirmed by three earthquake sequences (Oct18-1, Nov20, Dec20), outlining a NNE-SSW striking fault plane, as well as a NNW-SSE striking fault plane (Fig. 7.4, 7.6). Nevertheless, the other three detected earthquake sequences (Feb18, Sep19, Jan20) outline NW-SE striking dextral fault planes (Fig. 7.6). The location of the Feb18 earthquake sequence location coincides with the cluster C4. Furthermore, normal faulting is observed, which was so far not described at the ASZ.
  I observe at least three different fault zones (Fig. 7.9). A NNE-SSW striking sinistral strike-slip fault zone outlined by the continuous seismicity and the Nov20 and Dec20 earthquake sequences, which is in agreement with previous studies related with the ASZ. Additionally, I observe at 11 - 15 km depth a NW-SE striking dextral strike-slip fault zone

(Feb18, Sep19, Jan20), consisting of at least two almost parallel active faults. The depth range is based on the current observations of the three earthquake sequences and it may change with further observations and analyses. The third fault zone is located in 9 - 12 km depth and shows NNW-SSE striking sinistral strike-slip faulting (Oct18-1), as well as normal faulting components (Oct18-2). The third fault zone exists at the intersection of the NNE-SSW striking ASZ and the NW-SE striking deeper fault zone. The interaction of the two differently oriented fault zones may facilitate the complex faulting observed at the NNW-SSE striking fault zone.

Is there a relationship to the graben structures like the HZG? The newly discovered NW-SE striking fault zone is oriented almost parallel to the HZG and the related earthquake sequences (Feb18/cluster C4, Sep19, Jan20) are located close to the HZG graben boundary faults. A direct connection to the HZG is considered unlikely due to the depth difference and the steep dipping fault planes observed. Nevertheless, the development of the HZG may be facilitated by a zone of weakness in the upper crust leading to the coinciding location and strike of graben structure and seismicity.

How is the local stress field oriented and is there a change in the stress field with depth? By inverting the fault plane solutions of events in the area of the ASZ I determine the directions of the local stress field. The maximum horizontal compression $S_{H_{max}}$ has a NNW-SSW trend (140-149°) and is in good agreement with other studies. A change of the stress field with depth is observed, as the inversion of all fault plane solutions hinders the differentiation between σ_1 and σ_2 (Fig. 6.8). In the upper part of the upper crust $S_{H_{max}}$ exceeds S_V, below about 7-8 km depth S_V becomes the dominating stress component. The change of the stress field with depth may be due to a change in rock rheology or due to the increasing thickness of the overlying rocks, but this needs to be studied with more data.

What mechanisms and related stresses drive the intra-plate seismicity at the ASZ in the northern Alpine foreland? The determined local maximum stress direction $S_{H_{max}}$ is in good agreement with other studies, analyzing the stress field in Southwestern Germany as well as Central Europe (Müller et al., 1992; Heidbach et al., 2016). As dominating driving force of the local regional stress field the plate driving forces and the Alpine topography are identified (Müller et al., 1992; Heidbach et al., 2010a, 2016). The described NNE-SSW and NW-SE striking fault zones are favorably aligned in the current stress field facilitating the rupture process (Röckel et al., 2022). This is similarly observed at the New Madrid seismic fault zone, where also several different fault zones are activated (Zoback and Zoback, 1981). Not favorably aligned faulting like during the Oct18 earthquake sequence may occur due to the intersection of the NNE-SSW and NW-SE striking fault zones and a related stress change or strongly fractured rock (weakening zone). The fault intersection itself may also act as stress concentrator facilitating the occurrence of the seismicity in the area, like also observed in the Potiguar Basin in Brazil (Talwani, 1988; Fonsêca et al., 2021).

The location of the seismic activity of the ASZ on the Swabian Alb may be due to a weakening zone in the crust. Ring and Bolhar (2020) and Geyer and Gwinner (2011) find a correlation

of the location of the N-S striking ASZ with the boundary between a Triassic-Jurassic swell and basin structure (the Spaichingen High and the Mid Swabian Basin). This observation suggests that the ASZ may be a pre-existing structure or weakening zone, now activated in the current stress field. The comparison with the previously described models for intra-plate seismicity shows a good agreement with the activation of weakening zones or pre-existing fault structures favorably aligned in the stress field (Sykes and Sbar, 1973; Johnston and Kanter, 1990; Talwani, 2017). Furthermore, an analysis by Spooner et al. (2022) revealed a correlation between crustal strength and the location of seismicity in the northern Alpine foreland. The correlation is visible in the focusing of the seismicity at weakening zones within the crust like the URG. The NW-SE oriented fault zone is also assumed to be a weakening zone in the crust which enabled not only the observed seismicity but also the formation of the HZG at this location.

A comparable area where also seismicity in the foreland of a orogeny can be observed along existing fault zones or fracture zones is for example in the Himalayan foreland of North India. Here intra-plate seismicity is for example observed along the Kopili fault (Dey et al., 2022) or the Delhi Seismic Zone (Manglik et al., 2023). Here also existing fault zones are activated within the stress field dominated by the plate boundary forces and the ongoing plate collision and related orogeny (Dey et al., 2022; Manglik et al., 2023). However, in comparison with other intra-plate seismicity I observe a focusing of the seismicity of the ASZ to a much smaller area (lateral extension of 30 - 40 km). In comparison the intra-plate seismicity in the northeast of India occurs along the around 300 km long Kopili fault (Dey et al., 2022) or in the United States along the over 100 km long New Madrid seismic zone (Csontos and Van Arsdale, 2008).

The here presented results all need to be considered with respect to their related uncertainties. All events are located within a minimum 1D seismic velocity model, whereas the structure of the crust is most likely much more complicated (dipping layers, strong lateral variations). The station delay times account for some of those lateral variations, like here shown especially for the lateral depth variation of the crystalline basement. The used relocation algorithm NLL allows to include the final rms of the velocity model as uncertainty. Nevertheless, the rms hardly represents a true error. Other uncertainties included by NLL to determine an uncertainty are the phase arrival time uncertainties listed in the event catalog. Furthermore, the used calculation for hypocenter and uncertainty estimation has an influence. The resulting uncertainties of NLL based on the calculation with the L2 likelihood function differ, for example if one uses the equal differential time likelihood function (EDT) based calculation of NLL instead (see chapter 6, Fig. 6.5, B.4). The comparison indicates similar hypocenter location, but using EDT the uncertainties are for some events very large and unrealistic. This highlights that only relative uncertainties are determined to indicate a quality of the result. In this thesis I considered events of the complemented LED event catalog as well located if the lateral uncertainty is less than 1 km and the vertical uncertainty is less than 2 km (for detected events all uncertainties less than 2 km). Furthermore, the azimuthal gap needs to be smaller than 180° and an event has more than eight phase arrival times (for detected events at least six phase arrival times). The effect of a better station coverage and a larger number of observations per event can be observed by the reduced uncertainties after 2016 for the event locations due to the denisfied seismic station network (see chapter 6, Fig.

6.5, B.4). The relative event locations may overcome the uncertainties due to an incorrect seismic velocity model, also the absolute error of the whole relocated sequence stays the same. If I observe an earthquake sequence in a depth of 9-12 km the vertical extension of the earthquake sequence of 3 km is precisely determined ± some hundred meters (uncertainty of the relative event locations), whereas for the absolute location applies 9-12 km $\pm 2km$. The determined fault plane solutions also depend on the angles determined from the hypocenter locations. Nevertheless, I would consider the resulting solutions as reliable, as small variations in hypocenter location do not change the angles significantly. Furthermore, by comparing the results of different runs (unity weighting, relative weighting, allowance of more wrong polarities, see chapter 6) the result is very stable. The same applies for the stress inversion, where a maximum error for the strike, dip and rake angles can be included. The error is used to apply random noise to the input data.

The analysis of the continuous seismic activity revealed a new model for the rupture processes in the area of the ASZ. Nevertheless, not all research questions could be fully answered. Future work may further address the segmentation of the ASZ and the NW-SE oriented fault zone by applying the template matching routine to the whole time span from 2019 to 2022, when all seismic stations of the densified station network were recording (StressTransfer and AlpArray). Recording of the AlpArray seismic stations ended in 2022 (Hetényi et al., 2018; AlpArray Seismic Network (AASN), 2015). After event detection, relative event locations of the whole catalog may help to identify possible fault segmentations. If a clear segmentation of the ASZ is identified, the maximum expected magnitude based on the fault length could be estimated (Wells and Coppersmith, 1994). Furthermore, the analysis of the continuous seismic activity may also help to constrain the depth range of the newly detected NW-SE striking fault zone in greater detail.

Similar analysis like in this thesis may be conducted for the areas of the German Molasse Basin around the town Bad Saulgau and the Upper Rhine Graben, where also a densified seismic station network due to the StressTransfer (Mader and Ritter, 2021) and the AlpArray seismic network (Hetényi et al., 2018) existed from 2018 to 2021. Additional inversion for the stress field in those areas may allow a better understanding of the stress transfer from the Alpine collision into the northern Alpine foreland.

Acknowledgments

Funding

Bibliography

B. Aichroth, C. Prodehl, and H. Thybo. Crustal structure along the central segment of the EGT from seismic-refraction studies. *Tectonophysics*, 207(1-2):43–64, 1992.

K. Aki and P. G. Richards. *Quantitative Seismology: Theory and Methods*. University Science Books Sausalito, California, 2002. San Francisco, CA, Second Edition, 1, 558pp.

A. Akinci, J. Mejia, and A. L. Jemberie. Attenuative dispersion of P waves and crustal Q in Turkey and Germany. *Pure and Applied Geophysics*, 161:73–91, 2004.

AlpArray Seismic Network (AASN). AlpArray Seismic Network (AASN) temporary component, 2015. AlpArray Working Group, doi: `https://doi.org/10.12686/alparray/z3_2015`.

C. Amante and B. W. Eakins. ETOPO1 arc-minute global relief model: procedures, data sources and analysis, 2009. National Oceanic and Atmospheric Administration (NOAA) Technical Memorandum NESDIS NGDC-24, National Geophysical Data Center, Boulder, Colorado, 19 pp.

J. Angelier. Determination of the mean principal directions of stresses for a given fault population. *Tectonophysics*, 56(3-4):T17–T26, 1979.

K. Asch. IGME 5000 : 1 : 5 Million International Geological Map of Europe and Adjacent Areas - final version for the internet, 2005. BGR, Hannover, 1 map [data set], `https://www.bgr.bund.de/EN/Themen/Sammlungen-Grundlagen/GG_geol_Info/Karten/Europa/IGME5000/IGME_Project/IGME_Downloads.html?nn=1556388`.

G. H. Bachmann, M. Müller, and K. Weggen. Evolution of the molasse basin (Germany, Switzerland). *Tectonophysics*, 137:77–92, 1987.

A. Barth, J. R. R. Ritter, and W. F. Spatalvariations of earthquake occurrence and coseismic deformation in the Upper Rhine graben, central Europe. *Tectonophysics*, 651/652:172–185, 2015.

H. Baumann and A. Becker. Lokale Variation regionaler Spannungsfelder an zwei Beispielen aus SW-Deutschland und der Schweiz. In *ISRM International Symposium*. OnePetro, 1986.

A. Becker. An attempt to define a "neotectonic period" for central and northern Europe. *Geologische Rundschau*, 82:67–83, 1993.

M. Beyreuther, R. Barsch, L. Krischer, T. Megies, Y. Behr, and J. Wassermann. ObsPy: A Python toolbox for seismology. *Seismological Research Letters*, 81(3):530–533, 2010a.

M. Beyreuther, R. Barsch, L. Krischer, T. Megies, Y. Behr, and J. Wassermann. ObsPy: A Python toolbox for seismology [data set], 2010b. available at: `https://github.com/obspy/obspy/wiki` (last access:30 September 2020),.

P. Bird. An updated digital model of plate boundaries. *Geochemistry, Geophysics, Geosystems*, 4(3), 2003.

Black Forest Observatory (BFO). Black Forest Observatory data, 1971. GFZ Data Services, doi: `10.5880/BFO`.

K.-P. Bonjer. Seismicity pattern and style of seismic faulting at the eastern borderfault of the southern Rhine Graben. *Tectonophysics*, 275(1-3):41–69, 1997.

K.-P. Bonjer, C. Gelbke, B. Gilg, D. Rouland, D. Mayer-Rosa, and B. Massinon. Seismicity and dynamics of the Upper Rhinegraben. *J. Geophys.*, 55:1–22, 1984.

M. H. P. Bott. The mechanics of oblique slip faulting. *Geological magazine*, 96(2):109–117, 1959.

J. R. Bowman, G. Gibson, and T. Jones. Aftershocks of the 1988 January 22 Tennant Creek, Australia intraplate earthquakes: Evidence for a complex thrust-fault geometry. *Geophysical Journal International*, 100(1):87–97, 1990.

A. Brisbourne, J. Clinton, G. Hetényi, D. Pesaresi, C. Aubert, G. Bokelmann, K. Csicsay, Z. Gráczer, C. Haberland, and e. a. D. Hawthorn. Technical strategy for the mobile seismological components of AlpArray-Recommendations of the AlpArray Working Group 1 procedures and data management, 2013. available at `http://www.alparray.ethz.ch/export/sites/alparray/.galleries/dwn-experimentsAlpArray_TechnicalStrategy.pdf_2063069299.pdf` (last accessed January 2021).

Bulletin-Files des Landeserdbebendienstes B-W. Ref. 98 im Landesamt für Geologie, Rohstoffe und Bergbau im Regierungspräsidium Freiburg, Az478418_3303, 2011-2020.

Bundesanstalt für Geowissenschaften und Rohstoffe (BGR). Deutscher Erdbebenkatalog, 2012. Hannover, downloaded from: `https://geoportal.bgr.de/mapapps/resources/apps/geoportal/index.html?lang=de#/datasets/portal/572FF5BD-EA1A-4BE4-9C7C-9F9CF6EC351B` (last access: 7 October 2023).

C. J. Chamberlain, C. J. Hopp, C. M. Boese, E. Warren-Smith, D. Chambers, S. X. Chu, K. Michailos, and J. Townend. EQcorrscan: Repeating and near-repeating earthquake detection and analysis in Python. *Seismological Research Letters*, 89(1):173–181, 2018.

H. P. Crotwell, T. J. Owens, and J. Ritsema. The TauP Toolkit: Flexible seismic travel-time and ray-path utilities. *Seismological Research Letters*, 70(2):154–160, 1999.

R. Csontos and R. Van Arsdale. New Madrid seismic zone fault geometry. *Geosphere*, 4(5): 802–813, 2008.

C. Dey, S. Baruah, M. F. Abdelwahed, S. Saikia, N. Molia, P. Borthakur, T. Chetia, B. Bharali, N. Dutta, M. K. Phukan, A. Paul, Saitlunga, D. Hazarika, and J. R. Kayal. The 28 April 2021 Kopili Fault Earthquake (Mw 6.1) in Assam Valley of North East India: Seismotectonic Appraisal. *Pure and Applied Geophysics*, 179(6-7):2167–2182, 2022.

T. Diehl, E. Kissling, and P. Bormann. Tutorial for consistent phase picking at local to regional distances. In P. Bormann, editor, *New Manual of Seismological Observatory Practice 2 (NMSOP-2)*, pages 1–21. Potsdam: Deutsches GeoForschungsZentrum GFZ, 2012.

T. Diehl, J. Singer, G. Hetényi, D. Grujic, J. Clinton, D. Giardini, E. Kissling, and GANSSER Working Group. Seismotectonics of Bhutan: Evidence for segmentation of the Eastern Himalayas and link to foreland deformation. *Earth and Planetary Science Letters*, 471:54–64, 2017.

J. B. Edel, K. Fuchs, C. Gelbke, and C. Prodehl. Deep structure of the southern Rhinegraben area from seismic refraction investigations. *J. Geophys.*, 41:333–356, 1975.

Erdbebendienst Südwest Baden-Württemberg and Rheinland-Pfalz. Erdbebendienst Südwest [Data set], 2009. doi: `https://doi.org/10.7914/SN/LE`.

D. Fäh, M. Gisler, B. Jaggi, P. Käastli, T. Lutz, V. Masciadri, V. Matt, D. Mayer-Rosa, D. Rippmann, G. Schwarz-Zanetti, and et al. The 1356 Basel earthquake: An interdisciplinary revision. *Geophys. J. Int.*, 178:351–374, 2009.

Federal Institute for Geosciences and Natural Resources (BGR). German Regional Seismic Network (GRSN), 1976. Federal Institute for Geosciences and Natural Resources (BGR), doi: `10.25928/mbx6-hr74`.

J. Fonsêca, J. Ferreira, A. do Nascimento, F. Bezerra, H. L. Neto, and E. de Menezes. Intraplate earthquakes in the Potiguar Basin, Brazil: Evidence for superposition of local and regional stresses and implications for moderate-size earthquake occurrence. *Journal of South American Earth Sciences*, 110:103370, 2021.

C. Frohlich and S. D. Davis. Teleseismic b values; or, much ado about 1.0. *Journal of Geophysical Research: Solid Earth*, 98(B1):631–644, 1993.

D. Gajewski and C. Prodehl. Crustal structure beneath the Swabian Jura, SW Germany, from seismic refraction investigations. *Journal of Geophysics*, 56(2):69–80, 1985.

D. Gajewski, W. Holbrook, and C. Prodehl. A three-dimensional crustal model of southwest Germany derived from seismic refraction data. *Tectonophysics*, 142:49–70, 1987.

GEOFON Data Centre. GEOFON Seismic Network, 1993. Deutsches GeoForschungsZentrum GFZ, doi: `10.14470/TR560404`.

J. W. Gephart and D. W. Forsyth. An improved method for determining the regional stress tensor using earthquake focal mechanism data: application to the San Fernando earthquake sequence. *Journal of Geophysical Research: Solid Earth*, 89(B11):9305–9320, 1984.

O. F. Geyer and M. P. Gwinner. *Geologie von Baden-Württemberg*. Schweitzerbart, Stuttgart, Germany, 2011. Fifth Revised Edition.

F. Gräber. Lokalbebentomographie mit P-Wellen in Long Valley, Kalifornien, und die Möglichkeiten einer Anwendung im südlichen Rheingraben, 1993. Diplomarbeit (diploma thesis), Geophysical Institute, TU Karlsruhe, Germany and Institute of Geophysics, ETH Zürich, Switzerland, 144 pp.

J. C. Grimmer, J. R. R. Ritter, G. H. Eisbacher, and W. Fielitz. The Late Variscan control on the location and asymmetry of the Upper Rhine Graben. *International Journal of Earth Sciences (Geologische Rundschau)*, 106(3):827–853, 2017.

J. C. Groos and J. R. R. Ritter. Time domain classification and quantification of seismic noise in an urban environment. *Geophys. J. Int.*, 179(2):1213–1231, 2009.

J. C. Groos and J. R. R. Ritter. Seismic noise: A challenge and opportunity for seismological monitoring in densely populated areas. *Proc. of the Workshop: Induced Seismicity, Cahiers du Centre Européen de Géodynamique et de Séismologie*, 30:87–97, 2010.

G. Grünthal and the Global Seismic Hazard Assessment Program (GSHAP) Region 3 Working Group. Time domain classification and quantification of seismic noise in an urban environment. *Anali di Geofisica*, 42(6):999–1011, 1999.

G. Grünthal, D. Stromeyer, C. Bosse, F. Cotton, and D. Bindi. The probabilistic seismic hazard assessment of Germany-version 2016, considering the range of epistemic uncertainties and aleatory variability. *Bulletin of Earthquake Engineering*, 16:4339–4395, 2018.

H. Haessler, P. Hoang-Trong, R. Schick, G. Schneider, and K. Strobach. The September 3, 1978, Swabian Jura earthquake. *Tectonophysics*, 68:1–14, 1980.

O. Heidbach, J. Reinecker, M. Tingay, B. Müller, B. Sperner, K. Fuchs, and F. Wenzel. Plate boundary forces are not enough: Second-and third-order stress patterns highlighted in the World Stress Map database. *Tectonics*, 26(6), 2007.

O. Heidbach, M. Tingay, A. Barth, J. Reinecker, D. Kurfeß, and B. Müller. Global crustal stress pattern based on the World Stress Map database release 2008. *Tectonophysics*, 482:3–15, 2010a.

O. Heidbach, M. Tingay, A. Barth, J. Reinecker, D. Kurfeß, and B. Müller. Global crustal stress pattern based on the World Stress Map database release 2008. *Tectonophysics*, 482(1-4):3–15, 2010b.

O. Heidbach, M. Rajabi, K. Reiter, M. Ziegler, and W. Team. World Stress Map Database Release 2016, V. 1.1, 2016. GFZ Data Services, `https://doi.org/10.5880/WSM.2016.001`.

G. Hetényi, I. Molinari, J. Clinton, G. Bokelmann, I. Bondár, W. C. Crawford, J.-X. Dessa, C. Doubre, W. Friederich, F. Fuchs, and et al. The AlpArray Seismic Network - a large scale European experiment to image the Alpine orogen. *Surveys in Geophysics*, 39:1009–1033, 2018.

W. Hiller. Eine Erdbebenwarte im Gebiet der Schwäbischen Alb. *Z. Geophysik*, 9:230–234, 1933.

N. Houlié, J. Woessner, D. Giardini, and M. Rothacher. Lithosphere strain rate and stress field orientations near the Alpine arc in Switzerland. *Scientific reports*, 8:1–14, 2018.

J. Hürtgen, K. Reicherter, T. Spies, C. Geisler, and J. Schlittenhardt. The Paleoseismic Database of Germany and Adjacent Regions PalSeisDB v1.0. *Historical Earthquakes, Paleoseismology, Neotectonics and Seismic Hazard: New Insights and Suggested Procedures*, pages 73–136, 2020.

S. Husen, E. Kissling, N. Deichmann, S. Wiemer, D. Giardini, and M. Baer. Probabilistic earthquake location in complex three-dimensional velocity models: Application to Switzerland. *Journal of Geophysical Research: Solid Earth*, 108(B2):2077, 2003. doi: https://doi.org/10.1029/2002JB001778.

T. Ibele. Tectonics of the Hegau and Lake Constance region: a synthesis based on existing literature. *Nagra working report, NAB*, pages 12–23, 2015.

Y. Iio and Y. Kobayashi. A physical understanding of large intraplate earthquakes. *Earth, Planets and Space*, 54:1001–1004, 2002.

J. H. Illies. Der Hohenzollerngraben und Intraplattenseismizität infolge Vergitterung lamellärer Scherung mit einer Riftstruktur. *Oberrhein. Geol. Abh*, 31:47–78, 1982.

A. C. Johnston and L. R. Kanter. Earthquakes in Stable Continental Crust. *Scientific American*, 262(3):68–75, 1990.

U. Kastrup, M. L. Zoback, N. Deichmann, K. F. Evans, D. Giardini, and A. J. Michael. Stress field variations in the Swiss Alps and the northern Alpine foreland derived from inversion of fault plane solutions. *J. Geophys. Res.*, 109(B01402), 2004. doi: 10.1029/2003JB002550.

B. L. N. Kennett, E. R. Engdahl, and R. Buland. Constraints on seismic velocities in the Earth from traveltimes. *Geophysical Journal International*, 122:108–124, 1995.

E. Kissling, W. L. Ellsworth, D. Eberhart-Phillips, and U. Kradolfer. Initial reference models in local earthquake tomography. *Journal of Geophysical Research: Solid Earth*, 99(B10): 19635–19646, 1994.

E. Kissling, U. Kradolfer, and H. Maurer. Program VELEST user´s guide - Short Introduction, 1995. Int. Report, Institute of Geophysics, ETH, Zürich, available at: https://seg.ethz.ch/software/velest.html.

T. Kunze. Seismotektonische Bewegungen im Alpenbereich, 1982. PhD thesis, University Stuttgart, Germany, 167 pp.

Landesamt für Geologie, Rohstoffe und Bergbau. Landeserdbebendienst Baden-Württemberg [Data set], 2009. International Federation of Digital Seismograph Networks, doi: 10.7914/SN/LE.

T. Lecocq, S. P. Hicks, K. V. Noten, K. van Wijk, P. Koelemeijer, R. S. D. Plaen, F. Massin, G. Hillers, R. E. Anthony, M. Apoloner, and et al. Global quieting of high-frequency seismic noise due to COVID-19 pandemic lockdown measures. *Science*, 369(6509):1338–1343, 2020.

G. Leydecker. *Erdbebenkatalog für Deutschland mit Randgebieten für die Jahre 800 bis 2008*, volume 59. Schweizerbart´sche Verlagsbuchhandlung, Stuttgart, Germany, 2011.

L. Liu and M. D. Zoback. Lithospheric strength and intraplate seismicity in the New Madrid seismic zone. *Tectonics*, 16(4):585–595, 1997.

A. Lomax, J. Virieux, P. Volant, and C. Berge-Thierry. Probabilistic earthquake location in 3D and layered models: introduction to a Metropolis-Gibbs method and comparison with linear locations. In C. Thurber and N. Rabinowitz, editors, *Advances in seismic event location*, pages 101–134. Springer, 2000.

F. Lutz. Seismizität und Tektonik im südlichen Oberrheingraben, 2015. Bachelor Thesis, Karlsruhe Institut of Technology (KIT), Geophysikalisches Institut (GPI).

S. Mader and J. R. R. Ritter. StressTransfer [Data set], 2018. International Federation of Digital Seismograph Networks, doi: `10.7914/SN/5N_2018`.

S. Mader and J. R. R. Ritter. The StressTransfer Seismic Network - An Experiment to Monitor Seismically Active Fault Zones in the Northern Alpine Foreland of Southwestern Germany. *Seismological Research Letters*, 92(3):1773–1787, 2021.

S. Mader, J. R. R. Ritter, K. Reicherter, and the AlpArray Working Group. Seismicity and seismotectonics of the Albstadt Shear Zone in the northern Alpine foreland. *Solid Earth*, 12 (6):1389–1409, 2021.

A. Manglik, G. Pavankumar, and M. Demudu Babu. Stress state of the northwest Indian shield with emphasis on the Intraplate Delhi Seismic Zone. *Journal of Earth System Science*, 132 (55):1–20, 2023.

G. Mayer, P. M. Mai, T. Plenefisch, H. Echtler, E. Lüschen, V. Wehrle, and K. Fuchs. The stress field in the Rhine Graben area inferred from earthquake focal mechanisms and estimation of frictional parameters. *Tectonophysics*, 275(1-3):71–97, 1997.

M. Meschede and L. N. Warr. *The Geology of Germany: A Process-Oriented Approach.* Regional Geology Reviews, Springer Nature Switzerland AG, Cham, Switzerland, 2019.

A. J. Michael. Determination of stress from slip data: faults and folds. *Journal of Geophysical Research: Solid Earth*, 89(B13):11517–11526, 1984.

K. Mogi. Magnitude-frequency relation for elastic shocks accompanying fractures of various materials and some related problems in earthquakes (2nd paper). *Bulletin of the Earthquake Research Institute, University of Tokyo*, 40:831–853, 1962.

K. Mogi. Some discussions on aftershocks, foreshocks and earthquake swarms: the fracture of a semi-infinite body caused by an inner stress origin and its relation to the earthquake phenomena (third paper). *Bulletin of the Earthquake Research Institute, University of Tokyo*, 41:615–658, 1963.

B. Müller, M. L. Zoback, K. Fuchs, L. Mastin, S. Gregersen, N. Pavoni, O. Stephansson, and C. Ljunggren. Regional patterns of tectonic stress in Europe. *Journal of Geophysical Research: Solid Earth*, 97(B8):11783–11803, 1992.

NOAA National Geophysical Data Center. ETOPO1 1 Arc-Minute Global Relief Model [data set], 2009. NOAA National Centers for Environmental Information, `https://doi.org/10.7289/V5C8276M`.

M. C. Oncescu, M. Rizescu, and K.-P. Bonjer. SAPS-An automated and networked seismological acquisition and processing system. *Computers & Geosciences*, 22:89–97, 1996.

C. C. Paige and M. A. Saunders. LSQR: An algorithm for sparse linear equations and sparse least squares. *ACM Transactions on Mathematical Software (TOMS)*, 8(1):43–71, 1982.

J. Peterson. Observations and modeling of seismic background noise, 1993. U.S. Geol. Surv. Open-File Rept. 93-322, Albuquerque, New Mexico.

J. Piña-Valdés, A. Socquet, C. Beauval, M.-P. Doin, N. D'Agostino, and Z.-K. Shen. 3D GNSS velocity field sheds light on the deformation mechanisms in Europe: Effects of the vertical crustal motion on the distribution of seismicity. *Journal of Geophysical Research: Solid Earth*, 127(6):e2021JB023451, 2022.

T. Plenefisch. Untersuchungen des Spannungsfeldes im Bereich des Rheingrabens mittels der Inversion von Herdflächenlösungen und Abschätzung der bruchspezifischen Reibungsparameter, 1996. PhD thesis, University of Karlsruhe (TH), Karlsruhe.

T. Plenefisch and K.-P. Bonjer. The stress field in the Rhine Graben area inferred from earthquake focal mechanisms and estimation of frictional parameters. *Tectonophysics*, 275 (1-3):71–97, 1997.

A. Plešinger, M. Hellweg, and D. Seidl. Interactive high-resolution polarization analysis of broad-band seismograms. *Journal of Geophysics*, 59:129–139, 1986.

P. Podvin and I. Lecomte. Finite difference computation of traveltimes in very contrasted velocity models: a massively parallel approach and its associated tools. *Geophysical Journal International*, 105:271–284, 1991.

Regierungspräsidium Freiburg: Landesamt für Geologie, Rohstoffe und Bergbau. Last felt earthquakes in Baden-Württemberg, 2023. available at: `https://lgrb-bw.de/erdbeben/erdbebenmeldung`, last access: 19 October 2023.

Regierungspräsidium Freiburg: Landesamt für Geologie, Rohstoffe und Bergbau (Hrsg.). LGRB-Kartenviewer - Layer GüK300:Tektonik, 2019. available at: `https://maps.lgrb-bw.de/`, last access: 28 March 2019.

K. Reicherter, N. Froitzheim, Jarosiński, J. Badura, H.-J. Franzke, M. Hansen, C. Hübscher, R. Müller, P. Poprawa, J. Reinecker, and et al. Alpine tectonics north of the Alps. In T. McCann, editor, *The Geology of Central Europe*, volume 2, Mesozoic and Cenozoic, chapter 19, pages 1233–1286. Geological Society of London, 2008.

K. Reicherter, S. Baize, J. Hürtgen, F. Cinti, T. K. Rockwell, H. Jomard, G. Seitz, and J. Ritter. Paleoseismological trenching of the eastern Rhine graben boundary fault: The Ettlingen segment, 2020. EGU General Assembly, 4–8 May, Abstract EGU 2020-6187, doi: `10.5194/egusphere-egu2020-6187`.

J. Reinecker and G. Schneider. Zur Neotektonik der Zollernalb: Der Hohenzollerngraben und die Albstadt-Erdbeben. *Jahresberichte und Mitteilungen des Oberrheinischen Geologischen Vereins*, 84:391–417, 2002.

J. Reinecker, M. Tingay, B. Müller, and O. Heidbach. Presentday stress orientation in the Molasse basin. *Tectonophysics*, 482:129–138, 2010.

K. Reiter, O. Heidbach, B. Müller, J. Reinecker, and T. Röckl. Stress Map Germany 2016, 2016. doi: `https://doi.org/10.5880/WSM.Germany2016_en`.

RESIF. RESIF-RLBP French Broad-Band Network, RESIF-RAP strong Motion Network and Other Seismic Stations in Metropolitan France [Data Set], 1995. RESIF-Réseau Sismologique et géodésique Français, doi: `10.15778/RESIF.FR`.

U. Ring and R. Bolhar. Tilting, uplift, volcanism and disintegration of the South German block. *Tectonophysics*, 795:228611, 2020. doi: `https://doi.org/10.1016/j.tecto.2020.228611`.

L. Rivera and A. Cisternas. Stress tensor and fault plane solutions for a population of earthquakes. *Bulletin of the Seismological Society of America*, 80(3):600–614, 1990.

L. Röckel, S. Ahlers, B. Müller, K. Reiter, O. Heidbach, A. Henk, T. Hergert, and F. Schilling. The analysis of slip tendency of major tectonic faults in Germany. *Solid Earth*, 13(6):1087–1105, 2022.

I. Rupf and E. Nitsch. Das Geologische Landesmodell von Baden-Württemberg: Datengrundlagen, technische Umsetzung und erste geologische Ergebnisse, 2008. Regierungspräsidium Freiburg—Abteilung 9, Landesamt für Geologie, Rohstoffe und Bergbau, available at `https://produkte.lgrb-bw.de/schriftensuche/lgrb-informationen/informationen21?term=Landesmodell` (last accessed March 2021).

K. Schädel. Geologische übersichtskarte, 1:100.000 C7918 Albstadt und Erläuterungen, 1976. Geologisches Landesamt Baden-Württemberg, Freiburg im Breisgau„ 44 pp.

D. P. Schaff and P. G. Richards. Improvements in magnitude precision, using the statistics of relative amplitudes measured by cross correlation. *Geophysical Journal International*, 197(1): 335–350, 2014.

F. Scherbaum. *Of zeros and poles. Fundamentals of digital seismology*. Kluwer Academic Publishers, 1996.

A. Schlömer, J. Wassermann, W. Friederich, M. Korn, T. Meier, G. Rümpker, C. Thomas, F. Tilmann, and J. Ritter. UNIBRA/DSEBRA: The German Seismological Broadband Array and Its Contribution to AlpArray—Deployment and Performance. *Seismological Research Letters*, 93(4):2077–2095, 2022.

G. Schneider. Seismizität und Seismotektonik der Schwäbischen Alb, 1971. F. Enke Verlag, Stuttgart, Germany.

G. Schneider. *Die Erdbeben in Baden-Württemberg, 1963-1972.* Institut für Geophysik der Univ. Stuttgart, Germany, 1973.

G. Schneider. The earthquake in the Swabian Jura of 16 November 1911 and present concepts of seismotectonics. *Tectonophysics*, 53(3-4):279–288, 1979.

G. Schneider. Das Beben vom 3. September 1978 auf der Schwäbischen Alb als Ausdruck der seismotektonischen Beweglichkeit Südwestdeutschlands nordwestlichen Baden-Württemberg. *Jahresberichte und Mitteilungen des Oberrheinischen Geologischen Vereins*, pages 143–166, 1980.

G. Schneider. Beziehungen zwischen Erdbeben und Strukturen der Süddeutschen Großscholle. 189:275–288, 1993.

J. Schwarz, S. Beinersdorf, and H. Meidow. *Magnitudenorientierter Erdbebenkatalog für deutsche und angrenzende Gebiete EKDAG - erweiterter Ahorner-Katalog.* Bauhaus Universitätsverlag, 2019.

P. M. Shearer. *Introduction to seismology.* Cambridge University Press, 2009.

D. R. Shelly and J. L. Hardebeck. Precise tremor source locations and amplitude variations along the lower-crustal central San Andreas Fault. *Geophysical Research Letters*, 37(L14301), 2010.

Z. K. Shipton, M. Meghraoui, and L. Monro. Seismic slip on the west flank of the Upper Rhine Graben (France-Germany): Evidence from tectonic morphology and cataclastic deformation bands. In A. Landgraf, S. Kübler, E. Hintersberger, and S. Stein, editors, *Seismicity, Fault Rupture and Earthquake Hazards in Slowly Deforming Regions*, volume Special Publications 432, chapter 19, pages 147–161. Geological Society, London, 2017.

A. Sieberg and R. Lais. Das mitteleuropäische Erdbeben vom 16. November 1911, Beartbeitung der makroseismichen Beobachtungen. In O. Hecker, editor, *Veröffentlichungen der Reichsanstalt für Erdbebenforschungen in Jena*, volume 4, page 106. Gustav Fischer, Jena, 1925.

J. A. Snoke. Earthquake Mechanisms. In D. E. James, editor, *Encyclopedia of Geophysics*, pages 239–245. Van Nostrand Reinhold Company, New York, 1989.

J. A. Snoke. FOCMEC: Focal mechanism determinations. In W. H. Lee, H. Kanamori, P. Jennings, and C. Kisslinger, editors, *International Handbook of Earthquake & Engineering Seismology, Part B*, pages 1629–1630. Academic Press, San Diego, 2003.

C. Spooner, M. Scheck-Wenderoth, M. Cacace, and D. Anikiev. How Alpine seismicity relates to lithospheric strength. *International Journal of Earth Sciences*, 111:1201–1221, 2022.

S. Stange. Erdbebenüberwachung Baden-Württemberg - Das modernisierte Starkbeben- und Detektionsmessnetz, 2018. LGRB - Nachricht, Regierungspräsidium Freiburg, Nr. 2018/07.

S. Stange and W. Brüstle. Die Erdbebenserie von Bad Saulgau, 2001. *Jahresberichte und Mitteilungen des Oberrheinischen Geologischen Vereins*, 85:441–460, 2003.

S. Stange and W. Brüstle. The Albstadt/Swabian Jura seismic source zone reviewed through the study of the earthquake of March 22, 2003. *Jahresberichte und Mitteilungen des Oberrheinischen Geologischen Vereins*, 87:391–414, 2005.

Swiss Seismological Service (SED) at Eidgenössische Technische Hochschule (ETH) Zurich. National Seismic Networks of Switzerland, 1983. ETH Zürich, doi: `10.12686/sed/networks/ch`.

L. R. Sykes and M. L. Sbar. Intraplate Earthquakes, Lithospheric Stresses and the Driving Mechanism of Plate Tectonics. *Nature*, 245(5424):298–302, 1973.

P. Talwani. The intersection model for intraplate earthquakes. *Seismological Research Letters*, 59(4):305–310, 1988.

P. Talwani, editor. *Intraplate earthquakes*. Cambridge University Press, 2014.

P. Talwani. On the nature of intraplate earthquakes. *Journal of Seismology*, 21:47–68, 2017.

A. Tarantola and B. Valette. Inverse problems = quest for information. *Journal of Geophysics*, 50:159–170, 1982.

C. H. Thurber. Earth structure and earthquake locations in the Coyote Lake area, central California, 1981. Ph D thesis, Massachusetts Institute of Technology, Massachussets, USA.

B. Tozer, D. T. Sandwell, W. H. Smith, C. Olson, J. R. Beale, and P. Wessel. Global bathymetry and topography at 15 arc sec: SRTM15+. *Earth and Space Science*, 6(10):1847–1864, 2019.

V. Tron and J.-P. Brun. Experiments on oblique rifting in brittle-ductile systems. *Tectonophysics*, 188(1-2):71–84, 1991.

J. Turnovsky. Herdmechanismen und Herdparameter der Erdbebenserie 1978 auf der Schwäbischen Alb, 1981. PhD thesis, University Stuttgart, Germany, 109 pp.

S. Tyagunov, G. Grünthal, R. Wahlström, L. Stempniewski, and J. Zschau. Seismic risk mapping for Germany. *Natural Hazards and Earth System Sciences*, 6(4):573–586, 2006. doi: `https://doi.org/10.5194/nhess-6-573-2006`.

B. Valley and K. F. Evans. Stress state at Soultz-sous-Forêts to 5 km depth from wellbore failure and hydraulic observations. In *Proceedings, 32nd Workshop on Geothermal Reservoir Engineering*, 2007. Stanford University, Stanford, California.

V. Vavryčuk, F. Bouchaala, and T. Fischer. High-resolution fault image from accurate locations and focal mechanisms of the 2008 swarm earthquakes in West Bohemia, Czech Republic. *Tectonophysics*, 590:189–195, 2013.

V. Vavryčuk. Iterative joint inversion for stress and fault orientations from focal mechanisms. *Geophysical Journal International*, 199:69–77, 2014. doi: `https://doi.org/10.1093/gji/ggu224`.

V. Vavryčuk. STRESSINVERSE, 2020. available at: `https://www.ig.cas.cz/en/stress-inverse/`, last access 24 February 2021.

F. Waldhauser and W. L. Ellsworth. A double-difference earthquake location algorithm: Method and application to the northern Hayward fault, California. *Bulletin of the Seismological Society of America*, 90(6):1353–1368, 2000.

R. E. Wallace. Geometry of shearing stress and relation to faulting. *The Journal of geology*, 59 (2):118–130, 1951.

D. L. Wells and K. J. Coppersmith. New Empirical Relationships among Magnitude, Rupture Length, Rupture Width, Rupture Area and Surface Displacement. *Bulletin of Seismological Society of America*, 84(4):974–1002, 1994.

H. U. Wetzel and H. J. Franzke. Lassen sich über die Fernerkundung erweiterte Kenntnisse zur seismogenen Zone Bodensee-Stuttgart (9°-Ost) gewinnen? *Publikationen der Deutschen Gesellschaft für Photogrammetrie und Fernerkundung*, 12:339–347, 2003.

M. D. Zoback and M. L. Zoback. State of Stress and Intraplate Earthquakes in the United States. *Science*, 213(4503):96–104, 1981.

M. L. Zoback. First-and second-order patterns of stress in the lithosphere: The World Stress Map Project. *Journal of Geophysical Research: Solid Earth*, 97(B8):11703–11728, 1992.

J. J. Zucca. The crustal structure of the southern Rhinegraben from re-interpretation of seismic refraction data. *J. Geophys.*, 55(1):13–22, 1984.

A. Supplement to chapter 5

For completeness the properties of the horizontal recordings are shown in this supplement.

Figure A.1: Probabilistic power spectral densities of HHE channels.

Figure A.2: Probabilistic power spectral densities of HHN channels.

Figure A.3: Waveform comparison of HHE channels to check polarity and amplitude of the recordings.

Figure A.4: Waveform comparison of HHN channels to check polarity and amplitude of the recordings.
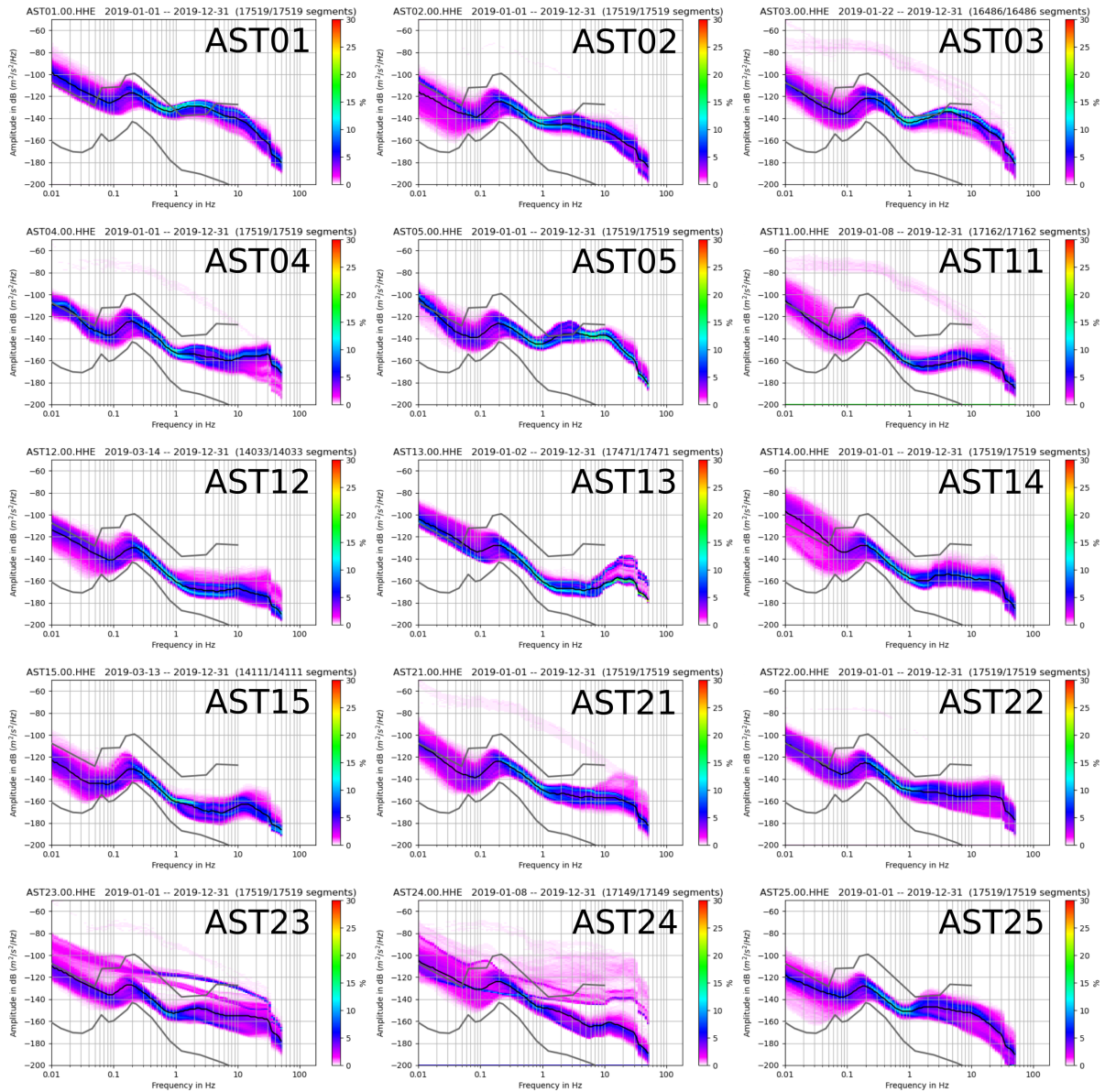
Figure A.1.: Probabilistic power spectral densities (PPSDs) for the year 2019 for each StressTransfer station, HHE channel (east-west component). The PSDs are calculated for one-hour segments and overlap by 50%. The color displays the probabilistic occurrence of an amplitude at a certain frequency. The black line represents the median of all PSDs. Gray lines mark the New Low Noise Model (NLNM) and the New High Noise Model (NHNM) after (Peterson, 1993).
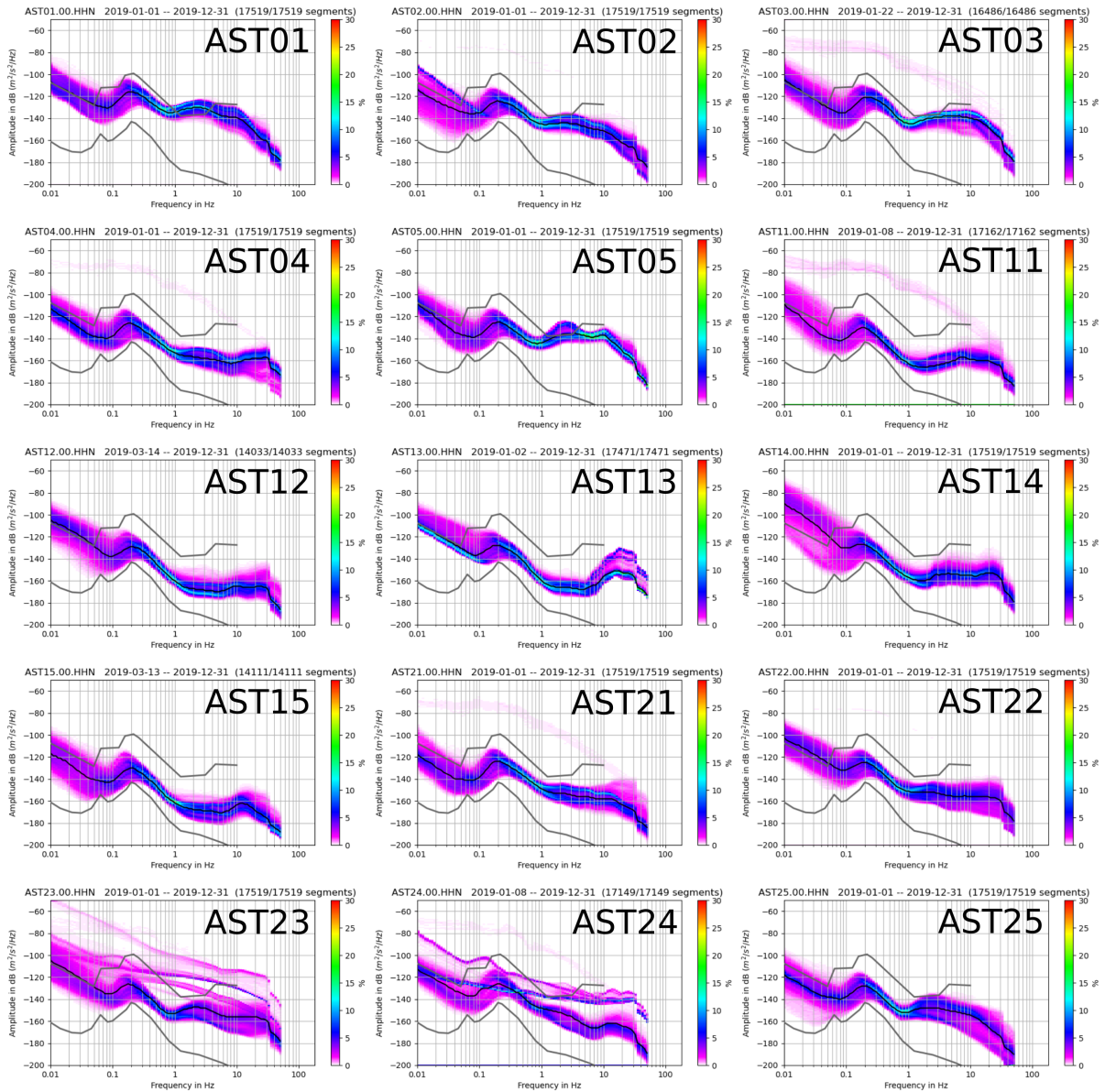
Figure A.2.: Probabilistic power spectral densities (PPSDs) for the year 2019 for each StressTransfer station, HHN channel (north-south component). The PSDs are calculated for one-hour segments and overlap by 50%. The color displays the probabilistic occurrence of an amplitude at a certain frequency. The black line represents the median of all PSDs. Gray lines mark the New Low Noise Model (NLNM) and the New High Noise Model (NHNM) after (Peterson, 1993).
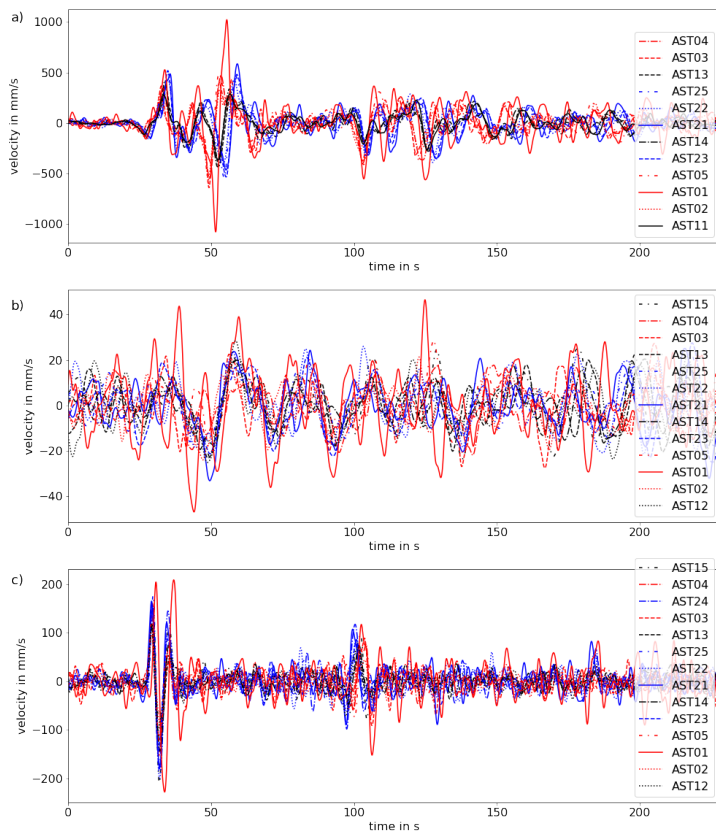
Figure A.3.: Teleseismic waveform recordings at all StressTransfer stations for channel HHE (east-west component) to check amplitude and polarity properties. The seismograms are shifted relative to expected shear wave arrival time of each event. a) SKS phase of the Mw 7.5 earthquake below the Peru-Ecuador border region in 46 km depth on 22nd February 2019, b) SS phase of the Mw 7.3 earthquake below the Kermadec Islands in 212 km depth on 15th June 2019, c) SKS phase of the Mw 7.3 earthquake below the Banda Sea in 132 km depth on 24th June 2019.
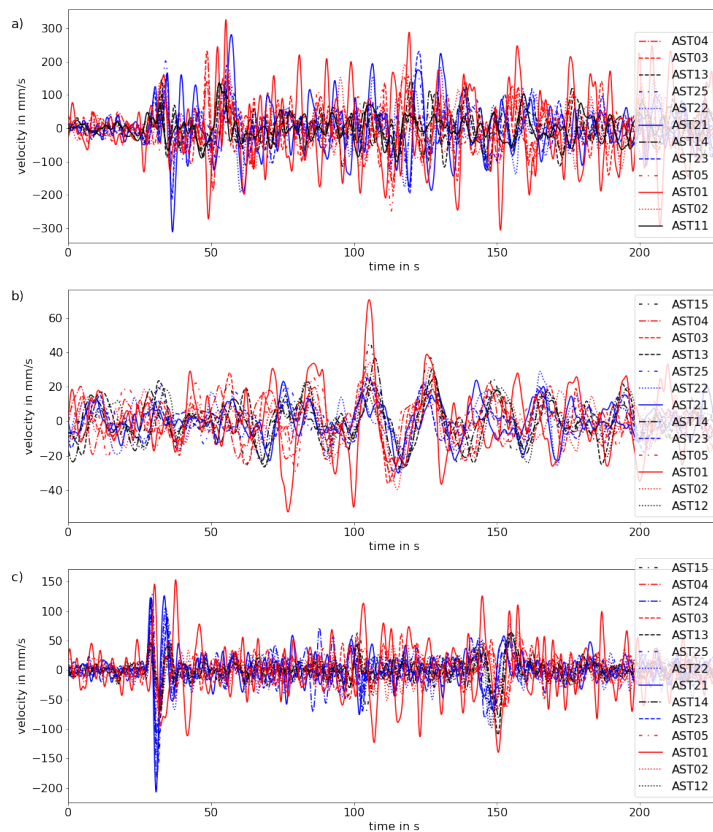
Figure A.4.: Teleseismic waveform recordings at all StressTransfer stations for channel HHN (north-south component) to check amplitude and polarity properties. The seismograms are shifted relative to expected shear wave arrival time of each event. a) SKS phase of the Mw 7.5 earthquake below the Peru-Ecuador border region in 46 km depth on 22nd February 2019, b) SS phase of the Mw 7.3 earthquake below the Kermadec Islands in 212 km depth on 15th June 2019, c) SKS phase of the Mw 7.3 earthquake below the Banda Sea in 132 km depth on 24th June 2019.

B. Appendix and Supplement to chapter 6

Table B.1.: Definition of the error quality relationship. lp-ep represents the time window in which the final pick is manually selected.

Pick time uncertainties	lp-ep ≤ 0.05	0.05 < lp-ep ≤ 0.1	0.1 < lp-ep ≤ 0.2	0.2 < lp-ep ≤ 0.4	lp-ep > 0.4
Quality	0	1	2	3	4

Table B.2.: Classification of the qualities used for focal mechanisms. Δx represents Δstrike, Δdip and Δrake. The lowest quality of all three parameters is given to the fault plane solution.

	Δx ≤ 10°	10° < Δx ≤ 20°	20° < Δx ≤ 30°	30° < Δx ≤ 40°	40° < Δx
Quality	0	1	2	3	4
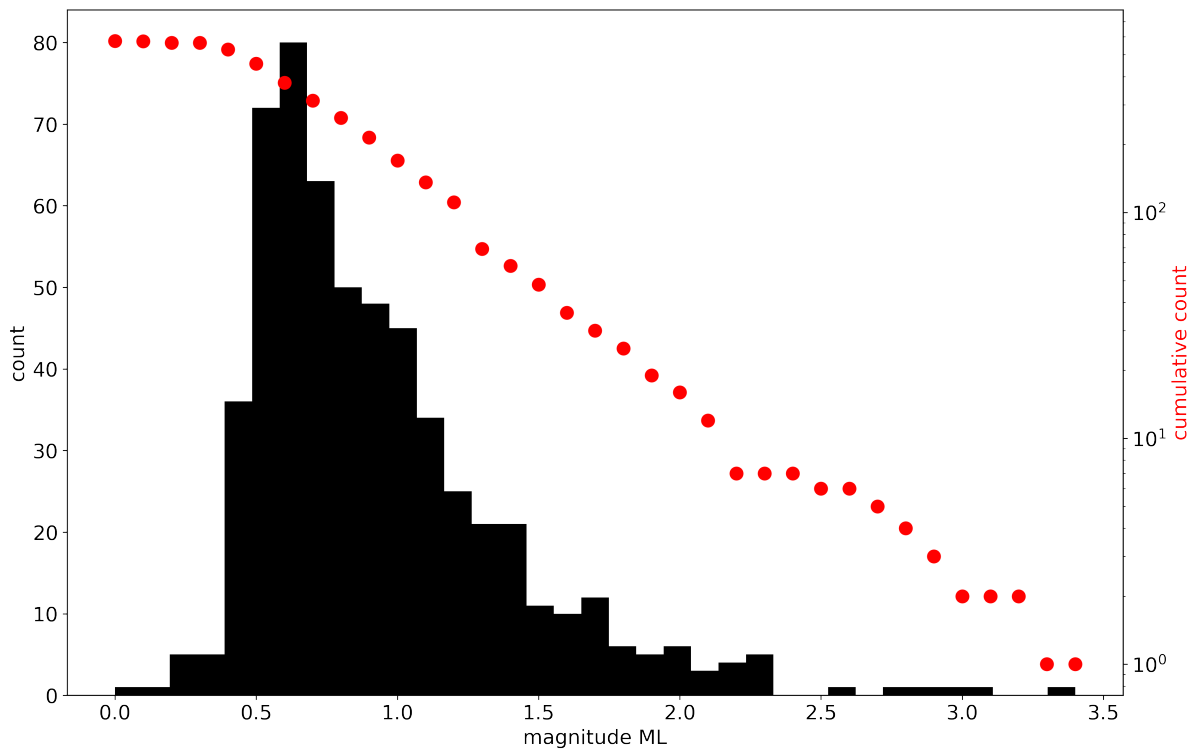
Figure B.1.: Frequency-magnitude distribution. The magnitude values are taken from the LED catalog, these are well determined (±0.2 units). The cumulative counting from high to low magnitudes implies a magnitude of completeness of about 0.6.
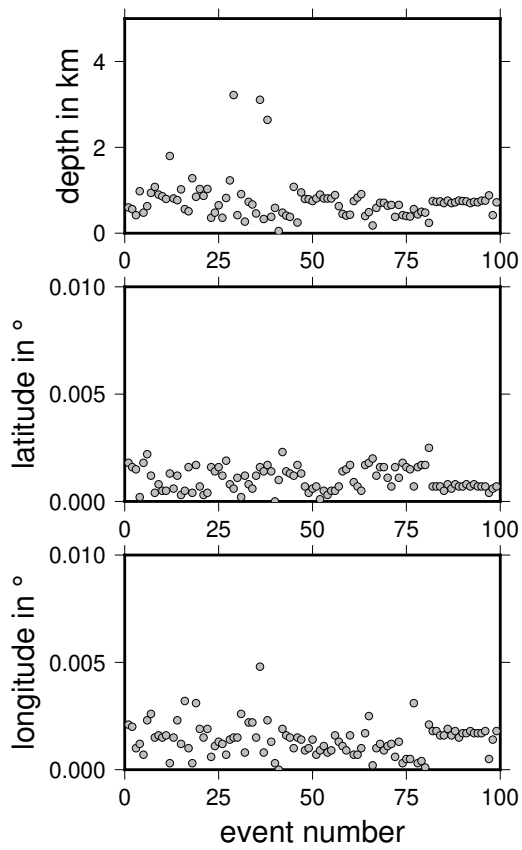
Figure B.2.: Deviation of hypocenter locations after the shift test with VELEST.
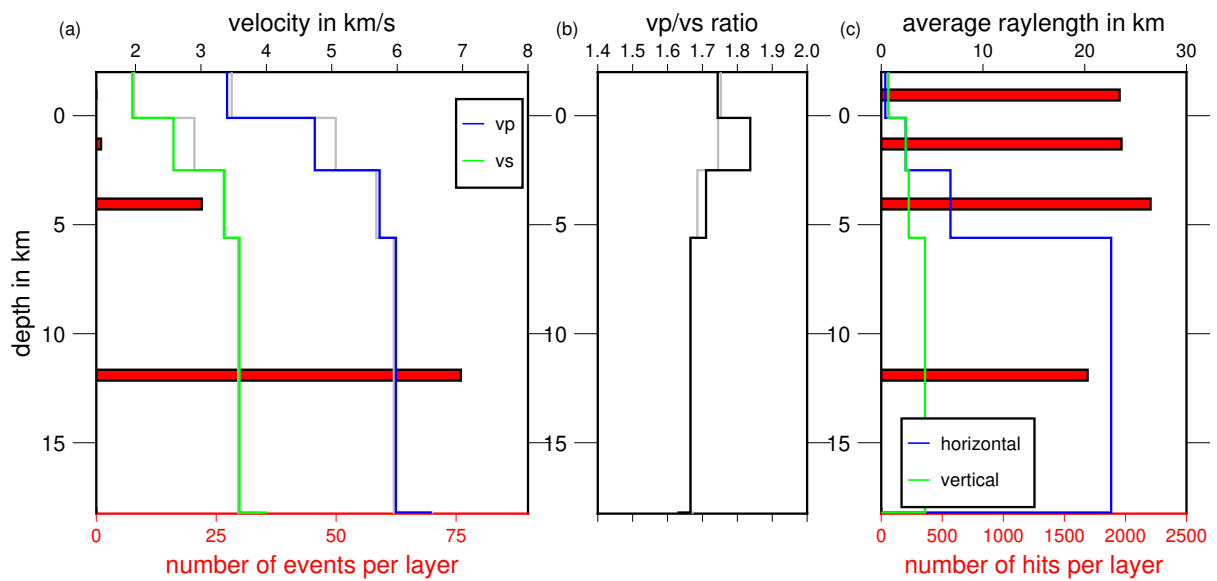
Figure B.3.: a) Velocity models after the shift test (green and blue). Grey lines represent input model ASZmod1. Red bars are scaled with the number of events in each layer of the velocity model.
b) vp/vs-ratio after the shift test.
c) Ray statistics of used ray paths. Red bars display number of hits per layer. Blue and green line give the average horizontal and vertical raylength.
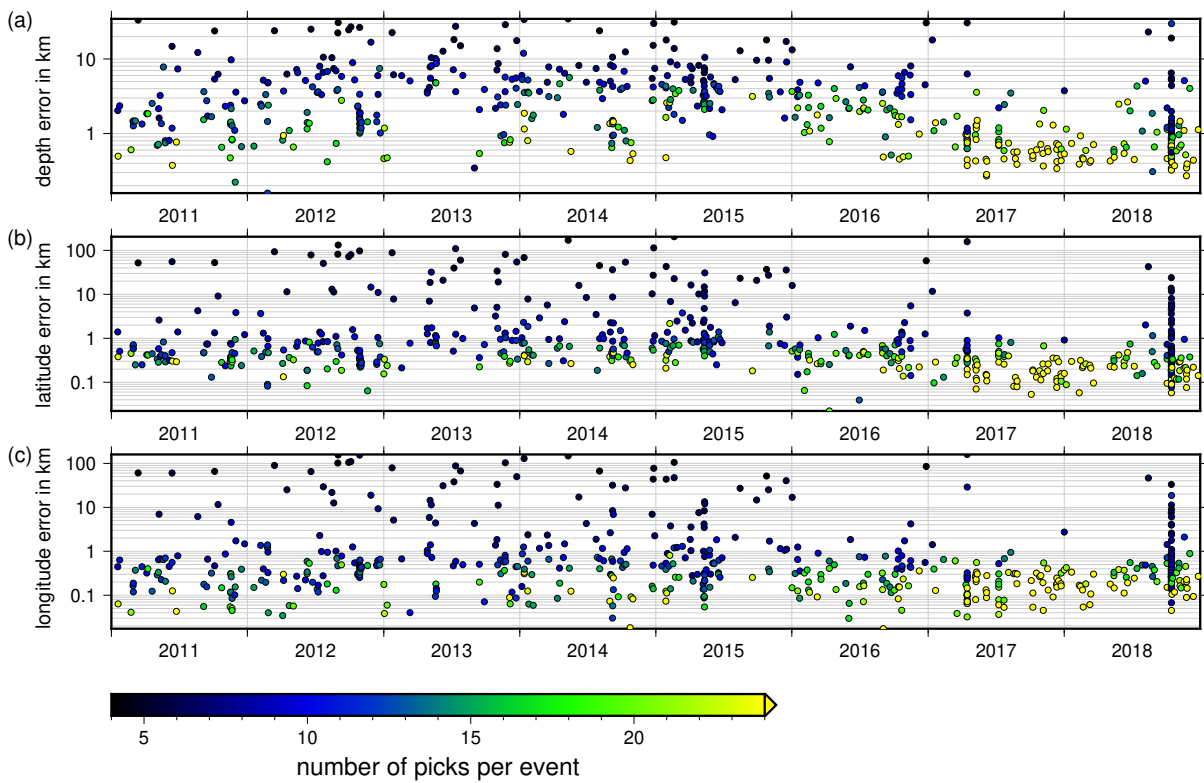
Figure B.4.: Errors calculated from the 68% confidence ellipsoid from NLL with EDT for each event in the catalog for (a) depth, (b) latitude, and (c) longitude. The error values are color-coded with the number of picks, with dark colors indicating few picks and bright colors indicating many picks. Earthquakes with many observations can be located with smaller errors in depth and horizontally.
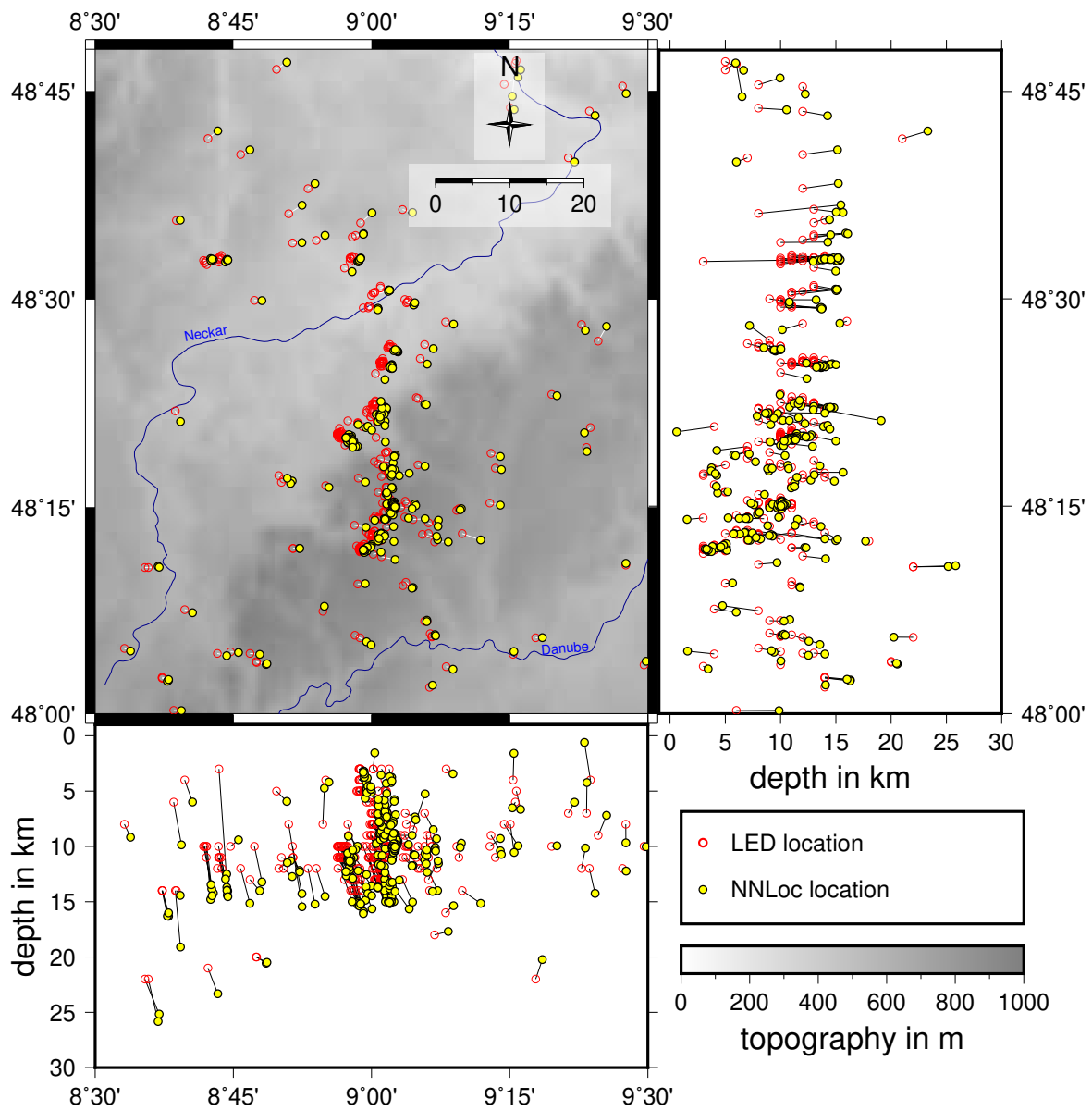
Figure B.5.: Comparison of our well located events (yellow filled circles with more than eight travel time picks, a GAP smaller than 180°, a horizontal error estimate of less than 1 km, and a depth error of less than 2 km) with the LED routine event locations (red circles). For some events there is a large deviation in depth. Topography is based on the ETOPO1 Global Relief Model (Amante and Eakins, 2009).
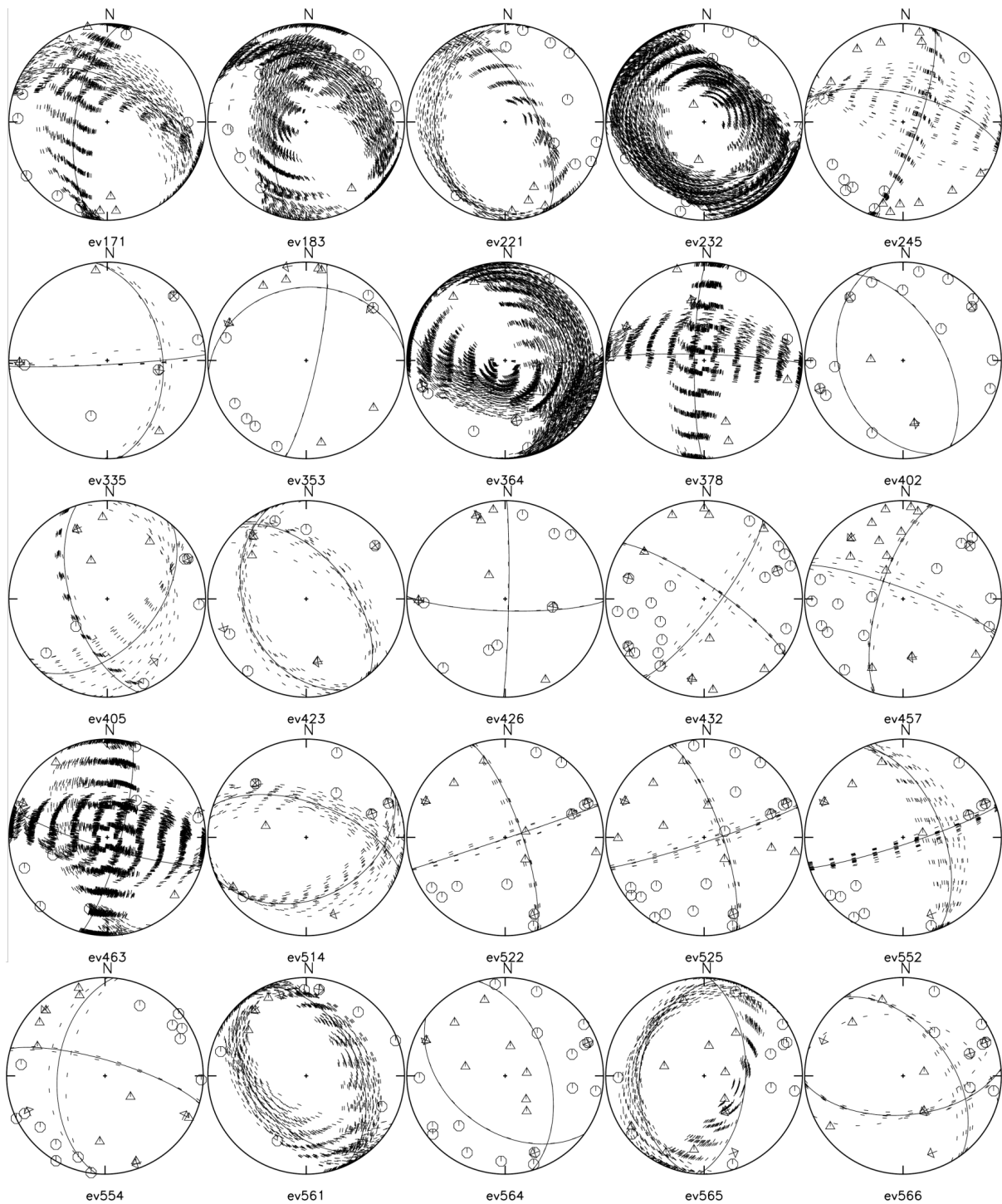
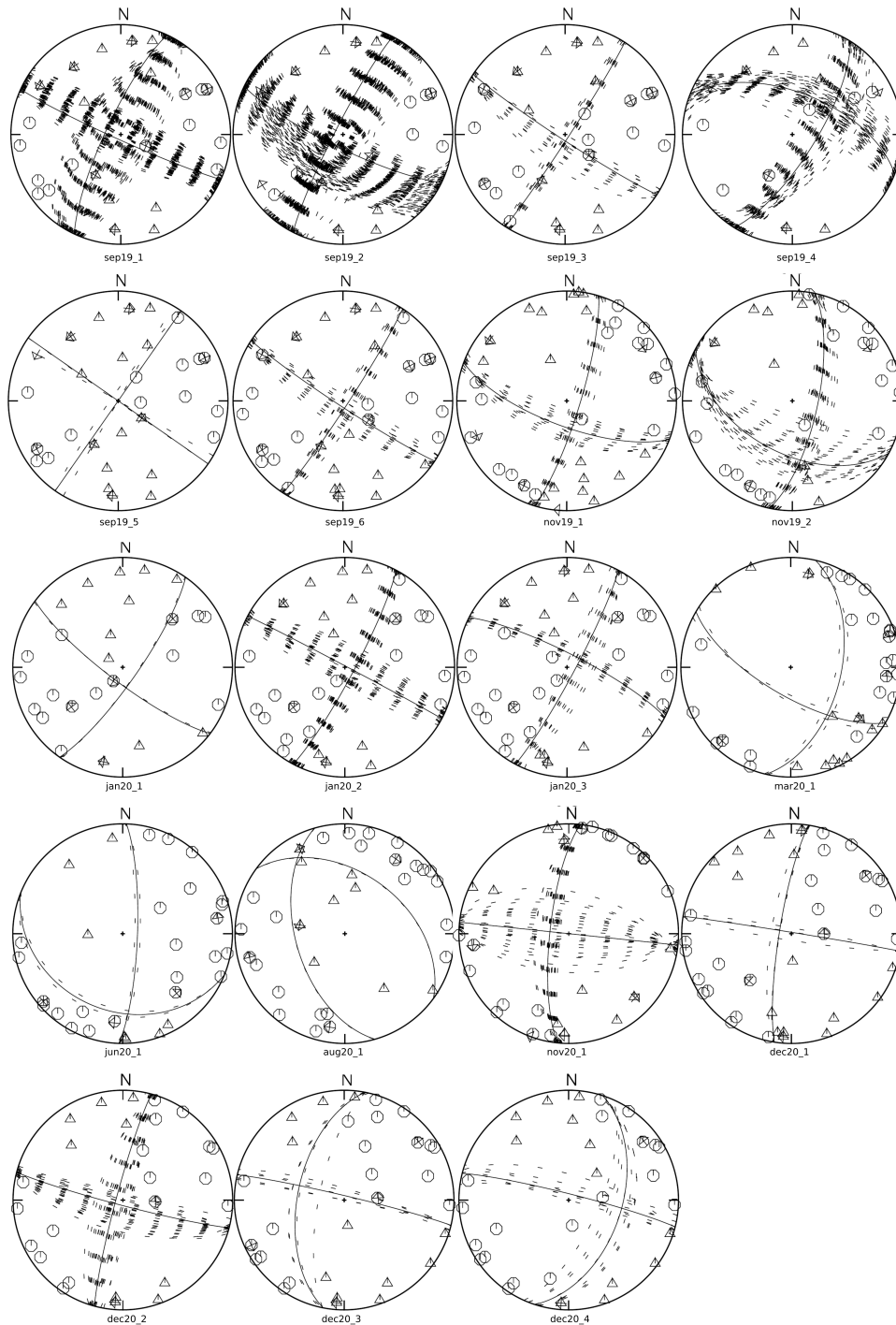**Figure B.6.:** All fault plane solutions with preferred (solid line) and all possible solutions (dashed lines). Triangles are negative and hexagon positive polarities. Arrows show in direction of SH-polarity. Fault plane solutions are labeled with their ID in Table 6.2.

C. Appendix and Supplement to chapter 7
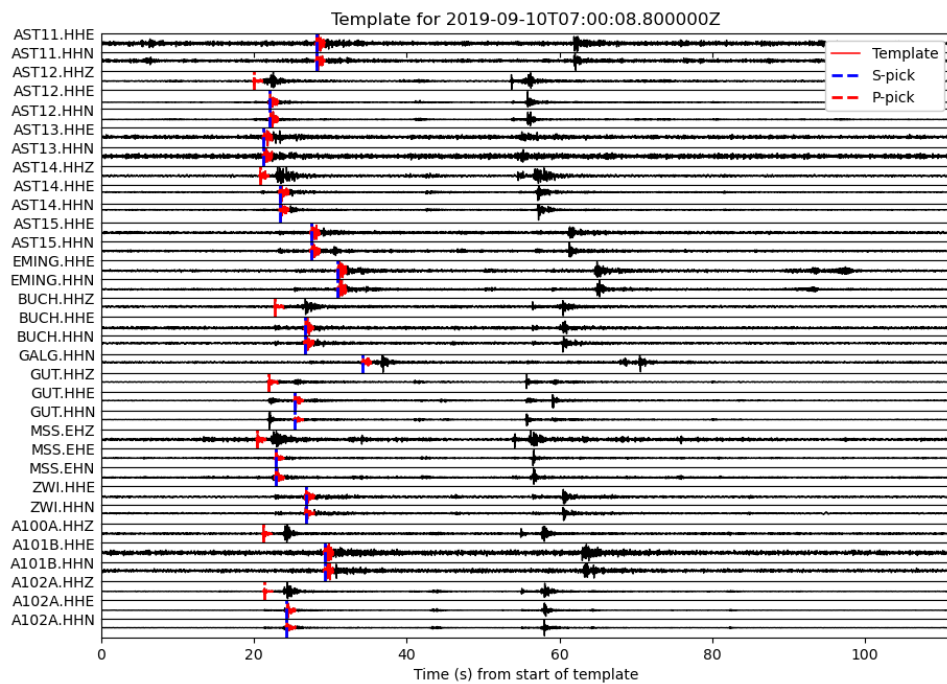
Figure C.1.: Exemplary waveform template for a ML 1.1 earthquake on 10 September 2019 at 07:00.
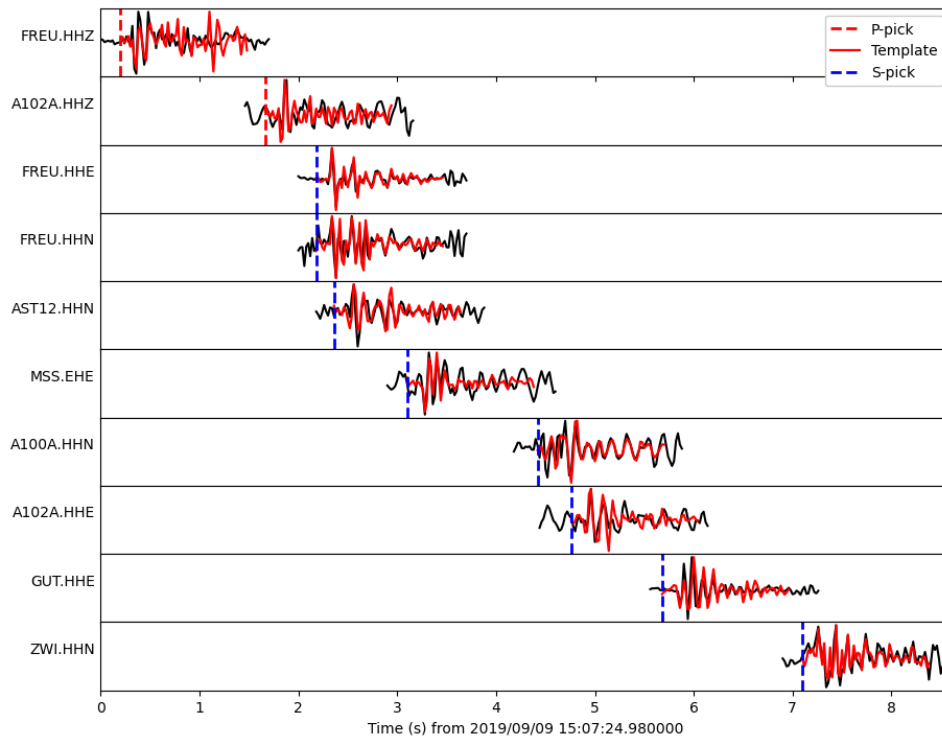
Figure C.2.: Exemplary waveforms for a detected event on 9 September 2019 at around 15:00 and the corresponding automatically determined phase arrival times. Here, the phase arrival times are not yet corrected for the 0.15 s offset due to the prepick time of the waveform template.
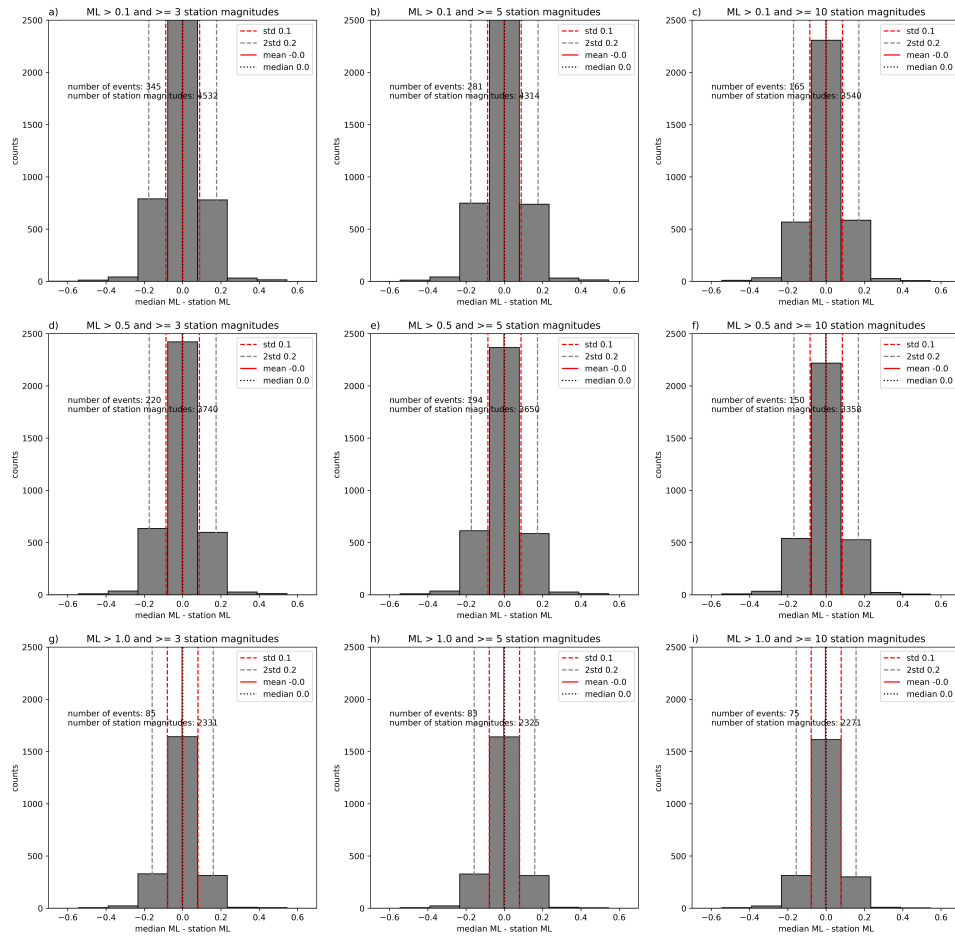
Figure C.3.: Histograms of differences between median and station relative magnitude, for different subsets of all determined relative magnitudes (a-i), with different minimum magnitude and number of station magnitudes allowed. In the histogram data templates are excluded. For all subsets median, mean and standard deviation (std) are determined and have neglectable variations.
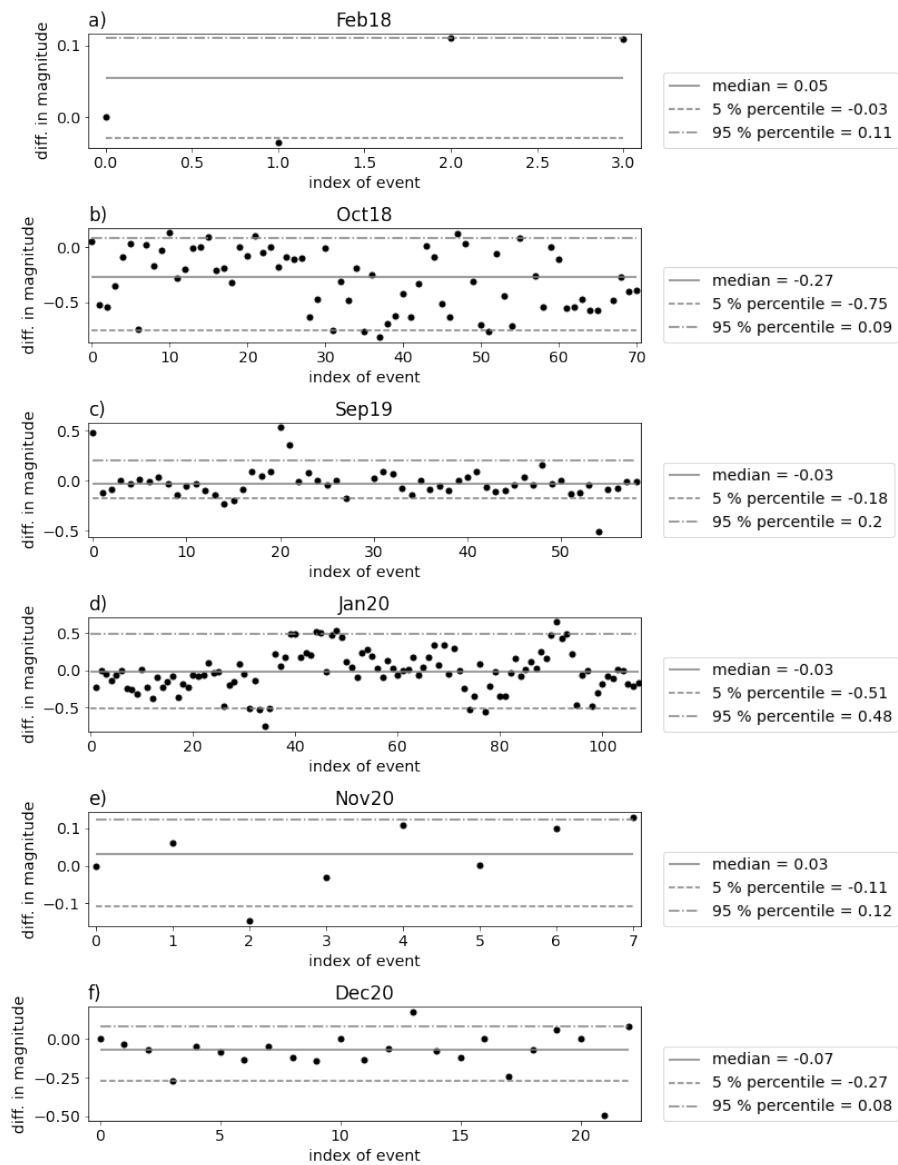
Figure C.4.: Difference between our relative magnitude result and the magnitude determined by the LED (Bulletin-Files des Landeserdbebendienstes B-W, 2011-2020) a) for Feb18, b) for Oct18, c) Sep19, d) Jan20, e) Nov20 and f) Dec20 earthquake sequences. Gray lines indicate the median (solid), 5 % percentile (dashed) and 95 % percentile (dashdot) of the differences in magnitude.

Figure C.5.: Overview of calculated fault plane solutions with preferred (solid line) and all possible solutions (dashed lines). Triangles are negative and hexagons are positive P-polarities. Arrows (mostly overlapping with other symbols) indicate direction of SH-polarity. Fault plane solutions are labeled with their ID from Table 7.3.
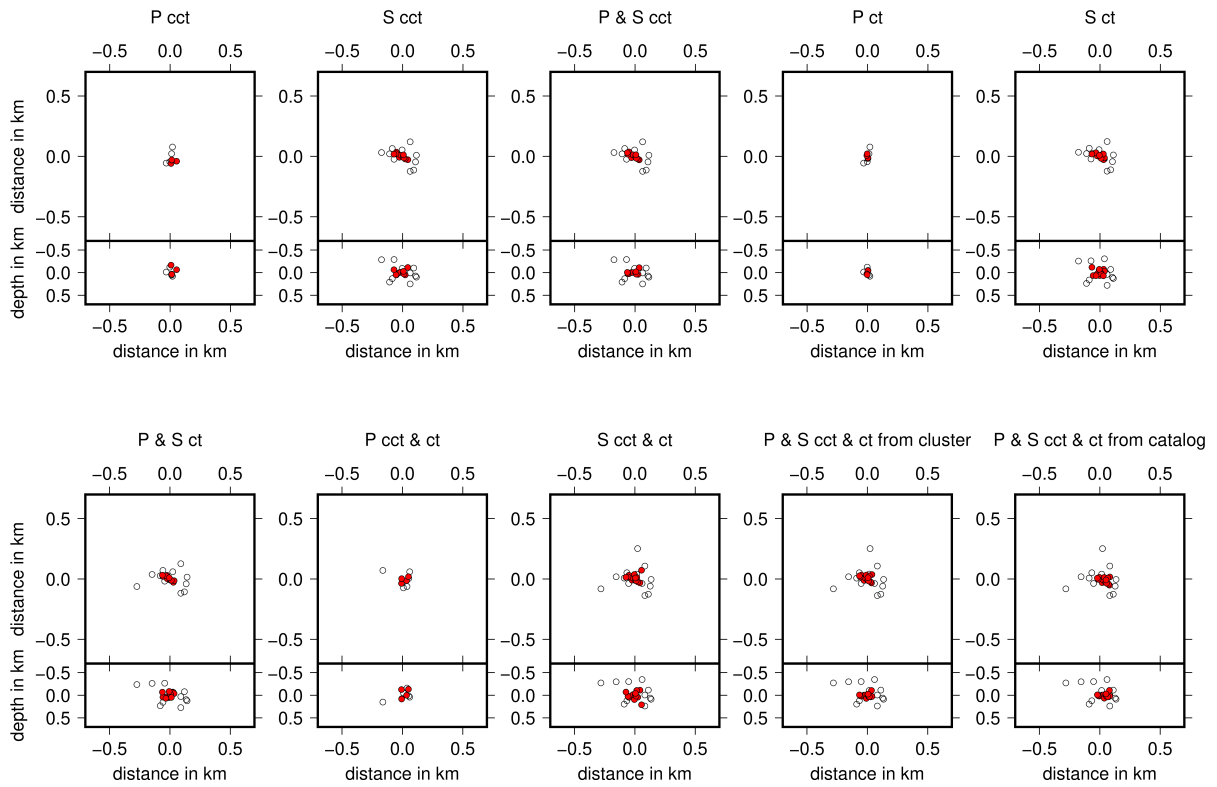
Figure C.6.: Comparison of HypoDD performance with different data sets on the Feb18 earthquake sequence. Black circles represent NLLoc hypocenter locations. Red filled circles show result of HypoDD. Title represents data set used (ct=catalog times, cct=cross-correlation times, from cluster or catalog represents the inversion starting point). Hypocenter locations are always displayed in map view and corresponding West-East depth slice below.
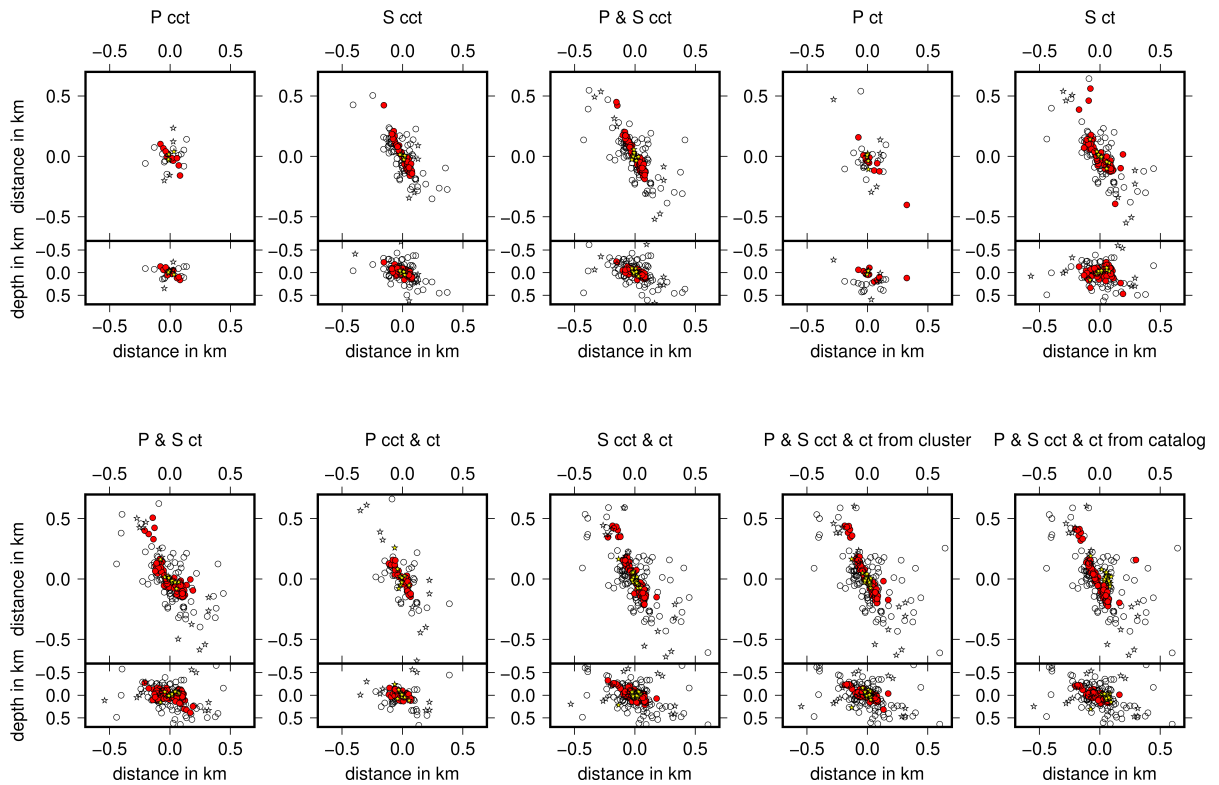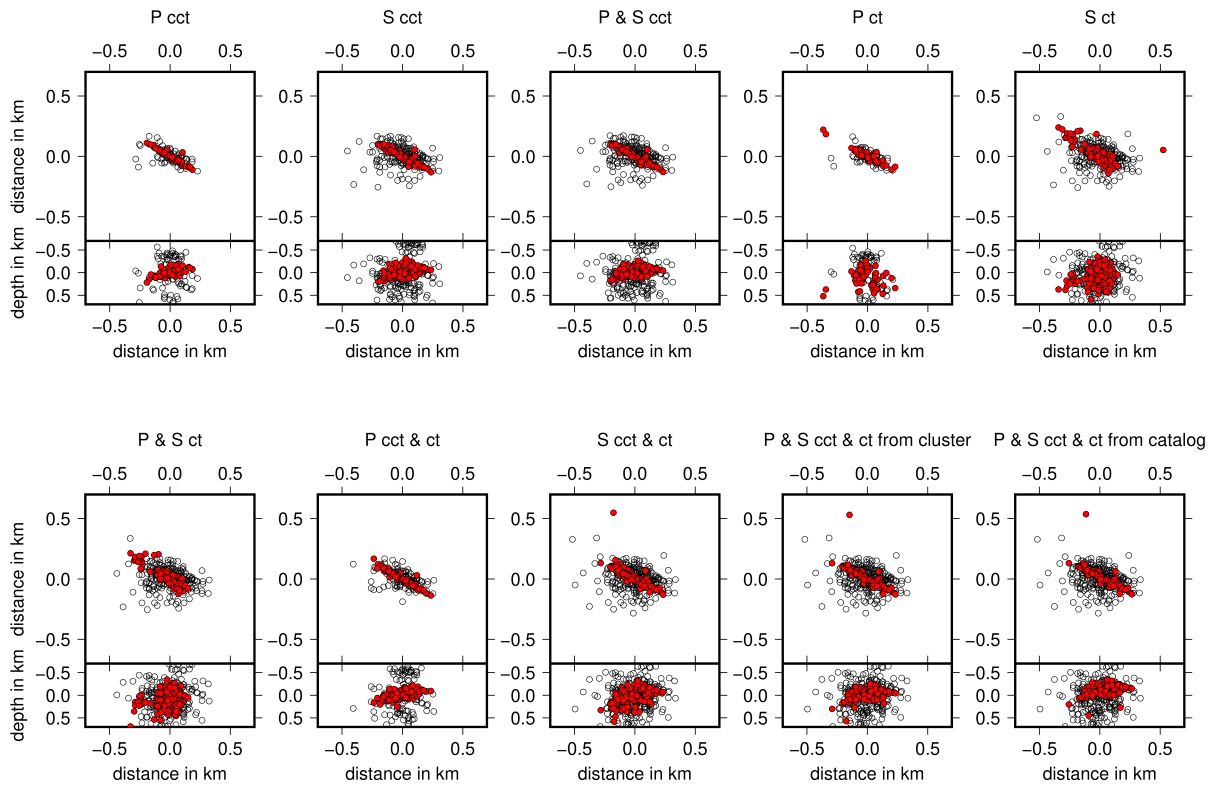
Figure C.7.: Comparison of HypoDD performance with different data sets on the Oct18 earthquake sequence. The Oct18 sequence is separated in two clusters. Hypocenter location is always relative to cluster center. Black circles (Oct18-1) and stars (Oct18-2) represent NLLoc hypocenter locations. Red filled circles (Oct18-1) and yellow filled stars (Oct18-2) show the result of HypoDD. Title represents data set used (ct=catalog times, cct=cross-correlation times, from cluster or catalog represents the inversion starting point). Hypocenter locations are always displayed in map view and corresponding West-East depth slice below.
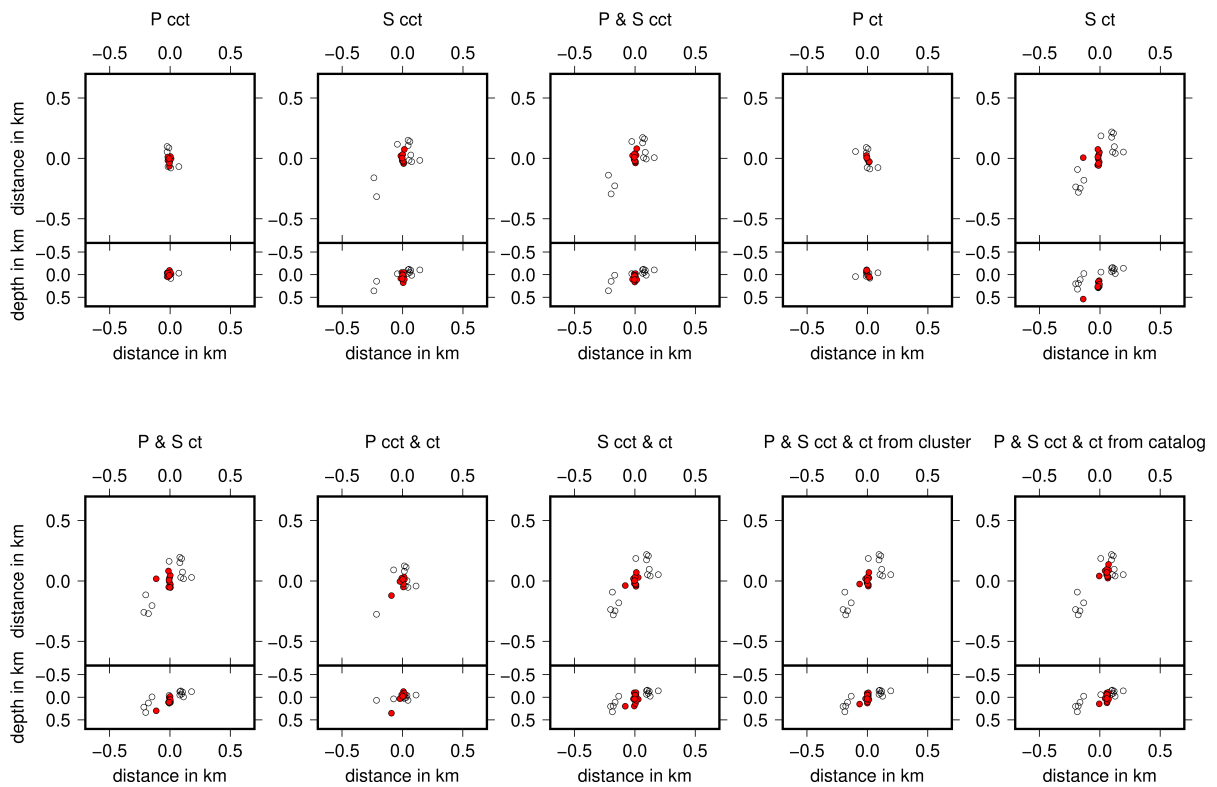
Figure C.8.: Comparison of HypoDD performance with different data sets on the Jan20 earthquake sequence. Black circles represent NLLoc hypocenter locations. Red filled circles show result of HypoDD. Title represents data set used (ct=catalog times, cct=cross-correlation times, from cluster or catalog represents the inversion starting point). Hypocenter locations are always displayed in map view and corresponding West-East depth slice below.

Figure C.9.: Comparison of HypoDD performance with different data sets on the Nov20 earthquake sequence. Black circles represent NLLoc hypocenter locations. Red filled circles show result of HypoDD. Title represents data set used (ct=catalog times, cct=cross-correlation times, from cluster or catalog represents the inversion starting point). Hypocenter locations are always displayed in map view and corresponding West-East depth slice below.
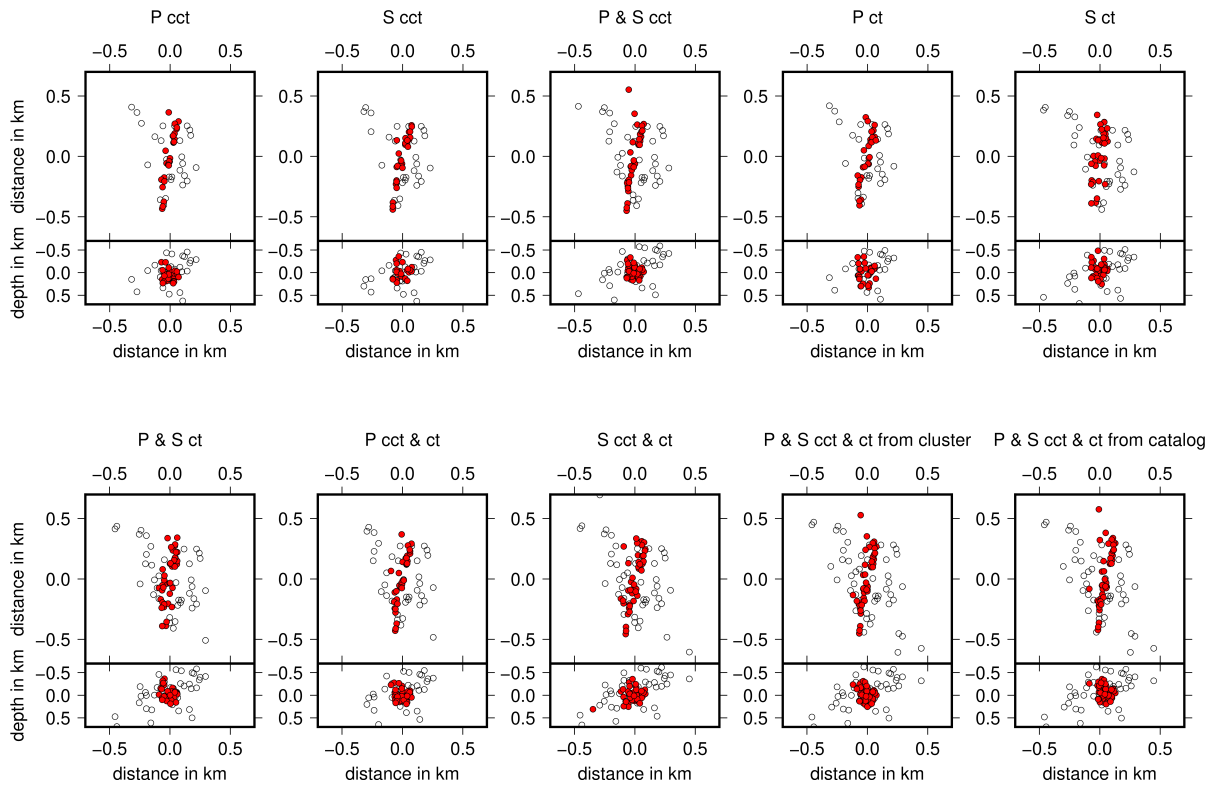
Figure C.10.: Comparison of HypoDD performance with different data sets on the Dec20 earthquake sequence. Black circles represent NLLoc hypocenter locations. Red filled circles show result of HypoDD. Title represents data set used (ct=catalog times, cct=cross-correlation times, from cluster or catalog represents the inversion starting point). Hypocenter locations are always displayed in map view and corresponding West-East depth slice below.
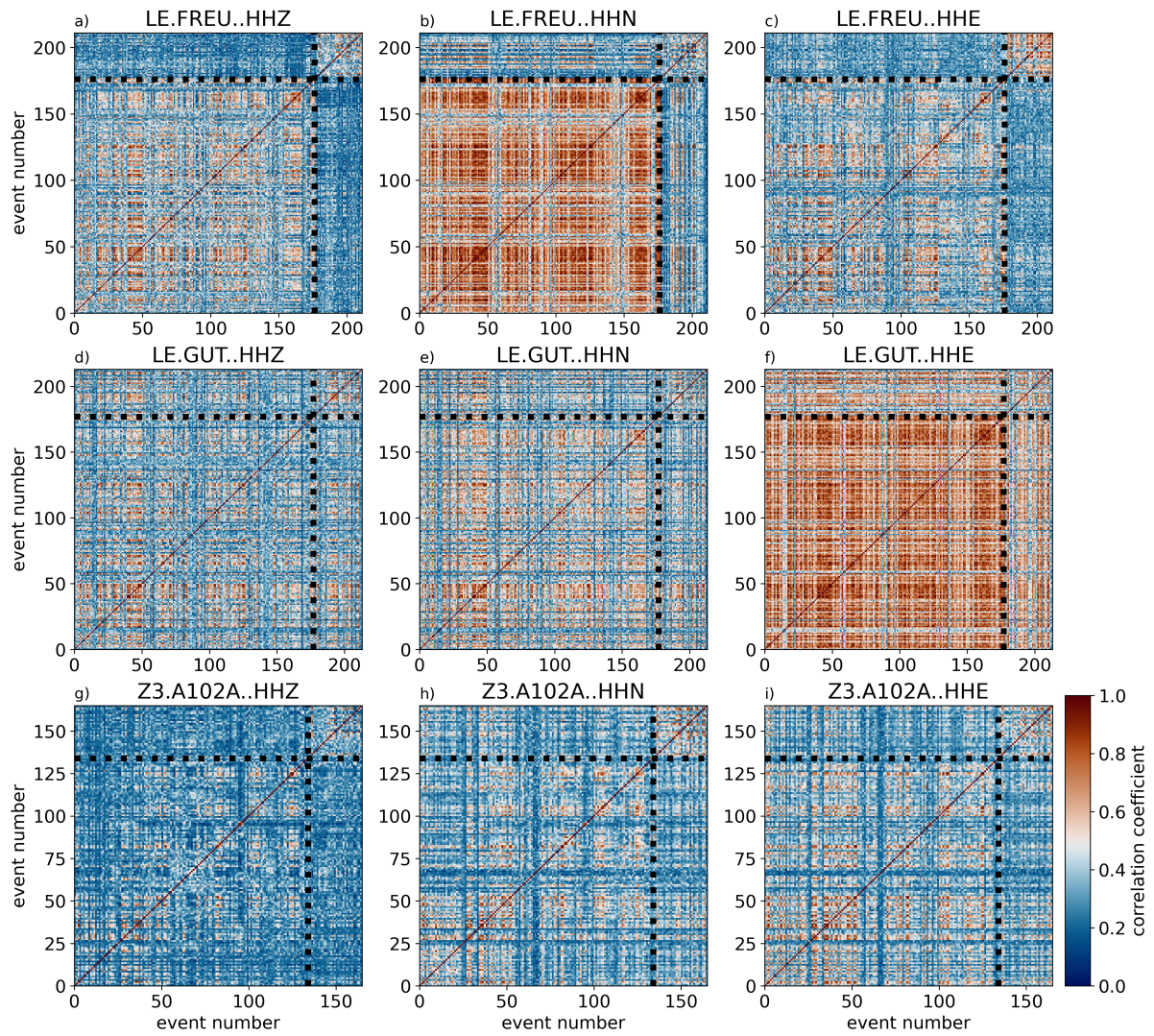
Figure C.11.: Similarity matrices for the Oct18 earthquake sequence at the seismic stations FREU, GUT, and A102A based on waveform similarity. The station FREU is the closest station to the earthquake sequence location (about 7 km). Black dashed lines display the boundary between events in October 2018 to events in November 2018. Event number is consecutive with time .